Nonlinearities facilitate the encoding of a wide range of beat frequencies and amplitudes in primary electrosensory afferents

Dissertation

zur Erlangung des Grades eines
Doktors der Naturwissenschaften

der Mathematisch-Naturwissenschaftlichen Fakultät
und
der Medizinischen Fakultät
der Eberhard-Karls-Universität Tübingen

vorgelegt
von

Alexandra Barayeu

2024

Tag der mündlichen Prüfung: 12.04.2024

Dekan der Math.-Nat. Fakultät: Prof. Dr. Thilo Stehle
Dekan der Medizinischen Fakultät: Prof. Dr. Bernd Pichler

1. Berichterstatter: Prof. Dr. Jan Benda

2. Berichterstatter: Prof. Dr. Benjamin Lindner

Prüfungskommission: Prof. Dr. Jan Benda

Prof. Dr. Benjamin Lindner

Prof. Dr. Anna Levina

Prof. Dr. Aristides Arrenberg

Erklärung / Declaration:

Ich erkläre, dass ich die zur Promotion eingereichte Arbeit mit dem Titel:

„Nonlinearities facilitate the encoding of a wide range of beat frequencies and amplitudes in primary electrosensory afferents“

selbständig verfasst, nur die angegebenen Quellen und Hilfsmittel benutzt und wörtlich oder inhaltlich übernommene Stellen als solche gekennzeichnet habe. Ich versichere an Eides statt, dass diese Angaben wahr sind und dass ich nichts verschwiegen habe. Mir ist bekannt, dass die falsche Abgabe einer Versicherung an Eides statt mit Freiheitsstrafe bis zu drei Jahren oder mit Geldstrafe bestraft wird.

*I hereby declare that I have produced the work entitled "*Nonlinearities facilitate the encoding of a wide range of beat frequencies and amplitudes in primary electrosensory afferents*", submitted for the award of a doctorate, on my own (without external help), have used only the sources and aids indicated and have marked passages included from other works, whether verbatim or in content, as such. I swear upon oath that these statements are true and that I have not concealed anything. I am aware that making a false declaration under oath is punishable by a term of imprisonment of up to three years or by a fine.*

Tübingen, den ....

Datum / Date Unterschrift /Signature

Abstract

In this work, the influence of nonlinearities on stimulus encoding in the primary sensory afferents of weakly electric fish of the species *Apteronotus leptorhynchus* was investigated. These fish produce an electric organ discharge (EOD) with a fish-specific frequency. When the EOD of one fish interferes with the EOD of another fish, it results in a signal with a periodic amplitude modulation, called beat. The beat provides information about the sex and size of the encountered conspecific and is the basis for communication. The beat frequency is predicted as the difference between the EOD frequencies and the beat amplitude corresponds to the size of the smaller EOD field. Primary sensory afferents, the P-units, phase-lock to the EOD and encode beats with changes in their firing rate. In this work, the influence of nonlinearities on the encoding of beat parameters such as frequency and amplitude was investigated. It was demonstrated that a smooth threshold nonlinearity at the synapse between electroreceptors and P-unit afferents enables the representation of high beat frequencies in a two-fish scenario, thus providing the basis for potential interspecies communication. Second-order susceptibility in the spiking response of regular firing P-units, was demonstrated to contribute to the detection of faint signals in a three-fish setting, the so-called "electrosensory cocktail party". Bursting was identified to increase this nonlinearity. Two-beat suppression and the reduced representation of the receiver EOD in the firing rate of P-units were found to contribute to the encoding of a wide range of beat amplitudes on a single-cell level.

Acknowledgments

First and foremost I would like to thank Jan Benda for his guidance and supervision of my PhD thesis. During my PhD time, I had the great opportunity to learn how to do experiments, analyze the resulting data and model neuronal activity. In addition, I could develop my interpersonal skills in a scientific setting in the lab and at several international meetings.

Second, I want to thank Jan Grewe for supporting my experimental work. Furthermore, I would like to thank my collaborators Benjamin Lindner and Maria Schlungbaum for their contribution to the work on the electrosensory cocktail party problem. Also, I would to thank our lab members, especially Philippa Hennessey, for their support. I am thankful for the funding I received from the DFG Priority Programme "Evolutionary Optimisation of Neuronal Processing" (SPP 2205) and to Britta Korkowsky, for the organization of this program.

Finally, I would like to thank my parents and my husband who have supported me in this journey.

Contents

1 Introduction **1**

1.1 The neuronal system shapes our perception . . . 1
1.2 Integration of information in neurons enables object perception . . . 1
1.3 The neuronal system as a black box . . . 2
1.4 Step stimuli to investigate information processing . . . 2
1.5 Stimuli in our sensory environment are dynamic . . . 3
1.6 Linear systems theory . . . 3
1.7 Fourier analysis . . . 4
1.8 Amplitudes and phases changed in a linear system . . . 5
1.9 Neurons encode stimuli with action potentials . . . 6
1.10 Tuning curves . . . 7
1.11 Noise instead of pure sine waves stimulation . . . 8
1.12 Neuronal systems are inherently nonlinear . . . 8
1.13 Nonlinear response theory . . . 9
1.13.1 The firing rate can be approximated by a Volterra series . . . 9
1.13.2 The necessity of the second-order response . . . 10
1.14 Weakly electric fish . . . 13
1.15 Beats, a social communication signal . . . 14
1.16 Wide dynamic range of beat amplitudes . . . 15
1.17 Beat frequency calculated as the difference frequency . . . 16
1.18 Three fish in the electrosensory cocktail party . . . 18
1.19 Overview . . . 19
1.19.1 Nonlinearity at high beat frequencies . . . 19
1.19.2 Second-order susceptibility in a three-fish setting . . . 19
1.19.3 Nonlinearities can improve faint signal detection . . . 19
1.19.4 Encoding of strong beat amplitudes . . . 19

2 Methods **21**

2.1 Experimental subject details . . . 21
2.2 Surgery . . . 21
2.3 Experimental setup . . . 21
2.4 Identification of P-units and ampullary cells . . . 22
2.5 Field recordings . . . 22
2.6 Stimulation . . . 22
2.6.1 High beat frequency stimuli in two-fish setting . . . 22
2.6.2 White noise stimuli . . . 23
2.6.3 Two-beat suppression stimuli . . . 23
2.7 Data analysis . . . 24
2.7.1 Baseline calculation . . . 24
2.8 High beat frequencies data analysis . . . 24

2.8.1 Firing rate calculation . . . 24
2.8.2 Spectral analysis . . . 24
2.9 Second-order susceptibility data analysis . . . 25
2.9.1 Bursting . . . 25
2.9.2 Response modulation . . . 25
2.9.3 Spectral analysis . . . 25
2.9.4 Nonlinearity index . . . 26
2.10 Faint signal detection data analysis . . . 27
2.10.1 Receiver operating characteristics (ROC) . . . 27
2.10.2 Area under the curve (AUC) . . . 27
2.10.3 Detection improvement by the female presence . . . 28
2.10.4 Spectral analysis: Nonlinearity quantification . . . 28
2.11 Data analysis for varying beat amplitudes . . . 28
2.11.1 F-I Curves . . . 28
2.11.2 Spectral analysis . . . 28
2.12 Leaky integrate-and-fire models . . . 29
2.12.1 Numerical implementation . . . 31
2.12.2 Model parameters . . . 31
2.13 Stimuli for the model . . . 31
2.14 Second-order susceptibility analysis of the model . . . 31
2.14.1 Model noise split into a noise and a stimulus component . . . 32
2.14.2 Artificial bursts in the model . . . 32
2.14.3 Field-distance calculation . . . 32
2.15 Behavioral experiments . . . 33
2.15.1 Jamming avoidance response . . . 33

3 Nonlinearity at high beat frequencies 35
3.1 Results . . . 36
3.1.1 High beat frequency encoding . . . 36
3.1.2 Responses to low difference frequencies . . . 36
3.1.3 Envelope frequency does not match difference frequency for high stimulus frequencies . . . 38
3.1.4 P-units respond to a wide range of stimulus frequencies . . . 38
3.1.5 Aliasing structure of beat responses . . . 39
3.1.6 Periodic amplitude tuning curve . . . 39
3.1.7 Amplitude tuning depends on post-synaptic filtering . . . 39
3.1.8 Sensitive cells respond to a larger frequency range . . . 41
3.1.9 Algorithms for extracting envelope frequencies . . . 41
3.1.10 Slow beating envelopes in superimposed cosine waves . . . 42
3.1.11 Analytic signal, squaring do not explain aliasing structure . . . 42
3.1.12 Thresholding explains aliasing at odd multiples of the carrier frequency . 44
3.1.13 Threshold cubed fills in frequencies at around twice the carrier frequency 46
3.1.14 Spiking dynamics cannot explain responses to higher beat frequencies . . 48
3.1.15 A power of three describes P-unit responses best . . . 48
3.1.16 Harmonics of the carrier are not sufficient to explain aliasing . . . 51
3.1.17 Beats with the same envelope frequency evoke similar behavioral responses 51
3.2 Discussion . . . 52
3.2.1 P-unit tuning to high difference frequencies . . . 52
3.2.2 Envelope extraction at high difference frequencies . . . 53
3.2.3 Extraction of secondary envelopes . . . 54

3.2.4 Sinusoidal amplitude modulations (SAMs) versus beats 54
3.2.5 Relation to the sampling theorem 54
3.2.6 Physiological mechanisms for beat extraction 55
3.2.7 Ambiguity in beat perception 55
3.2.8 Perception of other wave-type species 56
3.2.9 Beat perception in the auditory system 56
3.2.10 Nonlinear physiological mechanisms in the mammalian auditory periphery 56
3.2.11 Conclusion 57

4 Second-order susceptibility in a three-fish setting 59
4.1 Results 62
4.1.1 Low-CV P-units exhibit nonlinear interactions 62
4.1.2 High-CV P-units do not exhibit any nonlinear interactions 64
4.1.3 Ampullary cells exhibit strong nonlinear interactions 65
4.1.4 Full nonlinear structure visible only in P-unit models 65
4.1.5 Similar nonlinear effects with RAM and sine-wave stimulation 67
4.1.6 Low CVs are associated with strong nonlinearity on a population level . 68
4.1.7 Bursting boosts second-order susceptibility 69
4.1.8 More spikes in burst package increase the nonlinearity 71
4.1.9 Bursts influence nonlinearity on a population level 72
4.1.10 Nonlinearity in P-units of *Eigenmannia virescens* 72
4.2 Discussion 75
4.2.1 Methodological implications 75
4.2.2 Nonlinearity and CV 76
4.2.3 Bursting as a mechanism for amplitude encoding 76
4.2.4 Bursting increases nonlinearity and linearity in P-units 77
4.2.5 Encoding of secondary envelopes 77
4.2.6 Nonlinearity necessary to sustain in different species? 78
4.2.7 More fish would decrease second-order susceptibility 78
4.2.8 Conclusion 78

5 Nonlinearities can improve faint signal detection 81
5.1 Results 82
5.1.1 A faint intruder is not detectable alone 83
5.1.2 Intruder detection can be improved by female presence 84
5.1.3 Nonlinear interactions between intruder- and female-induced beat frequencies improve intruder detectability 85
5.1.4 The intruder detection is improved in larger homogeneous populations . . 87
5.1.5 Detection improvement only at certain beat frequencies 87
5.1.6 Detection improvement in low-CV cells 89
5.2 Discussion 90
5.2.1 Nonlinear effects mediate intruder detection 90
5.2.2 Readout from P-unit populations 91
5.2.3 Prerequisites for electrophysiological P-unit recordings for a ROC analysis 93
5.2.4 Electrosensory cocktail party problem for different species and cells . . . 95
5.2.5 Conclusion 95

6 Encoding of strong beat amplitudes **97**
6.1 Results . . . 99
6.1.1 Two-beat suppression in a LIF P-unit model . . . 99
6.1.2 High difference between the beat frequencies: only one beat representation will be decreased in the two-beat condition . . . 102
6.1.3 Similar beat frequencies: both beat representation will be decreased in the two-beat condition . . . 102
6.1.4 Two-beat suppression in recorded P-units . . . 104
6.1.5 High contrasts can reduce the EOD representation in the P-unit firing rate 104
6.2 Discussion . . . 106
6.2.1 Two-beat suppression in P-units . . . 106
6.2.2 Has the reduction of the EOD in the response of P-units an attention-orienting function? . . . 108
6.2.3 Nonlinear effects in P-units at high beat contrasts . . . 108
6.2.4 Dynamic range encoding of beat contrasts associated with two encoding regimes . . . 109
6.2.5 Encoding of strong beat amplitudes in the auditory system . . . 109
6.2.6 Conclusion . . . 110

7 Conclusion **111**

Bibliography **112**

A Appendix **125**
A.1 Mathematical derivations . . . 125
A.1.1 Analytic signal . . . 125
A.1.2 Squaring . . . 127
A.1.3 Thresholding . . . 127
A.1.4 Threshold cubed . . . 129
A.1.5 Thresholding a SAM . . . 130
A.1.6 Harmonics of the carrier . . . 130
A.1.7 Harmonics of the stimulus . . . 131
A.1.8 Tuning of P-units to EOD frequency . . . 131

B Statement of Contributions **133**
B.1 Chapter 3: Nonlinearity at high beat frequencies . . . 133
B.2 Chapter 4: Second-order susceptibility in a three-fish setting . . . 133
B.3 Chapter 5: Nonlinearities can improve faint signal detection . . . 133
B.4 Chapter 6: Encoding of strong beat amplitudes . . . 134

Chapter 1

Introduction

1.1 The neuronal system shapes our perception

We live in a very complex and diverse sensory environment that is captured by the neuronal system with different sensory modalities such as vision (Adelson and Bergen, 1985; Pugh Jr et al., 1999; Barlow et al., 1957), audition (Evans, 1981; Preyer and Gummer, 1996; Liberman, 1982), taste (Margolskee, 2002), olfaction (Amoore, 1986) and somatosensation (Lamore et al., 1986) in humans, magnetosensation in birds (Merkel and Wiltschko, 1965) and electrosensation in aquatic animals (Gussin et al., 2007; Bastian, 1981; Nelson et al., 1997; Benda et al., 2005). Sensory cells, also known as receptors, are the first stage, where the physical information (e.g. sound, vibration, or smell) is transferred into an electrical signal. Receptors are innervated by primary sensory afferent fibers, that transfer the information toward the central neural system and the brain. Each modality can represent wide ranges of stimuli in their primary sensory afferents with 20 Hz to 20 kHz audible frequencies (Kandel et al., 2000), 1 trillion odors (Bushdid et al., 2014), and up to 14 log units of luminance in the human visual system (Kunkel and Reinhard, 2010; Ferwerda et al., 1996). This detailed representation of the external surroundings is processed in the sensory pathway, leading to an unimodal percept as a picture, a smell or a sound. These unimodal percepts contribute to a multimodal experience as an exquisite taste, a captivating symphony, or a touching movie and evoke emotions leading to unique memory formation. With this, the neuronal system is the prism that defines and constrains how we perceive the world.

1.2 Integration of information in neurons enables object perception

The intriguing question is to understand how information is processed in the neuronal system. A well-studied example of information processing in a sensory pathway is the visual system. In the eye, the picture is focused on the retina, where photons lead to membrane potential changes in photoreceptors. From photoreceptors the information is integrated by bipolar cells and then by ganglion cells that process visual signals as pixels with center-surround responses (Caldwell and Daw, 1978). Several center-surround cells are integrated by so-called "simple cells" (Hubel and Wiesel, 1959), that respond to bar orientations. The information of several simple cells is integrated by so-called "complex cells", that respond not to bar orientations but to bar movements (Hubel and Wiesel, 1962, 1965). Complex cells can be described with a squaring nonlinearity in terms of the energy model (Adelson and Bergen, 1985). Neurons in higher processing areas can detect unique objects as described by the idea of the grandmother cell (Gross, 2002). An example of a grandmother cell is a neuron with selective activation after

the presentation of the face of Jennifer Aniston from different perspectives (Quiroga et al., 2005). Similar information processing, with simple elements being transformed into a more complex and meaningful representation, can be found in all sensory modalities (Koelsch and Siebel, 2005; Briand and Salles, 2016).

1.3 The neuronal system as a black box

Information processing in the neuronal system can be studied with different approaches on a single cell level (Benda et al., 2005; Gussin et al., 2007; Grewe et al., 2017), on a population level with EEG (Juergens et al., 1999; Cunningham et al., 2017) and fMRI (Dux et al., 2006) or with neuronal models (Voronenko and Lindner, 2017; Schlungbaum and Lindner, 2023). Despite the constant development of these methods many processing steps in the neuronal system are not comprehensively described and understood. Any investigated process in the neuronal system, whether it can be located in a single cell or the whole sensory pathway, can be pictured as a black box (Fig. 1.1). During an experiment, only the input or stimulus $s(t)$ and the output or response $r(t)$ of the black box are known. The input to the black box can be any stimulus, from a simple tone to a complex behavioral task, and the output can be any response, from an electrical signal recorded in a neuron to a behavioral reaction. A systematic variation of the input and the observation of the resulting response can help to retrieve the processing rules of the neuronal system, as described with $H\{s(t)\}$.

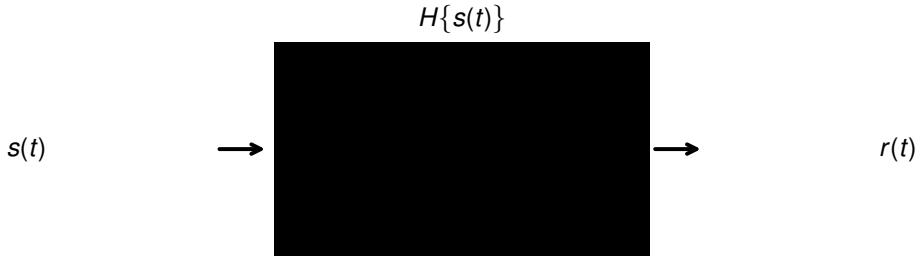

Figure 1.1: The neuronal system can be pictured as a black box, with only the stimulus $s(t)$ and the response $r(t)$ of the black box being known. $H\{s(t)\}$ describes the transformations of the stimulus in the black box.

1.4 Step stimuli to investigate information processing

A simple method to investigate information processing is the use of step stimuli (Fig. 1.2 A), where an initial stimulus, which will be termed baseline (black line), is increased (yellow, orange, red, purple lines) or decreased (cyan, light blue, blue, dark blue lines) in a stepwise manner for a limited duration, after that the baseline is restored. Each change in the stimulus $s(t)$ can be related to the corresponding response strength of the system (Fig. 1.2 B). The response function to step stimuli is often described by a sigmoidal function and the single datapoints can be fitted by a Boltzmann function $f_{(I)} = r_{max}(1 + e^{-k(I-I_{Base})})^{-1}$, where r_{max} is the maximal response range, k is a factor influencing the slope, I is the stimulus intensity, and I_{Base} is the stimulus intensity during baseline (vertical line, Fig. 1.2 B). For intensities close to I_{Base} (range between -1 and 1) the response strength is proportional to the stimulus intensity, with the system linearly encoding stimulus intensities. For stimulus intensities stronger deviating from the baseline intensity I_{Base} (above 2 and below -2) the response strength is not proportional to the stimulus intensity anymore. Instead, the system response saturates, with

different stimulus intensities leading to similar responses, as 1 for increasing stimuli and 0 for decreasing stimuli. Step stimulation is a common scientific paradigm that can e.g. be found in psychophysical experiments with humans (Leek, 2001; Treutwein and Strasburger, 1999) or in single-cell recordings (Kiskinis et al., 2018; Avoli and Olivier, 1989; Gussin et al., 2007; Benda et al., 2005).

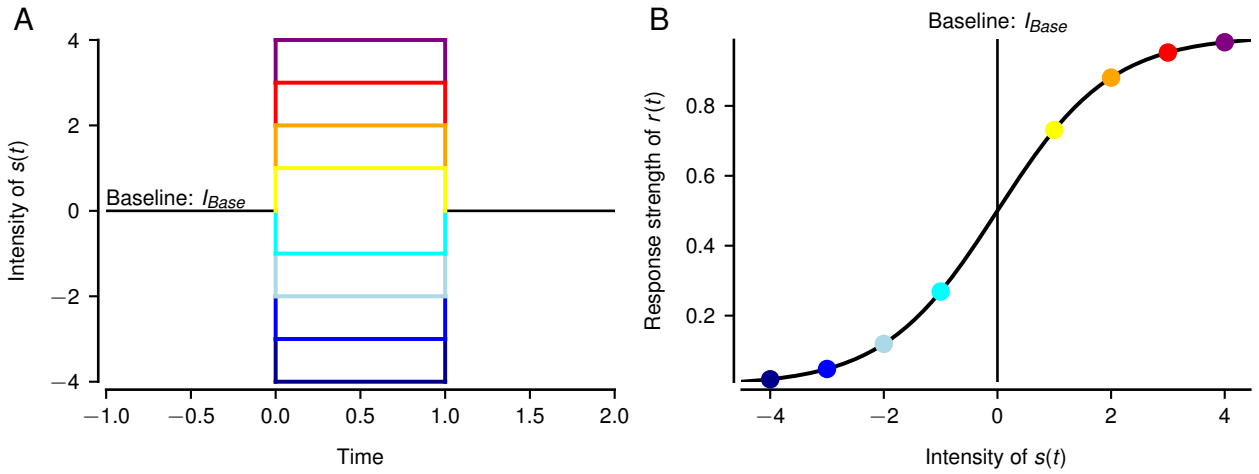

Figure 1.2: A scheme showing that step stimuli usually lead to a sigmoidal input-response relationship e.g. in psychometric functions of psychophysical investigations and on the single-cell level.
A Step stimuli. Black is the default stimulus (baseline) with an intensity of 0. The stimulus intensity is changed in a stepwise manner in the time window between 0 and 1. After that, the baseline stimulus is again restored. Stimulus step increases have the colors yellow, orange, red or purple. Stimulus step decreases have the colors cyan, light blue, blue or dark blue.
B In neuronal systems the response to step stimuli usually follows a sigmoidal shape. Vertical line – baseline intensity I_{Base}. The response of the system is proportional to the stimulus for values close to I_{Base}. For stimulus intensities below -2 or above 2, the response strength approaches saturation with the same response of 0 for decreasing and 1 for increasing step stimuli.

1.5 Stimuli in our sensory environment are dynamic

The advantage of step stimuli is that stimulus intensity is the only varied parameter, leading to a simple experimental paradigm. The disadvantage of step stimuli is that they are very artificial, as stimuli in natural environments change not discontinuously but vary dynamically. Instead of a step stimulus, the neuronal system can be probed with a more naturalistic stimulus, a sine wave (Fig. 1.3). Pure sine waves are used to investigate neuronal systems, eliciting behavioral reactions (Wöhr and Schwarting, 2007; Barayeu et al., 2023; Heiligenberg and Altes, 1978), responses on a population level with EEG (Juergens et al., 1999; Cunningham et al., 2017) or responses on a single cell level (Walz et al., 2014; Nelson et al., 1997; Hubel and Wiesel, 1959; Wypych et al., 2012).

1.6 Linear systems theory

The theory of linear systems maps the stimulus $s(t)$ with an operator $H\{s(t)\}$ to the response $r(t)$ (Fig. 1.3). $H\{s(t)\}$ can be described by different operations as an equation or a system

of differential equations. A system is described as linear if the homogeneity condition and the additivity condition both are satisfied. The homogeneity condition holds if the output is a scaled version of the input (Eq. (1.1)). The additivity condition holds if the sum of the inputs to the system is equal to the sum of the outputs of the system (Eq. (1.2)). This implies that no other frequencies, besides the input frequencies, are generated in the system.

$$H\{\alpha s(t)\} = \alpha H\{s(t)\} \tag{1.1}$$

$$H\{s_1(t) + s_2(t)\} = H\{s_1(t)\} + H\{s_1(t)\} \tag{1.2}$$

A linear system can be completely described by its impulse response $h(t)$, which can be measured once probing a system with a short impulse and recording the time-varying response. Once $h(t)$ is known, the response $r(t)$ can be computed by a convolution $r(t) = s(t) * h(t) = \int_{-\infty}^{\infty} s(t)h(t-t')dt'$. A convolution is an operation where one function is shifted to each position of the other function, multiplied with it and the results are summed up, leading to the response $r(t)$ of a linear system.

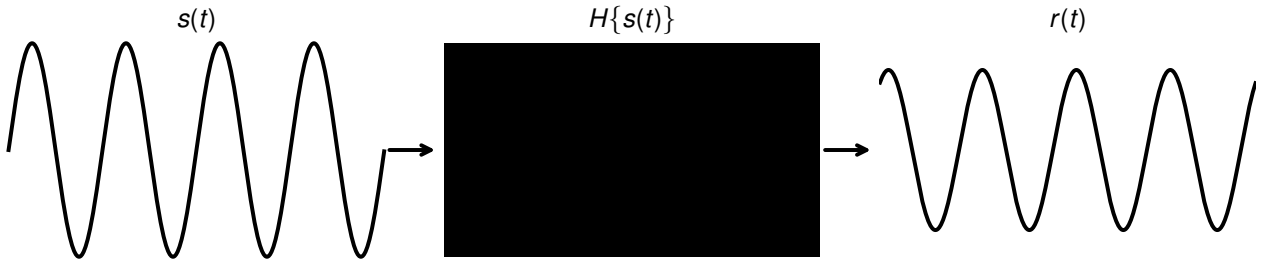

Figure 1.3: Linear systems theory. A stimulus $s(t)$ is the input into a black box where the stimulus is mapped with an operator $H\{s(t)\}$ to a response $r(t)$. In this example, $s(t)$ and $r(t)$ have the same frequency but differ by a phase shift and by a scaling factor: $s(t) = \sin(2\pi ft)$, $r(t) = 0.75\sin(2\pi ft + 1)$, $f = 40\,\text{Hz}$.

1.7 Fourier analysis

Linear transformations can induce changes in the amplitude of a sine wave (y-axis) and shifts in the phase (x-axis) between the input $s(t)$ and the output $r(t)$ (as in Fig. 1.3). When a linear system is probed only with one sine wave, changes in amplitude and phase can be easily identified by visual comparison between $s(t)$ and $r(t)$. In reality, stimuli often consist not only of a single sine wave but can be described by the linear combination of several sine waves. Even if only two sine waves with different frequencies interfere, those sine waves are not perceivable in the final signal anymore (Fig. 1.4 A). The phase and amplitude changes of the single sine waves cannot be visually detected when comparing the input signal $s(t)$ with the response $r(t)$ (compare Fig. 1.4 A and Fig. 1.4 B). Instead, the amplitude changes become clear when plotting the amplitude for all possible sine wave frequencies (Fig. 1.4 C, D). Such a transformation from the time domain (Fig. 1.4 A, B) to the frequency domain (Fig. 1.4 C, D) is possible with the Fourier transform. In the Fourier transform

$$\tilde{s}(\omega) = \int_{-\infty}^{\infty} dt\, s(t) \cdot e^{-i\omega t} \tag{1.3}$$

an integral over the time signal $s(t)$ and a complex number $e^{-i\omega t}$ results in a complex-valued function $\tilde{s}(\omega)$, containing the phase and the amplitude information for all frequencies ω.

Based on Euler's formula a complex number can be expressed as a sum of a real and an imaginary part $e^{i\varphi} = \cos(\varphi) + i\sin(\varphi) = a + ib$, where i is the imaginary unit and φ the phase. Historically $i = \sqrt{-1}$ was introduced to solve the equation $x^2 = -1$, which would have no solution if only real numbers would be considered. The real and imaginary parts span the complex plane, with the complex number being a vector with an amplitude and a phase φ. The phase can be calculated as the counter-clockwise angle between the vector and the real axis as the argument $\arg \tilde{s}(\omega)$. The absolute value or modulus of a complex number

$$|\tilde{s}(\omega)| = \sqrt{a^2 + b^2} = \sqrt{(a + ib)(a - ib)} \tag{1.4}$$

is calculated as the Pythagoras between the real and the imaginary part of a complex number and represents the amplitude of the signal. A power spectrum $|\tilde{s}(\omega)|^2$ can be used to compare the amplitude changes between the input signal $s(t)$ and the output signal $r(t)$ for all frequencies (compare Fig. 1.4 C and Fig. 1.4 D).

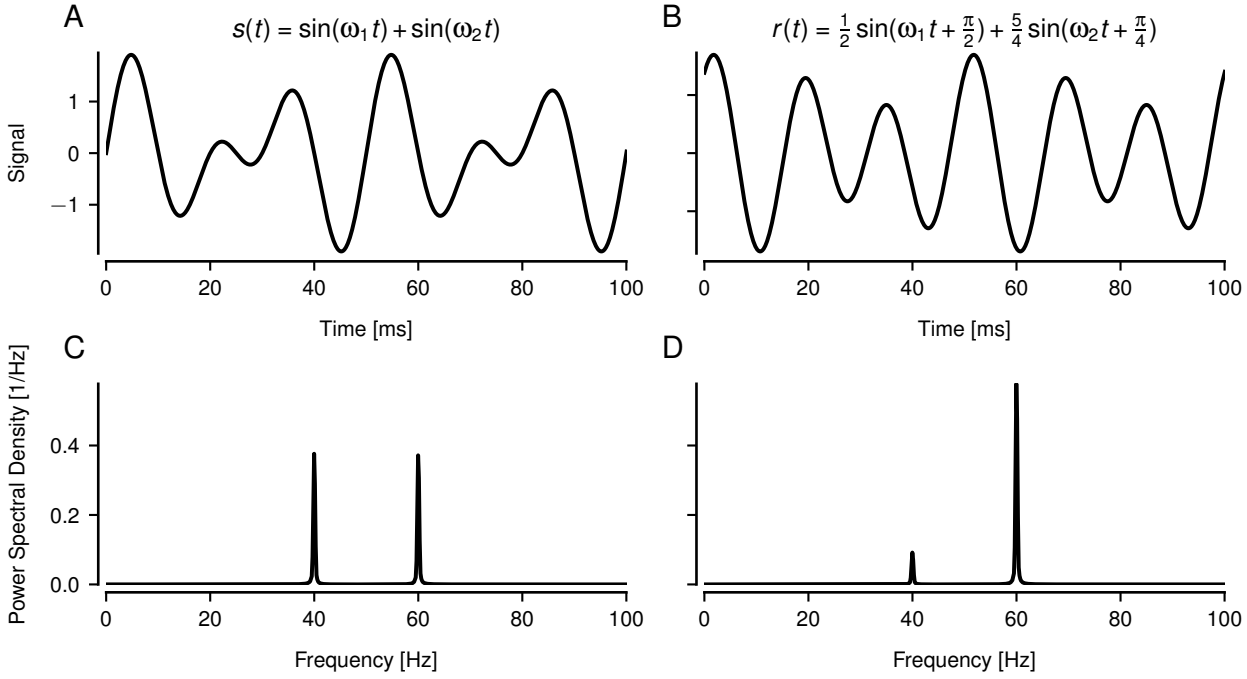

Figure 1.4: Relation between time domain and frequency domain. $\omega_1 = 2\pi \cdot 40\,\text{Hz}$. $\omega_2 = 2\pi \cdot 60\,\text{Hz}$
A Time-varying input signal $s(t)$.
B Time-varying output signal $r(t)$.
C Power spectrum of the signal in A.
D Power spectrum of the signal in B.

1.8 Amplitudes and phases changed in a linear system

As in the time domain a linear system can be fully described by the impulse response $h(t)$, in the frequency domain a linear system can be completely described by the complex-valued transfer function $\tilde{h}(\omega)$. Based on the convolution theorem, a convolution in the time domain $r(t) = s(t) * h(t)$ is the same as a multiplication in the frequency domain $\tilde{r}(\omega) = \tilde{s}(\omega) \cdot \tilde{h}(\omega)$. Since multiplication is a simpler mathematical operation than a convolution, the impulse response is

usually not measured in the time domain but calculated as the Fourier transform of the transfer function, which can be retrieved as $\tilde{h}(\omega) = \tilde{r}(\omega)/\tilde{s}(\omega)$. A linear system can be characterized when probing it with several sine waves with different frequencies and recording the amplitude changes described by the gain $|\tilde{h}(\omega)|$ (Fig. 1.5 A) and the phase shifts described by $\arg \tilde{h}(\omega)$ (Fig. 1.5 B).

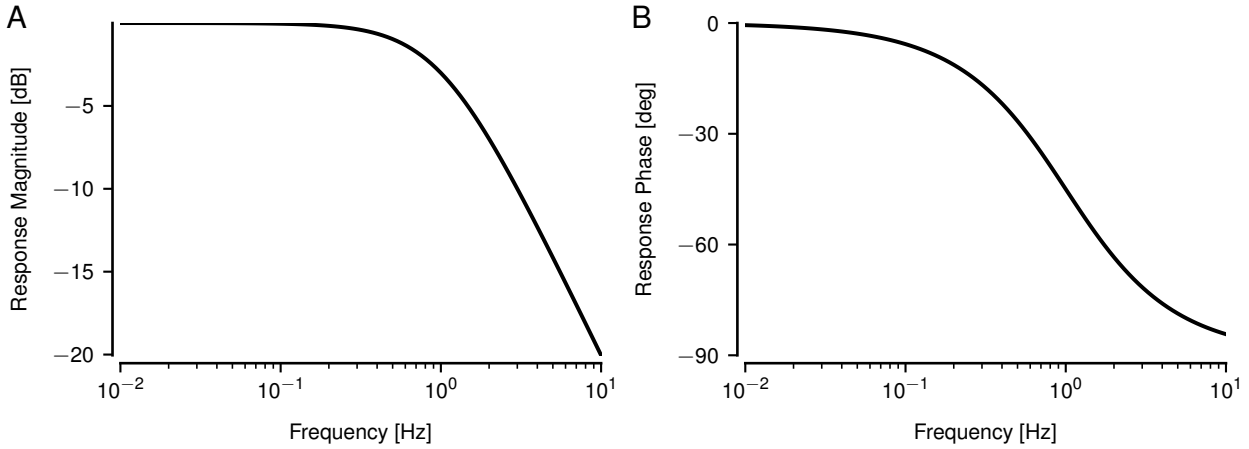

Figure 1.5: Bode plot of a linear system. Note that the changes are only an example and vary depending on the particular system.
A Response magnitude – log-normalized amplitude, calculated as $20 \log_{10} |\tilde{h}(\omega)|$.
B Phase changes calculated as $\arg \tilde{h}(\omega)$.

1.9 Neurons encode stimuli with action potentials

How neurons respond to different stimuli and how their response can be characterized will be presented in the following paragraph. A sensory pathway is a chain of several interconnected neurons. Inside a neuron, the information is transferred electrically, while between neurons the information can be transferred chemically via a synapse or electrically via a gap junction. The response of a neuron to stimuli can be measured with intracellular recordings, where the membrane potential changes of the neuron are recorded. Most of the time the membrane potential maintains a resting potential that is, depending on the cell type, between −50 and −75 mV. This resting potential is repeatedly interrupted by short (about 2 ms) and large voltage excursions (up to +40 mV) known as action potentials or spikes. Spikes are binary events, that can provide information about a stimulus (Fig. 1.6 A). Spikes are often visualized in a raster plot, with a tick at the time a spike occurred (Fig. 1.6 B). Neurons are inherently noisy and do not respond with the same spike train each time the same stimulus is presented (ticks are displaced between stimulus repetitions). Information between most neurons is transmitted chemically at the synapse between two neurons. At the synapse, spikes lead to the release of signaling molecules, so-called neurotransmitters, into the synaptic cleft, the space between two neurons. There the neurotransmitters bind to receptors in the membrane of the next-connected cell. A receptor is a protein structure that can change its form after the binding of a neurotransmitter, leading to a current outflux or influx into the next-connected cell. These are known as postsynaptic potentials (PSP) and can be excitatory (increasing the membrane potential) or inhibitory (decreasing the membrane potential). PSPs lead to smaller (several mV) and longer-lasting (several ms) voltage changes, than the ones induced by spikes. PSPs sum up in the next-connected cell and once a certain membrane potential threshold is reached a spike is generated. A PSP can be viewed as the impulse response of synaptic transmission

between two neurons. A PSP can be modeled by bins or filter kernels, that are convolved with the spike trains to compute the time-resolved firing rate (Fig. 1.6 C). Usually, PSPs low-pass filter the response, passing the low-frequency content and damping the high-frequency content (as in Fig. 1.5 A).

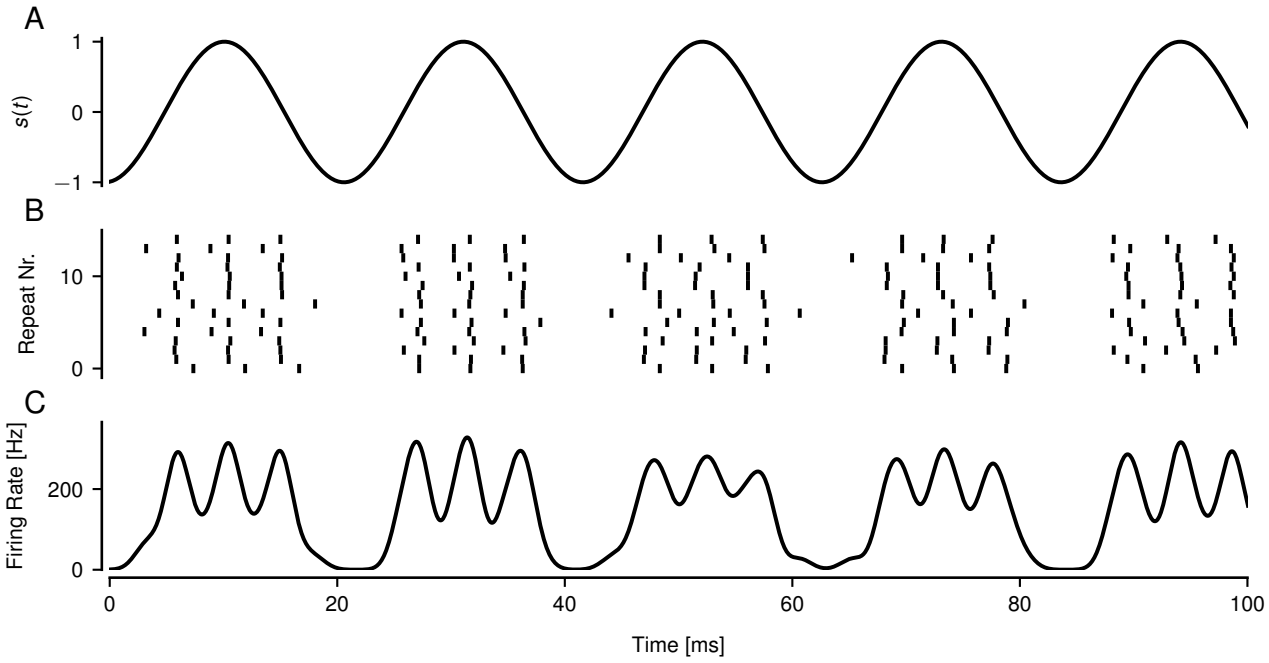

Figure 1.6: Neurons encode a stimulus with action potentials or spikes and with changes in their firing rate. Example spiking response, generated with a leaky integrate-and-fire (LIF) model of a neuron.
A Stimulus $s(t)$, with a frequency of 47 Hz.
B Spike trains of a LIF model in response to the stimulus above.
C Firing rate, derived by the convolution of the spike trains with a Gaussian filter kernel with a standard deviation of 1 ms, mimicking the PSPs induced by the spike trains in the next-connected cell.

1.10 Tuning curves

In neuronal systems it is a common paradigm to probe a neuron with pure sine waves with different frequencies and record the changes in the firing rate of a cell, resulting in a tuning curve (Hopkins, 1976; Palmer and Russell, 1986; Foster et al., 1985; Hawken et al., 1996). The response of a neuron can be characterized by different measures e.g. the mean firing rate changes (Hopkins, 1976), changes in the variation of a firing rate (Walz et al., 2013), or the amplitude of the strongest response peak in the power spectrum (Barayeu et al., 2023), leading to different tuning curves. A neuron is usually tuned best to a particular frequency, with the strongest response to it and a decreasing response for higher and lower frequencies. Such bell-shaped tuning is often associated with electric resonance in the receptors as in the auditory system (Hudspeth and Lewis, 1988) or in weakly electric fish (Viancour, 1979).

1.11 Noise instead of pure sine waves stimulation

Although tuning curves are often measured by probing a system with sine waves with different frequencies (Hopkins, 1976; Barayeu et al., 2023; Walz et al., 2013), it is a very time-consuming procedure, that might be not realistic for all recording protocols. Tuning curves can also be retrieved by probing the system with a band-pass filtered white noise stimulus, that simultaneously includes all frequencies of interest, each with randomly drawn amplitudes and phases (Fig. 1.7, Chacron et al., 2005; Grewe et al., 2017). Then the tuning curve can be retrieved as the transfer function. Noise stimuli are commonly used protocols in electrophysiological recordings and once recorded they can always be reused to retrieve the tuning curve of the neuron (Grewe et al., 2017; Neiman and Russell, 2011).

Figure 1.7: Band-pass filtered white noise $s(t)$, can be used to characterize the transfer function of a system and retrieve the tuning curve of a neuron. Left – input $s(t)$. Right – response $r(t)$.

1.12 Neuronal systems are inherently nonlinear

So far the linear systems theory has been introduced, but neuronal systems are inherently nonlinear with nonlinearities being observed in all sensory modalities (Adelson and Bergen, 1985; Brincat and Connor, 2004; Chacron et al., 2000, 2001; Nelson et al., 1997; Gussin et al., 2007; Middleton et al., 2007; Longtin et al., 2008).

One example of a nonlinearity is squaring $s(t)^2$, which doubles the input frequency and removes the fundamental in the response $r(t)$ (Fig. 1.8). Since squaring leads to frequencies in the response that were not present in the input, it violates the additivity condition necessary for linearity (see Eq. (1.2)). Squaring is utilized to explain the behavior of complex cells in the visual system in the framework of the energy model (Adelson and Bergen, 1985).

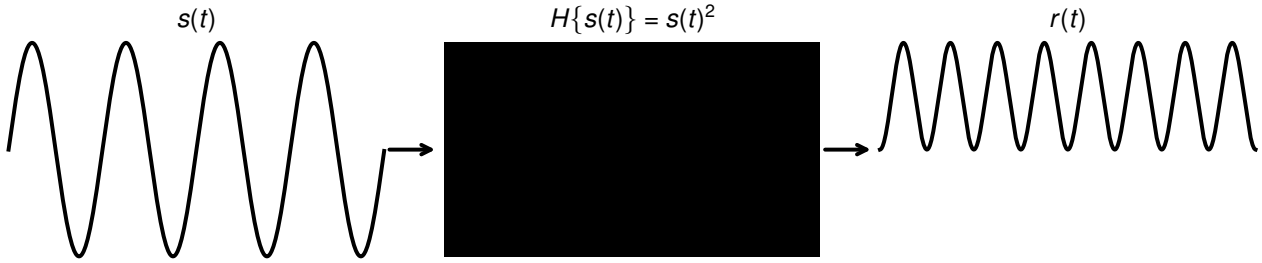

Figure 1.8: Squaring of the input signal $s(t)^2$ is a nonlinear operation. When a signal is squared $s(t)^2$, the fundamental is removed and the input frequency is doubled in the response $r(t)$.

Another example of a nonlinear operation is rectification $\lfloor s(t) \rfloor_0$, where all positive values remain unaltered but all negative values are discarded (Fig. 1.9). Rectification violates the additivity condition (Eq. (1.2)) since several sine waves are required to recreate the response $r(t)$. Rectification is assumed to be biologically plausible and to occur in sensory systems e.g. through the transduction machinery of inner hair cells (Peterson and Heil, 2019), signal rectification in receptor cells (Chacron et al., 2000, 2001) or the rheobase of action-potential generation (Middleton et al., 2007; Longtin et al., 2008).

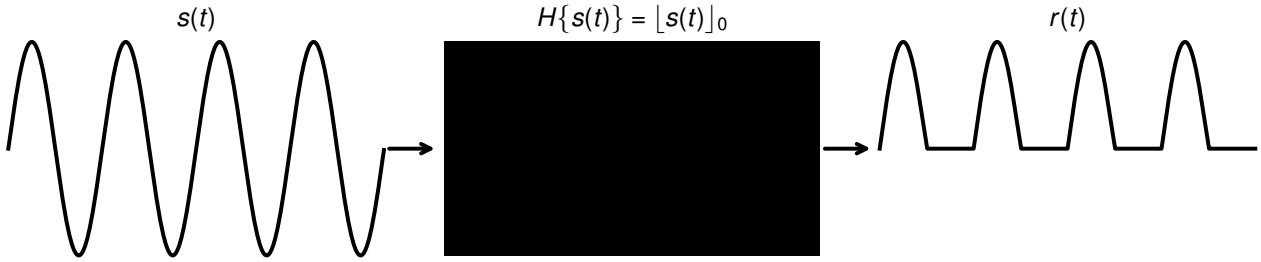

Figure 1.9: Rectification $\lfloor s(t) \rfloor_0$ is a nonlinear operation, with the positive values in the response $r(t)$ being maintained and the negative discarded.

1.13 Nonlinear response theory

1.13.1 The firing rate can be approximated by a Volterra series

Nonlinearities generated in a spiking response of neurons can be described with the nonlinear response theory, where the firing rate $r(t)$ of a neuron can be approximated by a Volterra series

$$r(t) = f_{Base} + \varepsilon \int dt_1' \, K_1(t_1') \cdot s(t - t_1') + \varepsilon^2 \int \int dt_2' dt_2'' \, K_2(t_2', t_2'') \cdot s(t - t_2') \cdot s(t - t_2'') + ... \quad (1.5)$$

where $s(t)$ is the input signal, ε its amplitude and f_{Base} the time-averaged firing rate during baseline when no stimulus is present (Rieke et al., 1999; Voronenko and Lindner, 2017; Schlungbaum and Lindner, 2023). A Volterra series consists of several n-th order convolutions of the input signal $s(t)$ with different kernels K_n. K_1 and K_2 are the first-order and second-order response kernels. If the spiking response of a neuron is linear its firing rate can be described only by the mean firing rate and the first-order response $r(t) = f_{Base} + \varepsilon \int dt_1' K_1(t_1') \cdot s(t - t_1')$ (first terms in Eq. (1.5)). Each next-order term allows more nonlinearity in the firing rate description. Depending on the nonlinearity of the neuron a finite Volterra series is sufficient to properly describe its dynamics.

As suggested by Voronenko and Lindner (2017), the Volterra series can be Fourier transformed to

$$\tilde{r}(\omega) = f_{Base}\delta(\omega) + \varepsilon \chi_1(\omega) \cdot \tilde{s}(\omega) + \varepsilon^2 \int d\omega' \, \chi_2(\omega - \omega', \omega') \cdot \tilde{s}(\omega - \omega') \cdot \tilde{s}(\omega') + ... \quad (1.6)$$

with $\chi_1(\omega) = \int dt \, K_1(t) \cdot e^{i\omega t}$ being the Fourier transform of the first-order response kernel and $\chi_2(\omega_1, \omega_2) = \int \int dt_1 dt_2 \, K_2(t_1, t_2) \cdot e^{i\omega_1 t_1} \cdot e^{i\omega_2 t_2}$ the Fourier transform of the second-order response kernel. Since the convolution in the time domain is a multiplication in the frequency domain, this simplifies the formulation.

1.13.2 The necessity of the second-order response

The firing rate of a neuron can be modeled with leaky integrate-and-fire (LIF) models, where the stimulus is transformed into a membrane voltage with spikes being generated once a threshold is reached. A recent study by Voronenko and Lindner (2017) revealed that the firing rate of a LIF model cannot be described by the linear response alone, but in addition requires the second-order response. In that study, it was demonstrated that when the frequency of the stimulus f_{stim} was equal to half f_{Base} the second harmonic $2f_{Stim}$ was visually perceivable in the firing rate, with two peaks present in a single stimulus cycle (Fig. 1.10 C). Not only the stimulus frequency f_{Stim} but also several of its harmonics appear in the power spectrum of the firing rate of the LIF model (Fig. 1.10 D). These harmonics cannot be captured by the linear term of the Volterra series alone and a second-order term of the Volterra series is required in addition.

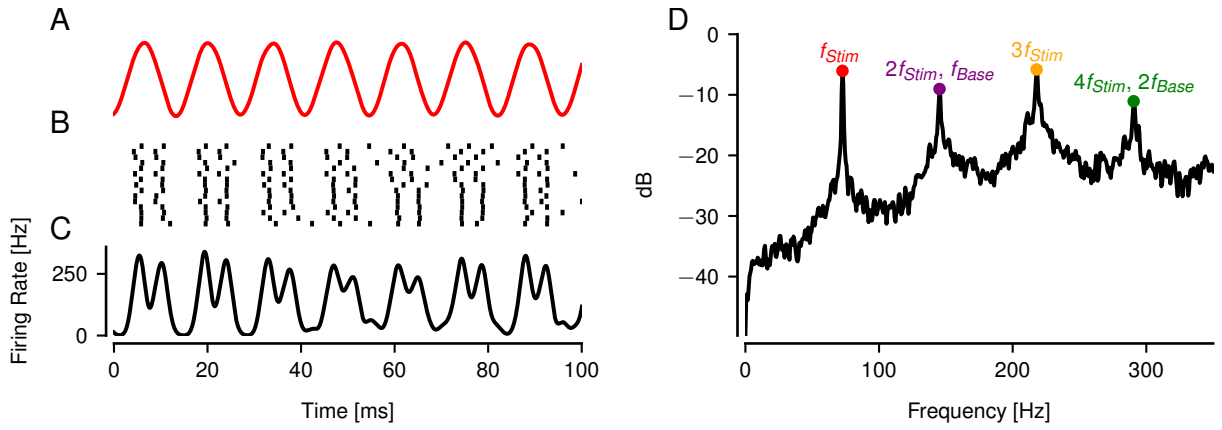

Figure 1.10: Based on Voronenko and Lindner (2017). A Volterra series with at least a second-order response is necessary to describe the nonlinearity appearing when f_{Stim} is equal to half f_{Base} in a LIF model.
A Stimulus with a frequency of $f_{Stim} = 72\,\text{Hz}$.
B Spike trains of a LIF model. The spike trains align with the stimulus above.
C Firing rate of the spike trains. Calculated as a convolution of the spike trains with a Gaussian kernel ($\sigma = 1\,\text{ms}$).
D Power spectrum of the firing rate in C. The fundamental f_{Stim} and its harmonics have pronounced peaks.

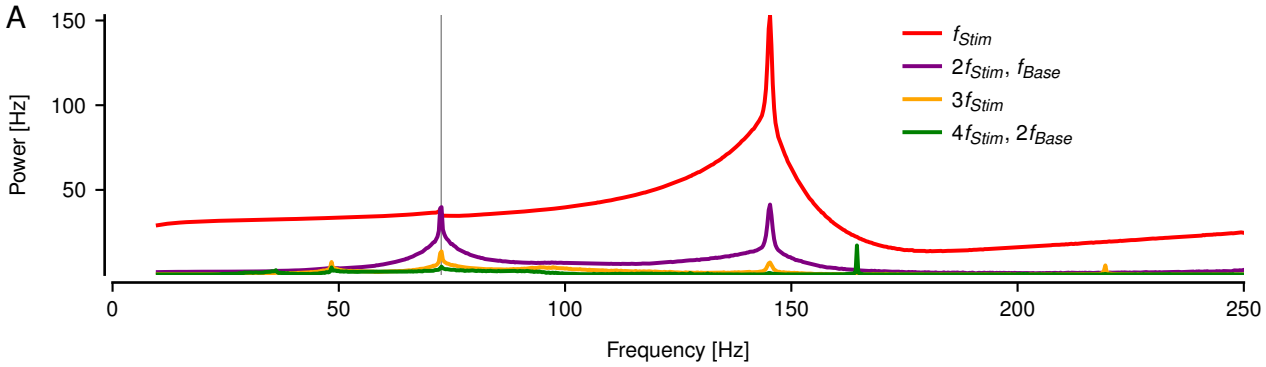

Figure 1.11: Based on Voronenko and Lindner (2017). Plotted are the peak amplitudes of the fundamental f_{Stim} and its harmonics in the power spectrum of the time-resolved firing rate of a LIF model. Nonlinear effects are especially strong when $f_{Stim} = f_{Base}/2$ (vertical line).

Voronenko and Lindner (2017) demonstrated that these strong nonlinear effects do not appear for most stimulus frequencies. This becomes apparent when plotting the peak size of all harmonics of f_{stim} in the power spectrum of the firing rate for different stimulus frequencies (Fig. 1.11). Then the second harmonic $2f_{Stim}$ has a higher value than the fundamental f_{Stim} once f_{Stim} is equal to half f_{Base} of the cell (gray vertical line). These findings highlight that at least a second-order response in the Volterra series is required to properly describe the firing rate of a LIF model for all stimulus frequencies.

The necessity of the second-order response has also been demonstrated when the stimulus consisted of two sine waves $\alpha\cos(\omega_1 t) + \beta\cos(\omega_2 t + \phi)$ with amplitudes α and β (Voronenko and Lindner, 2017). In that work, the sine waves were inserted into the Fourier-transformed Volterra series in Eq. (1.6), resulting in:

$$\begin{aligned} r(t) \approx [&f_{Base} + \frac{\varepsilon^2\alpha^2}{2}\chi_2(\omega_1,-\omega_1) + \frac{\varepsilon^2\beta^2}{2}\chi_2(\omega_2,-\omega_2)]_{Base} \\ &+ \varepsilon[\alpha|\chi_1(\omega_1)|\cos(\omega_1 t - \phi_1(\omega_1)) + \beta|\chi_1(\omega_2)|\cos(\omega_2 t + \phi - \phi_1(\omega_2))]_{LR} \\ &+ \frac{\varepsilon^2}{2}[(\alpha^2|\chi_2(\omega_1,\omega_1)|\cos(2\omega_1 t - \phi_2(\omega_1,\omega_1)) + \beta^2|\chi_2(\omega_2,\omega_2)|\cos(2\omega_2 t + 2\phi - \phi_2(\omega_2,\omega_2))]_{HH} \\ &+ \varepsilon^2\alpha\beta[|\chi_2(\omega_1,\omega_2)|\cos((\omega_1+\omega_2)t + \phi - \phi_2(\omega_1,\omega_2)) \\ &+ |\chi_2(\omega_1,-\omega_2)|\cos((\omega_1-\omega_2)t - \phi - \phi_2(\omega_1,-\omega_2))]_{MR} \end{aligned} \tag{1.7}$$

In this equation the terms in the bracket $[...]_{Base}$ described the average firing rate and in $[...]_{LR}$ the linear response. In the paragraphs before nonlinear effects as harmonics were demonstrated to appear in the LIF model firing rate in the one sine-wave setting (Fig. 1.10). In the two sine-wave setting nonlinear effects at the harmonics of the input frequencies are inside the brackets $[...]_{HH}$. Other than in the one sine-wave setting, in the two sine-wave setting nonlinearities can appear as a mixed response $[...]_{MR}$, at the difference and the sum of the two input frequencies.

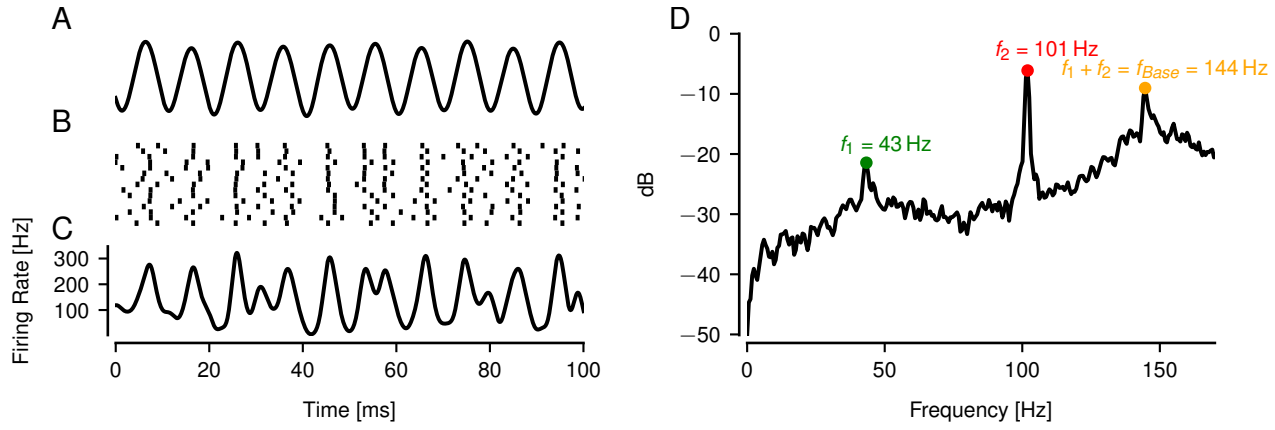

Figure 1.12: Based on Voronenko and Lindner (2017). Nonlinear effects occur when the input frequencies are in sum equal to f_{Base} (144 Hz) of the LIF model.
A Stimulus $s(t)$, consisting of two sine waves $s(t) = s_1(t) + s_2(t) = 3\sin(2\pi f_1 t) + 10\sin(2\pi f_2 t)$ with frequencies $f_1 = 43$ Hz and $f_2 = 101$ Hz.
B Spike trains of a LIF model. The spike trains align to the stimulus, especially to the strong stimulus component $s_2(t)$.
C Firing rate, calculated as a convolution of the spike trains with a Gaussian kernel ($\sigma = 1$ ms).
D Power spectrum of the firing rate in C. A nonlinear peak is present at $f_1 + f_2$. This peak is stronger than the weaker stimulus fundamental peak at f_1.

As in the one sine-wave setting, in a two sine-wave setting nonlinear interactions were described to occur only at specific frequency combinations (Voronenko and Lindner, 2017). Here those findings are illustrated with a LIF model, where the input consists of two sine waves $s(t) = s_1(t) + s_2(t) = 3\sin(2\pi f_1 t) + 10\sin(2\pi f_2 t)$ with the sum of the two frequencies being equal to f_{Base} ($f_1 = 43\,\text{Hz}$, $f_2 = 101\,\text{Hz}$, $f_{Base} = 144\,\text{Hz}$, Fig. 1.12). The sine wave with the smaller amplitude ($a_1 = 3$) is difficult to perceive in the stimulus (Fig. 1.12 A), in the firing rate (Fig. 1.12 C), and its frequency f_1 has only a small peak in the power spectrum of the firing rate (green marker, Fig. 1.12 D). The sine wave with the stronger amplitude ($a_2 = 10$) is clearly visible in the signal (Fig. 1.12 A), in the spike trains (Fig. 1.12 B), in the firing rate (Fig. 1.12 C), and its frequency f_2 is the strongest peak in the power spectrum of the firing rate (red marker, Fig. 1.12 D). The interesting response is the nonlinearity appearing at the sum of the two input frequencies $f_1 + f_2$, which is also equal to f_{Base} (orange marker, Fig. 1.12 D). This nonlinearity represents a mixed response, that is part of the second-order response in Eq. (1.7).

Such nonlinear effects in a two-sine wave setting have been predicted only for specific frequencies, as has been demonstrated by probing a neuronal model with all possible two sine-wave combinations (Voronenko and Lindner, 2017). Instead, the second-order response or second-order susceptibility can be retrieved by probing the neuron with a white noise stimulus and setting the bispectra of the input and output in relation (Eq. (2.6), Egerland, 2021; Neiman and Russell, 2011). Applying this method one can retrieve the second-order susceptibility in the response at the sum of the input frequencies (upper right and lower left quadrants) and at the difference of the input frequencies (lower right and upper left quadrants, Fig. 1.13). It was demonstrated previously (Voronenko and Lindner, 2017; Egerland, 2021; Schlungbaum and Lindner, 2023) that the nonlinear interactions in a LIF model are especially strong when the sum or the difference of the two input frequencies are equal to the mean baseline firing rate f_{Base} of the neuron (yellow diagonals, Fig. 1.13). Strong nonlinearities could also be observed when one of the input frequencies, irrespective of the other input frequency, was equal to f_{Base} (vertical and horizontal yellow lines).

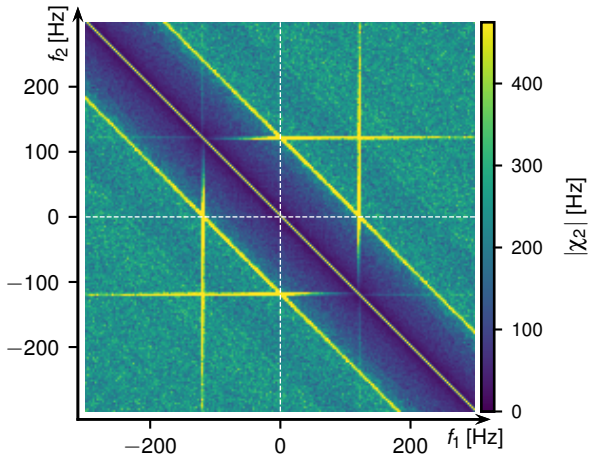

Figure 1.13: The absolute value of the second-order susceptibility of a LIF model, retrieved with white noise stimulation (Eq. (2.6)). White dashed lines – coordinate axis. Upper right and lower left quadrants: Nonlinearity at $f_1 + f_2$ in the firing rate of a neuron. Upper left and lower right quadrants: Nonlinearity at $|f_1 - f_2|$ in the firing rate of a neuron. Yellow corresponds to strong nonlinearity and blue to weak nonlinearity. Similar structures can be observed in Voronenko and Lindner (2017); Egerland (2021); Schlungbaum and Lindner (2023).

1.14 Weakly electric fish

In this work, nonlinearities are studied in the gymnotiform weakly electric fish of the species *Apteronotus leptorhynchus*. These fish are equipped with an electric organ (Salazar et al., 2013), that is constantly active and produces a quasi sinusoidal electric organ discharge (EOD), with a long-term stable and fish-specific frequency (f_{EOD}, Fig. 1.14 , Knudsen, 1975; Henninger et al., 2020). *Apteronotus leptorhynchus* is sexually dimorphic with females having lower EOD frequencies (500–750 Hz) and males having higher EOD frequencies (750–1000 Hz). These fish use their EOD for electrolocation (Fotowat et al., 2013; Nelson and MacIver, 1999) and communication (Fotowat et al., 2013; Walz et al., 2014; Henninger et al., 2018).

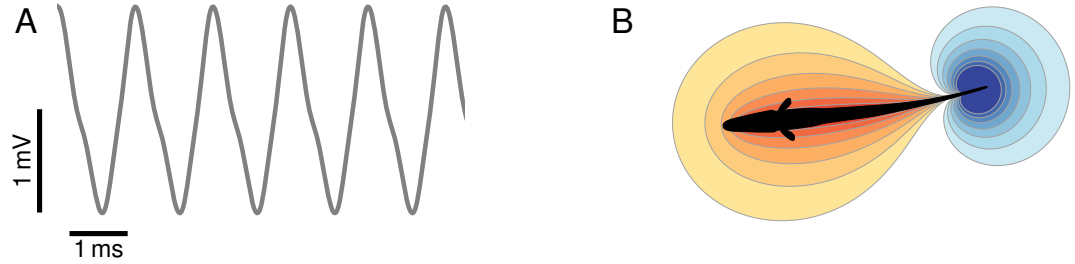

Figure 1.14: Weakly electric fish of the species *Apteronotus leptorhynchus* produce an electric field.
A Waveform of an electric organ discharge (EOD).
B Scheme of a weakly electric fish from above surrounded by isopotential lines. Red – positive potential. Blue – negative potential. The polarity of the potential changes over time, following the EOD waveform in A.

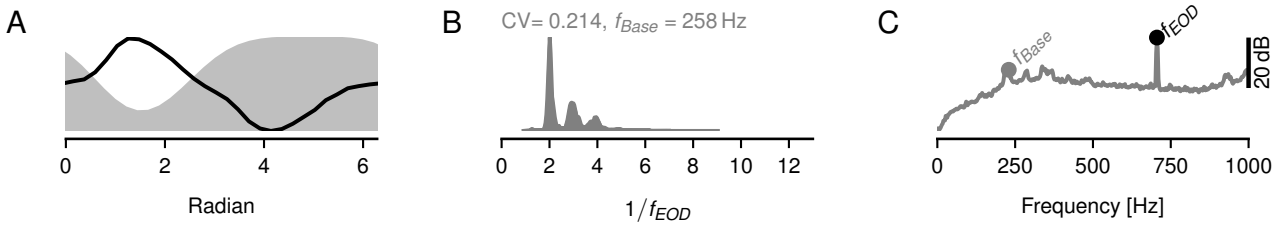

Figure 1.15: Example of an experimentally recorded P-unit during the baseline, where only the EOD of the fish with no stimulus is present.
A Gray area – probability that the P-unit spikes. Black line – one EOD cycle.
B Multimodal interspike interval (ISI) distribution of the spikes, with maxima at multiples of the EOD period.
C Power spectrum of the time-resolved firing rate.

Cutaneous tuberous organs, that are distributed all over the body of these fish (Carr et al., 1982), sense the actively generated electric field and its modulations. Within a single tuberous electroreceptor organ about 30 primary electroreceptors form ribbon synapses onto the dendrites of the same afferent fiber (Szabo, 1965; Wachtel and Szamier, 1966) that projects via the lateral line nerve to the hindbrain. There, the afferent fiber synapses onto pyramidal neurons in the electrosensory lateral line lobe (ELL, Maler, 2009). The EOD is encoded by the p-type electroreceptor afferents, the P-units. These fire phase-locked to the EOD of the fish with a spike at a similar phase in the EOD cycle (Fig. 1.15 A), with the phase depending on the receptor location (Hladnik and Grewe, 2023). P-units fire not once in every EOD cycle but in a probabilistic manner, resulting in an interspike interval (ISI) distribution with maxima at multiples of the EOD period (Fig. 1.15 B). The strongest peak in the power spectrum of the

time-resolved firing rate of P-units is the f_{EOD} peak, followed by the mean baseline firing rate peak f_{Base} (Fig. 1.15 C).

P-units have heterogeneous baseline firing properties with the mean baseline firing rate f_{Base} varying between 50 and 450 Hz (Grewe et al., 2017; Hladnik and Grewe, 2023) and the coefficient of variation (CV) of their ISIs varying between 0.2 and 1.7 (Grewe et al., 2017; Hladnik and Grewe, 2023). Some P-units are non-bursty during baseline, firing always an isolated spike, with at least two EOD periods to the next spike. Other P-units are bursty during baseline, firing burst packages of 2–5 spikes at subsequent EOD cycles, interleaved with quiescence. It has been demonstrated in P-unit models that a linear decoder is sufficient to describe the firing rate of non-bursty P-units, while bursty P-units require a nonlinear decoder (Chacron et al., 2004). Bursts are ubiquitous in sensory modalities as in chattering cells in the visual system (Nowak et al., 2003), in fast rhythmic bursting cells in the auditory system (Cunningham et al., 2004), Purkinje cells in the cerebellum (Womack and Khodakhah, 2004) or thalamic relay neurons (Destexhe et al., 1993). Bursts are known as nonlinear features that improve the signal-to-noise ratio e.g. in the auditory system (Eggermont and Smith, 1996) or in weakly electric fish (Oswald et al., 2004).

1.15 Beats, a social communication signal

When two fish are nearby the EOD of the receiver (EOD_1) and the EOD of the encountered fish (EOD_2) interfere and result in a new signal with a characteristic periodic amplitude modulation (AM), which is also called beat (Fig. 1.16). Beats are common stimuli in different sensory modalities enabling rhythm and pitch perception in human hearing (Roeber, 1834; Plomp, 1967; Joris et al., 2004; Grahn, 2012) and providing the context for electrocommunication in weakly electric fish (Engler and Zupanc, 2001; Hupé and Lewis, 2008; Henninger et al., 2018; Benda, 2020).

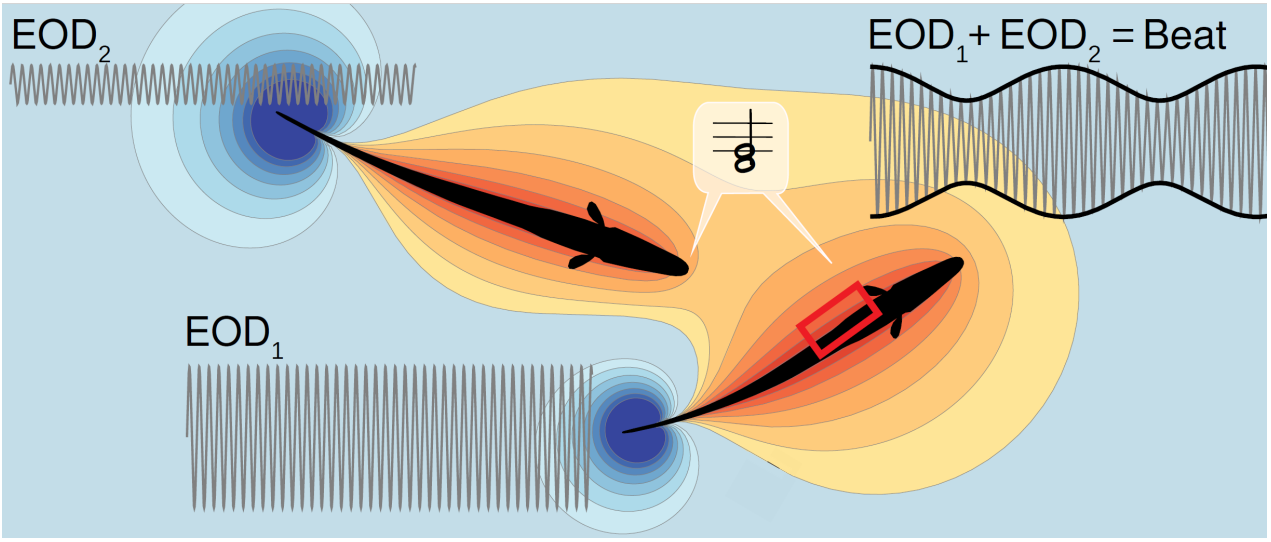

Figure 1.16: Adapted from Barayeu et al. (2023). Scheme of two weakly electric fish from above surrounded by isopotential lines. Red indicates a positive potential. Blue indicates a negative potential. When two fish are nearby their EODs (EOD_1, EOD_2) interfere and result in a new signal with a characteristic amplitude modulation, which is also called beat. The size of the beat is defined by the smaller EOD, here EOD_2. Beats are common features in all sensory modalities as during rhythm and pitch perception in human hearing (Roeber, 1834; Plomp, 1967; Joris et al., 2004; Grahn, 2012).

1.16 Wide dynamic range of beat amplitudes

The amplitude of a beat is defined by the amplitude of the smaller EOD, here EOD_2 (Fig. 1.16). To account for the varying field size of different fish the beat amplitude is expressed as a percentage of the receiver EOD and termed contrast. If EOD_2 is 20 % of the receiver EOD the beat contrast will also be 20 % (Fig. 1.17 B). The EOD and beat amplitudes decay with distances squared and when two fish are further apart the beat contrast is low (Fig. 1.17 A), whereas when two fish are close the beat contrast is high (Fig. 1.17 D). Usually contrasts used in electrophysiological experiments are between 10–20 % if a single contrast is recorded (Fig. 1.17 B, Walz et al., 2014; Barayeu et al., 2023) and between 0–40 % if the response to a range of contrasts is probed (Gussin et al., 2007; Benda et al., 2005). The behaviorally relevant beat contrasts of *Apteronotus leptorhynchus* have been measured by recording the transdermal potential of freely swimming fish during the encounter with another fish (Fotowat et al., 2013). In that work, it was demonstrated that during 70 % of all two fish encounters the beat contrasts were below 20 %. These findings verify that the usually used 10–20 % beat contrasts in electrophysiological studies are behaviorally reasonable (Walz et al., 2014; Barayeu et al., 2023). Still, beat contrasts can reach up to 100 % in freely swimming fish (Fotowat et al., 2013), corresponding to very strong amplitude modulations as in Fig. 1.17 D. In addition, the field strength of different fish can vary, e.g. 1.4–5.1 mV/cm in *Apteronotus rostratus* (Henninger et al., 2018). This implies that if the receiver has a smaller field than the encountered fish, this would result in contrasts exceeding 100 %. In such a scenario the beat amplitude is no longer defined by the encountered fish field size but by the receiver field size.

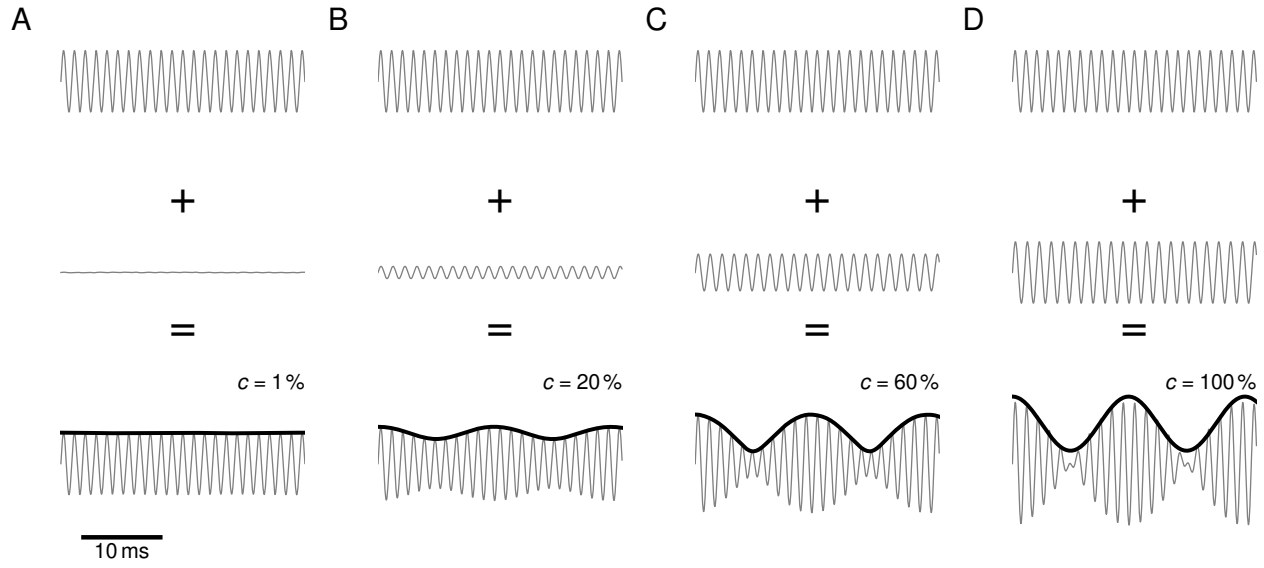

Figure 1.17: Different behaviorally relevant beat contrasts for *Apteronotus leptorhynchus*. The beat has a frequency of 70 Hz. Top – EOD of the receiver. Middle – EOD of the encountered fish. Bottom – Interference of the receiver EOD and the EOD of the encountered fish, leading to a beating amplitude modulation (black).
A Low beat contrast, $c = 1\,\%$.
B Intermediate beat contrast, $c = 20\,\%$.
C High beat contrast, $c = 60\,\%$.
D Very high beat contrast, $c = 100\,\%$.

P-units are known to saturate at contrasts between 10–30 % (Gussin et al., 2007; Benda et al., 2005). How is the wide behaviorally relevant range of contrasts 0.001–100 % encoded beyond the saturation of single P-units in weakly electric fish? Such questions are known as

the dynamic range problem and found in most sensory modalities, as in the auditory system with a wide range of different sound pressure levels (Evans, 1981; Preyer and Gummer, 1996; Liberman, 1982) or in the visual system with many log units of luminance (Pugh Jr et al., 1999; Barlow et al., 1957). Dynamic range problems are addressed by various neuronal mechanisms as the sound pressure compression of outer hair cells (Preyer and Gummer, 1996), by heterogeneous populations of auditory nerve fibers (Liberman, 1982), by sensitivity changes inside photoreceptors (Pugh Jr et al., 1999), by changes in receptive field size on the retina (Barlow et al., 1957) or by a match between the natural statistics and the cell sensitivity in the visual system (Laughlin, 1981). How P-units encode high contrasts, beyond the saturation of a single cell, will be addressed in chapter 6.

1.17 Beat frequency calculated as the difference frequency

The beat frequency is calculated as the difference between the two present EOD frequencies $\Delta f = f_2 - f_1$ (Joris et al., 2004; Walz et al., 2014). *Apteronotus leptorhynchus* is sexually dimorphic with females having lower EOD frequencies (500–750 Hz) and males having higher EOD frequencies (750–1000 Hz). When both encountered fish have the same sex, their frequencies are drawn from the same frequency distribution, resulting in a low beat frequency Δf and a slowly oscillating beat (Fig. 1.18 A, top). When both fish have different sexes, their frequencies are drawn from two different frequency distributions and a high beat frequency Δf and a fast oscillating beat occur (Fig. 1.18 C, top).

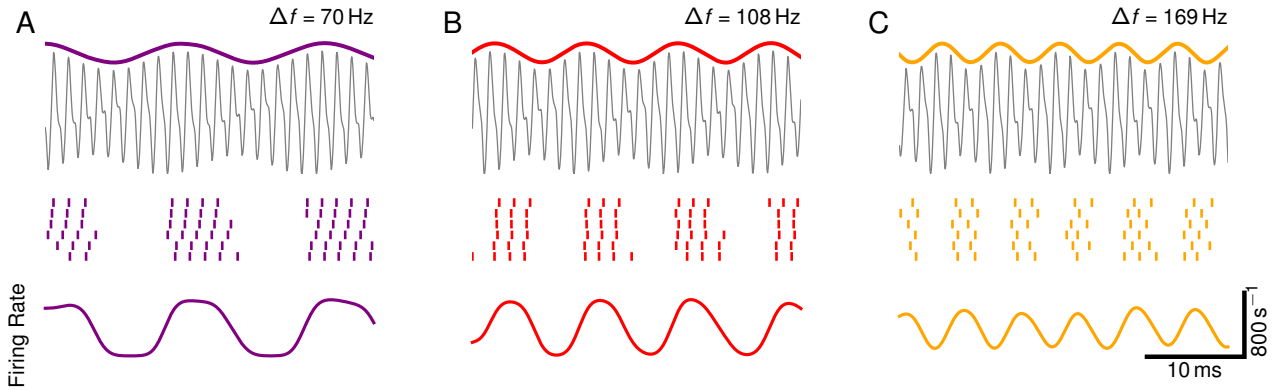

Figure 1.18: Responses of a P-unit to beats with different frequencies. All beats have a contrast of 20 %. Top: Gray – interference of EOD_1 and EOD_2. Color – beat. Middle: Spike trains in response to the signal above. Bottom: Time-resolved firing rate, calculated based on the spike trains above.
A Beat with a difference frequency Δf of 70 Hz.
B Beat with a difference frequency Δf of 108 Hz.
C Beat with a difference frequency Δf of 169 Hz.

Although the beat is visually perceivable on top of the superimposed signal (Fig. 1.18, top) the beat is not represented with a peak in the corresponding power spectrum (not shown). Mathematically, the beat can be extracted from the combined signal e.g. via the Hilbert transform (Stamper et al., 2012). Retrieving the beat in neurons requires a nonlinear operation e.g. a threshold, and subsequent low-pass filtering. Both mechanisms are biologically plausible to occur in sensory systems through the transduction machinery of inner hair cells (Peterson and Heil, 2019), signal rectification in receptor cells (Chacron et al., 2000, 2001), the rheobase of action-potential generation (Middleton et al., 2007; Longtin et al., 2008) and low-pass filtering through the biophysical properties of the membrane (Sinz et al., 2020).

P-units can phase-lock to several frequencies simultaneously and represent the EOD frequencies and the beat frequency Δf simultaneously in their firing rate (Sinz et al., 2020). The beat frequency is clearly perceivable in the spike trains and firing rate of P-units (Fig. 1.18, bottom). Low beat frequencies are encoded with a strong firing rate modulation depth, with high peak-to-peak firing rate values (Fig. 1.18 A). Higher beat frequencies induce a smaller modulation depth in the firing rate (Fig. 1.18 C). The beat frequency tuning curve has been measured up to 250–300 Hz in P-units in *Apteronotus leptorhynchus* (Fig. 1.19 C, Bastian, 1981; Benda et al., 2006; Walz et al., 2014). Due to spike-frequency adaptation (Benda et al., 2005), the tuning is strongly reduced at low beat frequencies (< 30 Hz). The beat frequency tuning curve has a maximum around 60 Hz and declines towards higher beat frequencies around 200 Hz. Such a decline is a common feature found in beat tuning curves of different sensory modalities, with no encoding of higher beat frequencies anticipated (Lamore et al., 1986; Carriot et al., 2017; Joris et al., 2004). High beat frequencies in weakly electric fish might be relevant for inter-species detection (Henninger et al., 2020). Field studies in the natural habitat of the weakly electric fish species *Apteronotus rostratus* in South America demonstrated that male-female interactions can be observed at beat frequencies up to 400 Hz (Fig. 1.19 A–B, orange markers, Henninger et al., 2018), exceeding the range of the so far measured beat tuning curve (Fig. 1.19 C). How these behaviorally relevant high beat frequencies are encoded in primary sensory afferents, despite the declining beat tuning curves, will be addressed in chapter 3.

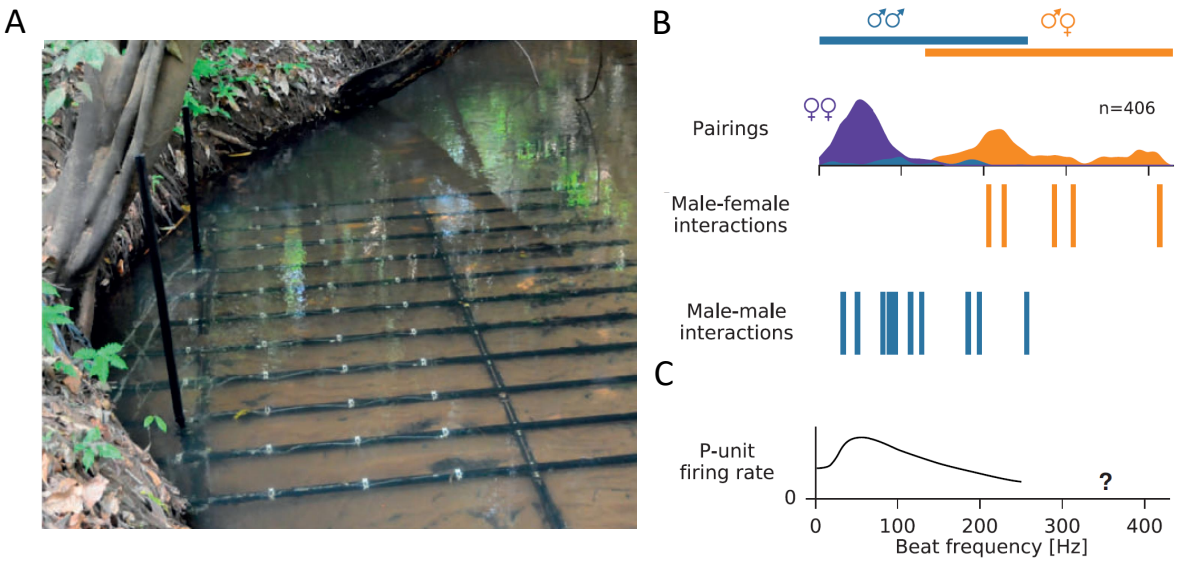

Figure 1.19: The behavioral relevance of high beat frequencies in *Apteronotus rostratus* in its natural habitat in South America.
A Electrode grid in a river in South America, recording the activity of weakly electric fish. Adapted from Henninger et al. (2017).
B Male-female (orange) and male-male (blue) interactions for different beat frequencies. Adapted from Henninger et al. (2018).
C Electrophysiologically recorded beat tuning curve of P-units. The measured range does not cover the behaviorally relevant range above. Adapted from Henninger et al. (2018). The tuning curve is based on Benda et al. (2005) and Walz et al. (2014).

1.18 Three fish in the electrosensory cocktail party

So far only a two-fish setting, with the beat frequency and amplitude being the only parameters, was introduced. In their natural habitats, weakly electric fish are often surrounded by several fish of the same but also of different species (Henninger et al., 2020). The interference of several EODs results in a complex signal where the amplitude modulation is characterized by several beats that can also be modulated by secondary envelopes (Middleton et al., 2006; Stamper et al., 2012).

In the natural habitat of *Apteronotus rostratus* a three-fish interaction, where a courting receiver male and female were approached by a male intruder from a large distance, could be observed repeatedly (Fig. 1.20 A left, Henninger et al., 2018). The intruder often elicited a reaction in the courting male, that chased away the distant intruder (Fig. 1.20 A, right). The beat and EOD amplitude of these fish decay with distance squared, with the female being a strong signal for the receiver and the intruder a faint signal (Fig. 1.20 B). P-units respond with reduced firing rate modulation depths to decreasing beat contrasts and contrasts smaller than 1 % (corresponding to intruder distances of 50 cm) have not been recorded in P-units (Fig. 1.20 D, Benda et al., 2006; Grewe et al., 2017; Bastian, 1981; Nelson et al., 1997). Still, attacks of the receiver towards the intruder could be observed at distances of 180 cm (Fig. 1.20 C). In the three-fish scenario, the distant intruder detection in P-units is even more complicated since the P-units' response is already driven by the strong and nearby female.

The here presented problem is reminiscent of the cocktail party problem (Cherry, 1953; Haykin and Chen, 2005), a sound source separation problem where a behaviorally relevant stimulus has to be separated from a noisy environment. Accordingly, the here-described detection problem in weakly electric fish will be referred to as the electrosensory cocktail party problem.

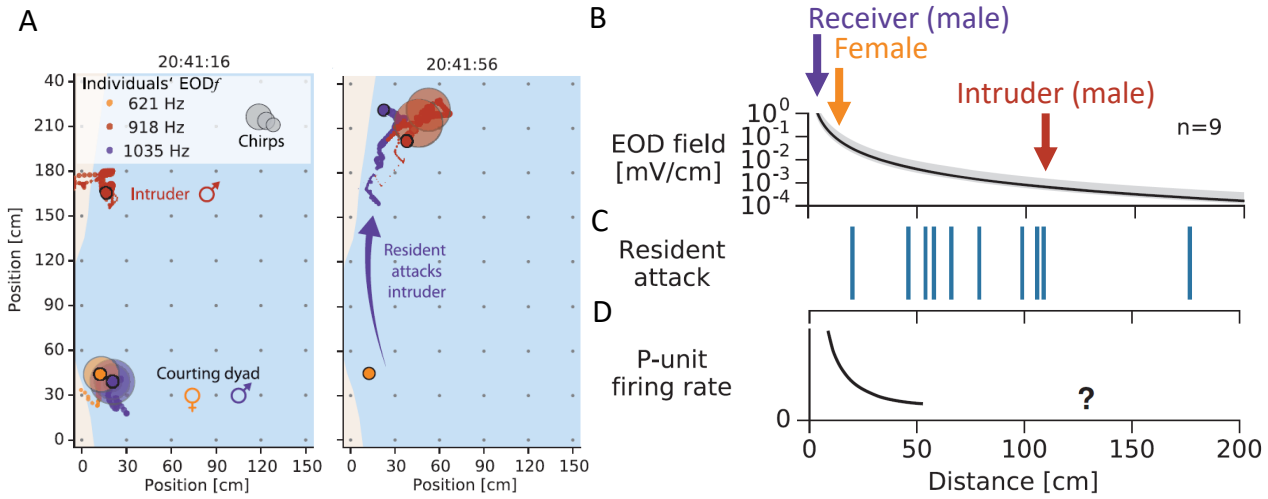

Figure 1.20: Electrosensory cocktail party problem in weakly electric fish. Adapted from Henninger et al. (2018).
A Left: The courting dyad is approached by a distant male intruder. Right: The receiver male chases away the distant intruder.
B The EOD and beat amplitude decay with distance squared. The intruder induces a faint beat and the female a strong beat.
C Attacks of the receiver towards the intruder have been recorded at 180 cm distances in the field.
D The firing rate modulation depth of P-units decays with distance. P-unit responses have not been recorded for stimuli beyond distances of 50 cm.

The potential solution for the detection of a faint intruder during an electrosensory cocktail party could be nonlinear interactions in the P-unit spiking response, as predicted in the framework of the nonlinear response theory for different input frequencies f_1, f_2 (section 1.13, Fig. 1.13, Voronenko and Lindner, 2017). The main driving force for P-units are not pure sine waves but beats with frequencies Δf_1, Δf_2. Whereas similar nonlinear effects arise during the two-beat or three-fish setting in P-units, will be addressed in chapter 4. In chapter 5 it will be investigated how these nonlinearities contribute to an improved detection of a faint and distant intruder despite a strong and nearby female during the electrosensory cocktail party.

1.19 Overview

In this work, the nonlinearities in primary sensory afferents in weakly electric fish were investigated. This work is subdivided into four chapters.

1.19.1 Nonlinearity at high beat frequencies

In chapter 3 it will be presented how difference frequencies greater than 250 Hz can be encoded in the electrosensory system. Recorded P-unit activities of *Apteronotus leptorhynchus* in response to a much wider range of difference frequencies ($-750 \leq \Delta f \leq 2500$ Hz) than before, will be presented. By mathematical reasoning and simulations of integrate-and-fire neurons the minimum functional requirements on single sensory cells to extract and respond to slow envelopes at large difference frequencies will be identified. These insights will be combined with behavioral experiments based on the jamming avoidance response (JAR, Watanabe and Takeda, 1963). This chapter has already been published as Barayeu et al. (2023).

1.19.2 Second-order susceptibility in a three-fish setting

In chapter 4 the second-order susceptibility in the spiking response of P-units in a three-fish setting will be addressed. For this a P-unit population analysis will be presented, testing how many cells exhibit nonlinear effects, as predicted in the framework of the weakly nonlinear theory by Voronenko and Lindner (2017). It will be demonstrated that heterogeneous baseline firing properties such as the CV or bursting influence the occurrence and strength of nonlinear interactions. Bursting will be identified as a mechanism to increase this nonlinearity.

1.19.3 Nonlinearities can improve faint signal detection

In chapter 5 the electrosensory cocktail party, where a courting dyad is approached by a distant intruder with the receiver chasing away the intruder, will be investigated. The question, how can a faint and distant intruder be detected despite the strong and nearby female, will be addressed. It will be demonstrated that intruder detection can be improved by the female presence in a homogeneous P-unit population. This improved detection will be connected to the nonlinear effects described in chapter 4.

1.19.4 Encoding of strong beat amplitudes

In chapter 6 the encoding of different beat amplitudes in P-units will be addressed. It will be demonstrated that two-beat suppression and the change in the EOD representation in the P-unit firing rate, can contribute to the encoding of a wide dynamic range of beat amplitudes on a single-cell level.

Chapter 2

Methods

2.1 Experimental subject details

Experiments were performed on male and female weakly electric fish of the species *Apteronotus leptorhynchus* obtained from a commercial tropical fish supplier (Aquarium Glaser GmbH, Rodgau, Germany). The fish were kept in tanks with a water temperature of 25 °C and a conductivity of around 270 µS/cm under a 12 h:12 h light-dark cycle. All experimental protocols complied with national and European law and were approved by the Ethics Committee of the Regierungspräsidium Tübingen (permit no: ZP1-16).

For chapter 3 recordings were conducted in 40 P-units of 7 weakly electric fish of the species *Apteronotus leptorhynchus*. JAR experiments were done in 5 fish of the species *Apteronotus leptorhynchus*.

No experiments were performed for chapter 4. Instead, cells recorded in *Apteronotus leptorhynchus* and *Eigenmannia virescens* at the Ludwig Maximilian University (LMU) München and at the Eberhard-Karls University Tübingen between 2010 and 2023 were used. The final sample consisted of 222 P-units and 45 ampullary cells from 71 weakly electric fish of the species *Apteronotus leptorhynchus* and 60 P-units and 18 ampullary cells from 17 weakly electric fish of the species *Eigenmannia virescens*.

For the project in chapter 6, experiments were performed in 35 P-units of 8 fish of the species *Apteronotus leptorhynchus* and 6 P-units in 3 fish of the species *Apteronotus rostratus*. In addition, 32 P-units from 12 fish of the species *Apteronotus leptorhynchus* recorded between 2010 and 2023 at the LMU München and at the Eberhard-Karls University Tübingen were reanalyzed.

2.2 Surgery

Before surgery, anesthesia was provided via bath application with a solution of MS222 (120 mg/l, PharmaQ, Fordingbridge, UK) buffered with Sodium Bicarbonate (120 mg/l). The posterior anterior lateral line nerve (pALLN) above the gills before its descent towards the anterior lateral line ganglion (ALLNG) was disclosed for subsequent P-unit recordings. During the surgery water supply was ensured by a mouthpiece, sustaining anesthesia with a solution of MS222 (100 mg/l) buffered with Sodium Bicarbonate (100 mg/l).

2.3 Experimental setup

During the experiments fish were immobilized by a single intramuscular injection of Tubocurarine (Sigma-Aldrich, Steinheim, Germany; 25–50 µl of 5 mg/ml solution). For the recordings

fish were positioned on a stage in a tank, with a major part of their body in the water. Analgesia was refreshed in intervals of two hours by cutaneous Lidocaine application (2 %; bela-pharm, Vechta, Germany) around the nerve. Electrodes (borosilicate; 1.5 mm outer diameter; GB150F-8P; Science Products, Hofheim, Germany) were pulled to a resistance of 50–100 MΩ (model P-97; Sutter Instrument, Novato, CA) and filled with 1 M KCl solution. Electrodes were fixed in a microdrive (Luigs-Neumann, Ratingen, Germany) and lowered into the nerve (Fig. 2.1, blue triangle). Recordings of electroreceptor afferents were amplified (SEC-05, npi-electronics, Tamm, Germany, operated in bridge mode). All signals, P-unit recording, recorded EOD and the generated stimulus, were digitized with sampling rates of 40 kHz (PCI-6229, National Instruments, Austin, TX). RELACS (`www.relacs.net`) running on a Linux computer was used for online spike and EOD detection, stimulus generation, and calibration.

2.4 Identification of P-units and ampullary cells

The neurons were classified into cell types during the recording by the experimenter. P-units were classified based on mean baseline firing rates of 50–450 Hz (Grewe et al., 2017; Hladnik and Grewe, 2023) and phase-locking to the EOD, leading to a multimodal interspike interval (ISI) distribution (as in Fig. 1.15 B). Ampullary cells were classified based on mean firing rates of 80–200 Hz and no phase-locking to the EOD with an unimodal ISI distribution. Only cells with a baseline recording were included in the final sample. Cells that ceased spiking during the baseline recording were excluded.

2.5 Field recordings

The EOD of fish without the stimulus was termed global EOD and measured with two vertical carbon rods (11 cm long, 8 mm diameter) in a head-tail configuration (Fig. 2.1, green bars). This signal was amplified 200–500 times and band-pass filtered (3 to 1 500 Hz passband, DPA2-FX; npi electronics, Tamm, Germany).

The EOD of the fish with the stimulus was termed local EOD and was measured between two 1 cm-spaced silver wires located next to the left gill of the fish and orthogonal to its longitudinal body axis (amplification 200–500 times, band-pass filtered with 3 to 1 500 Hz passband, DPA2-FX; npi-electronics, Tamm, Germany, Fig. 2.1, red markers). Unfortunately, these filter settings were too narrow for the high stimulus frequencies that were used in chapter 3. For Fig. 3.1 A–F the local EOD waveforms were recreated by adding the recorded stimulus output to the global EOD, to avoid unwanted phase shifts.

2.6 Stimulation

The stimulus was isolated from the ground (ISO-02V, npi-electronics, Tamm, Germany) and delivered via two horizontal carbon rods (30 cm length, 8 mm diameter) located 15 cm laterally to the fish (Fig. 2.1, gray bars).

2.6.1 High beat frequency stimuli in two-fish setting

For chapter 3 sine wave stimuli (10–3300 Hz), imitating another fish, were isolated (ISO-02V, npi-electronics, Tamm, Germany). Depending on the EOD frequency f_{EOD} of the fish, the stimuli resulted in difference frequencies between −750 and 2495 Hz. Each stimulus was repeated twice either for 0.5 s (20% of the trials) or 1 s (80% of the trials). The stimulus amplitude was fixed at 10 % or 20 % of the fish's local EOD amplitude (contrast) measured before each

stimulation. If both amplitudes were measured in a cell only the amplitude with the larger number of stimulus frequencies tested was considered for further analyses. Therefore, each cell contributed only once to the population analysis in chapter 3.

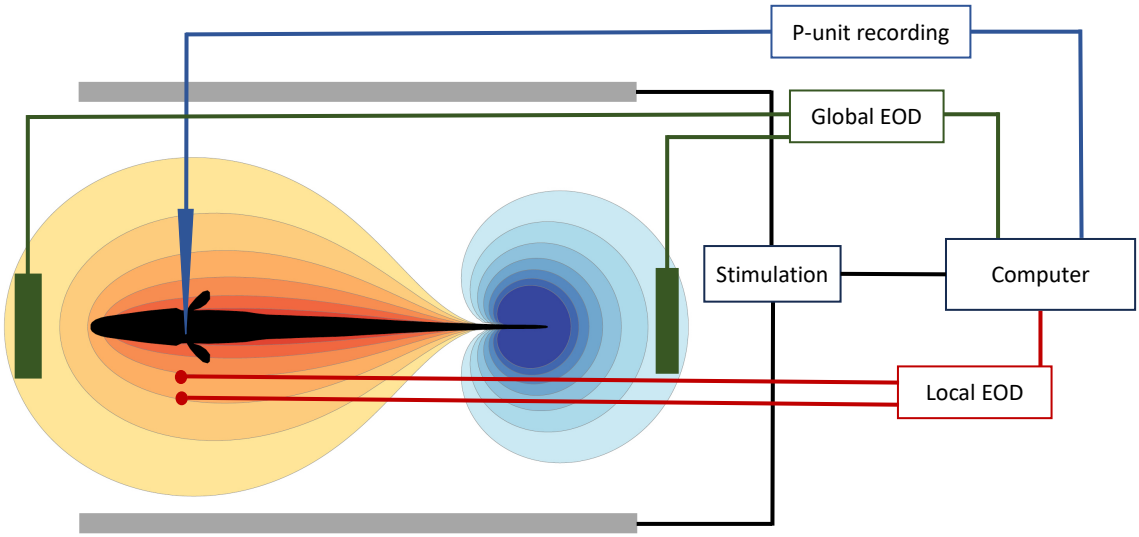

Figure 2.1: Electrophysiolocical recording set-up. The fish, depicted as a black scheme and surrounded by isopotential lines, was positioned in the middle of the tank. Blue triangle – electrophysiological recordings were conducted at the posterior anterior lateral line nerve (pALLN) above the gills. Gray horizontal bars – electrodes for the stimulation. Green vertical bars – electrodes to measure the global EOD (the EOD of the fish without the stimulus). Red dots – electrodes to measure the local EOD (the EOD of the fish with the stimulus). The local EOD was measured with a distance of 1 cm between the electrodes. All measured signals were amplified, filtered and stored on a local computer.

2.6.2 White noise stimuli

For chapter 4 the fish were stimulated with band-pass limited white noise stimuli with a cut-off frequency of 150, 300 or 400 Hz. The standard deviation of the white noise was expressed in relation to the EOD size of the fish in the experimental set-up and termed contrast. The contrast varied between 1 and 20 % for *Apteronotus leptorhynchus* and between 2.5 and 40 % for *Eigenmannia virescens*. Only cell recordings with at least 10 s of white noise stimulation were included for the analysis in chapter 4. When ampullary cells were recorded the white noise was directly applied as the stimulus. For P-unit recordings, the EOD of the fish was multiplied with the desired random amplitude modulation (RAM, MXS-01M; npi electronics).

2.6.3 Two-beat suppression stimuli

The stimuli in chapter 6 consisted either of one sine wave, resulting in the one-beat condition, or of two sine waves, leading to the two-beat condition. A stimulus was presented for a duration of 1 s. The contrasts of both sine waves were 10 %. For the results shown in Fig. 6.5 the frequency of one sine wave was varied between 400 and 900 Hz and the other frequency was set to 737, 813 or 927 Hz.

2.7 Data analysis

Data analysis was performed with Python 3 using the packages matplotlib, numpy, scipy, sklearn, pandas, nixio (Stoewer et al., 2014), and thunderfish (`https://github.com/bendalab/thunderfish`).

2.7.1 Baseline calculation

The mean baseline firing rate f_{Base} was calculated as the number of spikes divided by the duration of the baseline recording (on average 18 s). The coefficient of variation (CV) was calculated as the standard deviation of the interspike intervals ISI divided by the mean ISI: $\mathrm{CV} = \sqrt{\langle(\mathrm{ISI} - \langle\mathrm{ISI}\rangle)^2\rangle}/\langle\mathrm{ISI}\rangle$. If the baseline was recorded several times in a cell, the mean f_{Base} and mean CV were calculated.

2.8 High beat frequencies data analysis

The following analysis steps were conducted for the data analysis in chapter 3.

2.8.1 Firing rate calculation

To calculate the firing rate $f(t)$ the spike train was first converted into its binary representation. Therefore, the spike train was binned with a time step of 0.025 ms, where each spike was represented by a value of 40 kHz and all other time bins were set to zero. Time-resolved firing rates were computed by convolving these binary spike trains with a Gaussian kernel. The standard deviation of the kernels was set to $\sigma = 0.5$ ms, $\sigma = 1$ ms or $\sigma = 2$ ms. Convolution with kernels corresponds to constructing peri-stimulus time histograms but has the advantage that it avoids edge effects introduced by the histogram bins.

2.8.2 Spectral analysis

To investigate the high beat frequencies in chapter 3 power spectra of binary spike trains or time-resolved firing rates were computed from fast Fourier transforms on $n_{\mathrm{fft}} = 4096$ long data segments that overlapped by 50 %. The initial and last 5 ms of each spike train were excluded from the analysis.

Frequency tuning curves were calculated as the position f_{resp} of the largest peak in the power spectrum of the time-resolved firing rate as a function of stimulus frequency f_{stim}. Frequency tuning curves provide information on which frequency the firing rate was modulated by the stimulus. The modulation depth of this firing rate was quantified by the amplitude A_{resp} of the peak f_{stim}. A_{resp} was estimated as the square root of the integral over the five closest frequencies to the peak frequency f_{stim} in the power spectrum. Amplitudes of spectral peaks are closely related to the vector strength that is commonly used to quantify temporal modulation transfer functions of auditory neurons in response to SAMs (Sinz et al., 2020).

During each stimulus presentation f_{EOD} was estimated from the recorded global EOD as the frequency of the largest peak in power spectra computed with 65536 samples per FFT window. The stimulus frequency was confirmed in the same way. Difference frequencies and stimulus frequencies relative to f_{EOD} were reported based on these measurements.

Cells with less than 50 different stimulus frequencies, cells with no stimulus frequencies higher than 2.6 f_{EOD} and cells with no difference frequencies between 0 and 100 Hz were excluded from the analysis. Stimulus frequencies resulting in envelopes of periods larger than the analysis window were also excluded from the analysis.

To estimate how far cells follow the aliasing structure to higher stimulus frequencies (f_{max} in Fig. 3.3 A), for each stimulus frequency f_{stim} the quadratic deviation $\sigma = (f_{resp}/f_{EOD} - f_{exp}/f_{EOD})^2$ of the measured response frequency f_{resp} from the expected alias frequency of the stimulus $f_{exp} = |f_{stim} - f_{EOD}\lfloor f_{stim}/f_{EOD}\rceil|$ was calculated. Thereby $\lfloor x \rceil$ rounds x to the closest integer. It was then looped over all stimulus frequencies $f_{stim,i}$ and the corresponding bins $(f_{stim,i+1} - f_{stim,i-1})/2$ of the stimulus frequencies were added up, but only if the response frequency matched the expected one ($\sigma < 0.0005$). The resulting sum f_{max} quantifies the range of stimulus frequencies for which the response of the cell follows the expected alias frequencies.

2.9 Second-order susceptibility data analysis

The following analysis steps were conducted for the data analysis in chapter 4.

2.9.1 Bursting

Bursty cells are characterized by a bimodal ISI distribution, with the burst spikes having ISI values smaller than the burst threshold, which is usually set to 1.5 EOD periods in P-units (Chacron et al., 2004; Metzen et al., 2016). Here the bimodal ISI distribution of bursty P-units was not always properly separated by a threshold of 1.5 EOD periods. Therefore, a threshold best separating the bimodal distribution was set by visual inspection. In the final P-units sample, 149 cells had a burst threshold of 1.5 EOD periods, 59 cells had a burst threshold of 2.5 EOD periods, 7 cells had a burst threshold of 3.5 EOD periods, 4 cells had a burst threshold of 4.5 EOD periods and 1 cell had a burst threshold of 5.5 EOD periods. The burst fraction was calculated as the number of spikes below the burst threshold divided by all spikes.

The baseline characteristics (see methods section 2.7.1), as the mean baseline firing rate after burst correction $f_{BaseCorrected}$ and the baseline CV after burst correction $\mathrm{CV}_{BaseCorrected}$, were calculated based on the burst-corrected spike train, where all spikes in a burst package after the first spike were removed.

2.9.2 Response modulation

The firing rate of a cell is modulated around an average firing rate similar to f_{Base} in response to a stimulus. The response modulation was calculated based on the mean firing rate $f(t)$. For $f(t)$ the binary spike trains, with zero everywhere no spike occurred and the sampling rate everywhere a spike occurred, were convolved with a Gaussian with a standard deviation of 2.5 ms and the mean over the stimulus repeats was calculated. The response modulation $\sigma_M = \sqrt{\langle (f(t) - \langle f(t) \rangle)^2 \rangle}$ was calculated as the standard deviation of the mean firing rate $f(t)$, where the averages are taken over time. The response modulation was calculated as an estimate of the effective stimulus strength.

2.9.3 Spectral analysis

In chapter 4 the first-order and second-order susceptibility between the stimulus $s(t)$ and the response $r(t)$ were calculated (Eq. (2.3), Eq. (2.6)). The response $r(t)$ was the firing rate of the neuron, calculated as the binary spike train representation, with the sampling rate value when a spike occurred, zero everywhere else and the unit Hz. The noise stimulus $s(t)$ (see section 2.6.2), was expressed in relation to the EOD and had no unit. A stimulus had a duration of 10 s that were subdivided into $N = 20$ segments with no overlap, each with the duration of $T = 0.5$ s. Since the sampling rate S_r varied between cell recordings (20 kHz, 40 kHz or 100 kHz) n_{fft} was set to $S_r \cdot 0.5$ s, resulting in a frequency resolution of 2 Hz for each cell.

The Fourier transform of a time signal was calculated as $\tilde{s}(\omega) = \int_0^T s(t) \cdot e^{-i\omega t}\, dt$, with T being the signal duration. The power spectrum was calculated as

$$S_{ss}(\omega) = \frac{\langle \tilde{s}(\omega)\tilde{s}^*(\omega)\rangle}{T} \tag{2.1}$$

with $\tilde{s}^*$ being the complex conjugate and $\langle ... \rangle$ the averaging over the segments.

The cross-spectrum was calculated with Eq. (2.2), linear encoding was estimated with Eq. (2.3) and the higher-order cross-spectrum was calculated with Eq. (2.4).

$$S_{rs}(\omega) = \frac{\langle \tilde{r}(\omega)\tilde{s}^*(\omega)\rangle}{T} \tag{2.2}$$

$$\chi_1(\omega) = \frac{S_{rs}(\omega)}{S_{ss}(\omega)} \tag{2.3}$$

$$S_{rss}(\omega_1, \omega_2) = \frac{\langle \tilde{r}(\omega_1 + \omega_2)\tilde{s}^*(\omega_1)\tilde{s}^*(\omega_2)\rangle}{T} \tag{2.4}$$

The second-order susceptibility was calculated as

$$\chi_2(\omega_1, \omega_2) = \frac{S_{rss}(\omega_1, \omega_2)}{2S_{ss}(\omega_1)S_{ss}(\omega_2)} \tag{2.5}$$

by dividing the higher-order cross-spectrum by the power spectra. Applying the Fourier transform this can be rewritten resulting in:

$$\chi_2(\omega_1, \omega_2) = \frac{TN \sum_{n=1}^{N} \int_0^T dt\, r_n(t) e^{-i(\omega_1+\omega_2)t} \int_0^T dt'\, s_n(t') e^{i\omega_1 t'} \int_0^T dt''\, s_n(t'') e^{i\omega_2 t''}}{2 \sum_{n=1}^{N} \int_0^T dt\, s_n(t) e^{-i\omega_1 t} \int_0^T dt'\, s_n(t') e^{i\omega_1 t'} \sum_{n=1}^{N} \int_0^T dt\, s_n(t) e^{-i\omega_2 t} \int_0^T dt'\, s_n(t') e^{i\omega_2 t'}} \tag{2.6}$$

The absolute value of a second-order susceptibility matrix is visualized in Fig. 4.5. There the upper right and the lower left quadrants characterize the nonlinearity in the response $r(t)$ at the sum frequency of the two input frequencies. The lower right and upper left quadrants characterize the nonlinearity in the response $r(t)$ at the difference of the input frequencies.

2.9.4 Nonlinearity index

The structural changes in the absolute value of the second-order susceptibility (as the matrix in Fig. 4.5) were quantified in a nonlinearity index:

$$NLI(f_0) = \frac{\max_{f_0-5\,\mathrm{Hz} \le f \le f_0+5\,\mathrm{Hz}} D(f)}{\mathrm{med}(D(f))} \tag{2.7}$$

For this index, the second-order susceptibility matrix was projected on the diagonal $D(f)$, by taking the mean of the anti-diagonals. The peakedness of a frequency f_0 in $D(f)$ was quantified by finding the maximum of $D(f)$ in the range $f_0 \pm 5\,\mathrm{Hz}$ (Fig. 4.2 A_{vi}, gray marker) and dividing it by the median of $D(f)$. This was calculated for the frequencies f_{Base} and $f_{BaseCorrected}$ resulting in NLI(f_{Base}) and NLI($f_{BaseCorrected}$).

If the same frozen noise was recorded several times in a cell, each noise repetition resulted in a separate second-order susceptibility matrix. The mean of the corresponding NLI(f_{Base}) and NLI($f_{BaseCorrected}$) values was used for the population statistics in Fig. 4.6 and Fig. 4.9. The second-order susceptibility matrices depicted in Fig. 4.2, Fig. 4.3, Fig. 4.7 and Fig. 4.10 were calculated based on the first frozen noise repeat.

2.10 Faint signal detection data analysis

The following analysis steps were conducted for the data analysis in chapter 5.

2.10.1 Receiver operating characteristics (ROC)

The receiver operating characteristic (ROC) detection analysis for chapter 5 was adapted from Schlungbaum and Lindner (2023). For this four stimulus conditions were implemented, each with a duration of 25 s. In the baseline condition (R), only the receiver was present and the field was normalized to one. In the other conditions the receiver either encountered only the intruder (RI), the receiver encountered only the female (RF) or the receiver encountered both the intruder and the female (RIF). The stimulus repetition number in each of these conditions varied, mimicking the receptive field size of the next-connected cells in the electrosensory lateral line lobe (ELL). The receptive field size of the centromedial segment (CMS) was mimicked with $n = 20$, of the centrolateral segment (CLS) with $n = 100$ and of the lateral segment (LS) with $n = 1000$ (Maler, 2009). A time-resolved firing rate $f(t)$ was computed by convolving the binary spike trains with a Gaussian kernel, with a standard deviation of $\sigma = 0.5\,\mathrm{ms}$, and calculating the mean for all stimulus repetitions.

The ROC was used to determine if a signal is better detected in one condition than in another. For this, the firing rate $f(t)$ was subdivided into time windows, each with 1000 datapoints. The next time window started with an offset of $t_{off} = 10$ datapoints, thus randomizing the phases of the time windows. Detection thresholds were drawn horizontally through each time window and if any firing rate value was above a threshold this threshold was assigned a 1, otherwise it was assigned a 0. The detection rate was calculated as the average over all time windows.

In chapter 5 the question if a faint intruder is detectable was addressed. If the intruder was present in the stimulus, as in the conditions RI and RIF, this resulted in the correct-detection (CD) rate. If the intruder was not present, as in the conditions R and RF, this resulted in the false-positive (FP) rate. In the ROC curve, the CD rate was plotted against the FP rate. The intruder detection without the female ($\mathrm{ROC_{NoFemale}}$) was characterized by a ROC comparison between the condition where the intruder was present (RI, CD rate) and the condition where the intruder was not present (R, FP rate, Fig. 5.2). The intruder detection with the female ($\mathrm{ROC_{Female}}$) was retrieved by comparing the condition where the intruder and the female were present (RIF, CD rate) to the condition where the intruder was not present but the female was (RF, FP rate, Fig. 5.3).

2.10.2 Area under the curve (AUC)

The intruder detection performance was quantified by the area under the curve (AUC), calculated as the area between the ROC curve and the equality line.

$$\mathrm{AUC} = \left| \int_0^1 \mathrm{ROC}(\mathrm{FP})\,\mathrm{dFP} - 0.5 \right| \tag{2.8}$$

For this the ROC curve was integrated over the false-positive FP rate and the area under the equality line was subtracted. Since any change from the equality line indicates signal detection, the absolute value was taken. In the case of best detection, the AUC has a maximal value of 0.5 and in the case of worst detection the lowest value of 0.

2.10.3 Detection improvement by the female presence

The intruder detection improvement by the presence of the female was calculated at an intruder contrast of 3 % as $\mathrm{AUC_{Female}} - \mathrm{AUC_{NoFemale}}$. These AUC values were calculated with Eq. (2.8) based on the $\mathrm{ROC_{Female}}$ and $\mathrm{ROC_{NoFemale}}$ curves (see section 2.10.1). Positive values of $\mathrm{AUC_{Female}} - \mathrm{AUC_{NoFemale}}$ indicate that the female improves the intruder detection and negative values indicate that the female decreases the intruder detection.

2.10.4 Spectral analysis: Nonlinearity quantification

In chapter 5 the amplitude $A(\Delta f)$ of a frequency was quantified as the square root of the integral below the five closest frequencies to the frequency of interest in the power spectrum of a firing rate. The power spectrum was calculated based on $n_{\mathrm{fft}} = 32768$ datapoints with an overlap of 50 %. The windows were smoothed with a hanning window. The nonlinearity at the sum frequency $|\Delta f_{\mathrm{Female}}| + |\Delta f_{\mathrm{Intruder}}|$ was calculated by combining the amplitudes $A(|\Delta f_{\mathrm{Female}}| + |\Delta f_{\mathrm{Intruder}}|)$ and $A(\Delta f_{\mathrm{Intruder}})$ in the four stimulus conditions RIF, RI, RF and R (see section 2.10.1 for condition description).

$$\begin{aligned} A(\Delta f_{\mathrm{Sum}}) = & \frac{A(|\Delta f_{\mathrm{Female}}| + |\Delta f_{\mathrm{Intruder}}|)_{\mathrm{RIF}} - A(|\Delta f_{\mathrm{Female}}| + |\Delta f_{\mathrm{Intruder}}|)_{\mathrm{RI}}}{A(\Delta f_{\mathrm{Intruder}})_{\mathrm{RI}}} \\ & + \frac{-A(|\Delta f_{\mathrm{Female}}| + |\Delta f_{\mathrm{Intruder}}|)_{\mathrm{RF}} + A(|\Delta f_{\mathrm{Female}}| + |\Delta f_{\mathrm{Intruder}}|)_{\mathrm{R}}}{A(\Delta f_{\mathrm{Intruder}})_{\mathrm{RI}}} \end{aligned} \tag{2.9}$$

The numerators cancel out if there is no nonlinearity at $|\Delta f_{\mathrm{Female}}| + |\Delta f_{\mathrm{Intruder}}|$ with $A(\Delta f_{\mathrm{Sum}})$ being close to zero. This takes into account that the nonlinear sum frequency $|\Delta f_{\mathrm{Female}}| + |\Delta f_{\mathrm{Intruder}}|$ was equal to f_{Base} in the analysis in Fig. 5.5, Fig. 5.7 and Fig. 5.8. To take the sensitivity of different cells into account, the denominator is the amplitude of the intruder beat frequency $\Delta f_{\mathrm{Intruder}}$ in the power spectrum of the firing rate in the RI condition. For each cell in the population (Fig. 5.8), the nonlinearity was calculated at an intruder contrast of 3 %, the intruder-induced beat was equal to $0.3\, f_{Base}$ and the female-induced beat was equal to $0.7\, f_{Base}$, with $|\Delta f_{\mathrm{Female}}| + |\Delta f_{\mathrm{Intruder}}|$ being equal to f_{Base} for each cell.

2.11 Data analysis for varying beat amplitudes

The following analysis steps were conducted for the data analysis in chapter 6.

2.11.1 F-I Curves

Frequency-Intensity (F-I) curves were calculated to characterize the sensitivity of the recorded cell. For this, a step change in the EOD amplitude or intensity was presented to the cells. This EOD intensity I varied between -31 % and 31 % and was expressed as a contrast, the percentage of the baseline EOD field strength of the fish. The same intensity was presented several times (3 to 10 repeats). The resulting spikes were convolved with a Gaussian with the standard deviation of 0.5 ms and the mean over the stimulus repeats resulted in the time-resolved firing rate. The onset response was measured as the mean of this firing rate in the interval between 7–55 ms after the step stimulus onset. The steady-state response was measured as the mean firing rate between 330–390 ms after the step stimulus onset.

2.11.2 Spectral analysis

To calculate how a signal is represented in the firing rate of P-units in chapter 6 (e.g. in Fig. 6.5) the amplitude at the peak of interest $A(f)$ was calculated as the square root of the

integral of the closest frequency to the frequency of interest f in the power spectrum of the firing rate. The firing rate was calculated as described in section 2.8.1 with a Gaussian standard deviation of 0.5 ms. For the power spectrum calculation windows with $n_{\text{fft}} = 32768$ datapoints and an overlap of 50 % were used. The windows were smoothed with a hanning window. For the electrophysiologically recorded data, the duration of the signal was 1 s. For data retrieved from models, the duration was 25 s.

2.12 Leaky integrate-and-fire models

Leaky integrate-and-fire (LIF) models with a carrier were constructed to reproduce the specific firing properties of P-units (Chacron et al., 2001; Sinz et al., 2020). The input into the P-unit model during baseline was the fish's own EOD

$$x(t) = x_{EOD}(t) = \cos(2\pi f_{EOD} t) \tag{2.10}$$

with EOD frequency f_{EOD} and amplitude normalized to one.

In the model, the input $x(t)$ was first thresholded.

$$\lfloor x(t) \rfloor_0 = \begin{cases} x(t) & ; \quad x(t) \geq 0 \\ 0 & ; \quad x(t) < 0 \end{cases} \tag{2.11}$$

$\lfloor x(t) \rfloor_0$ denotes the threshold operation that sets negative values to zero (box left to Fig. 2.2 $\mathsf{A_i}$). Thresholding potentially happens at the synapse between the receptor cells and the afferent.

The resulting signal was then low-pass filtered with a time constant τ_d by the afferent's dendrite (box left to Fig. 2.2 $\mathsf{A_{ii}}$).

$$\tau_d \frac{dV_d}{dt} = -V_d + \lfloor x(t) \rfloor_0^p \tag{2.12}$$

Dendritic low-pass filtering was necessary to reproduce the loose coupling of P-unit spikes to the EOD while maintaining high sensitivity to small amplitude modulations. Because the input was unitless, the dendritic voltage was unitless, too. In chapter 3 the rectified stimulus was optionally taken to a power of p. If not stated otherwise the exponent p was set to one resulting in a pure threshold. This thresholding and low-pass filtering extracted the amplitude modulation of the input $x(t)$.

The dendritic voltage $V_d(t)$ was the input to a leaky integrate-and-fire (LIF) model

$$\tau_m \frac{dV_m}{dt} = -V_m + \mu + \alpha V_d - A + \sqrt{2D}\xi(t) \tag{2.13}$$

where τ_m is the membrane time constant, μ is a fixed bias current, α is a scaling factor for V_d, and $\sqrt{2D}\xi(t)$ is a white noise with strength D. All state variables in the LIF are unitless. The output of the model is in seconds.

The adaptation current A followed

$$\tau_A \frac{dA}{dt} = -A \tag{2.14}$$

with adaptation time constant τ_A.

Whenever the membrane voltage $V_m(t)$ crossed the threshold $\theta = 1$ a spike was generated, $V_m(t)$ was reset to 0, the adaptation current was incremented by ΔA, and integration of $V_m(t)$ was paused for the duration of a refractory period t_{ref} (Fig. 2.2 $\mathsf{A_{iv}}$).

$$V_m(t) \geq \theta \; : \begin{cases} V_m & \mapsto & 0 \\ A & \mapsto & A + \Delta A/\tau_A \end{cases} \tag{2.15}$$

The static nonlinearity $f(V_m)$ was equal to zero for the LIF. In the case of an exponential integrate-and-fire model (EIF), this function was set to

$$f(V_m) = \Delta_V e^{\frac{V_m - 1}{\Delta_V}} \tag{2.16}$$

(Fourcaud-Trocmé et al., 2003), where Δ_V was varied from 0.001 to 0.1.

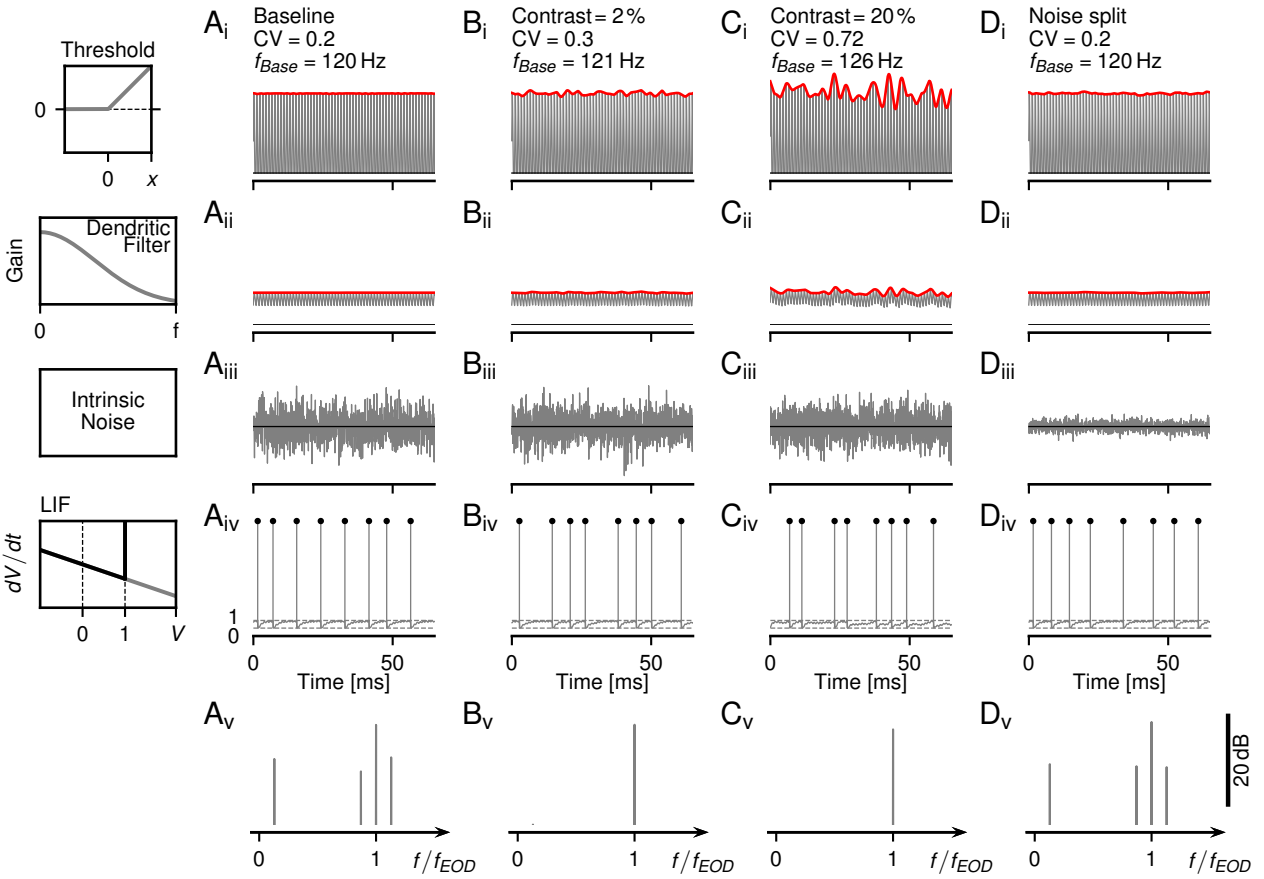

Figure 2.2: Flowchart of a LIF P-unit model with EOD carrier. Model cell identifier 2012-07-03-ak (see table 2.1 for model parameters).
$\mathsf{A_i}$–$\mathsf{D_i}$ Rectification of the input. Positive values are maintained and negative discarded (see box on the left).
$\mathsf{A_{ii}}$–$\mathsf{D_{ii}}$ Dendritic low-pass filtering.
$\mathsf{A_{iii}}$–$\mathsf{D_{iii}}$ The noise component in $\sqrt{2D}\,\xi(t)$ Eq. (2.13) or $\sqrt{2D\,c_{noise}}\,\xi(t)$ in Eq. (2.21).
$\mathsf{A_{iv}}$–$\mathsf{D_{iv}}$ Spikes generation in the LIF model. Spikes are generated when the voltage of 1 is crossed (markers). Then the voltage is again reset to 0.
$\mathsf{A_v}$–$\mathsf{D_v}$ Power spectrum of the spikes above. The first peak in panel $\mathsf{A_v}$ is the f_{Base} peak. The peak at 1 is the f_{EOD} peak. The other two peaks are at $f_{EOD} \pm f_{Base}$.
A Baseline condition: The input to the model is a sinus with frequency f_{EOD}.
B The EOD carrier is multiplied with a band-pass limited random amplitude modulation (RAM) with a contrast of 2 %, as in Eq. (2.18).
C The EOD carrier is multiplied with a band-pass limited RAM signal with a contrast of 20 %.
D The total noise of the model is split into a signal component regulated by c_{signal} in Eq. (2.19), and a noise competent regulated by c_{noise} in Eq. (2.21). The intrinsic noise in $\mathsf{D_{iii}}$ is reduced compared to $\mathsf{A_{iii}}$–$\mathsf{C_{iii}}$. To maintain the CV during the noise split in D comparable to the CV during the baseline in A the RAM contrast is increased in $\mathsf{D_i}$.

2.12.1 Numerical implementation

The ODEs were integrated by the Euler forward method with a time-step of $\Delta t = 0.00005\,\text{s}$.

For the intrinsic noise $\xi(t)$ (Eq. (2.13), Fig. 2.2 $\mathsf{A}_{\mathsf{iii}}$) in each time step i a random number was drawn from a normal distribution $\mathcal{N}(0,\,1)$ with zero mean and standard deviation of one. This number was multiplied with $\sqrt{2D}$ and divided by $\sqrt{\Delta t}$:

$$V_{m_{i+1}} = V_{m_i} + \left(-V_{m_i} + \mu + \alpha V_{d_i} - A_i + \sqrt{\frac{2D}{\Delta t}}\mathcal{N}(0,\,1)_i\right)\frac{\Delta t}{\tau_m} \tag{2.17}$$

2.12.2 Model parameters

The 8 free parameters of the P-unit model β, τ_m, μ, D, τ_A, Δ_A, τ_d, and t_{ref}, were fitted to both baseline activity (mean baseline firing rate, CV of ISIs, serial correlation of ISIs at lag one, and vector strength of spike coupling to EOD) and responses to step increases and decreases in EOD amplitude (onset-state and steady-state responses, effective adaptation time constant) of 42 specific P-units for a fixed power of $p = 1$ (table 2.1, Ott, 2020). When modifying the model (e.g. varying the threshold nonlinearity or the power p in Eq. (2.12)) the bias current μ was adapted to restore the original mean baseline firing rate. For each stimulus repetition the start parameters A, V_d and V_m were drawn randomly from a starting value distribution, retrieved from a 100 s baseline, recorded in the model after a 100 s transient.

The cells used for a particular model analysis are stated in the figure legend. The model cells used for the analysis in Fig. 3.8 have the identifiers 2012-04-20-ak, 2011-10-25-ad, 2012-12-20-ab, 2012-12-20-ad, 2012-12-20-ae, 2012-12-21-ai, 2014-06-06-ac, 2018-05-08-af, 2018-06-25-ad.

2.13 Stimuli for the model

For the beat protocols, the stimulus was the EOD of the receiving fish, normalized to an amplitude of one plus the EOD of a second or third fish. If not stated otherwise, a superposition of cosine waves was used to mimic the EODs (Eq. (3.1)). Realistic EODs, as in Fig. 3.8 I, were generated by summing up the first 10 harmonics whose relative amplitudes and phases have been extracted from head-tail recordings obtained during measurements of P-unit baseline activity using the thunderfish software, `https://github.com/bendalab/thunderfish`.

The input for the model during RAM stimulation in chapter 4 was the EOD multiplied with a random amplitude modulation $RAM(t)$:

$$x(t) = (1 + RAM(t)) \cdot \cos(2\pi f_{EOD} t) \tag{2.18}$$

The $RAM(t)$ was generated by drawing random numbers for each frequency up to 300 Hz in Fourier space. After back transformation, the resulting signal was scaled to the desired standard deviation relative to the EOD carrier, which was termed contrast.

2.14 Second-order susceptibility analysis of the model

The second-order susceptibility in the model was calculated with Eq. (2.6), resulting in matrices as in Fig. 4.4 and Fig. 4.5. For this, the model neuron was presented the input $x(t)$ for 2 s, with the first second being dismissed as the transient. The second-order susceptibility calculation was performed on the last second, resulting in a frequency resolution of 1 Hz.

2.14.1 Model noise split into a noise and a stimulus component

Based on the Furutsu-Novikov Theorem (Novikov, 1965; Furutsu, 1963) the total noise of a LIF model can be split up into several independent noise processes with the same correlation function. Based on this theorem a weak input signal to the LIF model can be approximated with no input signal but instead, a split of the total noise into a noise component and a signal component (Egerland, 2021). This signal component can be used for the cross-spectrum calculation in Eq. (2.6), where it is not a weak signal anymore. This approach has the advantage that the signal-to-noise ratio is increased and the number of noise stimulus realizations N, which would be required in case of a weak input signal for the same signal-to-noise ratio, is reduced. The signal component is regulated by c_{signal} in Eq. (2.19) and the noise component is regulated by c_{noise} in Eq. (2.21).

$$x(t) = (1 + \sqrt{\rho\, 2D\, c_{signal}} \cdot RAM(t)) \cdot \cos(2\pi f_{EOD} t) \tag{2.19}$$

$$\tau_d \frac{dV_d}{dt} = -V_d + \lfloor x(t) \rfloor_0^p \tag{2.20}$$

$$\tau_m \frac{dV_m}{dt} = -V_m + \mu + \alpha V_d - A + \sqrt{2D\, c_{noise}}\, \xi(t) \tag{2.21}$$

In chapter 4 a big portion of the total noise was assigned to the signal component ($c_{signal} = 0.9$) and the remaining part to the noise component ($c_{noise} = 0.1$, Fig. 2.2 $\mathsf{D_{iii}}$). Both components have to add up to the initial 100 % of the total noise, otherwise the Furutsu-Novikov Theorem (Novikov, 1965; Furutsu, 1963) would not be applicable. This is easily achieved in a model without a carrier if the condition $c_{signal} + c_{noise} = 1$ is satisfied (Egerland, 2021). In the here used LIF model with EOD carrier, this is more complicated since the noise stimulus $RAM(t)$ is first multiplied with the carrier (Eq. (2.19)), the signal is then subjected to rectification and subsequent dendritic low-pass filtering and becomes colored (Eq. (2.20)). This is the component that is added to the noise component in Eq. (2.21) and should in sum lead to a total noise of 100 %.

To compensate for these transformations, the generated noise $RAM(t)$ was scaled up by a factor ρ (Eq. (2.19), red in Fig. 2.2 $\mathsf{D_i}$). The ρ scaling factor was found by bisecting the space of possible ρ scaling factors by minimizing the error between the baseline CV (only carrier present) and the CV during stimulation (total noise split with c_{signal} and c_{noise}). The assumption behind this approach was that as long the CV stays the same between baseline and stimulation both components have added up to 100 % of the total noise and the noise split is valid.

2.14.2 Artificial bursts in the model

For the analysis in Fig. 4.8 the spikes in the non-busty model with identifier 2013-01-08-aa (see table 2.1 for model parameters) were supplemented by burst spikes after exactly one, two or three EOD periods. A spike was not added if the refractory time to the next spike could not be maintained.

2.14.3 Field-distance calculation

The input to the P-unit model was the EOD of the fish normalized to one plus the EOD of the encountered fish with the amplitude expressed as a contrast, a percentage of the receiver EOD. For the electrosensory cocktail party problem in chapter 5 this contrast had to be recalculated in the distance between the fish. Under ideal conditions the field potential Φ decays with distance d with a power p of two ($\Phi(d, F) = F/d^p$, Henninger et al., 2020). In this equation, F

is an amplitude factor influenced by water conductivity and the dipole moment, that provides information about the effective waveform strength. Due to the properties of the terrain (e.g. the shallowness of the rivers) the field potential decay with distance is usually not described by an ideal dipole, but the decay has an exponent smaller than 2 (Benda, 2020; Henninger et al., 2020; Fotowat et al., 2013). Here the contrast-distance relationship was based on a fit of the field potential decay recorded in the natural habitat of *Apteronotus rostratus* (Henninger et al., 2020) to the dipole function, resulting in the parameters $p = 1.61$ and $F = 24\,\mathrm{mv/cm}^q$. $\Phi(d, F)$ was approximated by the field amplitude of the encountered fish, which was calculated as the multiplication of the contrast with the mean of the values above the 95 % percentile of the zero-centered receiver EOD (Henninger et al., 2020).

2.15 Behavioral experiments

2.15.1 Jamming avoidance response

For measuring the jamming avoidance response a fish was placed in a $40 \times 50\,\mathrm{cm}^2$ tank filled with water from its home tank ($\sim 250\,\mu\mathrm{S/cm}$ conductivity). The water had a height of 20 cm and the fish stayed voluntarily in a plastic tube. With the same techniques and equipment as for the electrophysiology, the fish's EOD frequency was measured via two carbon electrodes placed in front and behind the tube where the fish was hiding. The fish was stimulated with another pair of carbon electrodes placed orthogonal to the measurement electrodes to the side of the fish about 10 cm apart. Within a time window of 10 s the EOD frequency of the fish was estimated from a power spectrum right before each stimulus presentation. Sine-wave stimuli were calibrated to an amplitude of 2 mV/cm measured at the position of the fish. Stimulus frequencies were fixed for the 30 s long duration (no frequency clamping) and set to k times f_{EOD} minus 5 Hz for $1 \leq k \leq 5$ and plus 5 Hz for $k = 0$, with f_{EOD} measured right before stimulus onset. Each stimulus frequency was presented once to each fish.

The spectrogram was computed from the recorded fish's EOD (FFT segment length of $n_{\mathrm{fft}} = 131072$, samples with an overlap of 50 %). The time course of the EOD frequency was estimated from the second harmonic's peak frequency in the spectrogram. To compute the frequency shift the baseline EOD frequency, estimated as the averaged EOD frequency within 10 s right before stimulus onset, was subtracted. The steady-state frequency shift was estimated as the average EOD frequency within 15 to 25 s after stimulus onset relative to baseline EOD frequency.

Table 2.1: Model parameters of LIF models, fitted to 42 electrophysiologically recorded P-units (Ott, 2020). See section 2.12 for model and parameter description.

cell	β	τ_m/**ms**	μ	D/**ms**	τ_A/**ms**	Δ_A	τ_d/**ms**	t_{ref}/**ms**
2011-10-25-ad	301.4	2.90	−34.38	0.440	116.08	0.16	4.08	0.74
2012-04-20-ak	373.7	1.74	21.88	0.130	294.95	0.34	4.29	0.93
2012-05-10-ad	267.2	2.03	−31.25	1.076	182.00	0.28	2.21	1.10
2012-06-27-ah	554.4	1.71	−148.44	0.368	117.84	0.21	10.61	1.21
2012-06-27-an	26.7	1.38	−4.88	0.006	130.36	0.03	3.99	0.90
2012-07-03-ak	10.6	1.38	−1.32	0.001	96.05	0.01	1.18	0.12
2012-07-12-ag	14.4	1.11	−0.10	0.008	111.57	0.04	1.81	1.15
2012-07-12-ap	44.1	1.46	1.17	0.131	71.43	0.08	1.32	0.97
2012-12-13-af	427.8	3.90	−111.72	0.165	137.55	0.13	10.03	0.96
2012-12-13-ag	95.4	8.83	−22.66	1.701	270.58	0.04	1.52	0.53
2012-12-13-ah	365.5	1.19	−87.50	0.099	135.01	0.16	13.14	1.42
2012-12-13-an	35.0	8.41	−3.52	0.071	158.27	0.04	1.09	0.91
2012-12-13-ao	16.7	2.21	−1.27	0.027	56.72	0.02	1.37	0.86
2012-12-20-aa	75.3	4.61	−17.97	0.117	69.35	0.04	2.23	0.06
2012-12-20-ab	46.6	1.35	−4.79	0.029	48.01	0.02	1.21	1.14
2012-12-20-ac	43.1	1.55	−5.66	0.025	69.75	0.03	2.53	0.86
2012-12-20-ad	124.2	1.06	−16.21	0.056	93.17	0.08	4.54	1.09
2012-12-20-ae	190.1	1.65	−31.84	0.071	61.15	0.07	5.37	0.92
2012-12-21-ai	291.2	2.10	−54.69	0.552	127.44	0.13	3.15	1.20
2012-12-21-ak	18.0	1.55	−3.22	0.072	87.20	0.01	1.49	1.12
2012-12-21-am	85.6	2.41	−21.48	0.061	54.47	0.04	5.00	1.13
2012-12-21-an	47.7	1.33	−8.98	0.073	84.49	0.03	2.16	1.26
2013-01-08-aa	4.5	1.20	0.59	0.001	37.52	0.01	1.18	0.38
2014-06-06-ac	382.9	4.98	−70.70	4.005	111.95	0.15	2.40	0.62
2014-06-06-ag	350.3	2.78	−81.25	5.419	112.50	0.26	6.21	1.20
2014-12-03-ai	537.3	3.40	−139.06	0.741	193.79	0.29	21.36	0.82
2014-12-11-aa	499.4	1.09	−50.00	0.827	864.45	1.52	22.74	1.03
2014-12-11-ad	81.4	5.61	−16.41	0.304	360.92	0.18	3.44	0.92
2015-01-15-ab	144.2	3.90	−18.75	4.264	84.07	0.23	2.76	0.58
2015-01-20-ac	57.6	3.11	−9.57	0.094	364.23	0.09	7.11	0.60
2015-01-20-ae	944.1	2.12	−280.47	1.566	228.32	0.24	12.92	1.29
2015-01-20-af	122.3	2.57	−31.25	2.566	34.86	0.12	3.04	1.22
2018-01-10-al	66.7	1.46	5.47	0.877	134.09	0.20	1.75	1.22
2018-05-08-aa	196.8	9.00	−38.28	18.657	83.42	0.18	1.50	1.22
2018-05-08-ab	74.4	2.10	−3.12	0.496	164.93	0.18	2.11	0.84
2018-05-08-ac	23.5	1.96	−1.56	0.174	141.67	0.05	1.22	0.92
2018-05-08-ad	32.9	1.13	−0.10	0.090	83.01	0.05	1.35	0.78
2018-05-08-ae	139.6	1.49	−21.09	0.214	123.69	0.16	3.93	1.31
2018-05-08-af	266.9	1.19	−35.16	0.168	61.96	0.16	8.87	1.10
2018-05-08-ai	58.6	1.14	−1.56	0.207	72.36	0.12	2.24	1.43
2018-06-25-ad	286.1	2.39	−29.69	2.437	96.35	0.24	1.88	1.09
2018-06-26-ah	32.3	1.30	−0.20	0.183	89.91	0.05	1.45	0.70

Chapter 3

Smooth threshold nonlinearity and high beat frequencies

This chapter has already been published in Barayeu et al. (2023). All figures in this chapter are adapted from this publication.

Periodic signals are key stimuli for different sensory modalities as the auditory system (Lewicki, 2002; Köppl, 1997; Romani et al., 1982) and the electrosensory system of wave-type electric fish (Hopkins, 1976). The superposition of two periodic signals with similar frequencies results in a periodic amplitude modulation (AM) that is known as "beat". The beat frequency is given by the frequency difference between the two signals and the beat amplitude is the amplitude of the smaller of the two signals. Auditory beats give rise to a unique beating perception (Roeber, 1834; Plomp, 1967). In wave-type electric fish, beats play a central role during electrocommunication (Benda, 2020).

Wave-type Gymnotiform electric fish generate a sinusoidal electric organ discharge (EOD) with a species and individual specific frequency (Knudsen, 1975; Henninger et al., 2020). The EODs of two nearby fish superimpose and produce a beat. Beat amplitudes decline with distance between two fish and thus are strongly influenced by relative movement (Yu et al., 2005). The periodic beat is modulated by different types of electrocommunication signals on time scales ranging from 10 ms to many seconds (Zakon et al., 2002; Smith, 2013). Cutaneous tuberous organs that are distributed all over the body (Carr et al., 1982) sense the actively generated electric field and its modulations. Within a single tuberous electroreceptor organ about 30 primary electroreceptors form ribbon synapse onto the dendrites of the same afferent fiber (Szabo, 1965; Wachtel and Szamier, 1966) which projects via the lateral line nerve to the hindbrain. There the afferent fiber synapses onto pyramidal neurons in the electrosensory lateral line lobe (Maler, 2009).

The time course of the activity of p-type electroreceptor afferents (P-units) follows the time course of AMs of the EOD (Bastian, 1981; Nelson et al., 1997; Benda et al., 2005). Similar encoding of AMs is also observed in auditory fibers (Joris et al., 2004). So far, beat frequency tuning of P-units has been analyzed in a range up to 300 Hz in *Apteronotus leptorhynchus* (Bastian, 1981; Benda et al., 2006; Walz et al., 2014). The strongest firing rate modulations were observed in response to beat frequencies between 60 and 100 Hz and beyond that at about 250 Hz the response declined down to baseline, with no firing rate modulations expected at even higher beat frequencies. However, recent field studies in the natural habitat of *Apteronotus*, demonstrated behaviorally relevant difference frequencies beyond 300 Hz in the context of courtship, synchronization of spawning (Henninger et al., 2018) and potential inter-species detection (Henninger et al., 2020).

In this chapter, it was studied how difference frequencies greater than 300 Hz are encoded in the electrosensory system. Therefore, P-unit activities of *Apteronotus leptorhynchus* in

response to a much wider range of difference frequencies ($-750 \leq \Delta f \leq 2500\,\mathrm{Hz}$) than before, were recorded. Mathematical reasoning and simulations of integrate-and-fire neurons identified the minimum functional requirements of single sensory cells to be able to extract and respond to slow envelopes, generated at large difference frequencies. These insights were tested in behavioral experiments based on the jamming avoidance response (JAR, Watanabe and Takeda, 1963).

These results in this chapter generate an interesting hypothesis for the mechanism underlying beat perception at mistuned octaves in humans. Experiments dating back to the 19th century demonstrated a beat perception not only for spectrally close frequencies but also for mistuned octaves where the second frequency is close to octaves of the carrier frequency (Roeber, 1834; König, 1876; Ohm, 1839; Helmholtz, 1875). Until now the physiological mechanisms underlying these percepts remain an open issue (Plomp, 1967; Joris et al., 2004).

3.1 Results

3.1.1 High beat frequency encoding

The spiking activity of $n = 40$ p-type electroreceptors afferents (P-units) of the electric fish *A. leptorhynchus* in response to sinusoidal electrical stimuli with absolute frequencies ranging from 20 up to 3200 Hz was recorded. These stimuli interfere with the own electric field of the fish and result in beat-like envelopes. In the following the term "beats" will be used for difference frequencies between the stimulus frequency and the EOD frequency of the fish below half an octave. For larger difference frequencies the term "beat-like envelopes" will be used.

3.1.2 Responses to low difference frequencies

P-units are known to respond to low-frequency beats by modulations of their firing rates (Bastian, 1981; Nelson et al., 1997; Benda et al., 2005; Walz et al., 2014). For a fish with an EOD frequency $f_{EOD} = 668\,\mathrm{Hz}$ and a stimulus with frequency $f_{stim} = 737\,\mathrm{Hz}$, mimicking a fish with higher EOD frequency, a beat at the difference frequency $\Delta f = f_{stim} - f_{EOD} = 69\,\mathrm{Hz}$ emerges (Fig. 3.1 C, top). A P-unit aligns its spike rasters and the corresponding time-resolved firing rate to such a amplitude modulation (Fig. 3.1 C, center). In the power spectrum of the spike response the strongest peaks are at the beat frequency (colored circle) and the receiver's EOD frequency (gray circle, Fig. 3.1 C bottom).

When f_{stim} is below f_{EOD} (here $\Delta f = -63\,\mathrm{Hz}$), the resulting beat has a negative difference frequency but is similar to the beat discussed before. The P-unit response has the same features as for the positive difference frequency and the spectrum also has peaks at the same frequencies (compare the beat frequency and f_{EOD} in Figs. 3.1 B and C). Signals generated by positive or negative Δf differ only in small phase shifts in the carrier, that are encoded by another population of electroreceptors, the T-units (Scheich et al., 1973).

As f_{stim} increases, the beat frequency increases and the P-unit's response strength, characterized by the modulation depth of the P-unit's firing rate, declines (Fig. 3.1 D), in accordance with previous results (Bastian, 1981; Nelson et al., 1997; Savard et al., 2011; Walz et al., 2014).

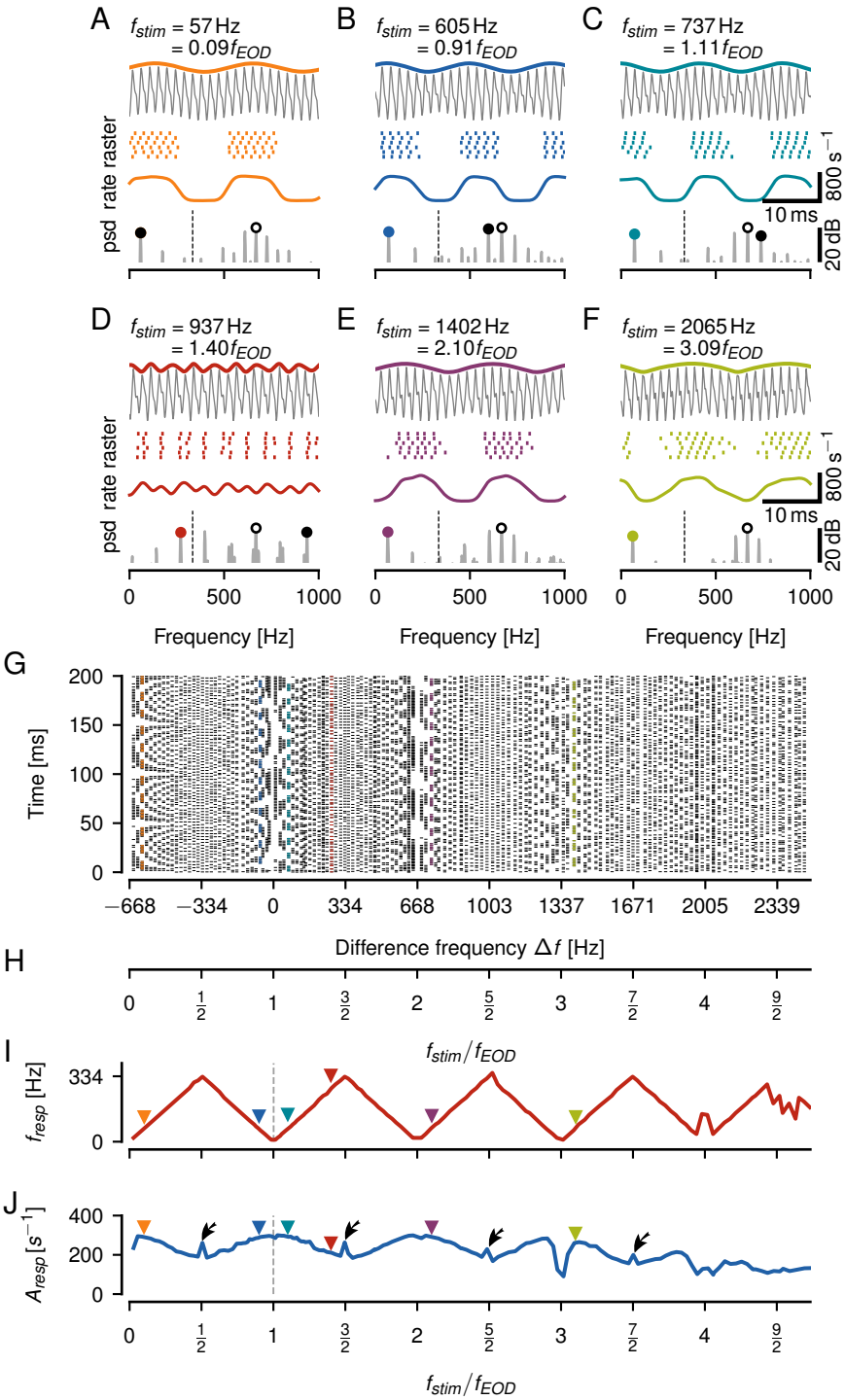
A
f_{stim} = 57 Hz
= 0.09 f_{EOD}
B
f_{stim} = 605 Hz
= 0.91 f_{EOD}
C
f_{stim} = 737 Hz
= 1.11 f_{EOD}
psd rate raster
800 s^{-1}
10 ms
20 dB
D
f_{stim} = 937 Hz
= 1.40 f_{EOD}
E
f_{stim} = 1402 Hz
= 2.10 f_{EOD}
F
f_{stim} = 2065 Hz
= 3.09 f_{EOD}
0
500
1000
Frequency [Hz]
G
Time [ms]
200
150
100
50
0
−668
−334
0
334
668
1003
1337
1671
2005
2339
Difference frequency Δf [Hz]
H
0
1/2
1
3/2
2
5/2
3
7/2
4
9/2
I
f_{stim}/f_{EOD}
f_{resp} [Hz]
334
0
J
A_{resp} [s^{-1}]
400
200
0
f_{stim}/f_{EOD}

Figure 3.1: Encoding of a wide range of difference frequencies in an example P-unit.
A–F Beating envelopes (colored lines) of the carrier EOD superimposed with a sine wave stimulus (gray, top), spike raster and firing rate of evoked P-unit responses (center), and corresponding power spectrum (psd, bottom, open circle: f_{EOD}, dashed line: $f_{EOD}/2$, colored circle: strongest frequency below $f_{EOD}/2$, black circle: f_{stim}) of a few selected stimulus frequencies as indicated. See supplementary Video S1 in Barayeu et al. (2023) for cell responses to all stimulus frequencies.
G Vertical raster plots showing spiking responses to a wide range of stimulus frequencies (one trial per frequency) indicate a repetitive structure of P-unit responses. Colored rasters mark examples shown in panels A–F.
H Alternative stimulus frequency axis in multiples of f_{EOD}, i.e. $\Delta f/f_{EOD} + 1$.
I Frequency tuning, f_{resp}, of the P-unit response, i.e. frequency of its firing rate modulation, retrieved as the strongest peak in the response spectrum below $f_{EOD}/2$, repeats every integer multiple of f_{EOD}. Colored triangles mark examples shown in panels A–F.
J Amplitude tuning curve, quantified as the amplitude of the peak at f_{resp} (square-root of the integral below the peak at f_{resp} of the power spectrum of the spike response convolved with a Gaussian kernel with $\sigma = 0.5\,\text{ms}$), also repeats at harmonics of f_{EOD}. The strongest responses are close to multiples of f_{EOD}. Exactly at odd multiples of $f_{EOD}/2$ peak amplitudes are increased (arrows).

3.1.3 Envelope frequency does not match difference frequency for high stimulus frequencies

In the three so far presented examples the beat envelope frequencies and $|\Delta f|$ are identical. Increasing (or decreasing) f_{stim} beyond $f_{EOD} \pm f_{EOD}/2$, breaks this relation. Instead, at $f_{stim} = 0.1f_{EOD}$, $2.1f_{EOD}$, or $3.1f_{EOD}$ the resulting beating envelopes have the same frequency as for $f_{stim} = 1.1f_{EOD}$, the classical beat for a stimulus frequency close to the receiver's EOD frequency (compare Fig. 3.1 A, E, F to C). As the stimulus frequency gets close to integer multiples of the EOD frequency, the envelope frequency goes towards zero even if the absolute difference frequency is larger than half the EOD frequency.

3.1.4 P-units respond to an extremely wide range of stimulus frequencies

It is well-known that slow envelopes of the fish's EOD, where $|\Delta f|$ is smaller than $f_{EOD}/2$, effectively modulate the spike responses of P-units. Reoccurring ranges of stimulus frequencies leading to strongly and slowly modulated responses can be observed beyond low $|\Delta f|$ for stimulus frequencies of about three times the EOD frequency (Fig. 3.1 G and supplementary Video S1 in Barayeu et al., 2023). Clear P-unit responses are also observable towards stimulus frequencies down to about 35 Hz (Fig. 3.1 A, G and first frames of supplementary Video S1 in Barayeu et al., 2023). Stimulus frequencies that lead to clear modulations of a P-unit's firing rate are centered on integer multiples of f_{EOD}. Thus, f_{EOD} defines the frequency scale in which f_{stim} has to be interpreted. Accordingly, from now on f_{stim} will be expressed relative to f_{EOD} (f_{stim}/f_{EOD}). This has the advantage that comparisons across animals with distinct EOD frequencies are possible (Fig. 3.1 H).

3.1.5 Aliasing structure of beat responses

Around integer multiples of f_{EOD} slow beat-like signals and correspondingly strongly modulated spike responses can be observed. Towards odd multiples of $f_{EOD}/2$, signal envelopes are oscillating faster and the strength of the spike responses decreases. In the following, the P-unit response characteristics are quantified by extracting the frequency and the respective strength of the response modulation from the power spectrum of the spiking response. The position of the strongest peak in the response power spectrum below $f_{EOD}/2$ is taken as an indicator for the main frequency of the P-unit's firing modulation. When this frequency is plotted as a function of f_{stim} a repetitive shaped pattern is revealed (Fig. 3.1 I). This zigzag pattern looks like a "Toblerone" and is reminiscent of aliasing known from the sampling theorem, with $f_{EOD}/2$ taking the role of the Nyquist frequency.

For stimulus frequencies that evoked no or only small peaks in a P-unit's response spectrum, the spectrum was dominated by the P-unit's baseline spectrum. This leads to a peak at the mean baseline firing rate or close to it. When the baseline peak amplitude was larger than the amplitude of the low-frequency alias of the stimulus, the frequency tuning curve deviated from the "Toblerone" pattern. This happened in some cells when the stimulus frequency was close to multiples of f_{EOD} (Fig. 3.1 I at 2005 Hz) or when the stimulus frequency exceeded the range to which a P-unit was tuned to (Fig. 3.3 B, D).

3.1.6 Periodic amplitude tuning curve

The amplitude A_{resp} of the respective peak in the response power spectrum reflects the strength of the P-unit response, i.e. the modulation depth of its time-resolved firing rate. The resulting tuning curve also has a repetitive structure (Fig. 3.1 J). Its response is strongest when f_{stim} is close to multiples of f_{EOD}. These maxima, however, become smaller for higher f_{stim}. Dips in the response amplitudes are observed directly at the f_{EOD} multiples. These dips can be attributed to the spike-frequency adaptation of P-units (Benda et al., 2005). Response amplitudes decline as the stimulus frequency approaches odd multiples of $f_{EOD}/2$. Because two peaks in the response power spectrum cross each other (supplementary Video S1 in Barayeu et al., 2023) response amplitudes are often markedly elevated at exactly odd multiples of $f_{EOD}/2$ (arrows in Fig. 3.1 J). For higher stimulus frequencies response amplitude again increases towards the next f_{EOD} multiple. This increase in the response amplitude beyond $f_{stim} = \frac{3}{2} f_{EOD}$ was not expected considering previous data on the encoding of amplitude modulations in P-units (Bastian, 1981; Nelson et al., 1997; Savard et al., 2011; Walz et al., 2014).

3.1.7 Amplitude tuning depends on post-synaptic filtering

P-unit electroreceptor afferents are connected to pyramidal neurons in the electrosensory lateral line lobe in the hindbrain. The synapse between these cells introduces a fast excitatory postsynaptic potential with a duration of about 1 ms (Berman and Maler, 1998). Postsynaptic potentials can be modeled by bins or filter kernels that are used to compute time-resolved firing rates. Therefore, the estimation of P-unit firing rates already includes assumptions about the postsynaptic readout. The P-units tuning curve shape strongly depends on the width of the chosen filter kernel. The reason is that the kernel low-pass filters the spike train, as does a postsynaptic potential. The tuning of P-units is relatively flat when computed directly from the spike trains since no low-pass filtering is involved (Fig. 3.2 A). The stronger the spike train is low-pass filtered (mimicking a wider postsynaptic potential), the more the response peaks closer to $f_{EOD}/2$ are attenuated (arrows in Fig. 3.2 B, C), leading to a stronger modulated tuning curve. If spikes are filtered by a physiologically plausible Gaussian kernel with $\sigma = 0.5$ ms

high envelope frequencies responses are decreased while the response to low envelope frequencies is not altered. Such low-pass filtering results in periodically modulated amplitude-tuning curves (Fig. 3.2 B).

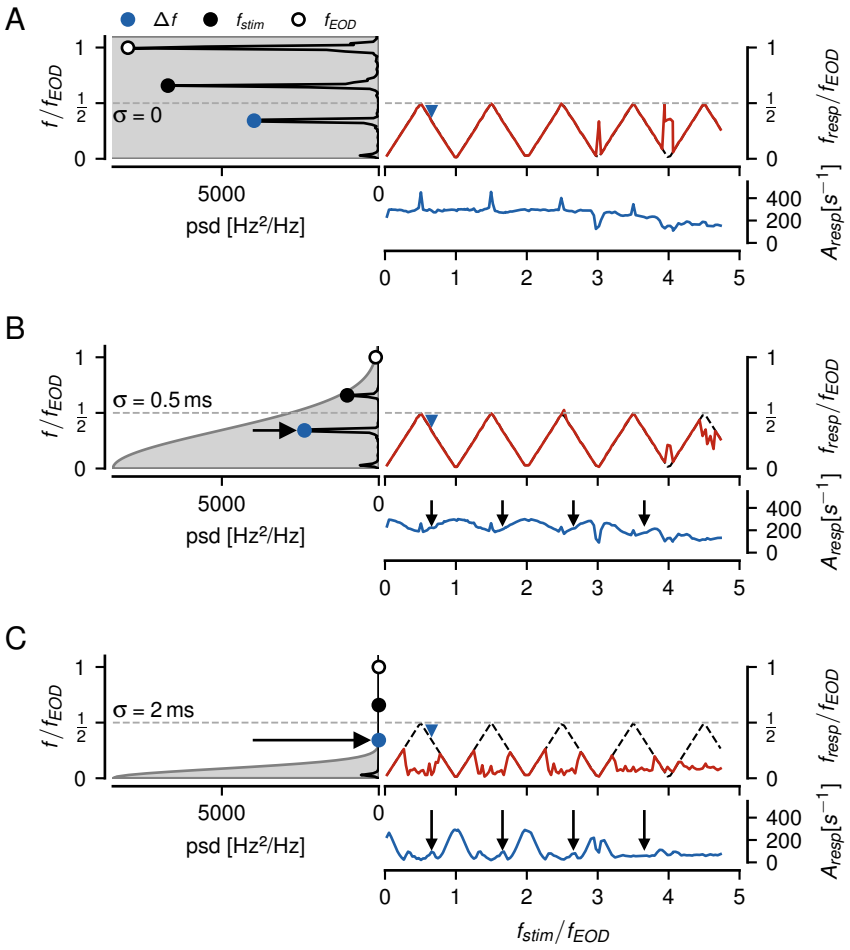

Figure 3.2: Influence of post-synaptic low-pass filtering on P-unit responses to beat-like stimuli. Left: Power spectral density of a P-unit's firing rate response (unit of firing rate squared, Hz^2, per frequency bin, Hz^{-1}, here not transformed to decibel) to a $\Delta f = -220\,\mathrm{Hz}$ beat (blue markers). The convolution kernel mimicking post-synaptic filtering is indicated by the Gaussian-shaped gray area. The horizontal dashed line indicates $f_{EOD}/2$. Right: Frequency tuning curve (top) together with the expected aliased frequencies (black dashed line) and amplitude tuning curve (bottom) estimated from the strongest peak of a P-unit's response below $f_{EOD}/2$.

A Spectrum and tuning curves of the raw, binary spike trains recorded with a resolution of 40 kHz. The strongest peak in the spectrum is at f_{EOD} (open circle), followed by the peak at the absolute value of the stimulus frequency f_{stim} (black circle). The peak at the difference frequency corresponding to the frequency of the resulting beat is even smaller but is the largest peak below $f_{EOD}/2$ (orange circle). Frequency tuning follows the aliased frequencies over almost the whole measured range up to $5f_{EOD}$. The amplitude tuning curve is mostly flat with pronounced peaks at odd multiples of $f_{EOD}/2$.

B A biological plausible post-synaptic filter, modeled by convolving the spike trains with a Gaussian kernel ($\sigma = 0.5\,\mathrm{ms}$), keeps the frequency tuning but reduces the amplitude of the P-unit's response for stimulus frequencies close to odd multiples of $f_{EOD}/2$ (arrows).

C A wider post-synaptic potential, modeled by a Gaussian with $\sigma = 2\,\mathrm{ms}$, degrades the frequency tuning curves and strongly modulates amplitude tuning.

3.1.8 Sensitive cells respond to a larger frequency range

It is known that the response of P-units scale with stimulus amplitude (Bastian, 1981; Nelson et al., 1997) and that different P-units differ in their sensitivities to a global stimulus (Grewe et al., 2017). To account for both, sensitivity and stimulus intensity, the response of P-units was quantified as the amplitude to a standard stimulus, a beat at $\Delta f = 50\,\text{Hz}$ (Grewe et al., 2017). Across the 40 P-unit recordings, the firing rate modulations evoked by the 50 Hz beat ranged from 70 to 360 Hz and were positively correlated with the mean baseline firing rates that ranged from 80 to 527 Hz ($r = 0.63$, $p < 0.0001$). The modulation depth in the P-unit firing rate is an indicator of the effective stimulus amplitude driving the P-unit's response.

The stronger the P-unit's response modulation depth, the more the P-unit tuning curves correspond to the low-frequency alias of the stimulus to higher stimulus frequencies (Pearson's $r = 0.51$, $p = 0.001$, Fig. 3.3 A). Since here the main interest was understanding the mechanisms behind the aliasing structure of the P-units' responses, the analysis further will be focused only on the $n = 14$ most sensitive cells with modulation depths greater than 265 Hz. These highly sensitive cells respond up to almost four times f_{EOD} (Fig. 3.3 B, C) whereas the less sensitive cells respond just up to about twice f_{EOD} on average (Fig. 3.3 D, E).

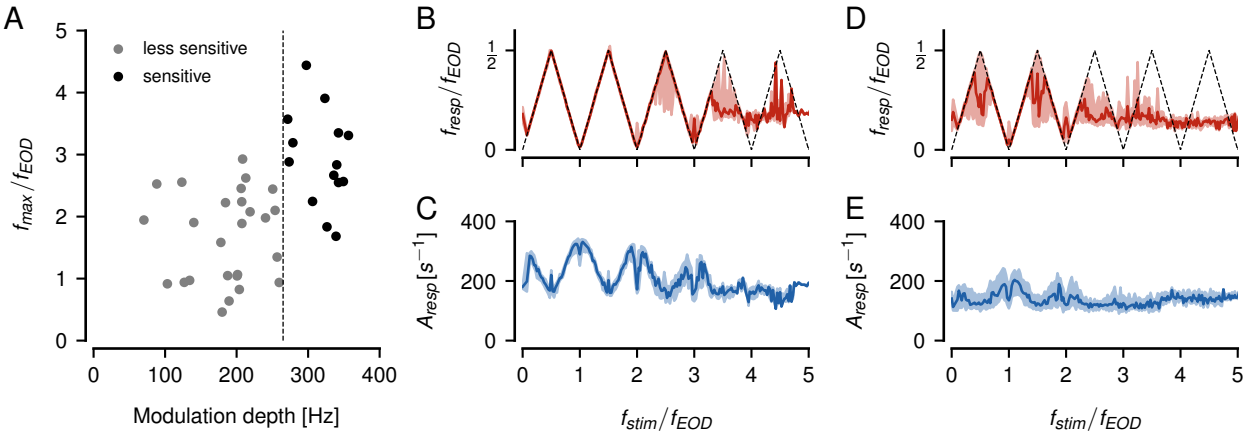

Figure 3.3: Dependence of the aliasing structure on sensitivity.
A For each of the recorded P-units we estimated the maximum stimulus frequency f_{max} up to which its frequency tuning curve indicated a response by following the predicted low-frequency aliases of the stimulus frequency (e.g. dashed line in panel B). The more sensitive a P-unit, as quantified by the modulation depth of its firing rate response to a 50 Hz standard beat, the higher the maximum frequency. Since we were primarily interested in understanding the mechanisms behind the aliasing structure of the P-units' responses, we focused our analysis on the most sensitive cells with modulation depths greater than 265 Hz (black).
B Frequency tuning of the $n = 14$ most sensitive cells reaches up to almost four multiples of f_{EOD} (medians with interquartile ranges).
C Corresponding amplitude tuning curves are stronger in comparison to the less sensitive cells in E.
D, E Frequency and amplitude tuning curves of the $n = 26$ less sensitive cells (gray dots in A).

3.1.9 Algorithms for extracting envelope frequencies at high stimulus frequencies

In the following sections the prerequisites necessary for neurons to extract the low-frequency alias of the stimulus, making up the amplitude modulations of beats, will be presented. The resulting theory explains the experimental observations, including the enhanced responses at

odd multiples of $f_{EOD}/2$ (arrows in Figs. 3.1 J). The details of the mathematical derivations and equations are provided in the supplement (see section A.1).

3.1.10 Slow beating envelopes in superimposed cosine waves

As suggested by Fig. 3.1, the aliasing structure of the P-unit response results from the envelopes of the interacting EODs. To understand how such responses can arise, the mechanism by which envelopes are retrieved from the superposition of the two EODs have to be understood. If the superimposed signal is considered in the Fourier domain, only peaks at f_{EOD} and f_{stim} will be present. Therefore, the question is how the spectral peak at the envelope frequency can be generated.

This is a generic problem independent of the electrosensory system, and thus the problem here is expressed in terms of two cosine waves: a carrier, the EOD of the receiving fish, with frequency $\omega_1 = 2\pi f_1$ and amplitude one and a stimulus, the EOD of another fish, with frequency $\omega_2 = 2\pi f_2$ and an amplitude α measured relative to the amplitude of the carrier (stimulus contrast). Here the focus is mainly on the case $\alpha \ll 1$, where a clear distinction between a large amplitude carrier signal with frequency ω_1 and a stimulus of smaller amplitude at frequency ω_2 can be made.

Both signals superimpose:

$$x(t) = \cos(\omega_1 t) + \alpha \cos(\omega_2 t) \tag{3.1}$$

The resulting signal $x(t)$ also has the characteristic beating envelopes reoccurring at multiples of the frequency ω_1 of the carrier signal (Fig. 3.4 $\mathsf{A_i}$–$\mathsf{A_v}$). A running average that attenuates the fast carrier signal results in flat lines, except for the stimulus frequencies close to zero (compare Fig. 3.4 $\mathsf{A_{ii}}$–$\mathsf{A_v}$ to $\mathsf{A_i}$). Because the stimulus cosine distorts the carrier cosine this can be observed even for ω_2 close to twice and four times ω_1, where upper and lower envelopes are out of phase. The respective power spectra have peaks only at the input stimulus frequencies ω_1 and ω_2 (Fig. 3.4 $\mathsf{B_i}$–$\mathsf{B_v}$) and there are no spectral peaks at the slow envelope frequencies (except for ω_2 close to zero), although the envelopes are clearly perceivable by visual inspection.

3.1.11 Neither the analytic signal nor squaring explains the aliasing structure of the beating envelopes

A nonlinear operation has to be applied to the signal to generate additional spectral peaks at the observed envelope frequencies. Commonly used nonlinearities to retrieve the beat amplitude modulation for two spectrally close signals are squaring, the absolute value of the analytic signal obtained using a Hilbert transform, or thresholding (Middleton et al., 2007; Stamper et al., 2012).

Both squaring and the analytic signal predict the frequency of the beating envelope to be equal to the difference frequency. This is also what is expected for low difference frequencies, i.e. for stimulus frequencies ω_2 close to ω_1. For higher difference frequencies the analytic signal suggests an amplitude modulation with growing frequency (Fig. A.1 A), although the signals are not necessarily amplitude-modulated signals anymore (e.g. panels $\mathsf{A_i}$, $\mathsf{A_{iii}}$ and $\mathsf{A_v}$ in Fig. 3.4, upper and lower envelopes are no mirror versions of each other). Squaring also predicts a spectral peak at the difference frequency, no matter how large the difference frequency is (Fig. A.1 B). These two types of nonlinearities can neither explain the aliasing structure that is observed in superimposed cosines (Fig. 3.4 A), nor in superimposed EODs and in the corresponding P-unit responses (Fig. 3.1).

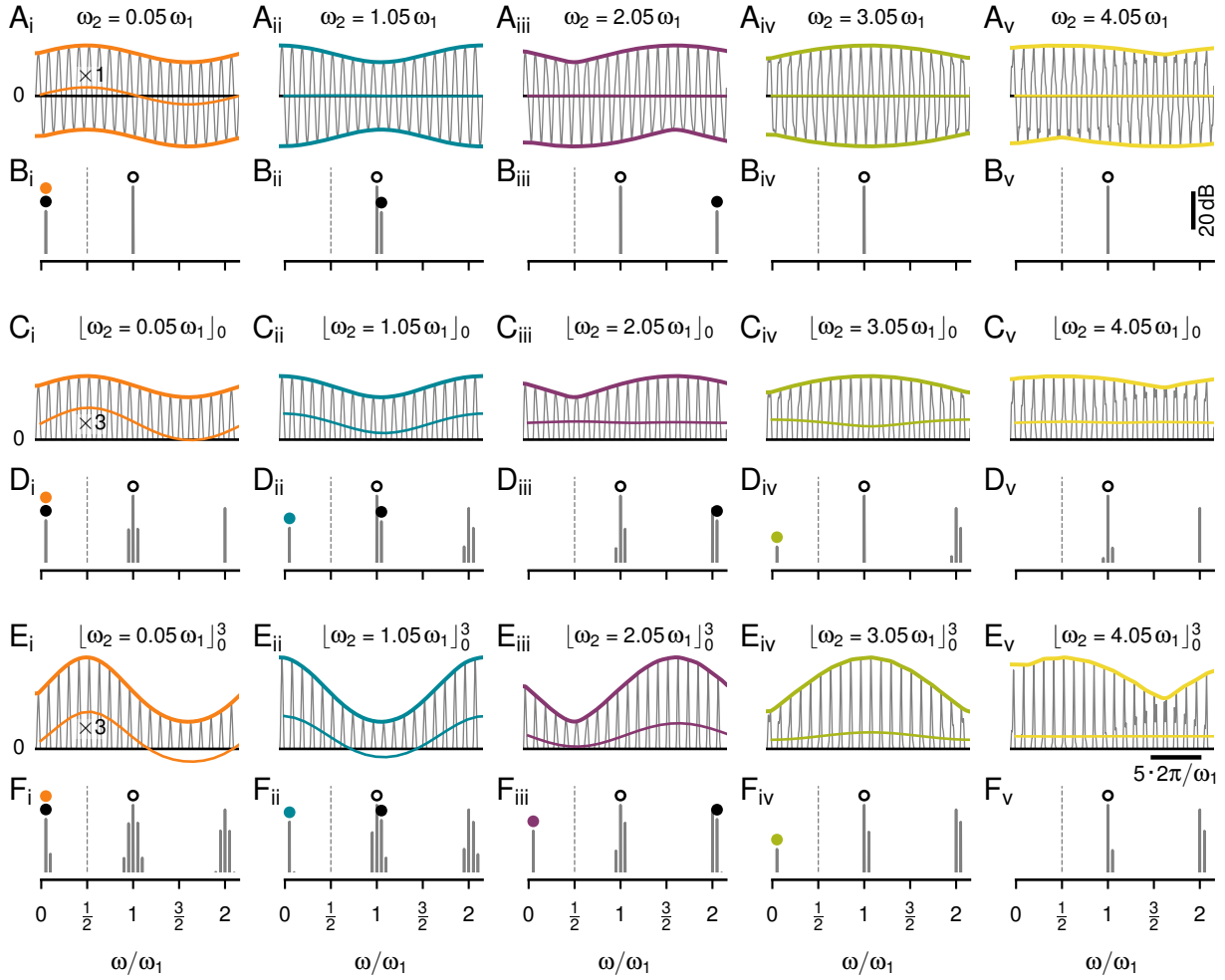

Figure 3.4: Slow envelopes resulting from the superposition of two cosine waveforms.
A The raw signals — superpositions of a cosine carrier with fixed frequency ω_1 and stimulus cosines of various frequencies ω_2 close to multiples of ω_1 as indicated and an amplitude of $\alpha = 0.2$ relative to the one of the carrier. Upper and lower envelopes are highlighted by thick colored lines. The thin colored lines are running averages over a single cycle of the carrier frequency, which keeps only frequency components smaller than ω_1. For stimulus frequencies similar to or larger than the carrier frequency, the running average is zero, even when the upper and lower envelopes are out of phase.
B Although slow envelopes are clearly visible in the waveforms shown in A, the corresponding power spectra have only peaks at ω_1 (open circle) and ω_2 (black circle) and not at the slow envelopes. Only when the stimulus frequency ω_2 is below $\omega_1/2$ it coincides with the envelope (orange circle in B_i).
C Thresholding cuts away the negative half-waves and leaves only the upper envelope intact. Now the running average (enlarged by a factor of three around its mean) follows the envelopes for ω_2 close to 0, 1, and 3 multiples of ω_1, but not for 2 and 4 multiples. Note, for $\omega_2 = 3.05\,\omega_1$ the running average is antiphasic to the envelope.
D Thresholding generates frequencies explaining the envelopes at odd multiples of the carrier frequency only (cyan and green circles in D_{ii} and D_{iv}).
E Raising the thresholded signal from C to a power of three narrows the half-waves of the carrier and slightly distorts the envelopes. The running average (enlarged by a factor of three) follows the upper envelope up to three multiples of ω_1, but with decreasing amplitudes.
F This operation adds a peak in the power spectrum for stimulus frequencies around the second multiple of the carrier (purple circle in F_{iii}).

3.1.12 Thresholding explains aliasing at odd multiples of the carrier frequency

A threshold operation is commonly used to retrieve amplitude modulation in neuronal data (Myers et al., 2003). A threshold nonlinearity

$$\lfloor x(t) \rfloor_0 = \begin{cases} x(t) & ; \quad x(t) \geq 0 \\ 0 & ; \quad x(t) < 0 \end{cases} \tag{3.2}$$

sets all negative values of a signal to zero and only the positive half-waves are passed through. The upper envelope is retained whereas the lower envelope of the signal is discarded (Fig. 3.4 C). For brevity this half-wave rectification will be called "thresholding". Indeed, thresholding generates spectral peaks in the resulting signal at some of the envelope frequencies, but not for stimulus frequencies close to the second or fourth multiple of the carrier frequency (Fig. 3.4 D). Consequently, low-pass filtering the thresholded signals results in flat lines when ω_2 is close to two and four times of ω_1, despite the obviously present envelope. Surprisingly, the stimulus distorts the carrier such that when ω_2 is close to $2\omega_1$ the running average generates a signal with the same frequency as the envelope, but in antiphase to the envelope (Fig. 3.4 C$_{\text{iv}}$).

To make the threshold operation, Eq. (3.2), analytically tractable, here it is approximated by a multiplication of the signal (Fig. 3.5 A) with a pulse train with the same frequency ω_1 as the carrier signal (Fig. 3.5 B):

$$\lfloor x(t) \rfloor_0 \approx x(t) \cdot p(\omega_1 t) \tag{3.3}$$

The pulse train is designed that way that it

$$p(\omega_1 t) = \begin{cases} 1 & ; \quad \cos(\omega_1 t) \geq 0 \\ 0 & ; \quad \cos(\omega_1 t) < 0 \end{cases} \tag{3.4}$$

multiplies positive half-waves of the carrier cosine with one and negative half-waves with zero (Fig. 3.5 C).

Note that this approximation is only valid in the limit $\alpha \to 0$, since for larger stimulus amplitudes the stimulus distorts the carrier, shifting the zero crossings. As a consequence of bigger α, additional side-peaks occur in the spectra (Fig. 3.4 D).

According to the convolution theorem, multiplication in the time domain equals a convolution in the Fourier domain. Thus, the Fourier spectrum of the thresholded signal (Fig. 3.5 C) can be calculated as the convolution of the spectrum of the signal (Fig. 3.5 A) and the spectrum of the pulse train (Fig. 3.5 B). The pulse train Fourier spectrum has a peak at zero frequency and peaks at all odd multiples of the carrier frequency ω_1.

The convolution of the carrier frequency ω_1 with the pulse train spectrum results in peaks at even multiples of ω_1 and at $\pm\omega_1$ (horizontal lines in Fig. A.1 C). Because these frequencies do not depend on ω_2 they cannot explain the beating envelope.

The convolution of the stimulus frequency ω_2 with the pulse train provides side peaks at $\pm\omega_2$ to all the pulse train peaks (Fig. A.1 C). These peaks can explain the aliasing structure of the beating signal envelopes and the frequency tuning curves of P-units around odd multiples of ω_1 and around zero frequency, but not around two times ω_1 (Fig. 3.5 D). The amplitudes of these peaks quantify the beating envelope amplitudes and are the basis for the amplitude tuning curves of P-units. These peaks decrease with higher carrier multiples (Fig. 3.5 E, see section A.1.3 of the supplement for a mathematical derivation of these amplitudes). Thereby this amplitude decrease is stronger than that of the signal's envelopes.

In contrast to the analytic signal amplitude and squaring, the threshold operation introduces many additional peaks in the spectrum. These peaks are necessary to explain some but not all of the aliasing structure of signal envelopes. Thresholding in particular does not generate low-frequency spectral peaks for stimulus frequencies around twice the carrier frequency.

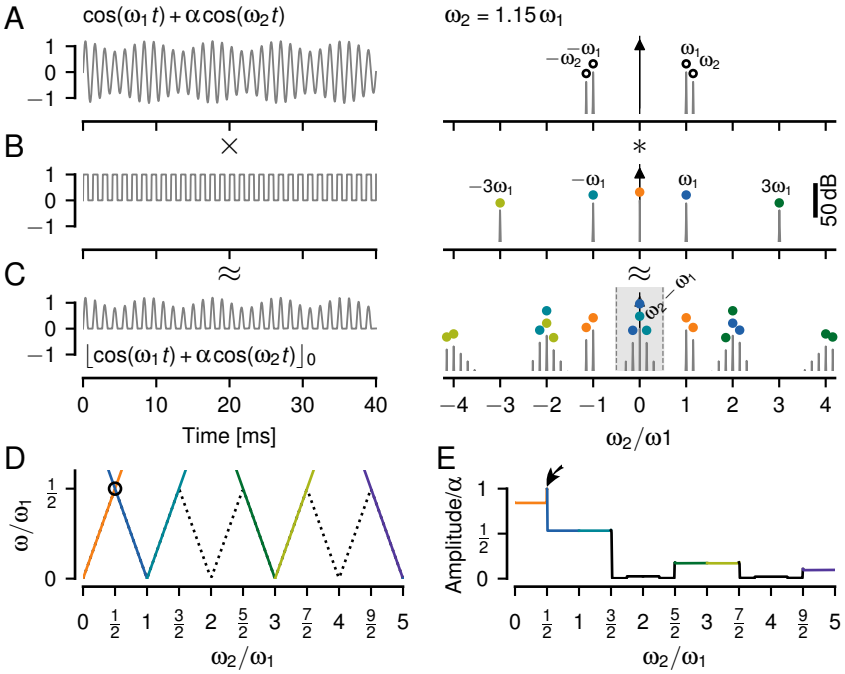

Figure 3.5: Thresholding is not sufficient to explain the full aliasing structure of beat-like envelopes.

A A beat generated by summing up two cosines with frequencies ω_1 and ω_2 (left) only contains these two frequencies in its Fourier spectrum (right). The amplitude $\alpha = 20\,\%$ of the stimulus cosine is smaller than the one of the carrier.

B A pulse train, Eq. (3.4), used to approximate a threshold operation, Eq. (3.2), has peaks at odd multiples of ω_1 and at zero.

C Thresholding the signal from A results in a rich spectrum. In the limit of vanishing stimulus amplitude α, the thresholded signal can be approximated by multiplying the signal from A with the pulse train in B. The corresponding spectrum is approximated by convolving the spectrum of the signal with the one of the pulse train (colored circles, one color for each peak of the pulse train). Here, for $\omega_2 = 1.15\,\omega_1$ a peak appears at the difference frequency $\omega_2 - \omega_1$ below $\omega_1/2$ (gray area). This peak describes the small amplitude modulation of the beat visible in A. Because the stimulus amplitude is not close to zero, this approximation does not explain all the side peaks in the spectrum.

D The position of peaks in the spectra of thresholded signals (colored lines) below $\omega_1/2$, as a function of stimulus frequency ω_2. This curve is a prediction for the frequency tuning curves of P-units. The dashed line marks the expected alias frequencies of the stimulus, and the circle the only crossing of spectral peaks. Note, that close to two and four multiples of ω_1 no peaks are created by thresholding below $\omega_1/2$. See Fig. A.1 C for spectral peaks also at higher frequencies.

E Amplitude of the peaks shown in D decrease with higher multiples of ω_1. At the crossing of spectral peaks (circle in D), amplitudes sum up (arrow). These amplitudes are measured relative to the amplitude α of the stimulus cosine and would drive the amplitude tuning curves of P-units.

3.1.13 Threshold cubed fills in frequencies at around twice the carrier frequency

How can the missing components in the spectrum around even multiples of ω_1 be filled in? The synaptic transfer function connecting P-units and pyramidal cells has not been measured until now. However, it is known that P-units share several properties with inner hair cells in the auditory system and their transfer function has been described by a power function with an exponent of three (Roux et al., 2006; Özçete and Moser, 2020; Peterson and Heil, 2019). Therefore here the thresholded signal will first be taken to a power of three:

$$x_c(t) = \lfloor x(t) \rfloor_0^3 \tag{3.5}$$

A power of three leads to narrower half-waves of the carrier in the resulting signals. In addition, the envelopes are slightly distorted in comparison to a pure threshold of the superimposed signal (Fig. 3.4 E). In the corresponding Fourier spectra peaks at the slow envelope frequencies up to the third multiple of f_{EOD} appear now (Fig. 3.4 F). In particular, peaks for stimulus frequencies close to the second f_{EOD} multiple are now prevalent (Fig. 3.4 F$_{iii}$). The running average now also produces signals of the same frequency and phase as the envelopes up to the third f_{EOD} multiple.

This can again be approximated by multiplying the signal to the power of three with a pulse train (Fig. 3.6 A–C). Now the spectrum of the two superimposed cosines cubed has more peaks, namely $2^3 = 8$ peaks. These peaks result from two times convolution of the two peaks with themselves (Fig. A.2 A). The peaks at $|2\omega_1 - \omega_2| = |\omega_1 - \Delta\omega|$ are the only relevant additional peaks in comparison to the threshold without any exponent. The convolution of these peaks with the zero-frequency peak of the pulse train already fills in the missing frequencies around twice the carrier frequency (Fig. 3.6 D, red and purple). With this, a threshold with a power of three is enough to explain the frequency tuning curve of P-units (Fig. 3.3 B) up to 3.5 f_{EOD} multiples.

The amplitudes of the peaks below $\omega_1/2$ decline in a step-wise manner for each multiple of ω_1 (Fig. 3.6 E). At $\omega_1/2$, $3\omega_1/2$, and $5\omega_1/2$ the spectral peaks cross each other (circles in Fig. 3.6 D) and their respective amplitudes add up resulting in elevated amplitudes exactly at these frequencies (Fig. 3.6 E, arrows). These peak crossings can explain the elevated P-unit responses at these frequencies (arrows in Fig. 3.1 J). See section A.1.4 in the supplement for a mathematical derivation of peak frequencies and amplitudes and Fig. A.2 B. With a cubed threshold, the peak amplitudes also decline faster than the amplitudes of the envelopes.

In this paragraph, it was demonstrated that a cubed threshold operation is sufficient to generate spectral peaks below half the carrier frequency for stimulus frequencies up to 3.5 multiples of ω_1. These peaks correspond to the aliasing structure that is there in the signal envelopes and can potentially explain the recorded P-unit responses. In contrast, a pure threshold fails in the extraction of slow envelopes around twice the carrier frequency. This nonlinear operation has to be followed by a low-pass filter, isolating the envelope frequencies by the attenuation of the carrier frequency and other spectral peaks beyond $\omega_1/2$.

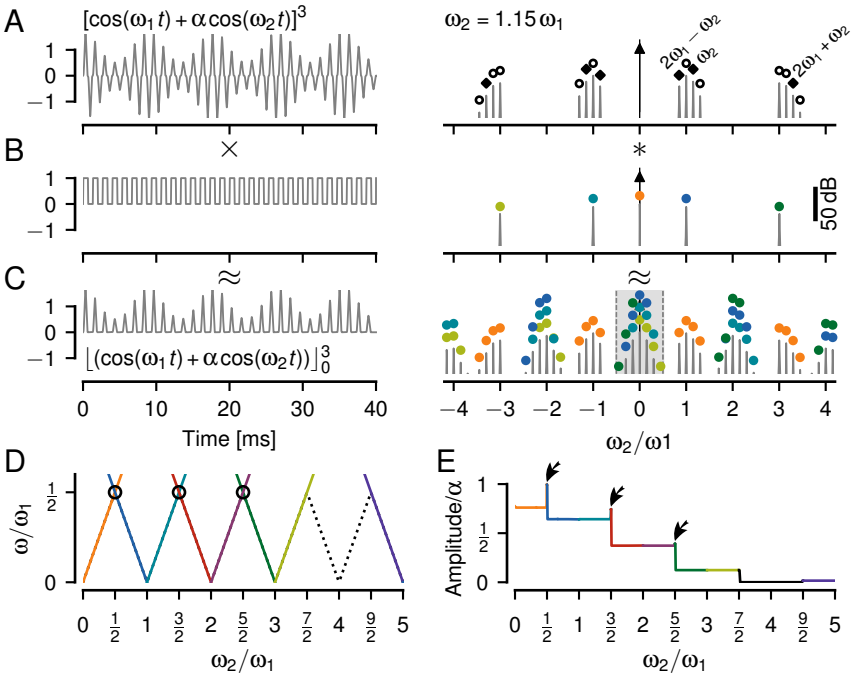

Figure 3.6: Cubing fills in frequencies corresponding to slow envelopes close to the second multiple of the carrier.
A The cubed signal (left) has a more pointed carrier waveform and eight peaks in the positive half of the Fourier spectrum (right, Fig. A.2 A).
B Again here the threshold operation is approximated by a multiplication with a pulse train.
C The threshold-cubed signal has a much richer power spectrum compared to the thresholded signal without exponent (Fig. 3.5 C). The convolution process is illustrated by the colored markers — the spectrum of the cubed signal from A is shifted to each of the individually colored peaks in the spectrum of the pulse train from B. In this process, many peaks fall on top of each other and add up. The gray shading marks frequencies below $\omega_1/2$.
D Position of the largest spectral peaks of thresholded and cubed signals as a function of stimulus frequency. This is the frequency tuning curve. See Fig. A.2 B for spectral peaks at higher frequencies. The dashed line indicates the expected alias frequencies of the stimulus, that are extracted by the cubed-threshold operation up to $\omega_2 = 3.5\,\omega_1$. Circles mark peak crossings.
E Amplitudes of the peaks in D describe the amplitude of the beat-like signal envelopes. Crossing spectral peaks in D (circles) add up and result in elevated amplitudes (arrows). These amplitudes are driving the P-unit responses and thus are relevant for their amplitude tuning curve.

3.1.14 Spiking dynamics cannot explain responses to higher beat frequencies

A spike generator, modeled here as a leaky integrate-and-fire neuron (LIF) with adaptation current, also encodes the extracted envelope in a train of action potentials (Fig. 3.7). LIF models with a threshold nonlinearity without an exponent (power of one instead), Eqs. (2.13), (2.14), (2.12) (Sinz et al., 2020), were fitted individually to baseline and step-response characteristics of $n = 9$ recorded P-units (Tab. 2.1).

The nonlinearity of the spiking generator on its own is not sufficient to extract and respond to a beating amplitude modulation resulting from two spectrally close frequencies. Although some models can generate a peak at the beat frequency, these responses are almost independent of stimulus amplitude (Fig. 3.7 A).

When applying a threshold nonlinearity sufficient large spectral peaks at the difference frequency are generated. The spike generator driven by this frequency can generate action potentials that are capable of beat encoding. Thresholding of the signal leads to modulations of the evoked firing rate responses that strongly depend on beat amplitude, faithfully reproducing the spiking properties of P-units (Fig. 3.7 B).

For stimulus frequencies close to twice the carrier frequency action potentials do not encode the apparent envelope of the signal (Fig. 3.7 C). The reason is that after thresholding and low-pass filtering, the input to the spike generator does not provide a frequency component at the envelope frequency as input.

It requires a power of three applied to the thresholded signal to make the spike generator respond to the envelope at stimulus frequencies close to twice the carrier frequency (Fig. 3.7 D). Neither the hard threshold nonlinearity the LIF applies on the membrane voltage nor a smooth voltage threshold, of an exponential integrate-and-fire neuron (EIF, data not shown, Fourcaud-Trocmé et al., 2003) can extract the envelope resulting from a stimulus at around twice the carrier frequency. The nonlinear dynamics of a spike generator cannot generate the aliasing structure of the P-unit responses. Instead, a sufficiently strong static nonlinearity (Fig. 3.7 $\mathsf{D_i}$) has to be applied to the signal, such that the necessary low-frequency peak in the spectrum is generated. Subsequent dendritic low-pass filtering isolates this peak (Fig. 3.7 $\mathsf{D_{ii}}$) and this is what the spike generator responds to.

3.1.15 A power of three describes P-unit responses best

For a more systematic evaluation of which exponent on the threshold operation describes the P-unit responses best, LIF models were simulated using threshold nonlinearity exponents ranging from $p = 0.2$ to 5. To find the best exponent all resulting frequency and amplitude tuning curves were compared to the experimentally measured ones (Fig. 3.8).

As predicted, a pure threshold without exponent leads to responses at the zeroth, first and third harmonic, but diverges from the measured tuning curves (Fig. 3.8 A) around the second harmonic (Fig. 3.8 C). Exponents that are higher (Fig. 3.8 D, E, F, G) and lower than one (Fig. 3.8 B) also respond at the second f_{EOD} multiple. Models with powers of 0.5, 1.5, and 4 also respond to the forth f_{EOD} multiple.

To quantify the model performance the root mean squared errors (RMSE) were computed for all data and model pairings that had a similar sensitivity. This led to a comparison between 14 experimentally measured cells and 9 model cells. The RMSEs between the frequency tuning curves were minimal for powers of about 0.8, 1.5, and 3 (Fig. 3.8 H, left) and the RMSEs for the amplitude tuning curves had similar minima but with the smallest RMSE at a power of three (Fig. 3.8 H, right). A threshold with a power of three describes both the frequency and amplitude tuning curves of P-unit responses best.

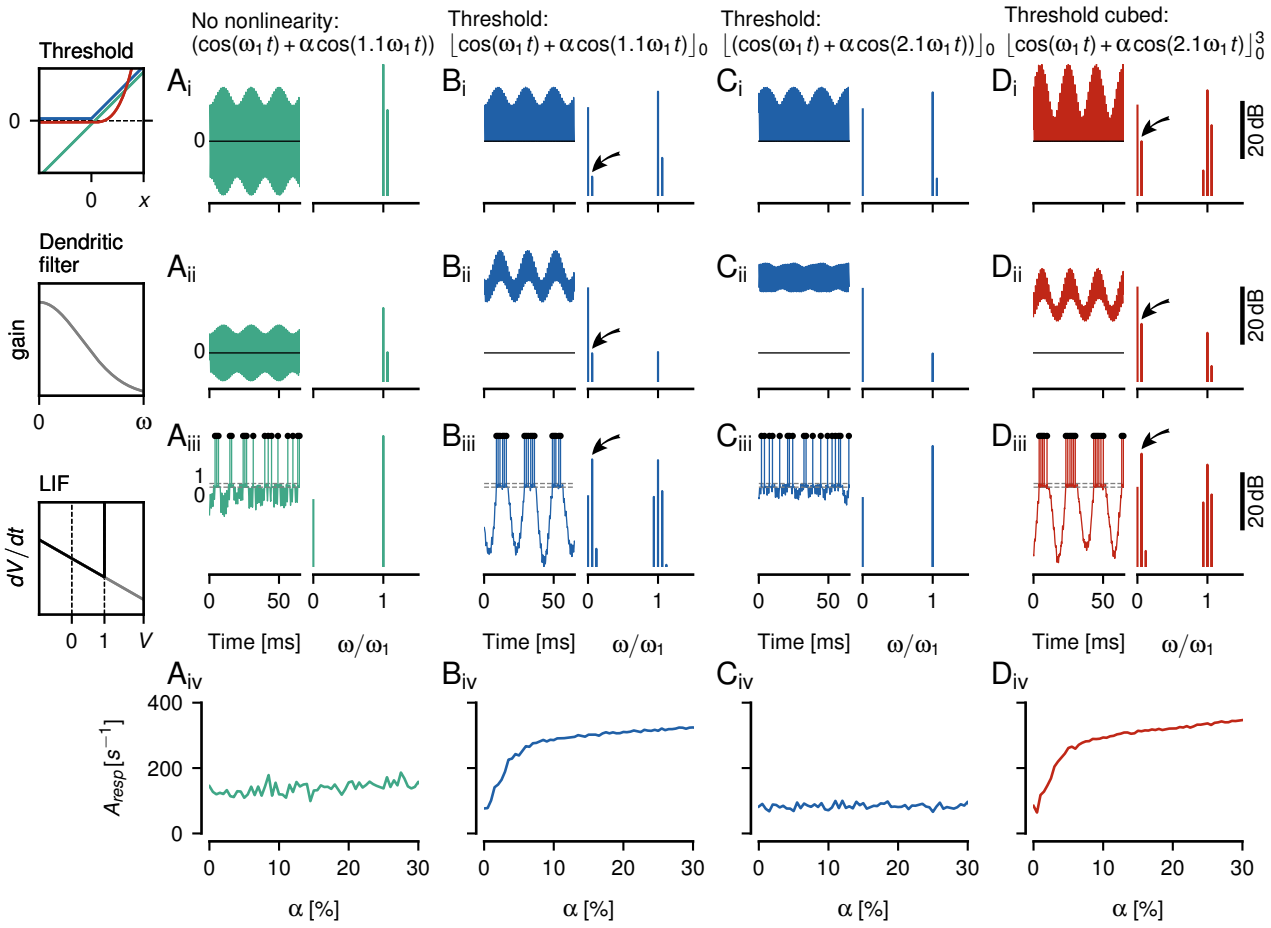

Figure 3.7: Integrate-and-fire models of P-unit spiking activity. As an example, simulations of the model for cell 2018-06-25-ad are shown (see Tab. 2.1 for parameters).
A$_{\text{i}}$ Waveform (left) and corresponding power spectrum (right, same reference for decibel scale for all spectra shown in top two rows and a different reference for the spectra of the third row) of two superimposed cosine waves. No nonlinearity is applied (green identity line in box).
A$_{\text{ii}}$ Passing the signal through a dendritic low-pass filter, Eq. (2.12), here $\tau_d = 1.88\,\text{ms}$, attenuates the two frequencies.
A$_{\text{iii}}$ A leaky integrate-and-fire neuron (LIF) does not encode the beating amplitude modulation in its spike train.
A$_{\text{iv}}$ The height of the spike-train spectrum at the beat frequency grows weakly with beat amplitude α.
B Applying a threshold (blue curve in threshold box) generates a peak in the power spectrum at the beat frequency (arrow), if the stimulus frequency ω_2 is close to the carrier frequency ω_1. This frequency component becomes more apparent after dendritic low-pass filtering and the LIF can generate spikes at the peaks of the beat. The spike times contain a spectral peak at the beat frequency (arrow) and the size of this peak strongly depends on beat amplitude.
C For a stimulus frequency close to twice the carrier frequency, however, a threshold does not produce a spectral peak that would represent the beating envelope. After the dendritic low-pass filter the waveform still oscillates symmetrically around a fixed mean value and the LIF responds with tonic spiking that is not modulated by the signal's envelope.
D A cubed threshold (red curve in threshold box), however, generates a peak at the envelope frequency (arrows). Dendritic low-pass filtering results in an oscillating signal that shifts up and down according to the signal's envelope. Consequently, the LIF can encode this envelope in its spiking activity and is also sensitive to the amplitude of the envelope.

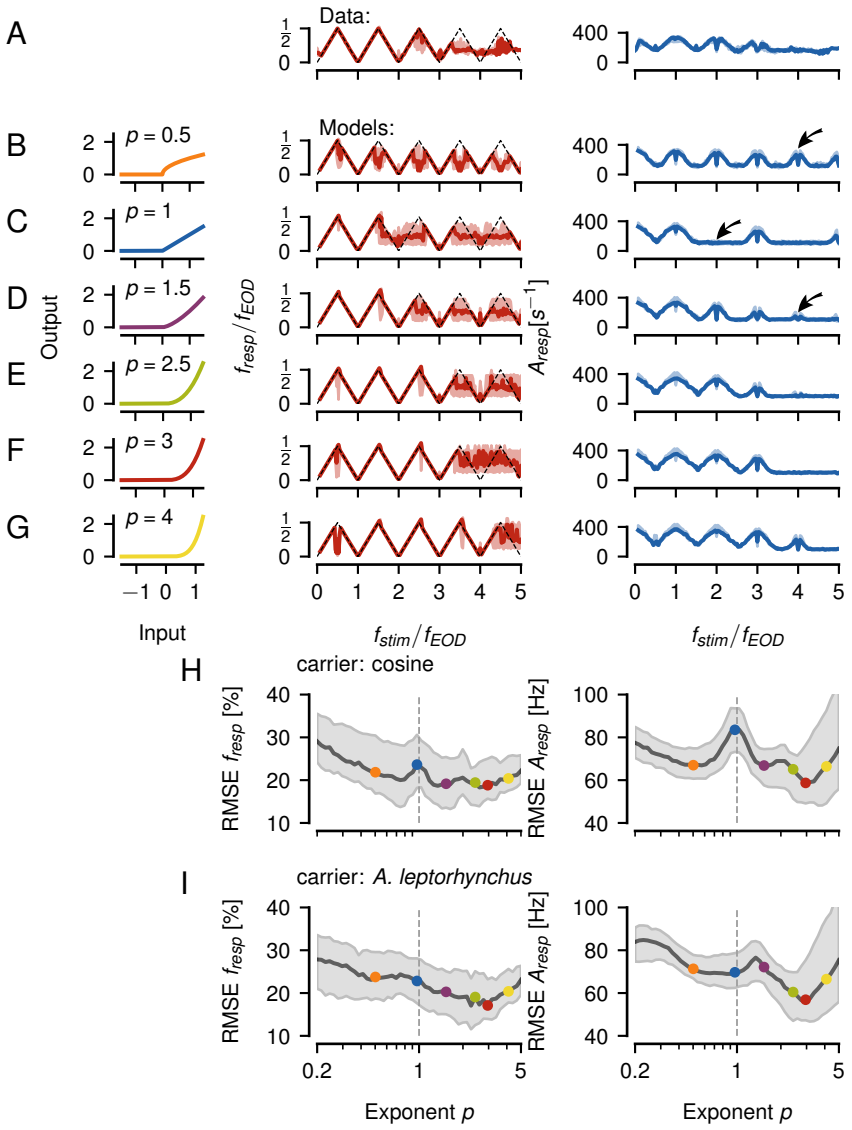

Figure 3.8: Dependence of LIF model performance on threshold exponent.
A Frequency (left) and amplitude tuning curves (right, population medians with interquartile ranges) of $n = 14$ experimentally measured P-units of highest sensitivity (same as Fig. 3.3 B, C).
B–G Tuning curves simulated from a population of $n = 9$ LIF models (Fig. 3.7) that have been fitted to individual P-units. Exponent p of the threshold nonlinearity applied to the signal as indicated and illustrated in the left column. Arrows indicate missing or additional responses in the amplitude tuning curve.
H Root mean squared error (RMSE, median with interquartile range) between the tuning curves of each experimentally measured P-unit shown in A and each LIF model in dependence on the threshold exponent used in the models. Examples from B–G are indicated by the correspondingly colored circles. Here, both the carrier and the stimulus are pure sine waves.
I Same as in H but with an EOD waveform of *A. leptorhynchus* as the carrier and a pure sine wave as the stimulus, resembling the situation in the electrophysiological experiments (see Fig. 3.9).

3.1.16 Harmonics of the carrier are not sufficient to explain aliasing

So far the reasoning in the previous paragraphs was based on pure sine waves. In electrophysiological recordings, however, the carrier is a real EOD waveform of *A. leptorhynchus*. To make the model more realistic and test if the optimal power operation would be altered by the presence of the harmonics of the waveform, here an EOD waveform was utilized as the carrier for the input in the model. This made the minimum at an exponent of $p = 3$ even more distinct (Fig. 3.8I). In a model with a pure threshold ($p = 1$), the harmonics of the carrier cannot contribute to shifting the stimulus frequency to all f_{EOD} multiples. A wider or narrower EOD waveform modifies the aliasing structure introduced by the threshold operation in a way that is not observed in the data. Applying a power of three to the threshold increases the robustness of the P-unit responses against changes in the EOD waveform (Fig. 3.9, see sections A.1.6 and A.1.7 in the supplement for a more detailed explanation).

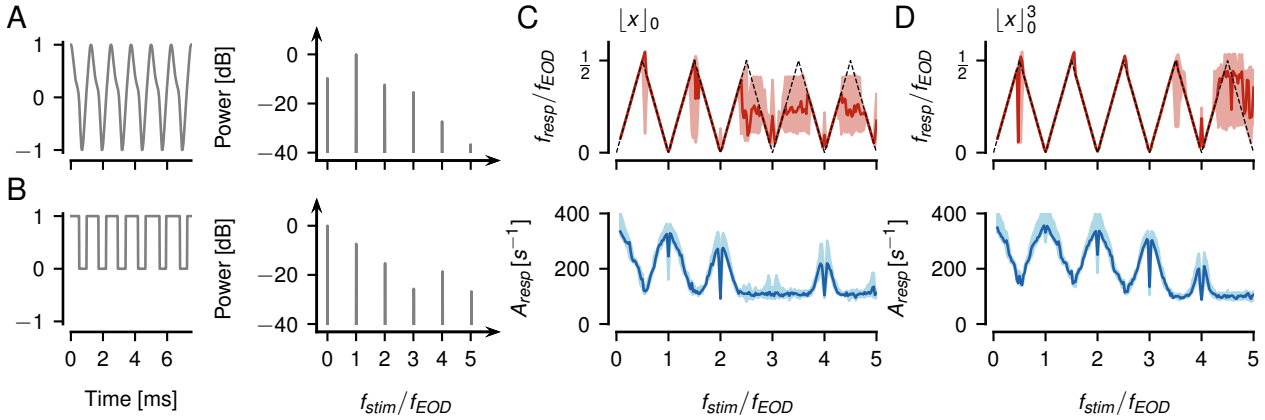

Figure 3.9: Influence of higher harmonics of the carrier on aliasing.
A An EOD waveform and the corresponding power spectrum of an *A. leptorhynchus* used as a carrier signal of frequency ω_1 for simulating P-unit responses with the LIF models from Fig. 3.8.
B The corresponding pulse train (left), needed to approximate the threshold operation, Eq. (3.2), has a duty cycle larger than 50 %. Its spectrum (right) has a peak at the second multiple of f_{EOD} in contrast to the spectrum of a pulse train with a 50 % duty cycle (Fig. 3.5 B).
C The enlarged duty cycle modifies the aliasing structure of the resulting frequency (top) and amplitude (bottom) tuning curves (medians with interquartile ranges of 9 simulated P-units), when using a threshold without exponent. For this shown example EOD waveform, the third harmonics and not the second as for a pure cosine wave is missing.
D Taking the thresholded signal to a power of three makes the tuning curves more independent of the duty cycle, and in particular fills in responses around three multiples of f_{EOD}.

3.1.17 Beats with the same envelope frequency evoke similar behavioral responses

So far it was demonstrated that P-unit responses to similarly mistuned multiples of f_{EOD} differ only in modulation depth of their firing rate responses. These results imply that P-unit responses are potentially indistinguishable concerning the absolute stimulus frequency. Here this hypothesis was tested behaviorally with the jamming avoidance response (JAR, Watanabe and Takeda, 1963). When a receiving fish is stimulated with a sine wave that is close to but below its own EOD frequency, the receiver will raise its EOD frequency by a few Hertz on a timescale of about 10 s (Fig. 3.10 A). Here this experiment was repeated with stimulus frequencies 5 Hz below one to five times f_{EOD}. Thereby, all the tested fish ($n = 5$) responded

with a significant EOD frequency increase to stimulus frequencies close to one, two and three multiples of their EOD frequency (Fig. 3.10 B). No fish responded to four times f_{EOD}, but some fish slightly elevated their EOD frequency by less than 1 Hz in response to five times f_{EOD}. The changes in frequency shift in response to non-zero multiples of f_{EOD} are similar to the amplitudes of the corresponding envelopes predicted by a cubed threshold. Only a single fish responded with a noticeable frequency shift to the stimulus at the zeroth multiple of f_{EOD}.

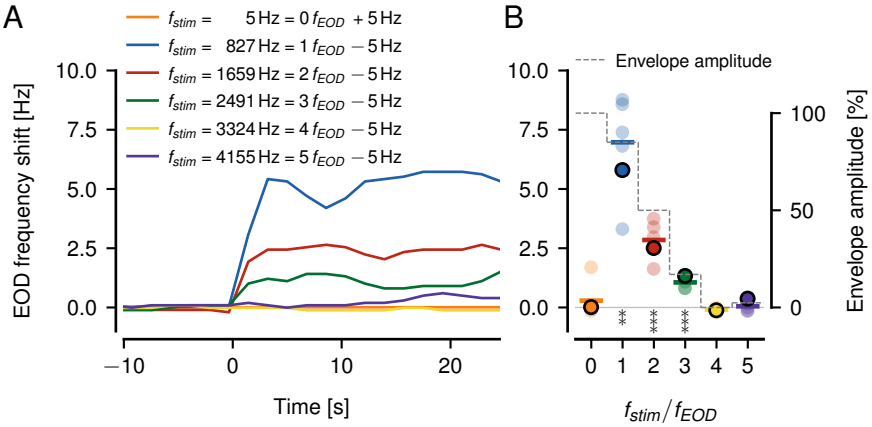

Figure 3.10: Jamming Avoidance Response (JAR) to stimuli close to multiples of f_{EOD}.
A Shifts in EOD frequency of a single example fish induced by sinusoidal stimuli switched on at 0 s. The stimulus frequency was set to 5 Hz above or below 0 to 5 times the EOD frequency of the fish as indicated. The fish responded to this stimulus by shifting its EOD frequency within about 10 s to a higher value.
B Steady-state frequency shifts measured between 15 and 25 s after stimulus onset of five fish as a function of f_{EOD} multiple. Frequency shifts of the fish shown in A are highlighted by circles with a black outline. The frequency shifts averaged over the five fish (colored horizontal lines) approximately follow the corresponding envelope amplitudes predicted by a cubed threshold (dashed line, see supplement section A.1.4 for equations) for non-zero multiples of f_{EOD}. Frequency shifts in response to low absolute stimulus frequencies are mostly absent, despite having the largest envelope amplitude. Asterisks indicate significant deviations of the steady-state frequency shifts from zero (t-Test, $^{**}p < 1\,\%$, $^{***}p < 0.1\,\%$)

3.2 Discussion

In this chapter, it was observed that P-units respond over a wide range of stimulus frequencies of up to about 3000 Hz (Fig. 3.1). This does not mean, that P-units for example encode a 3000 Hz stimulus frequency unambiguously. Instead, P-units are driven by their superimposed EOD and an exogenous stimulus, resulting in a beating signal envelope. At integer multiples of the carrier frequency (f_{EOD}) the envelopes are slow but between integer multiples they are fast. This pattern is reminiscent of aliasing known from the sampling theorem. The P-unit tuning curves are also periodic in integers of the f_{EOD} and the amplitude of the responses declines with higher stimulus frequencies.

3.2.1 P-unit tuning to high difference frequencies

So far P-unit tuning curves for beat stimuli have been measured only for difference frequencies up to 300 Hz (Bastian, 1981; Nelson et al., 1997; Benda et al., 2006; Walz et al., 2014). Thereby it was shown that the amplitude of the firing-rate modulation induced by beating envelopes

has a band-pass tuning shape: At frequencies close to zero the responses of P-units are strongly reduced (Nelson et al., 1997), reflecting the high-pass filter induced by fast spike-frequency adaptation (Benda et al., 2005). Towards higher beat frequencies the response was found to steadily decline as one would expect from a spiking neuron (Fourcaud-Trocmé et al., 2003) and as it is set by the neuron's baseline firing rate (Knight, 1972). This decline has also been observed in beat tuning curves in other modalities (Lamore et al., 1986).

The here reported experimental findings clearly demonstrate that P-units show responses to difference frequencies beyond 300 Hz. Instead, of the expected steady decline, the tuning of P-units repeats at EOD frequency multiples. This has profound consequences for the encoding of other electrocommunication signals, such as so-called chirps, that transiently change the difference frequency (Benda et al., 2005, 2006). In previous works, the P-unit response to chirps could be explained by transient firing rate modulations mediated by the shape of the P-units' amplitude tuning curve (Walz et al., 2014). The behavioral relevance of chirps at difference frequencies beyond 400 Hz and thus beyond $f_{EOD}/2$ has been observed in a field study (Henninger et al., 2018). A monotonously declining tuning curve would not be sufficient to explain how chirps could be encoded at such high difference frequencies. The here-described repetitive tuning retains the capability to change the modulation depth of the firing rate in response to chirps.

The low-pass filtering happening at the synapse between the afferents and their target neurons, the pyramidal cells in the electrosensory lateral line lobe, plays an important role in enabling chirp encoding (Fig. 3.2). If the filter kernel is too narrow, the tuning curve of P-units is almost flat and firing rate modulations caused by chirps would be quite small. If instead, the filter kernel is too wide, the tuning curve is only modulated within a narrow range of stimulus frequencies around carrier frequency multiples. Only for kernels resembling and mimicking the experimentally measured postsynaptic potentials ($\sigma = 0.5$ ms, Berman and Maler, 1998) the tuning curve is fully modulated without declining to the noise level between f_{EOD} multiples (Fig. 3.3). One hypothesis that can arise from these findings is that electric fish with lower EOD frequencies, like for example *Eigenmannia* spec., should have correspondingly wider postsynaptic potentials.

Surprisingly here it was observed that P-units show responses down to absolute stimulus frequencies of about 35 Hz, a range usually assumed to be primarily driving the ampullary electrosensory system and not P-units (Kalmijn, 1974; Engelmann et al., 2010; Grewe et al., 2017). Towards even lower stimulus frequencies P-unit responses vanish, although there seems to be a large variability between different cells (not shown). Future recordings with a finer frequency resolution of the stimulus frequencies are needed for in-depth exploration of this specific frequency range.

3.2.2 Envelope extraction at high difference frequencies

In a way the repetitive tuning curve of P-units is trivial since it simply follows the envelopes visible in the superimposed signals. But how are these envelopes extracted from the original signals, that do not contain the envelope frequencies in their power spectra?

Usually, the envelope frequency has been considered to be equal to the difference frequency (Walz et al., 2014; Joris et al., 2004). Here it was shown that extracting the envelope by the Hilbert transform or squaring of the signal (Middleton et al., 2007; Longtin et al., 2008; Stamper et al., 2012) is not sufficient to explain the experimental observations at higher difference frequencies (Fig. A.1 A, B). Both methods lead to spectral peaks reflecting the true envelope frequency for frequency differences below half the carrier frequency but not beyond. Furthermore, for stimulus frequencies close to even carrier frequency multiples, the resulting signals cannot be described as amplitude modulations, because their lower and upper envelope are out

of phase (Fig. 3.4 A).

Simple thresholding is often applied for the extraction of envelopes in EEG/EMG (Myers et al., 2003) or acoustic signals (Khanna and Teich, 1989). Such a threshold, also known as a Rectifying Linear Unit (ReLU) in deep learning, extracts envelope frequencies only at odd harmonics of the carrier (Fig. 3.5). The results presented in this chapter demonstrated that a threshold operation followed by exponentiation is required to explain the experimental findings (Figs. 3.6, 3.8). Neither the nonlinearity of spike generation (Fig. 3.7), nor higher harmonics of the carrier of the signal are sufficient to substitute the threshold with exponentiation (Fig. 3.9).

In deep learning approaches, using artificial neural networks, it has become common to apply smooth threshold functions such as ELU (Clevert et al., 2015) or Softplus (Glorot et al., 2011). Since these functions can be approximated by a ReLU raised to a power of three in the vicinity of their threshold, these functions are all potential alternatives for the threshold raised to a power of three suggested here. The same is true for sigmoidal activation functions which are discussed for the transformation of a hair-cells membrane voltage by their ribbon synapse (Peterson and Heil, 2019). Only for larger input amplitudes their saturation will lead to noticeable deviations.

3.2.3 Extraction of secondary envelopes

Secondary envelopes are defined as the amplitude modulation of beats and arise from relative movements between two fish (Yu et al., 2005) as well as from interactions between more than two fish (Middleton et al., 2006; Stamper et al., 2012). Secondary envelopes provide a context onto which electrocommunication signals are encoded in the thalamus (Wallach et al., 2022). However, they are mainly extracted downstream of P-units in the ELL (Middleton et al., 2006) utilizing threshold nonlinear response curves of the involved neurons (Middleton et al., 2007). The input from which the envelopes are extracted are not superpositions of sine waves anymore, but temporally modulated population firing rates. Therefore, the problem of encoding high stimulus frequencies does not exist when considering the context of encoding secondary envelopes. However, the results presented here demonstrate that secondary envelopes can also be expected on slow-beating envelopes close to carrier frequency multiples and that these should also be encoded in the electrosensory system.

3.2.4 Sinusoidal amplitude modulations (SAMs) versus beats

SAMs of various frequencies have been used to characterize signal processing in the electrosensory (Bastian, 1981), in the mechanosensory (Lamore et al., 1986) but also the mammalian auditory system (Joris et al., 2004). To create SAM stimuli a carrier – the EOD of an electric fish or a tone — is multiplied with a periodic amplitude modulation, like in Eq. (A.6). SAMs differ from superimposed cosines, Eq. (3.1), by having three spectral peaks instead of two spectral peaks. This additional side-peak of a SAM stimulus already fills in responses at the second multiple of the carrier frequency when used with a threshold without any exponent (Fig. A.2 C and section A.1.5 in the supplement). If SAMs had been used instead of realistic superimposed cosines, the necessity of the cubed threshold to retrieve the response to all carrier multiples would have been obscured.

3.2.5 Relation to the sampling theorem

In the limit to an infinitely high exponent, the thresholded and exponentiated carrier approaches Dirac delta functions positioned at multiples of the carrier's period. Thereby this pulse train can be thought of as sampling the stimulus waveform with the carrier frequency exactly as in

the setting of the sampling theorem. However, the stimulus waveform is also transformed by the threshold and the exponentiation. A higher exponent leads to a larger distortion of the extracted envelope. To maintain an accurate representation of the amplitude modulation, the exponent should be not too large. In this sense, a sharp threshold without any exponent would be ideal.

3.2.6 Physiological mechanisms for beat extraction

The presented theoretical considerations suggest an exponent of at least three. What are possible physiological substrates of such a nonlinearity?

First, it has to be noted that a perfect threshold is a mathematical abstraction. Any physiological mechanism that implements a threshold operation has some kind of smooth transition. A cubic power applied to the threshold approximates such a smooth transition (Fig. 3.7 D). In that sense, it can be considered biologically more plausible than a pure threshold.

The most probable site for such a smooth threshold operation can be considered the ribbon synapses of the electroreceptor cells onto their afferents the P-units (Szabo, 1965; Wachtel and Szamier, 1966) as has been suggested in previous works (Chacron et al., 2001). The voltage-gated calcium channels, that trigger synaptic transmitter release, implement a threshold operation by a sigmoidally-shaped activation function. Unfortunately, the synapse connecting primary electroreceptors and P-units are difficult to access and no transfer function recordings of these have been conducted so far.

A single afferent receives input from several primary electroreceptors. Before spike-generation in P-units, the postsynaptic potentials are most likely low-pass filtered by passive dendritic conduction (Sinz et al., 2020). With the right time-constant low-pass filtering isolates the low-frequency amplitude modulation but does not entirely remove the EOD (Fig. 3.7, second row). This is supported by the phase-locking of P-unit spikes to the EOD, with its vector strength being well below one (Grewe et al., 2017). Without low-pass filtering before the spike-generator, the vector strength would be expected to be much closer to one. With a stronger low-pass filtering P-units would lose their phase-locking to the EOD completely.

By silencing the EOD and probing the P-unit response to varying artificial EOD frequencies it has been shown that P-units are not only tuned to beats but also to the fish's own EOD frequency (Hopkins, 1976). Thereby the response of P-units is strongest to the fish's EOD frequency and close-by stimulus frequencies (Fig. A.3 A). The corresponding band-pass filter is assumed to be caused by electric resonance in the electroreceptor cell (Viancour, 1979). The P-unit tuning to the EOD frequency can be reproduced (Fig. A.3 A–B) when adding a damped oscillator, Eq. (A.27), to the P-unit models Eqs. (2.13) – (2.12) with no impairment to the beat responses at high difference frequencies (Fig. A.3 C–D).

3.2.7 Ambiguity in beat perception

It has been demonstrated that the decline of the envelope amplitude (Fig. 3.6 E) leads to a decline in response amplitude for carrier multiples (Fig. 3.3). The envelope amplitude also depends on the distance between two fish, with larger distances leading to smaller envelope amplitudes (Yu et al., 2005). Therefore, the amplitude of envelopes cannot be used to disambiguate different multiples of f_{EOD} and P-unit responses to similarly mistuned multiples of f_{EOD} are ambiguous. Based on the firing rate modulation of P-units fish should not be able to resolve absolute stimulus frequency.

Stimulus frequencies close to the receiver's own EOD frequency and also twice its EOD frequency were previously demonstrated to induce a jamming avoidance response (JAR, Watanabe and Takeda, 1963). In this chapter, stable JAR responses have been found even at the third

EOD frequency multiple. Thereby, the EOD frequency shift of the JAR up to five times the EOD frequency approximately follows the corresponding envelope amplitude as extracted by a cubed threshold (Fig. 3.10). In previous literature, it has been demonstrated that the behavioral detection threshold of a stimulus frequency (Knudsen, 1974) at least qualitatively follows the repetitive tuning curve of the P-units presented here. These findings suggest that wave-type electric fish indeed are not capable of disambiguating stimuli at different multiples of their EOD frequency.

In contrast, although the envelope amplitude is largest at the zeroth multiple of f_{EOD}, most fish did not respond with a JAR to a stimulus frequency close to it. This is in line with the finding that the P-unit response vanishes at stimulus frequencies below 35 Hz (Figs. 3.1 A, J, 3.3 C). This is the range of low-frequency stimuli that also evoke responses in ampullary cells of the passive electrosensory system (Kalmijn, 1974; Engelmann et al., 2010; Grewe et al., 2017). The activation of ampullary cells might allow the fish to disambiguate the (weak) P-unit responses and inhibit the JAR response at these low stimulus frequencies.

3.2.8 Perception of other wave-type species

The wide range of difference frequencies covered by P-units responses (Fig. 3.3) extends far beyond the EOD frequencies range observed in conspecific wave-type electric fish, which are usually about one octave. Therefore, *Apteronotus leptorhynchus* should be able to detect the sympatric species presence with signals in higher or lower frequency ranges (Steinbach, 1970; Hopkins, 1974; Kramer et al., 1981; Stamper et al., 2010; Henninger et al., 2020). How and whether the different species communicate or interact remains an open question that could be addressed by analyzing electrode-array data recorded in the field (Henninger et al., 2020).

3.2.9 Beat perception in the auditory system

Psychophysical experiments in the 19th century with interacting pure tones revealed that humans can perceive beats not only at low difference frequencies but also at mistuned octaves when the second tone is close to octaves of the first tone (Roeber, 1834; König, 1876). These experimental findings were then formalized by Ohm (Ohm, 1839) and Helmholtz (Helmholtz, 1875). It was demonstrated that beats at higher octaves are better perceived the louder the signal and the lower the frequency of the carrier (Plomp, 1967). Masking experiments could rule out interactions with combination tones and aural harmonics as possible mechanisms underlying beat perception (Plomp, 1967). Our observations of clearly modulated firing rate responses at mistuned octaves suggest a smooth threshold nonlinearity within auditory fibers as a potential mechanism.

3.2.10 Nonlinear physiological mechanisms in the mammalian auditory periphery

Distortion-product otoacoustic emissions (DPOEs) are a hallmark of nonlinear phenomena in the cochlea. They have been attributed to the mechanical properties of the cochlea as the active amplification of outer hair cells (Brownell, 1990). The most important DPOEs are the quadratic distortion, $\omega_2 - \omega_1$, that is the difference frequency, and the cubic distortion, $2\omega_1 - \omega_2$ (Kujawa et al., 1995). These distortions could explain beat-like responses to stimuli close to one and two multiples of a tone, but not to higher carrier multiples.

The focus of auditory neuroscience has mostly been on the encoding of SAMs (Joris et al., 2004), often applied in neurons with quite high characteristic frequencies, with only the initial

declining part of the temporal modulation transfer functions being observed (Rhode and Greenberg, 1994). Therefore, a neuronal correlate of beat perception at high difference frequencies is not known yet. Our findings in the electrosensory system predict that a smooth threshold operation within a single auditory nerve fiber could generate distortion products necessary to extract the aliasing structure of signal envelopes at high difference frequencies.

Both the sigmoidal mechanosensory transducer function (Howard and Hudspeth, 1988) as well as the transfer function of the hair-cell ribbon synapse (Moser and Starr, 2016) are good candidates to implement such a nonlinear transformation. Cooperativity of calcium channels in the presynapse has been discussed for hair cells to result in powers of three or higher (Roux et al., 2006; Özçete and Moser, 2020; Peterson and Heil, 2019).

The two superimposed tones need to enter the hair cell with sufficient amplitudes for these mechanisms to take effect. The louder the two tones and the lower the characteristic frequency of an auditory fiber, the wider will its effective tuning be (Evans, 1972; Sumner and Palmer, 2012). Such wider tuning might potentially allow superimposed tones that differ by multiple octaves to interact within a single auditory fiber. This reasoning is in line with the frequency and intensity dependence of beat perception discussed above (Plomp, 1967).

For testing the here presented hypothesis, single auditory fibers should be stimulated with two tones symmetrically centered within their tuning curves. The resulting frequency and amplitude tuning curves would then allow to retrieve the effective exponent on the threshold operations implemented in this auditory fiber (Fig. 3.8). Manipulations of the hair cell synapse function or knock-outs of outer hair cells would then allow to access the respective contributions.

3.2.11 Conclusion

A pure threshold operation with its sharp edge is a mathematical abstraction. Any physiological mechanism implementing this nonlinearity, as for example the activation curve of voltage-gated calcium currents or the transfer function of a synapse, has a rather smooth transition. The cubed threshold derived from the P-unit recordings is a mathematically simple way to model such a physiologically realistic smooth threshold. In this sense, the P-units' ability of beat extraction at carrier frequency multiples is an epiphenomenon of their physiology. For the same reason, mammalian auditory fibers are bound to respond to mistuned octaves and thus should make a contribution to the percept of beats at higher difference frequencies.

Chapter 4

Second-order susceptibility in a three-fish setting

In the previous chapter, it was elaborated that the encoding of high beat frequencies requires a nonlinearity at the synapse between the electroreceptors and the afferent P-unit. In previous works, P-units have been mainly considered to be linear encoders (Xu et al., 1996; Benda et al., 2005; Gussin et al., 2007; Grewe et al., 2017). Still, P-units exhibit nonlinear effects, especially for strong beat amplitudes (Nelson et al., 1997). Although some P-units can be described by a linear decoder, other P-units require a nonlinear decoder (Chacron et al., 2004). In the following chapter, the focus will be on nonlinear effects, as the second-order susceptibility in the time-resolved firing rate, that has been analytically derived based on leaky integrate-and-fire (LIF) models by Voronenko and Lindner 2017. In that framework, second-order susceptibility was predicted to appear in the spiking response at specific frequencies in the one and two sine-wave settings (see section 1.13.2). Whereas such nonlinearities exist in P-units when at least three fish are present will be addressed in the following chapter.

In the following, a three-fish setting and its encoding in P-units in *Apteronotus leptorhynchus* will be introduced. When the receiver fish with EOD frequency f_{EOD} is alone, a peak at the mean baseline firing rate f_{Base} is present in the power spectrum of the firing rate of a recorded P-unit (Fig. 4.1 A, bottom, see section 2.7.1). P-units also represent f_{EOD} with a peak in the power spectrum of their firing rate, but this peak is beyond the range of frequencies addressed in this figure. If two fish with the EOD frequencies f_{EOD} and f_1 meet, their EODs interfere and result in a new signal with a characteristic periodic amplitude modulation, that will be called beat. The beat amplitude is defined by the smaller EOD of the encountered fish, is expressed in relation to the receiver EOD and is termed contrast (contrast of 20 % in Fig. 4.1 B). The beat frequency is defined as the difference between the two EOD frequencies ($\Delta f_1 = f_1 - f_{EOD}$). *Apteronotus leptorhynchus* is sexually dimorphic with females having lower EOD frequencies (500–750 Hz) and males having higher EOD frequencies (750–1000 Hz). If two fish with the same sex and with similar EOD frequencies meet, this results in a low beat frequency Δf_1 and a slowly oscillating beat (Fig. 4.1 B, top). A P-unit represents this beat frequency in its spike trains and firing rate (Fig. 4.1 B, middle). When two fish from opposite sex with different frequencies meet a high difference frequency Δf_2 and a fast beating signal occurs (Fig. 4.1 C, top). This beat is represented in the spike trains and firing rate of the P-unit (Fig. 4.1 C, middle). In this example, Δf_2 is similar to f_{Base} of the cell, with a strong beat/baseline peak in the power spectrum of the firing rate when both fish are present (green circle in Fig. 4.1 C, bottom). When three fish encounter, as e.g. during an electrosensory cocktail party observed the field (see section 1.18, Henninger et al., 2018), all their waveforms interfere with both beats with frequencies Δf_1 and Δf_2 being present in the superimposed signal (Fig. 4.1 D, top). The power spectrum of the firing rate contains both beat frequencies Δf_1 and Δf_2, but also

nonlinear peaks at the sum frequency $||\Delta f_1|+|\Delta f_2||$ and the difference frequency $||\Delta f_1|-|\Delta f_2||$ of the two beat frequencies (Fig. 4.1 D, bottom).

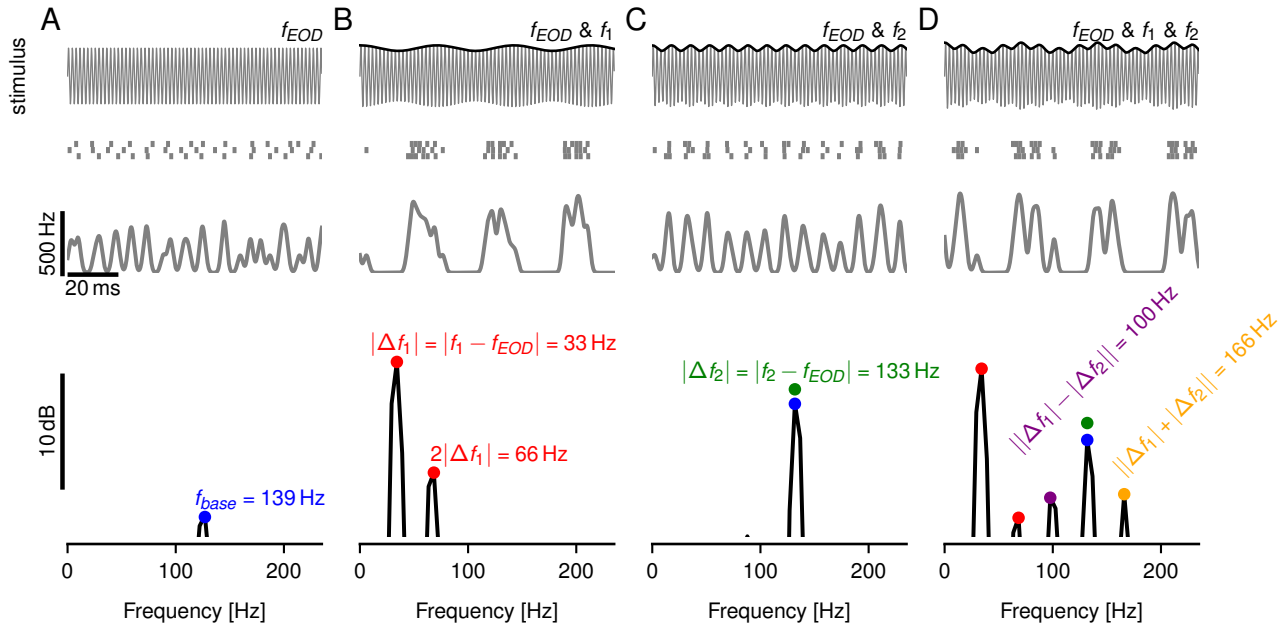

Figure 4.1: Nonlinearity in an electrophysiologically recorded P-unit of *Apteronotus leptorhynchus* in a three-fish setting. Receiver with EOD frequency $f_{EOD} = 664\,\text{Hz}$ encounters fish with EOD frequencies $f_1 = 631\,\text{Hz}$ and $f_2 = 797\,\text{Hz}$. Both encountered fish lead to a beat contrast of 10 %. Top: Interference of the receiver EOD with the EODs of other fish. Second row: Spike trains of the P-unit. Third row: Firing rate, retrieved as the convolution of the spike trains with a Gaussian kernel ($\sigma = 1\,\text{ms}$). Bottom row: Power spectrum of the firing rate.
A Baseline condition: Only the receiver is present. The mean baseline firing rate f_{Base} dominates the power spectrum of the firing rate.
B The receiver and the fish with EOD frequency $f_1 = 631\,\text{Hz}$ are present.
C The receiver and the fish with EOD frequency $f_2 = 797\,\text{Hz}$ are present.
D All three fish with the EOD frequencies f_{EOD}, f_1 and f_2 are present. Nonlinear peaks occur at the sum and difference of the two beat frequencies in the power spectrum of the firing rate.

As described by Voronenko and Lindner (2017) such nonlinearities, at the sum and difference frequencies, are expected only for certain frequencies, that can be predicted based on the mean baseline firing rate f_{Base} of the cell. In their work, the second-order susceptibility was analytically retrieved based on LIF models, where the input were two pure sine waves. A triangular nonlinear shape was predicted, with nonlinearities appearing at the sum of the two input frequencies $f_1 + f_2$ in the response, if one of the beat frequencies f_1, f_2 or the sum of the beat frequencies $f_1 + f_2$ was equal to f_{Base} (see diagonal, vertical and horizontal lines in the upper right quadrant in Fig. 1.13, Voronenko and Lindner, 2017). In addition, a triangular nonlinear shape was predicted, with nonlinearities appearing at the difference of the two input frequencies $|f_1 - f_2|$ in the response, if one of the input frequencies f_1, f_2 or the difference of the input frequencies $|f_1 - f_2|$ was equal to f_{Base} (see diagonal, vertical and horizontal lines in the lower right quadrant in Fig. 1.13, Voronenko and Lindner, 2017). Whereas these predictions of the nonlinear response theory presented in Voronenko and Lindner (2017) apply to P-units, where the main driving force are beats and not the whole signal, will be addressed in the following chapter.

The EOD with frequency f_{EOD} is fixed, thus the varied parameters in a three-fish setting are the EOD frequencies f_1 and f_2, resulting in a two-dimensional stimulus space spanned by the two corresponding beat frequencies Δf_1 and Δf_2. It is challenging to sample this whole stimulus

space in an electrophysiological experiment. A different solution has to be implemented, where nonlinear frequency candidates can be quickly identified and then only these be probed in an electrophysiological recording. For this white noise stimulation, where all behaviorally relevant frequencies are present at the same time, has been proposed (Egerland, 2021). During this procedure, the cell has to be presented with several white noise stimulus realizations, each time with randomly drawn amplitudes and phases. Setting the stimulus in relation to the firing rate response in the frequency domain, as in Eq. (2.6), allows to quantify the second-order susceptibility of the system and highlight the frequency combinations prone to nonlinearity. This method was utilized with bandpass limited white noise being the direct input to a LIF model in previous literature (Egerland, 2021). In the communication context of weakly electric fish white noise stimuli are implemented as random amplitude modulations (RAM) of the EOD (see methods section 2.6.2 and Eq. (2.18)). Whether it is possible to access the second-order susceptibility of P-units with RAM stimuli will be addressed in the following chapter.

Nonlinearity can be influenced not only by the stimulus properties, as the input frequencies, but also by the cell properties during baseline, as the coefficient of variation (CV) of the interspike intervals (ISI) or the mean baseline firing rate f_{Base} (Voronenko and Lindner, 2017; Savard et al., 2011). P-units are very heterogeneous in their baseline firing properties (Grewe et al., 2017; Hladnik and Grewe, 2023). Bursting, the repeated firing of groups of spikes interleaved with quiescence, is also an important factor influencing nonlinearity (Chacron et al., 2004; Oswald et al., 2004). Some P-units are non-bursty, always firing a single spike interleaved with quiescence. Others are bursty, firing a burst package with several spikes at subsequent EOD periods followed by quiescence. Bursting has been investigated in P-unit models, where the detailed time course of the stimulus was better encoded by non-bursty neurons, while feature extraction of the rising stimulus phase was better performed by bursty cells (Chacron et al., 2004). In addition, it was demonstrated that a linear decoder is sufficient for non-bursty firing but a nonlinear decoder is necessary to describe bursty neurons (Chacron et al., 2004). Slice recordings revealed that the ISI statistics of P-units are transported to higher-order neurons, the pyramidal cells in the electrosensory line lobe (ELL, Khanbabaie et al., 2010), making burst information potentially available to pyramidal cells. Bursting has been found not only in primary sensory afferents of the *Apteronotus leptorhynchus* but has also been observed in pyramidal cells of the ELL, where bursts better encode low-frequency events whereas single spikes encode the whole frequency range (Oswald et al., 2004). There it was also demonstrated that the first spike in a burst package carries linear information about the stimulus, that is not increased by additional spikes in a burst package. Instead, bursts were shown to improve feature detection in pyramidal cells, by improving the signal-to-noise ratio (Oswald et al., 2004). An improved signal-to-noise ratio and sharpened tuning curves by bursts have also been found in the auditory system (Eggermont and Smith, 1996). This improved signal-to-noise ratio might be related to bursts supporting reliable synaptic transmission (Csicsvari et al., 1998). Bursts in higher order neurons are often generated via feedback loops on a network level (Zeldenrust et al., 2018; Krahe and Gabbiani, 2004) that can be influenced by environmental variables (Krahe and Gabbiani, 2004). P-units do not receive feedback from other cells and are considered to be intrinsic bursters. Bursting has behavioral implications e.g. for avoidance behavior in crickets, where bursts provide information about the stimulus (Marsat and Pollack, 2010, 2012). Bursts are ubiquitous in sensory modalities as in chattering cells in the visual system (Nowak et al., 2003), fast rhythmic bursting cells in the auditory system (Cunningham et al., 2004), Purkinje cells in the cerebellum (Womack and Khodakhah, 2004) or thalamic relay neurons (Destexhe et al., 1993).

In this chapter, the second-order susceptibility in the spiking responses of P-units will be accessed with white noise stimulation. The influence of the baseline firing properties, such as the CV, on nonlinear interactions will be investigated. It will be demonstrated that some P-

units exhibit nonlinearities in relation to f_{Base}, as predicted by Voronenko and Lindner (2017), but some cells diverge from this theoretical prediction, with bursting influencing the occurrence of the nonlinearities. P-unit models will be used to highlight bursting as a mechanism to boost nonlinearity.

4.1 Results

4.1.1 Low-CV P-units exhibit nonlinear interactions

P-units are heterogeneous in their baseline firing properties (Grewe et al., 2017; Hladnik and Grewe, 2023) and differ in their noisiness, which is represented by the coefficient of variation (CV) of the interspike intervals (ISI). Low-CV P-units have a regular firing pattern and are less noisy, whereas high-CV P-units have a less regular firing pattern. Second-order susceptibility is expected to be especially pronounced for low-CV cells (Voronenko and Lindner, 2017). In the following first low-CV P-units will be addressed in Fig. 4.2 A.

P-units probabilistically phase-lock to the EOD of the fish, firing at the same phase but not in every EOD cycle, resulting in a multimodal ISI histogram with maxima at integer multiples of the EOD period (Fig. 4.2 $\mathsf{A_i}$, left). The strongest peak in the baseline power spectrum of the firing rate of a P-unit is the f_{EOD} peak, and the second strongest peak is the mean baseline firing rate f_{Base} peak (Fig. 4.2 $\mathsf{A_i}$, right). The power spectrum of P-units is symmetric around half f_{EOD}, with baseline peaks appearing at $f_{EOD} \pm f_{Base}$.

Noise stimuli, as random amplitude modulations (RAM) of the EOD, are common stimuli during P-unit recordings. In the following, the amplitude of the noise stimulus will be quantified as the standard deviation and will be expressed as a contrast (unit %) in relation to the receiver EOD. The spikes of P-units slightly align with the RAM stimulus with a low contrast (light purple) and are stronger driven in response to a higher RAM contrast (dark purple, Fig. 4.2 $\mathsf{A_{ii}}$). The linear encoding (see Eq. (2.3)) is comparable between the two RAM contrasts in this low-CV P-unit (Fig. 4.2 $\mathsf{A_{iii}}$).

To quantify the second-order susceptibility in a three-fish setting the noise stimulus was set in relation to the corresponding P-unit response in the Fourier domain, resulting in a matrix where the nonlinearity at the sum frequency $f_1 + f_2$ in the firing rate is depicted for two noise frequencies f_1 and f_2 (Eq. (2.6), Fig. 4.2 $\mathsf{A_{iv}}$–$\mathsf{A_v}$). Note that the RAM stimulus can be decomposed in frequencies f, that approximate the beat frequencies Δf, occurring in case of pure sine-wave stimulation (Fig. 4.1 D). Thus the nonlinearity accessed with the RAM stimulation at $f_1 + f_2$ (Fig. 4.2 $\mathsf{A_{iv}}$) is comparable to the nonlinearity appearing during pure sine-wave stimulation at $||\Delta f_1| + |\Delta f_2||$ (orange peak, Fig. 4.1 D). Based on the theory (Voronenko and Lindner, 2017) nonlinearities should arise when f_1, f_2 or $f_1 + f_2$ are equal to f_{Base} (upper right quadrant in Fig. 1.13), which would imply a triangular nonlinearity shape highlighted by the pink triangle corners in Fig. 4.2 $\mathsf{A_{iv}}$–$\mathsf{A_v}$. A slight diagonal nonlinearity band appears for the low RAM contrast when $f_1 + f_2 = f_{Base}$ is satisfied (yellow diagonal between pink edges, Fig. 4.2 $\mathsf{A_{iv}}$). Since the matrix contains only anti-diagonal elements, the structural changes were quantified by the mean of the anti-diagonals, resulting in the projected diagonal (Fig. 4.2 $\mathsf{A_{vi}}$). For a low RAM contrast the f_{Base} peak in the projected diagonal is slightly enhanced (Fig. 4.2 $\mathsf{A_{vi}}$, gray dot on light purple line). For the higher RAM contrast, the overall second-order susceptibility is reduced (Fig. 4.2 $\mathsf{A_v}$), with no pronounced f_{Base} peak in the projected diagonal (Fig. 4.2 $\mathsf{A_{vi}}$, dark purple line). In addition, there is an offset between the projected diagonals, demonstrating that the second-order susceptibility is reduced for RAM stimuli with a higher contrast (Fig. 4.2 $\mathsf{A_{vi}}$).

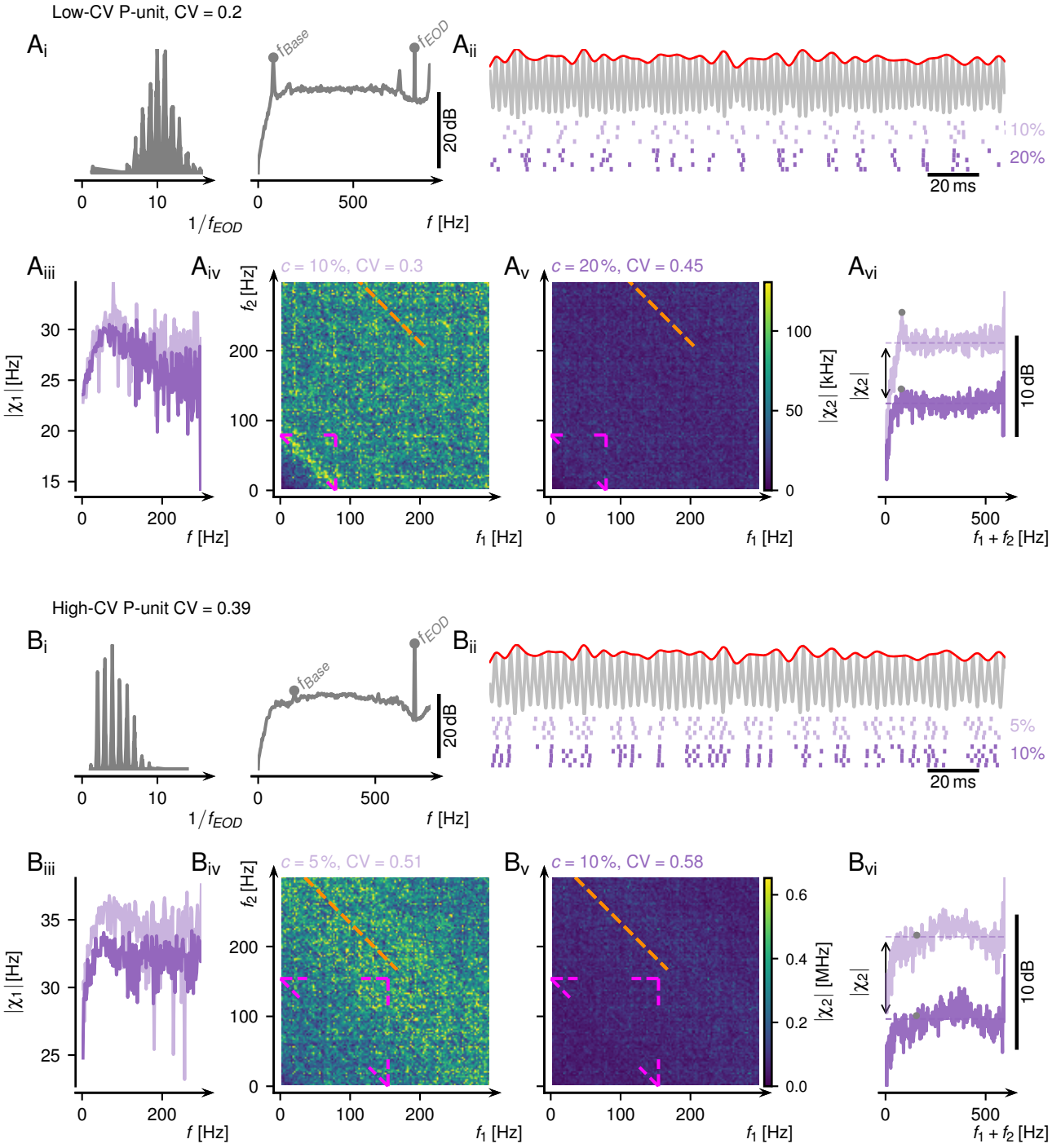

Figure 4.2: Response of experimentally measured P-units to RAM stimuli. Light purple – low RAM contrast. Dark purple – high RAM contrast.
A Regular firing low-CV P-unit.
$\mathbf{A}_{\mathrm{i}}$ Left: Interspike intervals (ISI) distribution during baseline. Right: Baseline power spectrum of the firing rate.
$\mathbf{A}_{\mathrm{ii}}$ Top: EOD carrier (gray) with RAM (red). Middle: Spike trains in response to a low RAM contrast. Bottom: Spike trains in response to a high RAM contrast.
$\mathbf{A}_{\mathrm{iii}}$ First-order susceptibility (see Eq. (2.3)).
$\mathbf{A}_{\mathrm{iv}}$ Absolute value of the second-order susceptibility, Eq. (2.6), for the low RAM contrast. Pink lines – edges of the structure when f_1, f_2 or $f_1 + f_2$ are equal to f_{Base}. Orange line – part of the structure when $f_1 + f_2$ is equal to half f_{EOD}.
$\mathbf{A}_{\mathrm{v}}$ Absolute value of the second-order susceptibility for the higher RAM contrast.
$\mathbf{A}_{\mathrm{vi}}$ Projected diagonals, calculated as the mean of the anti-diagonals of the matrices in $\mathbf{A}_{\mathrm{iv,v}}$. Gray dots: f_{Base}. Dashed lines: Medians of the projected diagonals.
B Noisy high-CV P-Unit. Panels as in A.

4.1.2 High-CV P-units do not exhibit any nonlinear interactions

Based on the theory strong nonlinearities in spiking responses are not predicted for cells with irregular firing properties and high CVs (Voronenko and Lindner, 2017). CVs in P-units can range up to 1.5 (Grewe et al., 2017; Hladnik and Grewe, 2023) and as a next step the second-order susceptibility of high-CV P-units will be presented. As low-CV P-units, high-CV P-units fire at multiples of the EOD period (Fig. 4.2 B_i, left). In contrast to low-CV P-units high-CV P-units are noisier in their firing pattern and have a less pronounced mean baseline firing rate peak f_{Base} in the power spectrum of their firing rate during baseline (Fig. 4.2 B_i, right). High-CV P-units do not exhibit any nonlinear structures related to f_{Base} neither in the second-order susceptibility matrices (Fig. 4.2 B_{iv}–B_v), nor in the projected diagonals (Fig. 4.2 B_{vi}). As in low-CV P-units (Fig. 4.2 A_v), the mean second-order susceptibility decreases with higher RAM contrasts in high-CV P-units (Fig. 4.2 B_v).

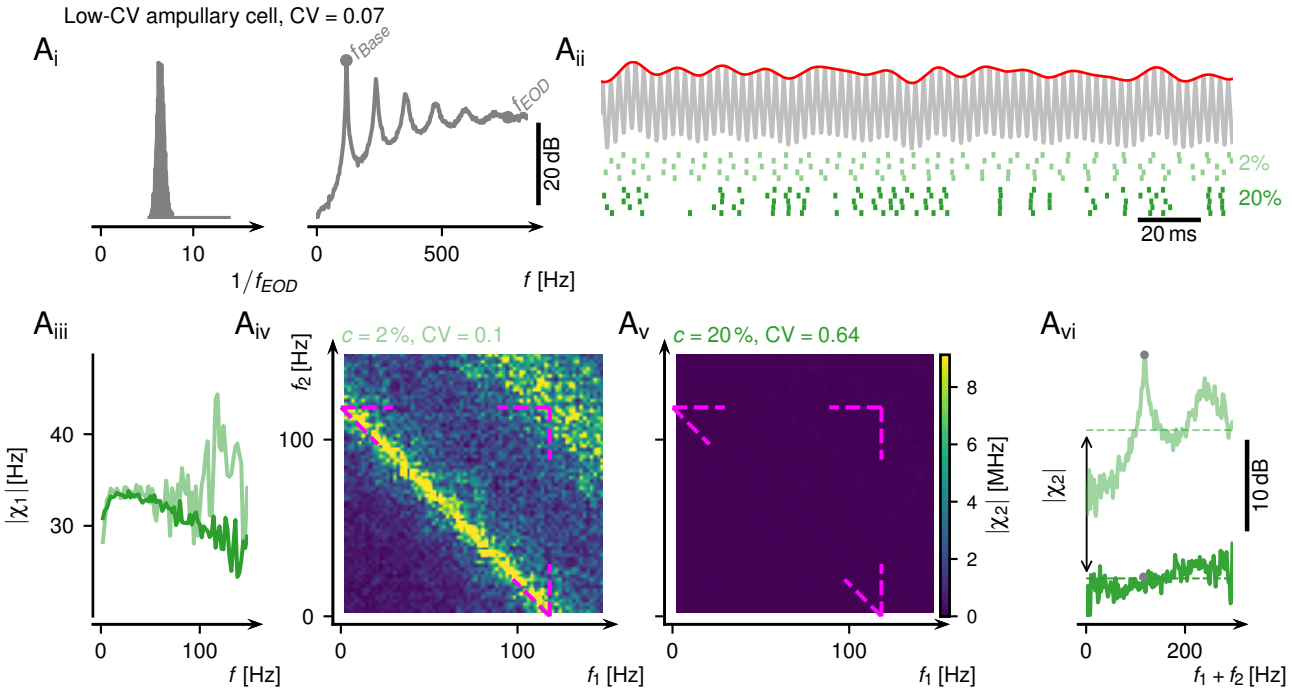

Figure 4.3: Response of an experimentally measured ampullary cell. Light green – low noise stimulus contrast. Dark green – high noise stimulus contrast.
A_i Left: ISI distribution during baseline. Right: Baseline power spectrum of the firing rate.
A_{ii} Top: EOD carrier (gray) plus a band-pass limited white noise (red, see methods section 2.6.2). Middle: Spike trains in response to a low noise stimulus contrast. Bottom: Spike trains in response to a high noise stimulus contrast.
A_{iii} First-order susceptibility (see Eq. (2.3)).
A_{iv} Absolute value of the second-order susceptibility (Eq. (2.6)) for the low noise stimulus contrast. Pink lines – edges of the structure when f_1, f_2 or $f_1 + f_2$ are equal to f_{Base}. Orange line – part of the structure when $f_1 + f_2$ is equal to half f_{EOD}.
A_v Second-order susceptibility matrix for the higher noise stimulus contrast. Colored lines as in A_{iv}.
A_{vi} Projected diagonals, calculated as the mean of the anti-diagonals of the matrices in $A_{iv,v}$. Gray dot: f_{Base}. Dashed lines: Medians of the projected diagonals.

4.1.3 Ampullary cells exhibit strong nonlinear interactions

Apteronotus leptorhynchus posses another primary sensory afferent population, the ampullary cells, with overall low f_{Base} (80–200 Hz) and low CV values (0.08–0.22, Grewe et al., 2017). Ampullary cells do not phase-lock to the EOD, with no maxima at multiples of the EOD period and smoothly unimodal distributed ISIs (Fig. 4.3 $\mathsf{A_i}$, left). Ampullary cells do not have a peak at f_{EOD} in the baseline power spectrum of the firing rate with no symmetry around it (Fig. 4.3 $\mathsf{A_i}$, right). Instead, the f_{Base} peak is very pronounced with clear harmonics. When being exposed to a noise stimulus with a low contrast, ampullary cells exhibit very pronounced bands when $f_1 + f_2$ is equal to f_{Base} or its harmonic in the second-order susceptibility matrix, implying that this cell is especially nonlinear at these frequency combinations (yellow diagonals, Fig. 4.3 $\mathsf{A_{iv}}$). With higher noise stimuli contrasts these bands disappear (Fig. 4.3 $\mathsf{A_v}$) and the projected diagonal is lowered (Fig. 4.3 $\mathsf{A_{vi}}$, dark green).

These nonlinearity bands are more pronounced in ampullary cells than they were in P-units (compare Fig. 4.3 and Fig. 4.2). Ampullary cells with their unimodal ISI distribution are closer than P-units to the LIF models without EOD carrier, where the predictions about the second-order susceptibility structure have mainly been elaborated on (Voronenko and Lindner, 2017). All here analyzed ampullary cells had CVs lower than 0.3 and exhibited strong nonlinear effects in accordance with the theoretical predictions (Voronenko and Lindner, 2017).

4.1.4 Full nonlinear structure visible only in P-unit models

In the following nonlinear interactions were systematically compared between an electrophysiologically recorded low-CV P-unit and the according P-unit LIF models with a RAM contrast of 1 % (red, Fig. 4.4 $\mathsf{A_i}$). For a homogeneous population with size $N = 11$ one could observe a diagonal band in the absolute value of the second-order susceptibility at $f_1 + f_2 = f_{Base}$ of the recorded P-unit (yellow diagonal in pink edges, Fig. 4.4 $\mathsf{A_{ii}}$) and in the according model (Fig. 4.4 $\mathsf{A_{iii}}$). A nonlinear band appeared at $f_1 + f_2 = f_{EOD}/2$, but only in the recorded P-unit (orange line, Fig. 4.4 $\mathsf{A_{ii}}$). The signal-to-noise ratio and estimation of the nonlinearity structures can be improved if the number of RAM stimulus realizations is increased. Models have the advantage that they allow for data amounts that cannot be acquired experimentally. Still, even if a RAM stimulus is generated 1 million times, no changes are observable in the nonlinearity structures in the model second-order susceptibility (Fig. 4.4 $\mathsf{A_{iv}}$).

Based on the Furutsu-Novikov Theorem (Novikov, 1965; Furutsu, 1963) the intrinsic noise of a LIF model can be split up into several independent noise processes with the same correlation function. Based on this a weak RAM signal as the input to the P-unit model (red in Fig. 4.4 $\mathsf{A_i}$) can be approximated by a model where no RAM stimulus is present (red) but instead the total noise of the model is split up into a reduced intrinsic noise component (gray) and a signal component (purple), maintaining the CV and f_{Base} as during baseline (Fig. 4.4 $\mathsf{B_i}$, see methods section 2.14.1 for more details). This signal component (purple) can be used for the calculation of the second-order susceptibility. With the reduced noise component the signal-to-noise ratio increases and the number of stimulus realizations can be reduced. This noise split cannot be applied in experimentally measured cells. If this noise split is applied in the model with $N = 11$ stimulus realizations the nonlinearity at $f_1 + f_2 = f_{Base}$ is still present (Fig. 4.4 $\mathsf{B_{iii}}$). If instead, the RAM stimulus is drawn 1 million times the diagonal nonlinearity band is complemented by vertical and horizontal lines appearing at $f_1 = f_{Base}$ and $f_2 = f_{Base}$ (Fig. 4.4 $\mathsf{B_{iv}}$). These nonlinear structures correspond to the ones observed in previous works (Voronenko and Lindner, 2017). If now a weak RAM stimulus is added (Fig. 4.4 $\mathsf{C_i}$, red), simultaneously the noise is split up into a noise and signal component (gray and purple) and the calculation is performed on the sum of the signal component and the RAM (red plus purple) only the diagonal band is present with $N = 11$ (Fig. 4.4 $\mathsf{C_{iii}}$) but also with 1 million stimulus realizations (Fig. 4.4 $\mathsf{C_{iv}}$).

If a high-CV P-unit is investigated (not shown), there would be no nonlinear structures, neither in the electrophysiologically recorded data nor in the according model, corresponding to the theoretical predictions (Voronenko and Lindner, 2017).

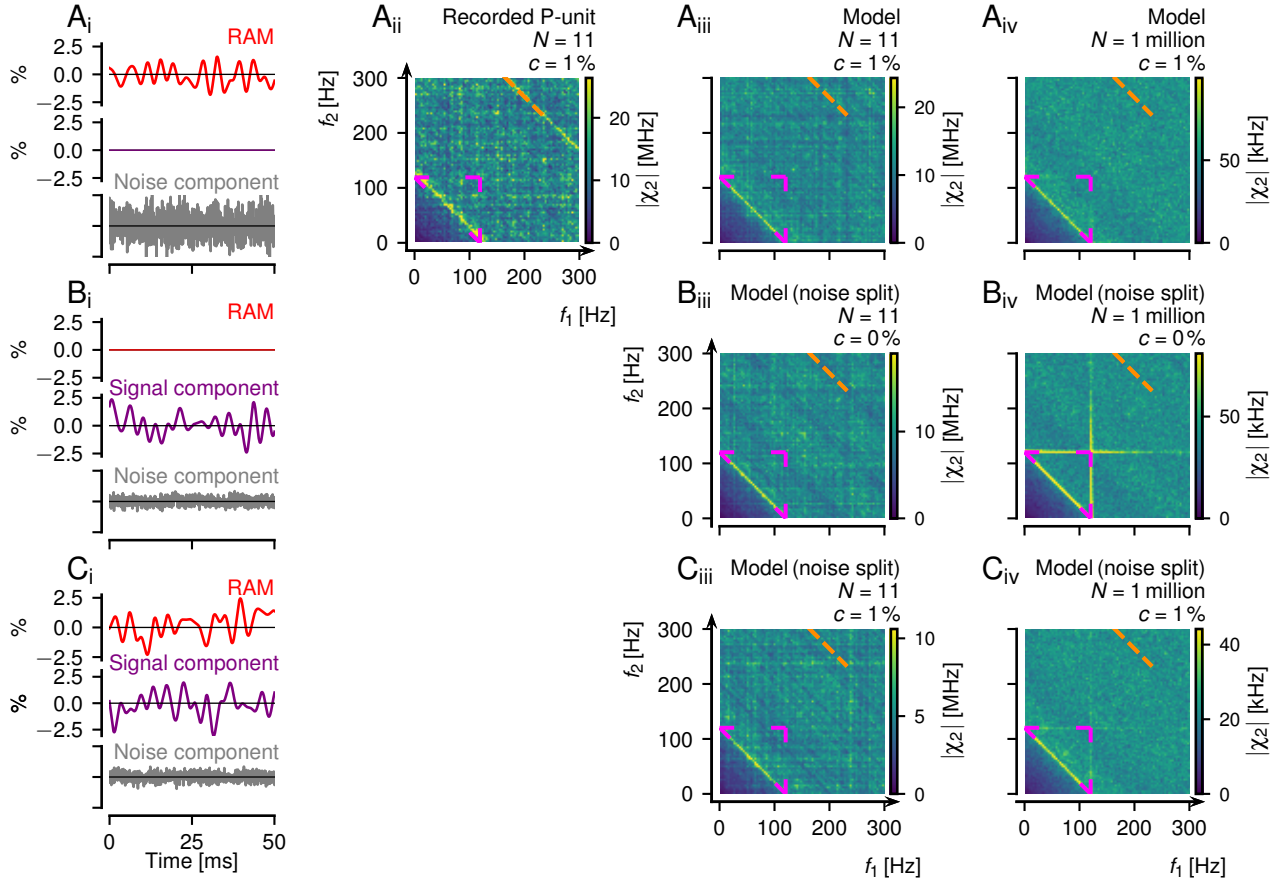

Figure 4.4: The influence of the RAM stimulus realization number N, the RAM contrast c, and the split of the total intrinsic noise in a signal and noise component on the nonlinearity structures of the second-order susceptibility of an electrophysiologically recorded low-CV P-unit and its LIF model (see table 2.1 for model parameters of 2012-07-03-ak). Pink lines in the matrices mark the edges of the structure when f_1, f_2 or $f_1 + f_2$ are equal to f_{Base}. The orange line in the matrices marks a part of the line at $f_1 + f_2 = f_{EOD}/2$.
A$_{\text{i}}$, **B**$_{\text{i}}$, **C**$_{\text{i}}$ Red – RAM stimulus. The total intrinsic noise can be split into a noise component (gray) and a signal component (purple), maintaining the same CV and f_{Base} as before the split (see methods section 2.14.1). The calculation is performed on the sum of the signal component (purple) and the RAM (red) in Eq. (2.6).
A$_{\text{ii}}$ Absolute value of the second-order susceptibility of an electrophysiologically recorded P-unit, with $N = 11$ RAM stimulus realizations.
A$_{\text{iii}}$, **B**$_{\text{iii}}$, **C**$_{\text{iii}}$ Absolute value of the model second-order susceptibility with $N = 11$ RAM stimulus realizations.
A$_{\text{iv}}$, **B**$_{\text{iv}}$, **C**$_{\text{iv}}$ Absolute value of the model second-order susceptibility with 1 million RAM stimulus realizations.
A RAM contrast of 1 %. The band at $f_1 + f_2 = f_{Base}$ is visible in the matrices.
B No RAM stimulus, but a total noise split into a signal component (purple) and a noise component (gray). The band at $f_1 + f_2 = f_{Base}$ is visible in **B**$_{\text{iii}}$ and **B**$_{\text{iv}}$. Besides that horizontal and vertical nonlinearities appear at $f_1 = f_{Base}$ and $f_2 = f_{Base}$ in **B**$_{\text{iv}}$.
C A RAM stimulus (red) and a total noise split into a signal component (purple) and a noise component (gray). Only the band at $f_1 + f_2 = f_{Base}$ is visible in the matrices.

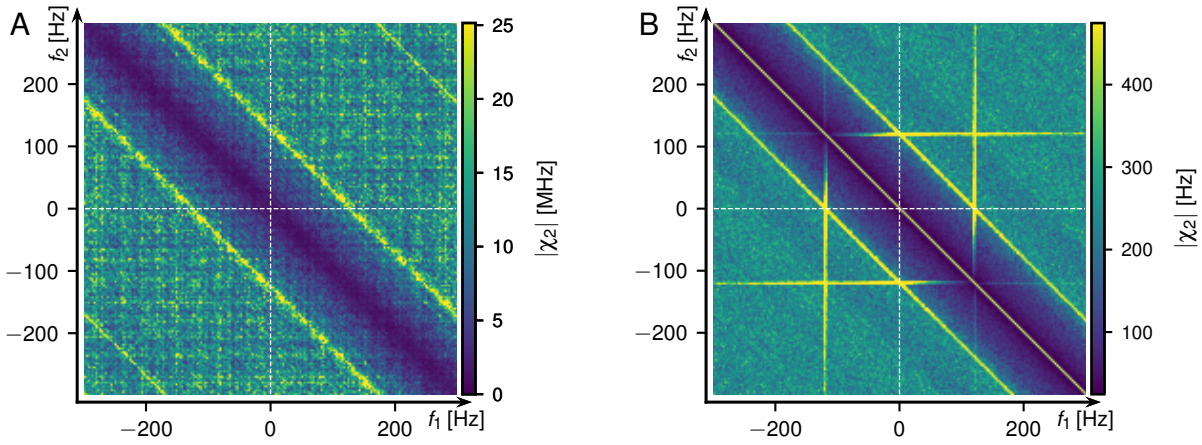

Figure 4.5: Second-order susceptibility of an electrophysiologically recorded P-unit and of the corresponding model (see table 2.1 for model parameters of 2012-07-03-ak). White lines – coordinate axis. The nonlinearity at $f_1 + f_2$ in the firing rate is quantified in the upper right and lower left quadrants (Eq. (2.6)). The nonlinearity at $|f_1 - f_2|$ in the firing rate is quantified in the upper left and lower right quadrants. Mean baseline firing rate $f_{Base} = 120\,\text{Hz}$.
A Absolute value of the second-order susceptibility of an electrophysiologically recorded P-unit. RAM stimulus realizations $N = 11$. Diagonal bands appear when the sum of the frequencies $f_1 + f_2$ or the difference $|f_1 - f_2|$ is equal to f_{Base}.
B Absolute value of the model second-order susceptibility, with $N = 1$ million stimulus realizations and the intrinsic noise split (see methods section 2.14.1). The diagonals, that were present in A, are complemented by vertical and horizontal lines when f_1 or f_2 are equal to f_{Base}.

4.1.5 Similar nonlinear effects with RAM and sine-wave stimulation

In the previous paragraphs, the nonlinearity at $f_1 + f_2$ in the P-unit response was identified for the RAM frequencies f_1 and f_2. This RAM-based second-order susceptibility can be used to approximate the nonlinearity in the three-fish setting, where two beats with frequencies Δf_1 and Δf_2 are the driving forces for the P-unit response. In the previously shown three-fish setting a nonlinear peak occurred at the sum of the two beat frequencies (orange circle, Fig. 4.1 D). In that example Δf_2 was similar to f_{Base}, corresponding to the horizontal line in the RAM-based second-order susceptibility matrix in Fig. 4.4 B_{iv}. In the three-fish example, there was a second less prominent nonlinearity at the difference of the two beat frequencies (purple circle, Fig. 4.1 D), that cannot be explained with the second-order susceptibility matrix in Fig. 4.4 B_{iv}, where only the nonlinearity at $f_1 + f_2$ in the response is addressed.

Instead, the full second-order susceptibility matrix in Fig. 4.5, which depicts nonlinearities in the P-unit response at $f_1 + f_2$ in the upper right and lower left quadrants and nonlinearities at $|f_1 - f_2|$ in the lower right and upper left quadrants (Eq. (2.6), Voronenko and Lindner, 2017), has to be considered. Once calculating this full second-order susceptibility matrix based on the experimentally recorded data (Fig. 4.5 A) and the corresponding model (Fig. 4.5 B), one can observe that the diagonal structures are present in the upper right quadrant and for the upper left quadrants. The vertical and horizontal lines at $f_1 = f_{Base}$ and $f_2 = f_{Base}$ are very pronounced in the upper right quadrant for the nonlinearity at $f_1 + f_2$ and are prolonged to the upper left quadrant with lower nonlinearity values at $|f_1 - f_2|$ in the P-unit response.

The small $|f_1 - f_2|$ peak in the power spectrum of the firing rate appearing during pure sine-wave stimulation (Fig. 4.1 D) can be explained by the horizontal line in the upper left quadrant (Fig. 4.5 B, Schlungbaum and Lindner, 2023). The here presented full second-order susceptibilities matrix was retrieved based on data and models with EOD carrier (Fig. 4.5) and

is in accordance with the second-order susceptibilities calculated based on models without a carrier (Fig. 1.13, Voronenko and Lindner, 2017; Schlungbaum and Lindner, 2023).

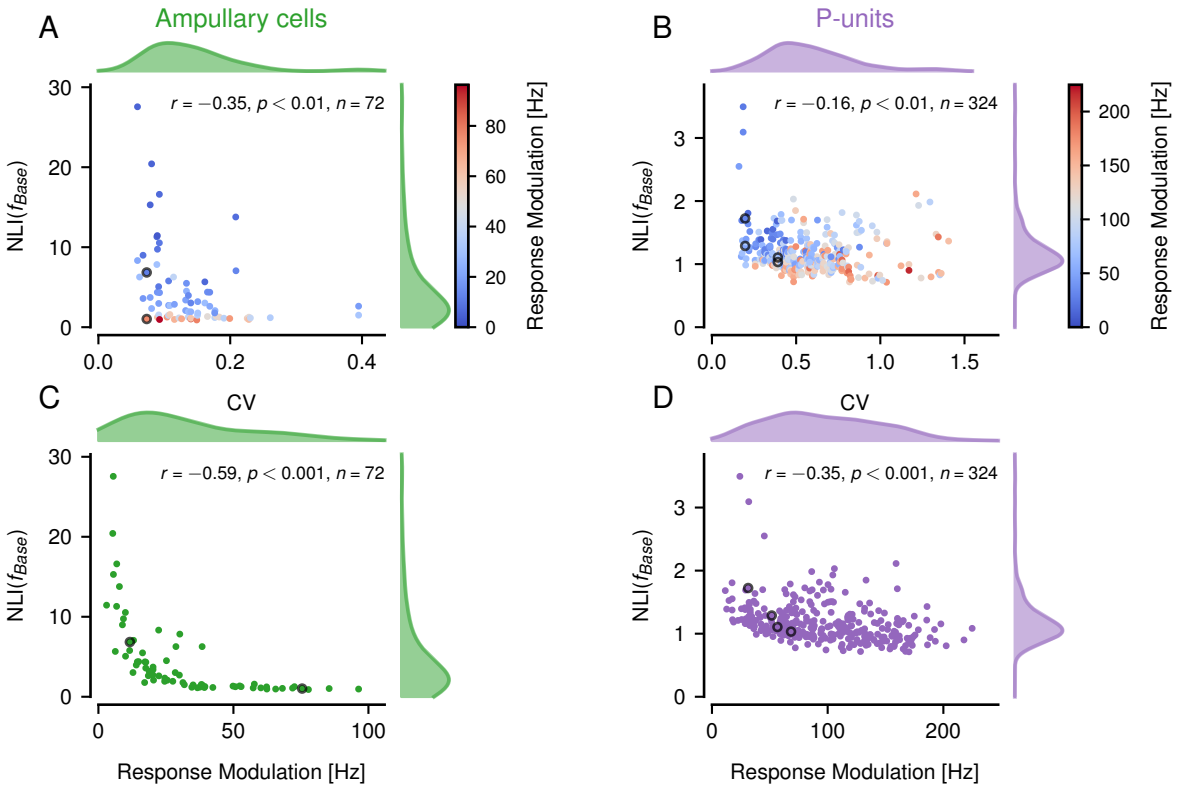

Figure 4.6: Nonlinearity for a population of ampullary cells (A, C) and P-units (B, D). NLI(f_{Base}) is calculated as the maximal value in the range $f_{Base} \pm 5$ Hz of the projected diagonal divided by its median (see Eq. (2.7)). There are maximally two noise contrasts per cell in a population.
A, B There is a negative correlation between the CV during baseline and NLI(f_{Base}).
C, D Response modulation, Eq. (2.9.2), is an indicator of the subjective stimulus strength for a cell. There is a negative correlation between response modulation and NLI(f_{Base}).

4.1.6 Low CVs are associated with strong nonlinearity on a population level

So far second-order susceptibility was illustrated only with single-cell examples (Fig. 4.2, Fig. 4.3). For a P-unit comparison on a population level, the second-order susceptibility of P-units was expressed in a nonlinearity index NLI(f_{Base}), see Eq. (2.7), that characterized the peakedness of the f_{Base} peak in the projected diagonal (Fig. 4.2 A_{vi}). NLI(f_{Base}) has high values when the f_{Base} peak in the projected diagonal is especially pronounced, as in the low-CV ampullary cell (Fig. 4.3 A_{vi}, light green). The two noise stimulus contrasts of this ampullary cell are highlighted in the population statics of ampullary cells with dark circles (Fig. 4.6 A). The higher noise stimulus contrast is associated with a less pronounced peak in the projected diagonal (Fig. 4.3 A_{vi}, dark green) and is represented with a lower NLI(f_{Base}) value (Fig. 4.6 A, dark circle close to the origin). In an ampullary cell population, there is a negative correlation between the CV during baseline and NLI(f_{Base}), meaning that the diagonals are pronounced for low-CV cells and disappear towards high-CV cells (Fig. 4.6 A). Since the same stimulus can be strong for some cells and faint for others, the noise stimulus contrast is not directly comparable between cells. A better estimation of the subjective stimulus strength is the response

modulation of the cell (see methods section 2.9.2). Ampullary cells with stronger response modulations have lower NLI(f_{Base}) scores (red in Fig. 4.6 A, Fig. 4.6 C). The so far shown population statistics comprised several RAM contrasts per cell and if instead each ampullary cell is represented with the lowest recorded contrast, then NLI(f_{Base}) significantly correlates with the CV during baseline ($r = -0.46$, $p < 0.001$), the response modulation ($r = -0.6$, $p < 0.001$) but not with f_{Base} ($r = 0.2$, $p = 0.16$).

The P-unit population has higher baseline CVs and lower NLI(f_{Base}) values (Fig. 4.6 B) that are weaker correlated than in the population of ampullary cells. The negative correlation (Fig. 4.6 B) is increased when NLI(f_{Base}) is plotted against the response modulation of P-units (Fig. 4.6 D). The two example P-units shown before (Fig. 4.2) are highlighted with dark circles in Fig. 4.6 B, D. High-CV P-units and strongly driven P-units have lower NLI(f_{Base}) values (Fig. 4.6 B, D). In a P-unit population where each cell is represented not by several contrasts but by the lowest recorded contrast, NLI(f_{Base}) significantly correlates with the CV during baseline ($r = -0.17$, $p = 0.01$), the response modulation ($r = -0.35$, $p < 0.001$) and f_{Base} ($r = -0.32$, $p < 0.001$).

4.1.7 Bursting boosts second-order susceptibility

Although most high-CV P-units have overall low NLI(f_{Base}) values, some high-CV P-units have high NLI(f_{Base}) values (upper right corner in Fig. 4.6 B). To understand what makes these cells different, in the following bursting of P-units will be considered.

The example cells discussed so far did not burst, mostly firing isolated spikes interleaved with quiescence (Fig. 4.2, Fig. 4.3). Bursting P-units fire a burst package of spikes interleaved with quiescence (Fig. 4.7 A_{ii}). When cells burst, an overall bimodal ISI distribution occurs, with the first distribution containing the intra-burst intervals and the second the inter-burst intervals (Fig. 4.7 A_i, left). In most cells the intra-burst distribution is below 1.5 EOD periods, meaning that during the burst the cell fires after each EOD cycle. In some cells, the ISI distribution is better separated by a threshold of 2.5 or even more EOD periods. To get a burst-corrected spike train all spikes after the first spike in a burst package were removed (Fig. 4.7 A_{ii}, dark purple spikes). Based on the baseline burst-corrected spike train the mean firing rate $f_{BaseCorrected}$ and $\mathrm{CV}_{BaseCorrected}$ were calculated (see methods sections 2.9.1). $f_{BaseCorrected}$ is represented with a peak in the baseline power spectrum of the firing rate before burst correction (Fig. 4.7 A_i, right). Burst correction during RAM stimulation leads to a reduction of the linear encoding when comparing the linear encoding of all spikes (light purple) and of the burst-corrected spike train (dark purple, Fig. 4.7 A_{iii}). Bursting induces wide bands in the absolute value of the second-order susceptibility (Fig. 4.7 A_{iv}) that disappear after burst correction (Fig. 4.7 A_v). In the second-order susceptibility after burst correction nonlinearity bands appear at $f_1 + f_2 = f_{BaseCorrected}$ (pink triangle edges, Fig. 4.7 A_v). Burst correction leads to a reduced CV (compare the title of Fig. 4.7 A_{iv} and Fig. 4.7 A_v) and reduces the projection diagonal values and the $f_{BaseCorrected}$ peak size in it (Fig. 4.7 A_{vi}, gray marker on dark purple line). Based on this bursts seem to increase the second-order susceptibility at the frequencies related to $f_{BaseCorrected}$ (Fig. 4.7 A_{vi}).

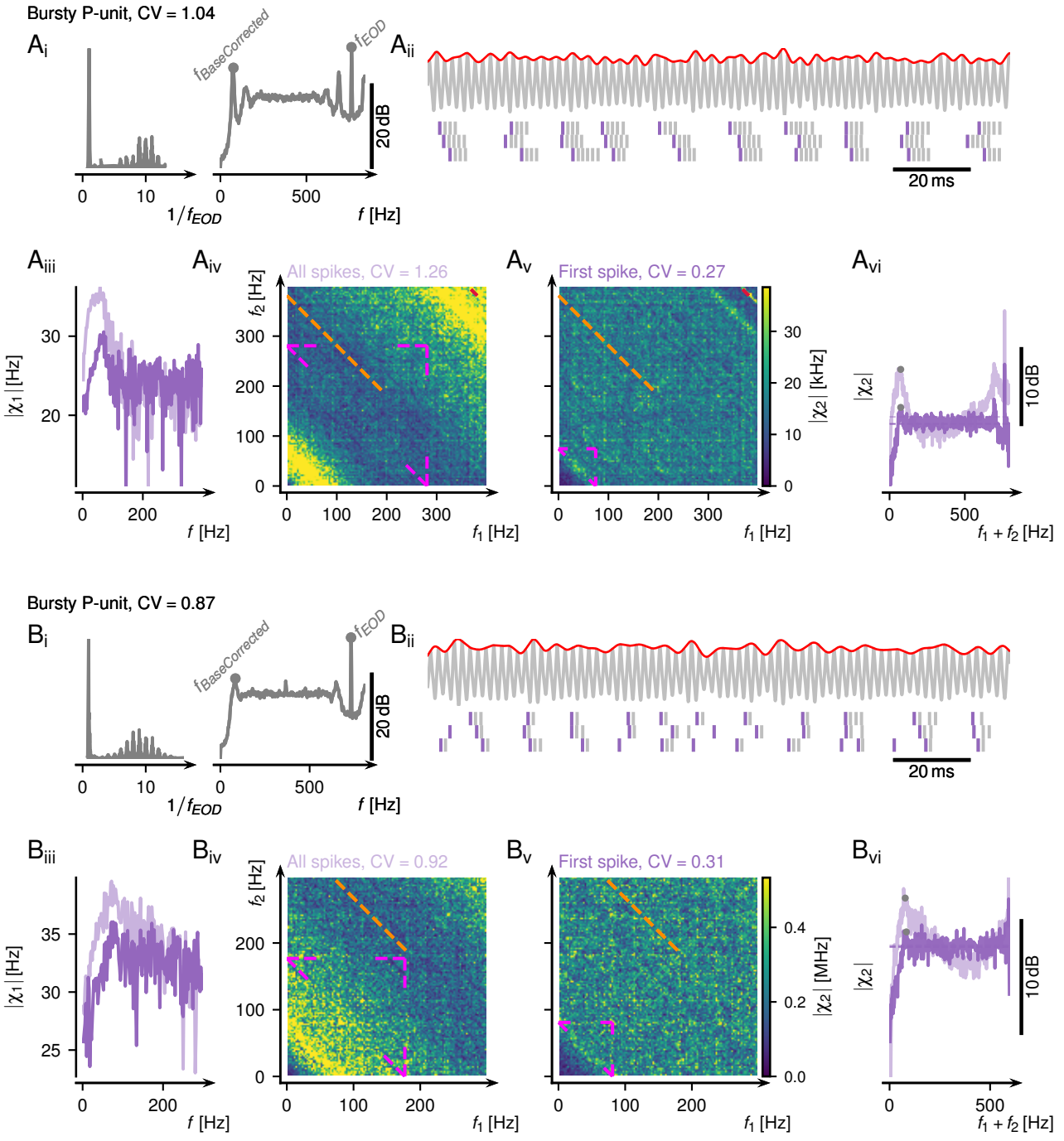

Figure 4.7: Response of two experimentally measured bursty P-units before and after burst correction (A, B). Burst correction has three effects: 1) It lowers the baseline frequency from f_{Base} to $f_{BaseCorrected}$. 2) It decreases the overall second-order susceptibility. 3) It decreases the size of the $f_{BaseCorrected}$ peak in the projected diagonal.

A$_{\text{i}}$ Left: ISI distribution during baseline. Right: Baseline power spectrum of the firing rate.

A$_{\text{ii}}$ Top: EOD carrier (gray) with RAM (red). Bottom: Dark purple – spikes after burst correction.

A$_{\text{iii}}$ First-order susceptibility (Eq. (2.3)). Light purple – based on all spikes (before burst correction). Dark purple – based only on the first spike of a burst package (after burst correction).

A$_{\text{iv}}$ Absolute value of the second-order susceptibility without burst correction. Pink lines – edges of the structure when f_1, f_2 or $f_1 + f_2$ are equal to f_{Base}. Orange line – part of the structure when $f_1 + f_2$ is equal to half f_{EOD}.

A$_{\text{v}}$ Absolut value of the second-order susceptibility after burst correction. Pink lines – edges of the structure when f_1, f_2 or $f_1 + f_2$ are equal to $f_{BaseCorrected}$. Orange line as in A$_{\text{iv}}$.

A$_{\text{vi}}$ Projected diagonals, calculated as the mean of the anti-diagonals in the matrices in A$_{\text{iv,v}}$. Colors as in A$_{\text{iii}}$. Gray marker – $f_{BaseCorrected}$. Dashed lines – median of the projected diagonals.

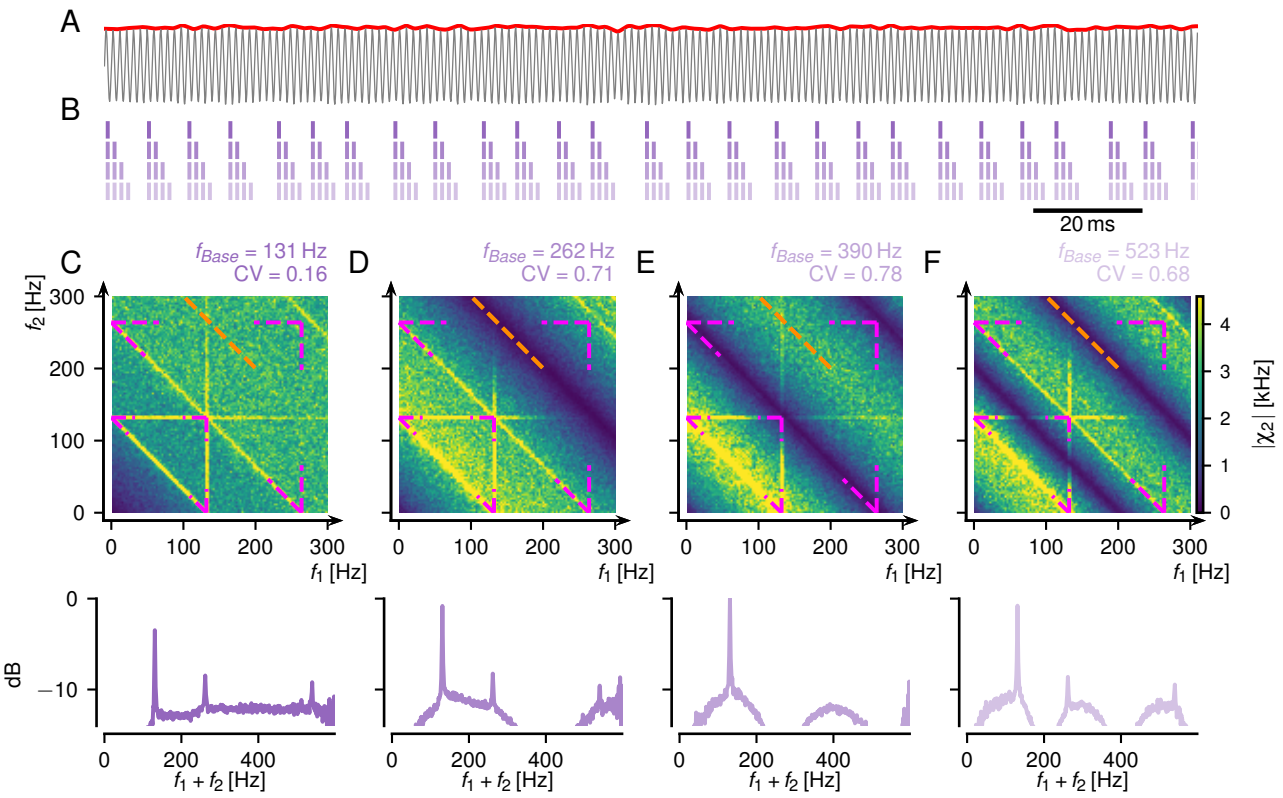

Figure 4.8: Adding spikes to a burst package increases the second-order susceptibility in low-CV models with 1 million stimulus realizations (see table 2.1 for model parameters of 2013-01-08-aa). A model with an intrinsic noise split (see methods section 2.14.1).
A Carrier (gray) with a RAM stimulus (red).
B Spike trains with increasing number of spikes per bust package. The colors connect the spikes trains and the resulting analysis of the model in C–F.
C–F Top: Absolute value of the second-order susceptibility. Bottom: Projected diagonal (see methods section 2.9.4).
C Original model 2013-01-08-aa (see table 2.1 for model parameters).
D Two-spikes burst packages: A spike was added after an EOD period to each spike in the original model in C (see methods section 2.14.2). Pink lines – edges of the structure that occur when f_1, f_2 and $f_1 + f_2$ are equal to f_{Base} or its harmonic. Orange line – part of the structure when $f_1 + f_2$ is equal to half f_{EOD}.
E Three-spikes burst packages: A spike was added after one and two EOD cycles to each spike in the original model in C.
F Four-spikes burst packages: A spike was added after one, two and three EOD cycles to each spike in the original model in C.

4.1.8 More spikes in burst package increase the nonlinearity

The two shown P-units differ in their average number of spikes per burst package (Fig. 4.7 A_{ii}, B_{ii}). In the following the influence of the spike number in a burst package on nonlinearity was investigated in a low-CV P-unit model (spikes in the first row in Fig. 4.8 B). In this model, the nonlinear structures occur in relation to $f_{BaseCorrected}$ and its harmonic (yellow lines in pink edges, Fig. 4.8 C, top). Spikes were added after exactly one, two or three EOD periods, creating artificial burst packages (Fig. 4.8 B, see section 2.14.2). Adding one spike adds a wide band in the second-order susceptibility (Fig. 4.8 D, top) and elevations in the projected diagonal (Fig. 4.8 D, bottom). Increasing the number of spikes in a burst to three (Fig. 4.8 E) or four spikes (Fig. 4.8 F) adds more bands in the second-order susceptibility (Fig. 4.8 E, F, top) and

introduces several elevations in the projected diagonals (bottom).

Although with more spikes per burst package the overall nonlinearity increases (more yellow in Fig. 4.8 F than in Fig. 4.8 C), some frequencies are enhanced but others are dampened. The peak at $f_{BaseCorrected}$ in the projected diagonal is increased with more spikes in a burst package (compare Fig. 4.8 C and Fig. 4.8 D–F). The frequencies on the vertical and horizontal lines at $f_1 = f_{BaseCorrected}$ and $f_2 = f_{BaseCorrected}$ in the second-order susceptibility are enhanced or dampened depending on their position in the antidiagonal bands induced by bursts. Adding bursts in the model revealed that the burst-induced increase of the second-order susceptibility is mediated not by the timing of the first spikes but by the number of spikes in a burst package.

4.1.9 Bursts influence nonlinearity on a population level

So far, bursting was identified to increase nonlinearity on a single cell level (Fig. 4.7) and in the following its influence on a population level will be addressed. Burst correction leads to a reduction of the CV during baseline from CV_{Base} to $\mathrm{CV}_{BaseCorrected}$ and of the firing rate during baseline from f_{Base} to $f_{BaseCorrected}$ in a population of P-units in *Apteronotus leptorhynchus* (compare purple in Fig. 4.9 $\mathsf{A}_{\mathsf{i,ii}}$). CV_{Base}, that previously has been identified to increase nonlinearity (Fig. 4.6 A, B), is highly correlated with the burst fraction, the number of spikes in a burst package divided by the number of all spikes (see methods section 2.9.1, $r = 0.81$, $p < 0.001$, Fig. 4.9 $\mathsf{A}_{\mathsf{iii}}$). Here, the nonlinearity was characterized as the peakedness of $f_{BaseCorrected}$ in the projected diagonal with the score $\mathrm{NLI}(f_{BaseCorrected})$ (Eq. (2.7)). Bursty cells have higher nonlinearity values $\mathrm{NLI}(f_{BaseCorrected})$ than non-bursty cells (Fig. 4.9 A_{iv}). When correlating $\mathrm{NLI}(f_{Base})$ with $\mathrm{NLI}(f_{BaseCorrected})$ bursty cells strongly deviate from the equality line but non-bursty cells do not change in their NLI values (Fig. 4.9 A_{v}). These non-bursty cells have high $\mathrm{NLI}(f_{BaseCorrected})$ values in the cluster close to the origin in Fig. 4.9 A_{iv} and simultaneously are the low-CV cells that contributed to the high $\mathrm{NLI}(f_{Base})$ values in Fig. 4.6 B.

Most cells increase bursting with higher RAM contrasts (red circles are above blue circles and above the equality line, Fig. 4.9 A_{vi}). These findings highlight that some P-units use bursting as a mechanism to encode a wide dynamic range of contrasts. Cells that already possess high burst fractions during baseline cannot increase their firing even further (high burst fractions values close to the equality line, Fig. 4.9 A_{vi}) and thus cannot use bursting as a mechanism for contrast encoding.

4.1.10 Nonlinearity in P-units of *Eigenmannia virescens*

So far it was demonstrated in *Apteronotus leptorhynchus* that P-units implement intermediate nonlinearity values with non-bursty low-CV cells and high nonlinearity values with bursty high-CV P-units (Fig. 4.9 A_{iv}). P-units of *Eigenmannia virescens* do not burst but have lower CVs than the P-units of *Apteronotus leptorhynchus* (Fig. 4.9 B_{i}). Similar nonlinearity values are implemented in these low-CV P-units of *Eigenmannia virescens* (Fig. 4.9 B_{ii}) as they were observed in bursty P-units of *Apteronotus leptorhynchus* (Fig. 4.9 A_{iv}).

The baseline firing rate power spectrum of P-units of *Eigenmannia virescens* is also mirrored around half f_{EOD} (Fig. 4.10 A_{i}, right). Pronounced nonlinearity bands can be observed at $f_1 + f_2 = f_{Base}$ in the second-order susceptibility of low-CV P-units (Fig. 4.10 A_{iv}). *Eigenmannia virescens* have lower EOD frequencies than *Apteronotus leptorhynchus* and the f_{Base} of P-units can be as high as the f_{EOD} of *Eigenmannia virescens*. In some P-units f_{Base} is close to $f_{EOD}/2$, with very pronounced nonlinearity bands at $f_1 + f_2 = f_{Base}$ and $f_1 + f_2 = f_{EOD}/2$ (Fig. 4.10 B_{iv}). Nonlinearities at $f_1 + f_2 = f_{EOD}/2$ can also be observed in *Apteronotus leptorhynchus* (Fig. 4.4 A_{ii}), still the mean baseline firing rates f_{Base} of these fish are usually below half f_{EOD}, with no overlap of the according nonlinearities.

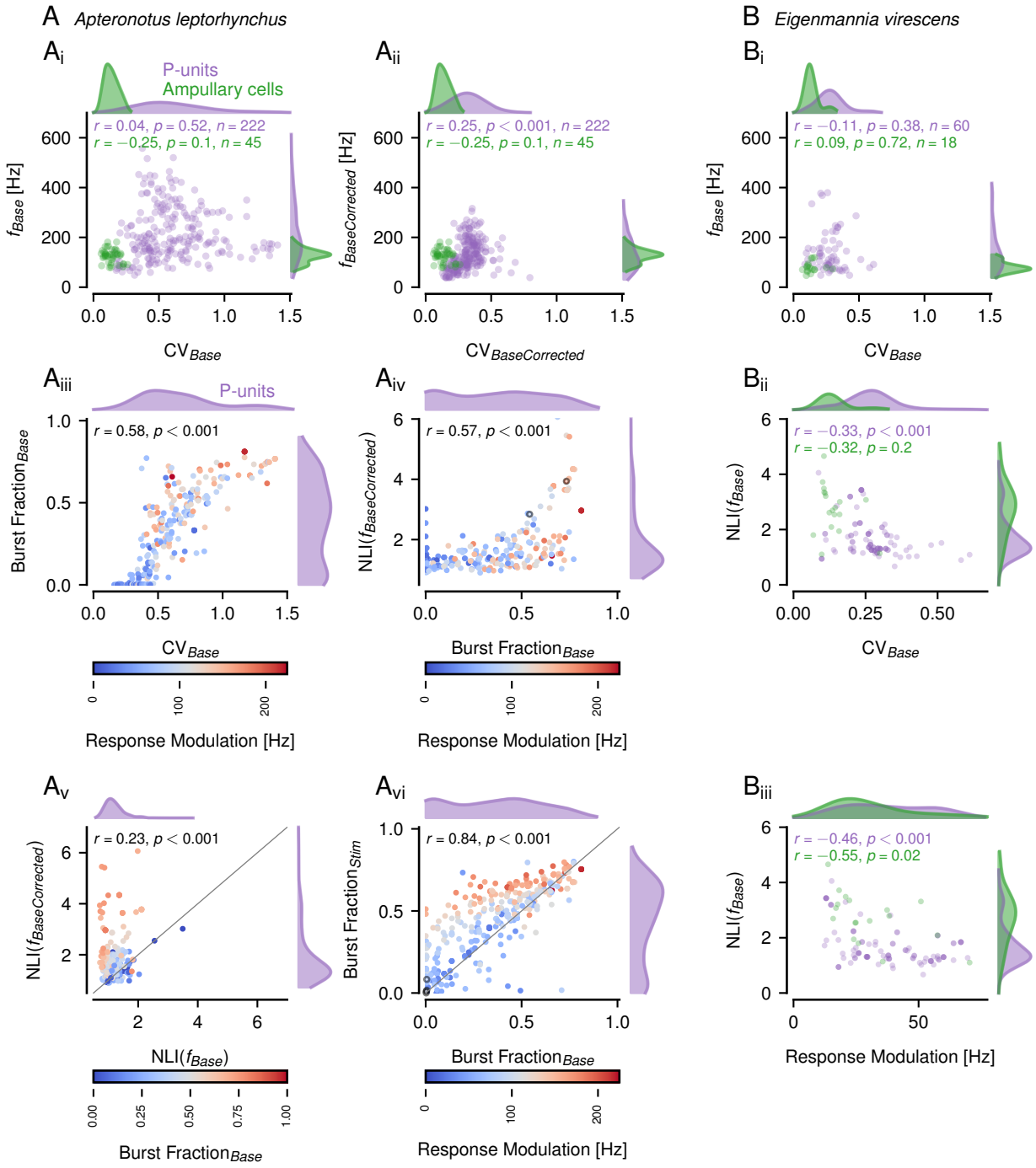

Figure 4.9: Population statistics of ampullary cells (green) and P-units (purple) in *Apteronotus leptorhynchus* (A) and *Eigenmannia virescens* (B). If only P-units are presented in the subplots (A_{iii-vi}), the marginal distributions are purple and the scatter is color-coded, as indicated in the color bar below the subplot. f_{Base} – mean baseline firing rate before burst correction. $f_{BaseCorrected}$ – mean baseline firing rate after burst correction. CV_{Base} – baseline CV before burst correction. $CV_{BaseCorrected}$ – baseline CV after burst correction. $NLI(f_{Base})$ $NLI(f_{BaseCorrected})$ – see methods section 2.9.4. Burst fraction – see methods section 2.9.1. Response modulation – see methods section 2.9.2.
A_i, A_{ii}, B_i Baseline statistics. Burst correction leads to a reduction of baseline CVs and mean firing rates in *Apteronotus leptorhynchus* ($A_{i,ii}$). *Eigenmannia virescens* has lower CVs (B_i).
A_{iv} Gray circles – the lower marker corresponds to Fig. 4.7 B and the higher marker to Fig. 4.7 A.
A_v Cells with a high burst fraction deviate from the equality line.
A_{vi} High bust fraction cells do not increase their bursting during stimulation ($_{Stim}$) and are close to the gray equality line. The example cells in Fig. 4.2 are marked with gray circles.

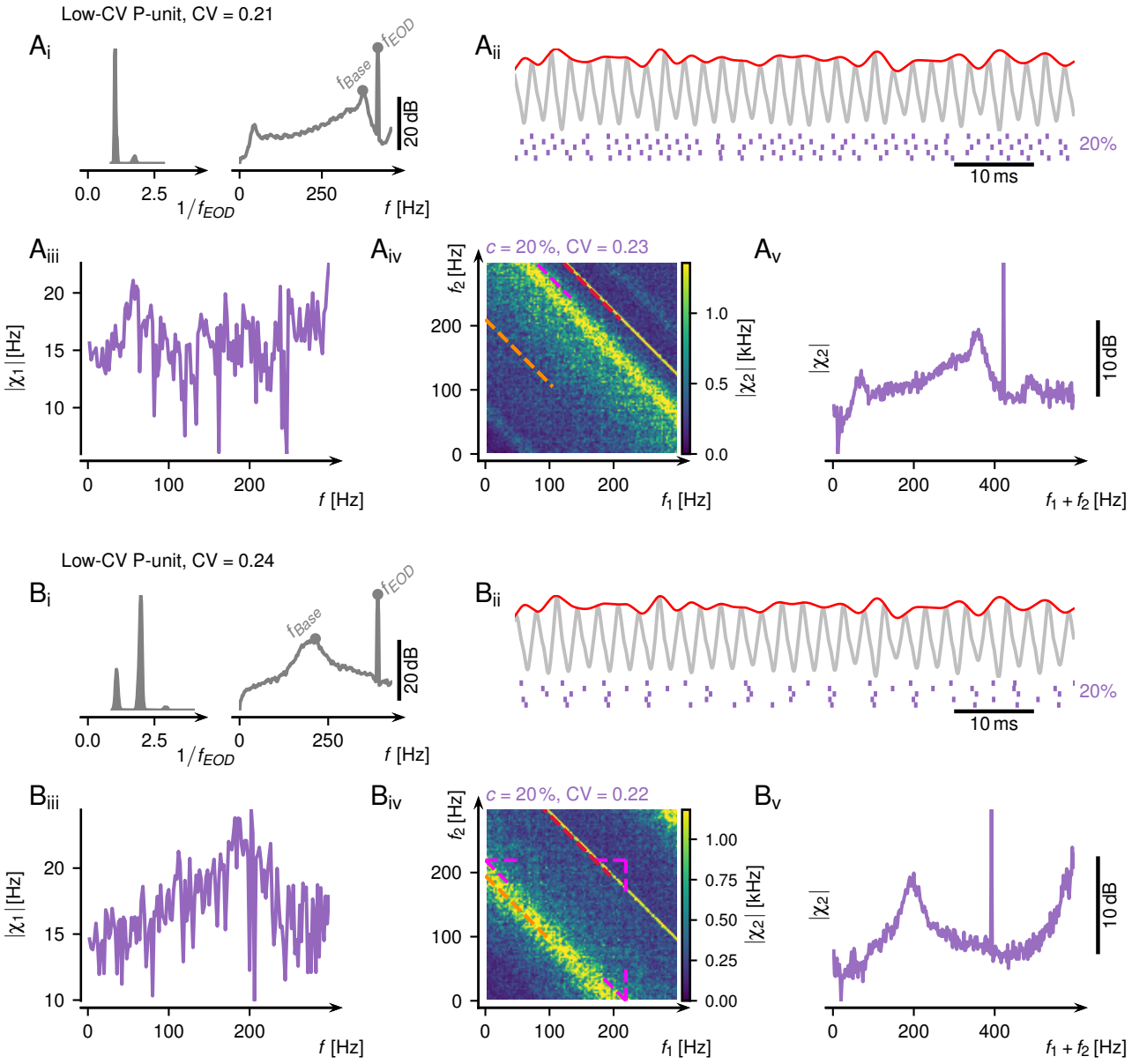

Figure 4.10: Response of experimentally measured P-units of *Eigenmannia virescens* with two low-CV P-unit examples.
A Low-CV P-unit with strong second-order susceptibility when $f_1 + f_2 = f_{Base}$.
$\mathbf{A}_{\text{i}}$ Left: ISI distribution during baseline. Right: Baseline power spectrum of the firing rate.
$\mathbf{A}_{\text{ii}}$ Top: EOD carrier (gray) with a RAM (red). Bottom: Spike trains.
$\mathbf{A}_{\text{iii}}$ First-order susceptibility (Eq. (2.3)).
$\mathbf{A}_{\text{iv}}$ Absolute value of the second-order susceptibility. Pink lines – edges of the structure when f_1, f_2 or $f_1 + f_2$ are equal to f_{Base}. Orange line – part of the structure when $f_1 + f_2$ is equal to half f_{EOD}. Red line – edges of the structure when $f_1 + f_2$ is equal to f_{EOD}.
$\mathbf{A}_{\text{v}}$ Projected diagonal, calculated as the mean of the anti-diagonals of the matrix in $\mathbf{A}_{\text{iv}}$.
B Low-CV P-unit with strong second-order susceptibility when $f_1 + f_2 = f_{Base}$ (pink) and $f_1 + f_2 = f_{EOD}/2$ (orange, in $\mathbf{A}_{\text{iv}}$).

4.2 Discussion

In this chapter, the second-order susceptibility in spiking responses of P-units was characterized for the scenario where at least three fish are present. A low-CV subpopulation of P-units in *Apteronotus leptorhynchus* was demonstrated to have increased nonlinearity values when f_1, f_2, $f_1 + f_2$ or $|f_1 - f_2|$ were equal to the mean baseline firing rate f_{Base}. Ampullary cells, with even lower CVs, exhibited even stronger nonlinearity. These nonlinear structures in low-CV cells confirmed the predictions from the nonlinear theory described in Voronenko and Lindner (2017). High-CV P-units did not exhibit any nonlinear interactions, except for bursting high-CV P-units that processed very strong nonlinearities in relation to the burst-corrected mean baseline firing rate $f_{BaseCorrected}$. Bursting was identified as a factor to increase the already present nonlinearities with a higher burst fraction, namely more spikes in a burst package. P-units of *Eigenmannia virescens*, that do not burst but have very low CVs, exhibited strong nonlinearities, similar to the nonlinearities of bursty P-units of *Apteronotus leptorhynchus*. These two implementations highlighted that nonlinearity might be a critical feature necessary to sustain in these fish. The nonlinearities appearing for the noise frequencies f_1, f_2 were confirmed as a proxy for nonlinearities that might arise in response to the beat frequencies Δf_1, Δf_2, when at least three fish are present. A three-fish setting might be especially interesting when it becomes the electrosensory cocktail party (Henninger et al., 2018), where a faint signal has to be detected despite the presence of a strong signal. The here presented second-order susceptibility might provide the boost necessary for improved faint signal detection. How this might be implemented will be discussed in the chapter 5.

4.2.1 Methodological implications

Full nonlinear structure present in LIF models with and without carrier

In this chapter, it was demonstrated that in small homogeneous populations of electrophysiological recorded cells, a diagonal structure appeared when the sum of the input frequencies was equal to f_{Base} in the second-order susceptibility (Fig. 4.2, Fig. 4.3). The size of a population is limited by the possible recording duration in an experiment, but there are no such limitations in P-unit models, where an extended nonlinear structure with diagonals, vertical and horizontal lines at $f_1 + f_2 = f_{Base}$, $|f_1 - f_2| = f_{Base}$, $f_1 = f_{Base}$ or $f_2 = f_{Base}$ appeared with increased stimulus realizations (Fig. 4.5). This nonlinear structure is in line with the one predicted in the framework of the nonlinear response theory, which was developed based on LIF models without carrier (Fig. 1.13, Voronenko and Lindner, 2017) and was here confirmed to be valid in models with carrier (Fig. 4.4).

Noise stimulation approximates the nonlinearity in a three-fish setting

In this chapter, the nonlinearity of P-units and ampullary cells was retrieved based on white noise stimulation, where all behaviorally relevant frequencies were simultaneously present in the stimulus. The nonlinearity of LIF models (Egerland, 2021) and of ampullary cells in paddlefish (Neiman and Russell, 2011) has been previously accessed with bandpass limited white noise.

Here it was demonstrated that the second-order susceptibility for the two RAM noise input frequencies f_1 and f_2 can approximate a three-fish setting, where the driving force for the P-unit are two beats with frequencies Δf_1 and Δf_2. This was confirmed by a low-CV P-unit, where nonlinearities in the P-unit response occurred at the sum and difference of the beat frequencies for pure sine-wave stimulation (Fig. 4.1). In this P-unit the nonlinearity appeared in a three-wave setting with Δf_1 being close to f_{Base}, corresponding to a frequency combination on the vertical line at $f_1 = f_{Base}$ in the second-order susceptibility (Fig. 4.5 B). This implies

that even if only the diagonal structure can be accessed with noise stimulation in the second-order susceptibility in an experiment (Fig. 4.5 A), it can be taken as an indicator that the whole nonlinear structure should be present during pure sine-wave stimulation in the same cell. With this RAM stimulation was demonstrated to be an effective method to scan the three-fish or two-beat plane and estimate the whole theoretically predicted nonlinear structure in experimentally recorded cells.

4.2.2 Nonlinearity and CV

In this chapter, the CV has been identified as an important factor influencing nonlinearity in the spiking response, with strong nonlinearity in low-CV cells (Fig. 4.6 A–B). These findings of strong nonlinearity in low-CV cells are in line with previous literature, where it has been proposed that noise linearizes the system (Roddey et al., 2000; Chialvo et al., 1997; Voronenko and Lindner, 2017). More noise has been demonstrated to increase the CV and reduce nonlinear phase-locking in vestibular afferents (Schneider et al., 2011). Reduced noise of low-CV cells has been associated with stronger nonlinearity in pyramidal cells of the ELL (Chacron, 2006).

In this chapter strong nonlinear interactions were found in a subpopulation of low-CV P-units and low-CV ampullary cells (Fig. 4.6 A, B). Ampullary cells have lower CVs than P-units, do not phase-lock to the EOD, and have unimodal ISI distributions. With this, ampullary cells have very similar properties as the LIF models, where the theory of weakly nonlinear interactions was developed on (Voronenko and Lindner, 2017). Almost all here investigated ampullary cells had pronounced nonlinearity bands in the second-order susceptibility for small stimulus amplitudes (Fig. 4.3). With this ampullary cells are an experimentally recorded cell population close to the LIF models that fully meets the theoretical predictions of low-CV cells having very strong nonlinearities (Voronenko and Lindner, 2017). Ampullary cells encode low-frequency changes in the environment e.g. prey movement (Engelmann et al., 2010; Neiman and Russell, 2011). The activity of a prey swarm of *Daphnia* strongly resembles Gaussian white noise (Neiman and Russell, 2011), as it has been used in this chapter. How such nonlinear effects in ampullary cells might influence prey detection could be addressed in further studies.

4.2.3 Bursting as a mechanism for amplitude encoding

In this chapter, bursty and non-bursty cells during baseline were identified as two subpopulations of P-units with different stimulus amplitude encoding mechanisms. One subpopulation were P-units that already bursted during baseline (Fig. 4.7) and could not increase bursting even further for stronger stimulus amplitudes (Fig. 4.9 A_{vi}, equality line), with bursting not contributing to the encoding of amplitude changes. The other identified subpopulation were P-units that did not burst during baseline, but gradually increased bursting with stronger stimulus amplitudes (Fig. 4.2 , Fig. 4.9 A_{vi}). In these cells bursting contributed to the encoding of a wide dynamic range of stimulus amplitudes. An increasing burst fraction is known to encode different stimulus strengths as e.g. temperature changes (Longtin and Hinzer, 1996), muscle stretch intensity (Birmingham et al., 1999) or the strength of electrical white noise signals in ampullary cells of paddlefish (Neiman and Russell, 2011).

The two subpopulations identified here are in line with previous literature, where it has been demonstrated that different features are in parallel encoded in bursty and non-bursty P-units (Chacron et al., 2004). In slice recordings it was shown that the ISI statistics of P-units are transported to higher-order neurons, the pyramidal cells in the electrosensory line lobe (ELL, Khanbabaie et al., 2010), where bursting might have an impact on higher-order cells.

4.2.4 Bursting increases nonlinearity and linearity in P-units

In this chapter, bursty high-CV P-units in *Apteronotus leptorhynchus* were identified to have strong nonlinearity, exceeding the one of non-bursty low-CV P-units (Fig. 4.9 $\mathsf{A_{iv}}$). These findings are in line with previous literature, where it was derived in P-unit models that non-bursty cells can be described by a linear decoder, whereas bursty cells require a nonlinear decoder (Chacron et al., 2004). Bursting has previously been associated with an increased second-order susceptibility in ampullary cells of paddlefish (Neiman and Russell, 2011).

In bursty cells two nonlinearity structures were present in the second-order susceptibility: the wide burst-induced bands and the sharp bands at $f_{BaseCorrected}$ (Fig. 4.7 $\mathsf{A_{iv}}, \mathsf{B_{iv}}$), that were enhanced by bursts (Fig. 4.8 D–F). It was derived in the model that the enhanced nonlinearity is not driven by the timing of the first spike in the burst package but is defined by the number of spikes in a burst package, with more burst spikes inducing higher nonlinearity and increasing the signal-to-noise ratio. In pyramidal cells of the ELL, it was demonstrated that bursting improves feature detection by improving the signal-to-noise ratio (Oswald et al., 2004; Gabbiani et al., 1996). An improved signal-to-noise ratio and sharpened tuning curves have been associated with bursts in the auditory system (Eggermont and Smith, 1996). The reason behind an improved signal-to-noise ratio might be a decrease of the synaptic failure probability (Lisman, 1997) and a more reliable synaptic transmission (Csicsvari et al., 1998) induced by bursts.

Besides the influence on the nonlinearity, bursting was demonstrated to contribute to the linear encoding of the stimulus, which is reduced after burst correction (Fig. 4.7). Usually, bursts in P-units have been discussed considering their contribution to nonlinearity (Chacron et al., 2004) with their impact on linear encoding being mainly neglected. The increase of linearity via bursts is not universal since in other cells, as in pyramidal cells of the ELL, the linear encoding of the stimulus is attributed to isolated spikes and not to bursts (Oswald et al., 2004).

The investigation of bursts is important since bursts are ubiquitous in sensory modalities as in chattering cells in the visual system (Nowak et al., 2003), in fast rhythmic bursting cells in the auditory system (Cunningham et al., 2004), Purkinje cells in the cerebellum (Womack and Khodakhah, 2004) or thalamic relay neurons (Destexhe et al., 1993). Bursts have an important application and are successfully used for chronic pain treatment with neuromodulation of the spinal cord (De Ridder et al., 2010a; Chakravarthy et al., 2018; Karri et al., 2020), but also for tinnitus suppression (De Ridder et al., 2010b). The dynamics leading to bursting have been addressed with bifurcation analysis and are well understood (Izhikevich, 2000).

4.2.5 Encoding of secondary envelopes

The RAM stimulus used in this chapter is an approximation of the three-fish scenario, where the two generated beats are often slowly modulated at the difference between the two beat frequencies $||\Delta f_1| - |\Delta f_2||$, known as secondary or social envelope (Stamper et al., 2012). Low-frequency secondary envelopes are extracted downstream of P-units in the ELL (Middleton et al., 2006) utilizing threshold nonlinear response curves of the involved neuron (Middleton et al., 2007). The encoding of social envelopes can also be attributed to P-units with stronger nonlinearities, lower firing rates and higher CVs (Savard et al., 2011). In this chapter high CVs were associated with increased bursting (Fig. 4.9 $\mathsf{A_{iii}}$). Thus it is likely that the high-CV nonlinear envelope encoding P-units found by Savard et al. (2011) are bursty. Then these findings (Savard et al., 2011) would be in line with the in this chapter demonstrated increased nonlinearity in bursty cells (Fig. 4.7, Fig. 4.8).

4.2.6 Nonlinearity necessary to sustain in different species?

In this chapter, it was demonstrated that similar nonlinearity values can be implemented with different mechanisms, namely with low-CV P-units in *Eigenmannia virescens* or bursting in *Apteronotus leptorhynchus* (Fig. 4.9 $\mathsf{A}_{\mathsf{iv}}, \mathsf{B}_{\mathsf{ii}}$). This suggests that nonlinearity might be an important feature, necessary to sustain in different species of weakly electric fish. If traits develop independently, with the trait not being present in a common ancestor, the process is termed convergent evolution. Examples of convergent evolution are blue eyes and light skin in humans (Edwards et al., 2010), the camera eye present in mammals, jellyfish and squids (Kozmik et al., 2008) or the evolution of wave-type and pulse-type weakly electric fish (Lavoué et al., 2012). Slightly different traits in closely related species imply divergent evolution. An example of divergent evolution are dogs and wolfs that descend from the same ancestor (Vilà et al., 1999) or Darwin's finches that developed beaks with different shapes (Ford et al., 1973). *Apteronotus leptorhynchus* and *Eigenmannia virescens* are closely related species belonging to the same superfamily Apteronotoidea, but to different families of Apteronotidae and Sternopygidae (Albert, 2001). The nonlinearity in the primary sensory afferents of more weakly electric fish species should be accessed in further studies, to increase the certainty if such nonlinearity might have been present in the common ancestor of *Eigenmannia virescens* and *Apteronotus leptorhynchus* and test whereas this sustained nonlinearity might be an example of divergent evolution.

4.2.7 More fish would decrease second-order susceptibility

When using noise stimulation strong nonlinearity was demonstrated to appear for small noise stimuli but to decrease for stronger noise stimuli (Fig. 4.2). A white noise stimulus is a proxy of many fish being present simultaneously. When the noise amplitude is small, those fish are distant and the nonlinearity is maintained. When the stimulus amplitude increases, many fish close to the receiver are mimicked and a decrease of nonlinear effects can be observed. These findings imply that the nonlinear effects arising in the presence of three fish decline the more fish join. *Eigenmannia virescens* can usually be found in groups of three to four fish (Tan et al., 2005) and *Apteronotus leptorhynchus* in groups of two (Stamper et al., 2010). Thus the here described second-order susceptibility might still be behaviorally relevant for both species. The decline of nonlinear effects when several fish are present might be adaptive for the receiver, reducing the number of frequencies represented in its primary sensory afferents to a minimum. Such representation would still leave room to create nonlinear effects at later processing steps in higher-order neurons. How nonlinear effects might influence the three-fish setting known as the electrosensory cocktail party (see section 1.18, Henninger et al., 2018) will be addressed in the next chapter.

4.2.8 Conclusion

In this chapter, noise stimulation was confirmed as a method to access the second-order susceptibility in P-unit responses when at least three fish or two beats were present. Nonlinear effects were identified in experimentally recorded non-bursty low-CV cells and bursty high-CV P-units. It was demonstrated that the theory of weakly nonlinear interactions (Voronenko and Lindner, 2017) is valid in P-units where the stimulus is an amplitude modulation of the carrier and not the whole signal. P-units could be subdivided into two populations, where some P-units did not burst during baseline and increased bursting to encode stimulus amplitudes, and others bursted during baseline and did not use bursting as an amplitude encoding mechanism. Bursting was identified as a factor increasing linear and nonlinear encoding in P-units. Such nonlinearity was identified as a feature potentially necessary to sustain in primary sensory afferents of different weakly electric fish species. Nonlinearity was found to be decreased the more fish were present,

thus keeping the signal representation in the firing rate simple. The behavioral implications of second-order susceptibility in P-units will be discussed in the following chapter, where the detection of a faint signal in a three-fish setting, the electrosensory cocktail party (Henninger et al., 2018), will be addressed.

Chapter 5

Nonlinear interactions can improve faint signal detection

In the previous chapter, the second-order susceptibility of electroreceptor afferents, the so-called P-units, was characterized in a three-fish setting. A nonlinearity can be just a byproduct of the physiology of the neuronal system, as it is often assumed about distortion products measured in the ear (Kemp, 1978; Abel and Kössl, 2009; Young and Sachs, 1979). Only if a nonlinearity has behavioral implications (as e.g. the smooth synaptic nonlinearity associated with the jamming avoidance response in chapter 3), it might be important for the neuronal system. Potential behavioral implications of the second-order susceptibility, characterized in chapter 4, will be addressed in the following chapter.

The nonlinearities in chapter 4 were identified for a scenario when at least three fish were present. A three-fish setting is especially interesting when it becomes an electrosensory cocktail party problem, described in the natural habitat of *Apteronotus rostratus* (Henninger et al., 2018). In the field, it could be observed repeatedly that a courting male and female were approached by a male intruder from a large distance (Fig. 1.20 A, left). The intruder often elicited a reaction in the courting receiver male, that chased away the distant intruder (Fig. 1.20 A, right). The beat and EOD amplitude of these fish decays with distance squared, with the female being a strong signal for the receiver and the intruder a faint signal (Fig. 1.20 B). P-units respond with reduced firing rate modulation depths to decreasing stimulus amplitudes and contrasts smaller than 1 % (distance of 50 cm) have not been recorded in P-units (Fig. 1.20 D, Benda et al., 2006; Grewe et al., 2017; Bastian, 1981; Nelson et al., 1997). Still, attacks of the receiver towards the intruder could be observed at distances of 180 cm (Fig. 1.20 C). This leaves the question open how P-units can encode signals at such large distances, despite the reduced firing rate modulation depth at contrast of 1 % or distances of 50 cm (Fig. 1.20 D). In the three-fish scenario, the distant intruder detection in P-units is even more complicated, since a large percentage of the P-units response is already driven by the strong and nearby female. The here presented problem is reminiscent of the cocktail party problem (Cherry, 1953; Haykin and Chen, 2005), a sound source separation problem where a behaviorally relevant stimulus has to be separated from a noisy environment. Accordingly, the here-described detection problem in weakly electric fish will be referred to as the electrosensory cocktail party problem.

The fundamental problem in the electrosensory cocktail party problem is that the beat amplitude decays with distance squared, with the intruder not being detectable in the firing rate of P-units for large intruder distances (Bastian, 1981; Benda et al., 2006; Grewe et al., 2017). One solution to improve the faint intruder detection might be nonlinear frequency interactions, emerging during the electrosensory cocktail party. Such nonlinearities were characterized by the second-order susceptibility in a three-wave setting in the previous chapter. There nonlinearities were found in low-CV P-units and bursty high-CV P-units at the sum and difference of the

two beat frequencies (Fig. 4.1 D, purple and orange markers). These nonlinearities might be a boost for intruder detection at large distances. How these nonlinearities might improve the detection of an intruder is studied utilizing simulations of leaky integrate-and-fire (LIF) P-unit models in the following chapter.

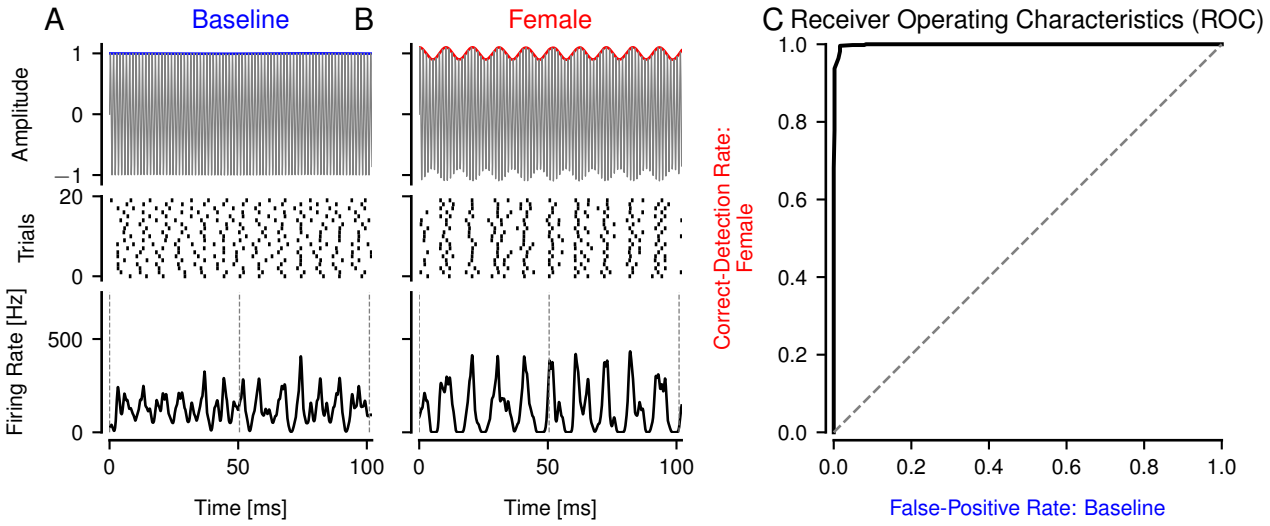

Figure 5.1: Detection of a nearby female with a Receiver Operating Characteristic (ROC) (see methods section 2.10.1), comparing the baseline condition (no female present in A) to the condition where the female is present in B. The model has the cell identifier 2013-01-08-aa (see table 2.1 for model parameters).
A–B Top: Gray – field around the receiver. Colored line – beat. Middle: Spike trains in response to the signal above. Bottom: The firing rate, calculated as the convolutions of the spike trains with a Gaussian kernel ($\sigma = 0.5\,\text{ms}$). Vertical dashed lines – time windows that are the basis for the ROC curve in C.
A Only the receiver is present (top).
B Receiver and female are present, leading to a fast oscillating beat with a frequency of 98 Hz (top), an aligned spike response (middle), and a firing rate with high peak-to-peak values (bottom).
C Black – ROC curve of female detection. The correct-detection rate (female detected when receiver and female are present), is plotted against the false-positive rate (female detected even though only the receiver is present). Gray line – equality line.

5.1 Results

The Receiver Operating Characteristic (ROC) for the detection of faint signals based on the firing rate has been proposed by Schlungbaum and Lindner (2023). In the following, the ROC will be explained using a simple detection task of the strong and nearby female (Fig. 5.1, see methods section 2.10.1). For this the baseline condition, where only the receiver with EOD frequency f_{EOD} is present (Fig. 5.1 A), is compared to the condition in which the receiver encounters a nearby female with EOD frequency f_{Female}, leading to a strong beat in the superimposed signal (Fig. 5.1 B). The beat frequency is calculated as the difference between the two present frequencies $\Delta f_{\text{Female}} = f_{\text{Female}} - f_{\text{EOD}}$ (Walz et al., 2014). Since *Apteronotus leptorhynchus* is sexually dimorphic, the male receiver and female frequencies are drawn from two different frequency distributions, leading to a high difference frequency and a fast oscillating beat. The female-induced beat leads to high peak-to-peak values in the firing rate of the model P-unit (Fig. 5.1 B, bottom).

The ROC curve (Fig. 5.1 C) compares the female detection in the P-unit firing rate in the condition where the female is present (correct-detection – CD, Fig. 5.1 B) with the condition where the receiver is alone (false-positive – FP, Fig. 5.1 A). For this detection task, the firing rates are subdivided into time windows and detection thresholds are drawn horizontally between the minimal and maximal firing rate in each time window. If any firing rate value in the time window is above a threshold, the female is detected and this threshold is assigned a detection value of 1, otherwise a value of 0. The mean of the female detection over all time windows results in the CD rate for the female-induced firing rate (Fig. 5.1 B) and the FP rate for the baseline firing rate (Fig. 5.1 A). For the ROC curve the CD rate is plotted against the FP rate (Fig. 5.1 C). In the case of perfect detection, if both firing rates have different firing rate modulation depths, the ROC curve follows a triangular shape, reaching the upper left or the lower right corner. If the two firing rates are not distinguishable, the ROC curve follows the equality line. The resulting ROC curve (Fig. 5.1 C) captures the intuition that the female-induced firing rate has higher peak-to-peak values than the baseline firing rate (Fig. 5.1 A–B).

5.1.1 A faint intruder is not detectable alone

If instead, the receiver encounters only the intruder, both fish are male and their frequencies are drawn from the same frequency distribution, leading to a beat with a low beat frequency $\Delta f_{\text{Intruder}}$ (Fig. 5.2 B, top). Since the intruder has a large distance to the receiver (Fig. 1.20 B), the intruder-induced beat has a small amplitude. It is difficult to see the differences in the spike trains or the firing rates between the baseline and intruder conditions (middle and bottom, Fig. 5.2 A, B). This intuition is reflected in the ROC curve; it is close to the gray equality line, meaning that the intruder is equally detected in both conditions with and without intruder (Fig. 5.2 C).

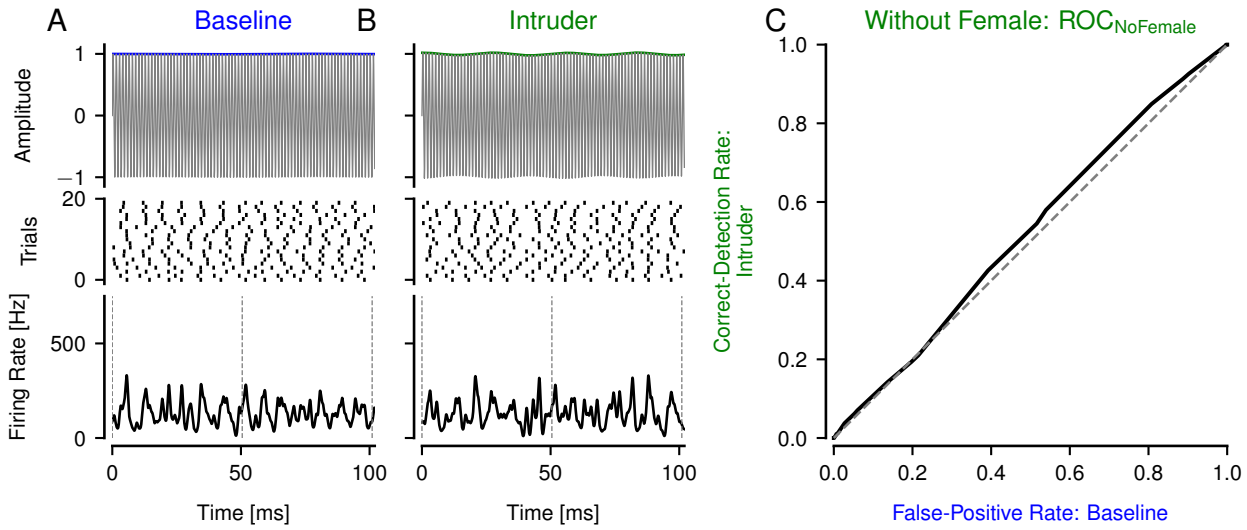

Figure 5.2: ROC detection of a faint and distant (70 cm) intruder without the female being present. The model has the cell identifier 2013-01-08-aa (see table 2.1 for model parameters). See methods section 2.10.1 for further details.
A–B Top: Gray – field around the receiver. Colored line – beat. Middle: Spike trains. Bottom: Firing rate of the spike trains. See Fig. 5.1 for details.
A Only the receiver is present.
B Receiver and faint intruder are present, with a faint beat with a low frequency of 36 Hz.
C Black – ROC curve. Gray – equality line.

5.1.2 Intruder detection can be improved by female presence

This poor intruder detection (Fig. 5.2) can be improved if all three fish (receiver, intruder, and female) join the cocktail party. The firing rate has higher peak-to-peak values if the receiver encounters the intruder and the female (Fig. 5.3 B) compared to the scenario where only the receiver and female are present (Fig. 5.3 A). This intruder detection, improved by the presence of the female, is captured in the ROC curve, which clearly deviates from the equality line (Fig. 5.3 C).

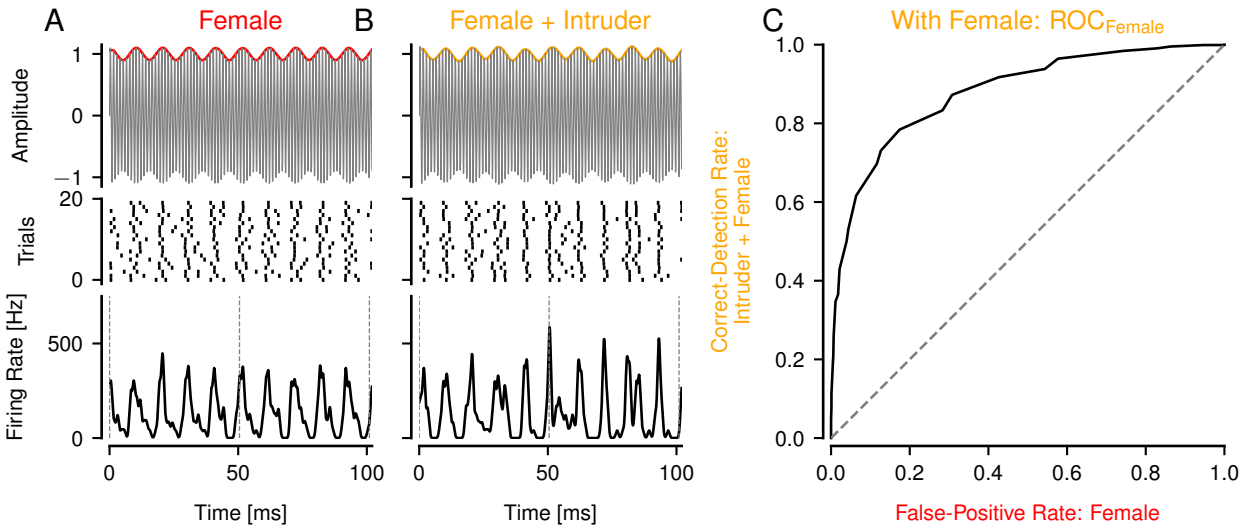

Figure 5.3: ROC detection of a faint and distant (70 cm) intruder with the female being present. The model has the cell identifier 2013-01-08-aa (see table 2.1 for model parameters). See methods section 2.10.1 for further details.
A–B Top: Gray – field around the receiver. Colored line – beat. Middle: Spike trains. Bottom: Firing rate. See Fig. 5.1 for details.
A Only the receiver and the female are present, leading to a beat with the frequency of 98 Hz.
B Top – Receiver, female, and faint intruder are present. $\Delta f_{\text{Female}} = 98\,\text{Hz}$, $\Delta f_{\text{Intruder}} = 36\,\text{Hz}$.
C Black – ROC curve. Gray – equality line.

Combining the ROC curves from the previous paragraphs in Fig. 5.4 A visualizes that the intruder detection without the female (green area) can be improved if the female joins the cocktail party (orange area). A ROC curve can be summarized in a single value, by calculating the area between the ROC curve and the equality line, leading to the area under the curve (AUC, see methods section 2.10.2). The EOD and beat amplitudes and the intruder detection decay with distance (Fig. 5.4 B–C). In this model, there is no intruder detection without the female at a distance of 70 cm (green circle, Fig. 5.4 C). The intruder detection (green line) can be improved by the presence of the female (yellow line), shifting the AUC detection curve towards larger intruder distances (black arrow).

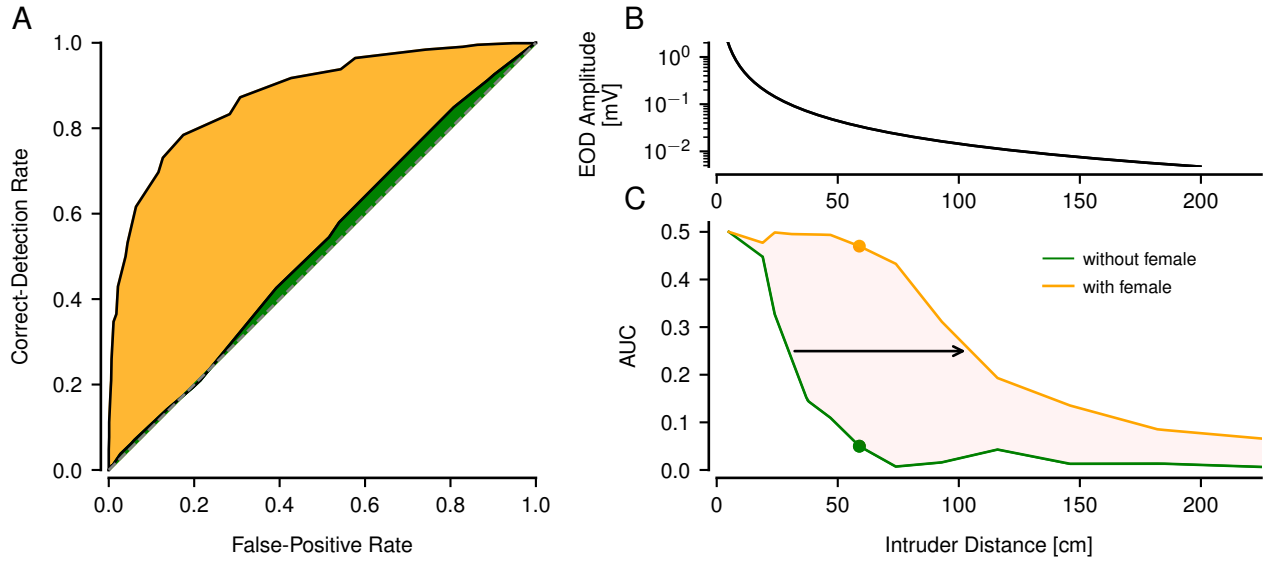

Figure 5.4: The female presence can improve the detection of the intruder for large distances. ROC and AUC values are based on beats with frequencies $\Delta f_{\text{Intruder}} = 36\,\text{Hz}$ and $\Delta f_{\text{Female}} = 98\,\text{Hz}$. The model has the cell identifier 2013-01-08-aa (see table 2.1 for model parameters).
A Intruder detection at a distance of 70 cm. The colored area visualizes the area under the curve (AUC) between the ROC curve (black) and the equality line (gray dashed line, see method section 2.10.2). Green – intruder detection without the female, as in Fig. 5.2 C. Orange – intruder detection with the female, as in Fig. 5.3 C.
B The EOD and the beat decay with distance squared.
C Detection of the intruder without the female (green) can be improved by the presence of the female (orange). The AUC values of the ROC curves in A are highlighted with markers at a distance of 70 cm in C.

5.1.3 Nonlinear interactions between intruder- and female-induced beat frequencies improve intruder detectability

The intruder detection improved by the presence of a female (arrow, Fig. 5.5 A) can be explained if the power spectra of the firing rates are considered (Fig. 5.5 B, C, bottom). When the receiver encounters only the female, the fundamental of the female-induced beat and its harmonic are present in the power spectrum of the firing rate (red circles, Fig. 5.5 B). When all three fish (receiver, female and intruder) are present simultaneously the intruder-induced beat frequency (green circle) and the female-induced beat frequency (red circle) are present in the power spectrum of the firing rate (Fig. 5.5 C, bottom). Nonlinear peaks occur at the frequencies $2|\Delta f_{\text{Female}}| + |\Delta f_{\text{Intruder}}|$ (yellow circle) and $|\Delta f_{\text{Female}}| + |\Delta f_{\text{Intruder}}|$ (orange circle). The nonlinear peak at $|\Delta f_{\text{Female}}| + |\Delta f_{\text{Intruder}}|$ is equal to the mean baseline firing rate f_{Base} of this model cell (blue circle, see methods section 2.7.1). The intruder detection improved by the presence of the female (arrow, Fig. 5.5 A) coincides with the increased nonlinearity $A(\Delta f_{\text{Sum}})$ (Fig. 5.5 D), quantified as the amplitude of the sum peak $|\Delta f_{\text{Female}}| + |\Delta f_{\text{Intruder}}|$ in the power spectrum of the firing rate (see methods section 2.10.4 for details).

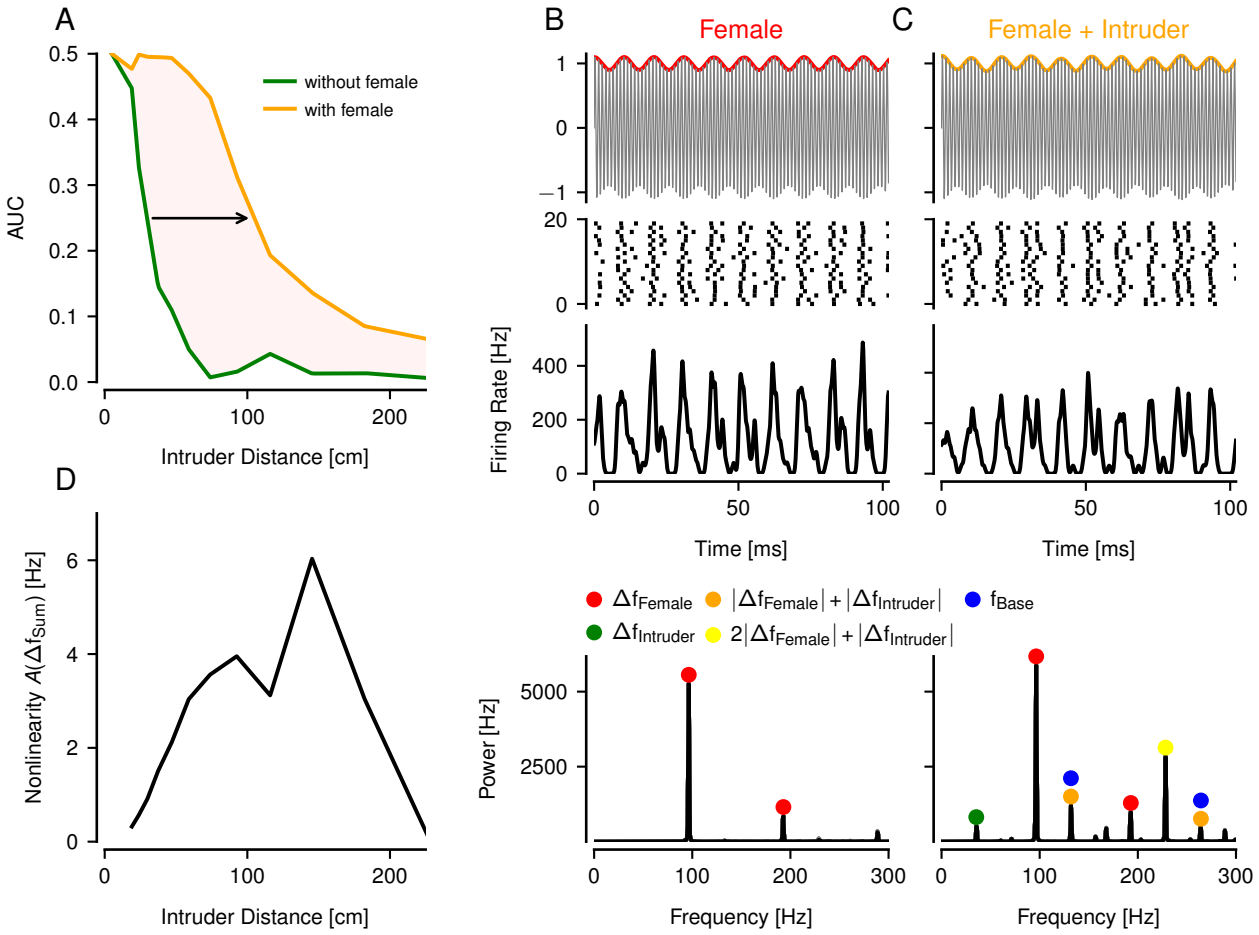

Figure 5.5: The improved detection of a faint and distant intruder in the presence of a female is associated with nonlinearity at the sum of the two beat frequencies $|\Delta f_{\text{Female}}| + |\Delta f_{\text{Intruder}}|$ in the P-unit response. The model has the cell identifier 2013-01-08-aa (see table 2.1 for model parameters).

A The intruder detection without the female (green line) can be improved by the presence of the female (orange line).

B–C Top: EOD of the receiver interfering with the EODs of other fish. Colored line – beat. Middle: Spike trains and firing rate in response to the signal above. Bottom: Power spectrum of the firing rate.

B Only the receiver and the female are present (top). $\Delta f_{\text{Female}} = 98\,\text{Hz}$.

C Receiver, female, and faint intruder are present (top). $\Delta f_{\text{Female}} = 98\,\text{Hz}$. $\Delta f_{\text{Intruder}} = 36\,\text{Hz}$.

D Nonlinearity $A(\Delta f_{\text{Sum}})$, measured as the amplitude of the peak at the sum frequency $|\Delta f_{\text{Female}}| + |\Delta f_{\text{Intruder}}|$ in the power spectrum of the P-unit firing rate (see methods section 2.10.4).

5.1.4 The intruder detection is improved in larger homogeneous populations

If the same stimulus is repeated to the same model a homogeneous population, consisting of cells with the same baseline characteristics (e.g. same CV and f_{Base}), can be assembled. The so far presented ROC curves (Fig. 5.4) were calculated based on a homogeneous P-unit population with size $n = 20$ (light orange and light green in Fig. 5.6 A). The intruder detection without the female can be increased if instead of a population of $n = 20$ (light green) a population of $n = 100$ (green) or a population of $n = 1000$ (dark green, Fig. 5.6 A) are considered. The best intruder detection without the female with a population size of $n = 1000$ (dark green) is comparable to the intruder detection with the female with a small population of $n = 20$ (light orange). The intruder detection with the female can be improved with a larger population of $n = 1000$ (dark orange line). The intruder detection improvement due to the population size is higher if all three fish are present in the cocktail party (compare light orange to dark orange circle) as if the receiver only encounters the intruder (compare light green to dark green circle, Fig. 5.6 B).

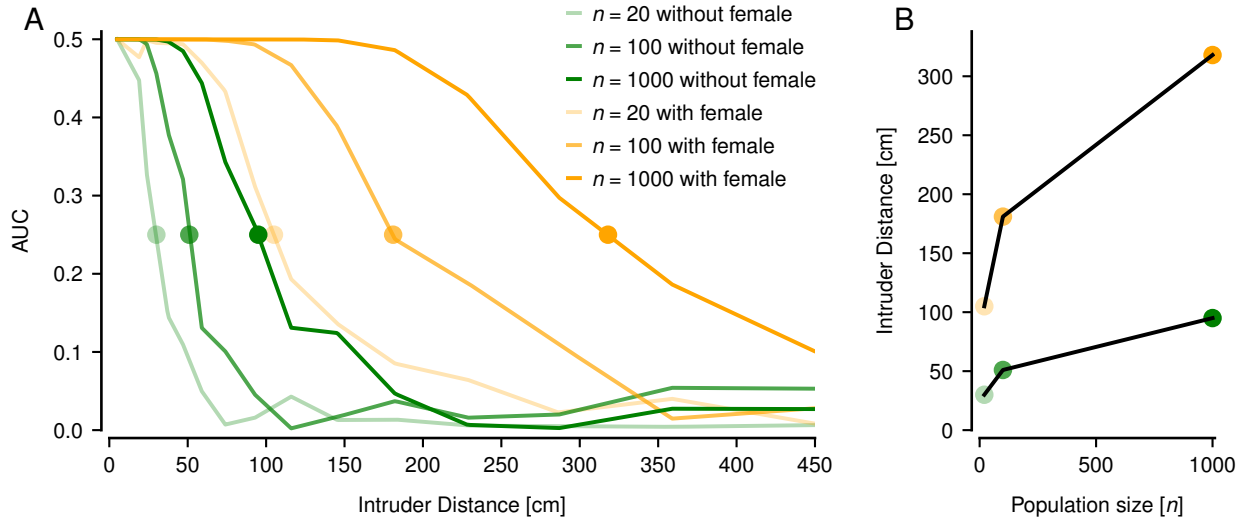

Figure 5.6: The intruder detection without the female (green) and with the female (orange), for different homogeneous P-unit population sizes. AUC values are based on $\Delta f_{\text{Female}} = 98\,\text{Hz}$ and $\Delta f_{\text{Intruder}} = 36\,\text{Hz}$. The model has the cell identifier 2013-01-08-aa (see table 2.1 for model parameters).
A Intruder detection for different homogeneous population sizes.
B The intruder distances with a 0.25 AUC value in A are plotted for different population sizes n (the circles in A correspond to the same-colored circles in B).

5.1.5 Detection improvement only at certain beat frequencies

So far only a beat frequencies combination, fulfilling the condition $|\Delta f_{\text{Female}}| + |\Delta f_{\text{Intruder}}| = f_{\text{Base}}$, was considered (Fig. 5.7 A). There an improved intruder detection (Fig. 5.7 A, top) was associated with nonlinear effects at $|\Delta f_{\text{Female}}| + |\Delta f_{\text{Intruder}}|$ in the P-unit firing rate (Fig. 5.7 A, bottom). For other beat frequencies, the presence of the female was in fact decreasing the intruder detection (Fig. 5.7 B, top) with no nonlinearity at $|\Delta f_{\text{Female}}| + |\Delta f_{\text{Intruder}}|$ in the P-unit firing rate (Fig. 5.7 B, bottom).

When calculating the difference between the AUC intruder detection with and without female ($\text{AUC}_{\text{Female}} - \text{AUC}_{\text{NoFemale}}$, see methods section 2.10.3), at most beat frequencies the

intruder detection is decreased by the presence of the female (blue) and only at some beat frequencies the intruder detection is increased by the female presence (red, Fig. 5.7 C). To understand this pattern the intruder detection (Fig. 5.7 C) can be compared with the second-order susceptibility of a low-CV P-unit model with a similar mean baseline firing rate f_{Base} that was presented in chapter 4 (Fig. 4.5 B). The red diagonal of improved intruder detection (highlighted with 1 in Fig. 5.7 C), that is associated with a nonlinear peak at $|\Delta f_{\text{Female}}| + |\Delta f_{\text{Intruder}}|$ in the P-unit response (Fig. 5.7 A, bottom), can be explained by the diagonal in the upper right quadrant in the second-order susceptibility matrix, that characterizes the nonlinearity at the sum of the input frequencies (Fig. 4.5 B). The other red diagonal of improved intruder detection (highlighted with 3 in Fig. 5.7 C) has no corresponding diagonal in the upper right quadrant in the second-order susceptibility matrix (Fig. 4.5 B). Instead, the improved intruder detection can be explained, when mirroring the second-order susceptibilities values on the x-axis from the lower right quadrant to the upper right quadrant, as has been described by Schlungbaum and Lindner (2023). In the lower right quadrant, the second-order susceptibility is characterized at the difference of the input frequencies. Accordingly, the nonlinearity at the difference of the two beat frequencies $||\Delta f_{\text{Female}}| - |\Delta f_{\text{Intruder}}||$ in the P-unit firing rate is the driving force of the improved intruder detection at the diagonal marked with 3 (not shown).

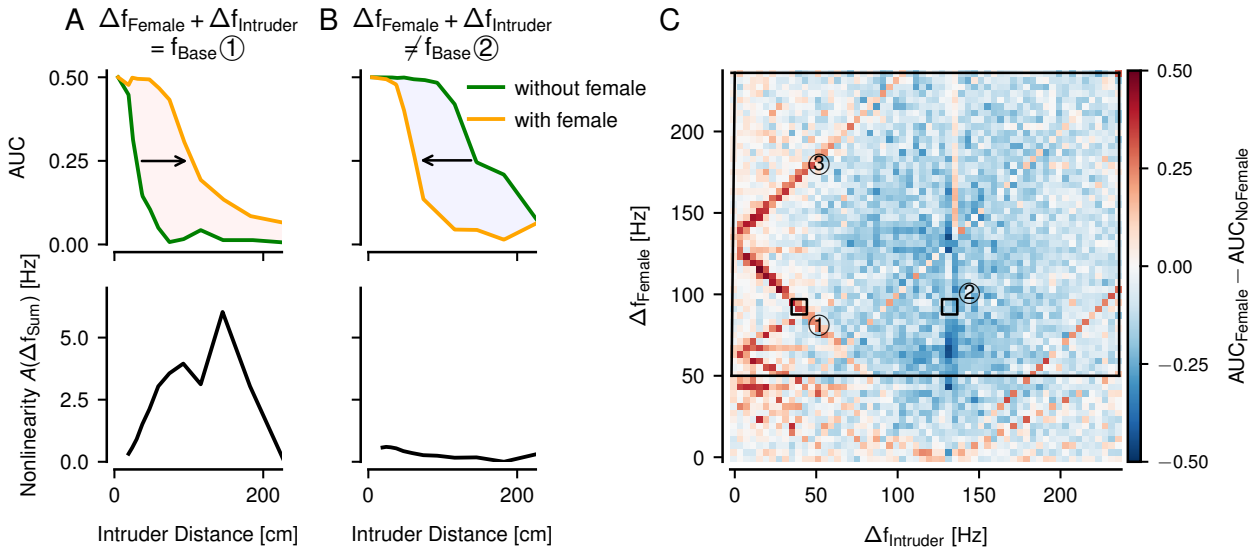

Figure 5.7: The intruder detection can be improved or deteriorated by the presence of the female depending on the beat frequencies. The intruder detection pattern can be explained with the second-order susceptibility (Fig. 4.5 B). The model has the cell identifier 2013-01-08-aa (see table 2.1 for model parameters).

A–B Top: Intruder detection. Bottom: Nonlinearity $A(\Delta f_{\text{Sum}})$, measured as the amplitude of the sum frequency $|\Delta f_{\text{Female}}| + |\Delta f_{\text{Intruder}}|$ peak in the power spectrum of the P-unit firing rate (see methods section 2.10.4).

A The condition $|\Delta f_{\text{Female}}| + |\Delta f_{\text{Intruder}}| = f_{\text{Base}}$ holds. $\Delta f_{\text{Female}} = 98\,\text{Hz}$, $\Delta f_{\text{Intruder}} = 36\,\text{Hz}$, $f_{\text{Base}} = 134\,\text{Hz}$.

B The condition $|\Delta f_{\text{Female}}| + |\Delta f_{\text{Intruder}}| \neq f_{\text{Base}}$ holds. $\Delta f_{\text{Intruder}} = 134\,\text{Hz}$, $\Delta f_{\text{Female}} = 98\,\text{Hz}$.

C The intruder detection change induced by the female presence ($\text{AUC}_{\text{Female}} - \text{AUC}_{\text{NoFemale}}$, see method section 2.10.3). The values are based on an intruder distance of 70 cm. Red – intruder detection improved by the presence of the female. Blue – intruder detection decreased by the female presence. The behaviorally relevant frequency combinations for the electrosensory cocktail party problem are inside the big black square. The small black squares with the numbers 1 and 2 highlight the beat frequencies examples from panel A and B.

5.1.6 Detection improvement in low-CV cells

The behaviorally important frequencies for the electrosensory cocktail party problem are highlighted by the black square in Fig. 5.7 C. The intruder detection improved by the presence of the female (red) is associated with the mean baseline firing rate of the cell ($f_{\mathrm{Base}} = 134\,\mathrm{Hz}$), with the black square not being completely covered in red in a single cell. Integrating from a heterogeneous P-unit population with different mean baseline frequencies f_{Base} (50–450 Hz, Grewe et al., 2017; Hladnik and Grewe, 2023) might potentially cover the area relevant for the electrosensory cocktail party (black square), by a vertical displacement of the red diagonals for different f_{Base}. In the following a population analysis of 42 heterogeneous LIF model P-units, fitted to the baseline characteristics of recorded P-units, will be presented (see table 2.1 for model parameters). The sample is representative considering the CVs of P-units but it does not include bursty cells. For each cell in the population, the intruder-induced beat was equal to $0.3\,f_{\mathrm{Base}}$ and the female-induced beat was equal to $0.7\,f_{\mathrm{Base}}$, with $|\Delta f_{\mathrm{Female}}| + |\Delta f_{\mathrm{Intruder}}|$ being equal to f_{Base} for each cell.

In this population, low-CV P-units had stronger nonlinear effects (Fig. 5.8 A). Only the low-CV P-unit cell with strong nonlinearity had an intruder detection improved by the presence of the female (upper right corner in Fig. 5.8 B, see method section 2.10.3 for description of $\mathrm{AUC}_{\mathrm{Female}} - \mathrm{AUC}_{\mathrm{NoFemale}}$).

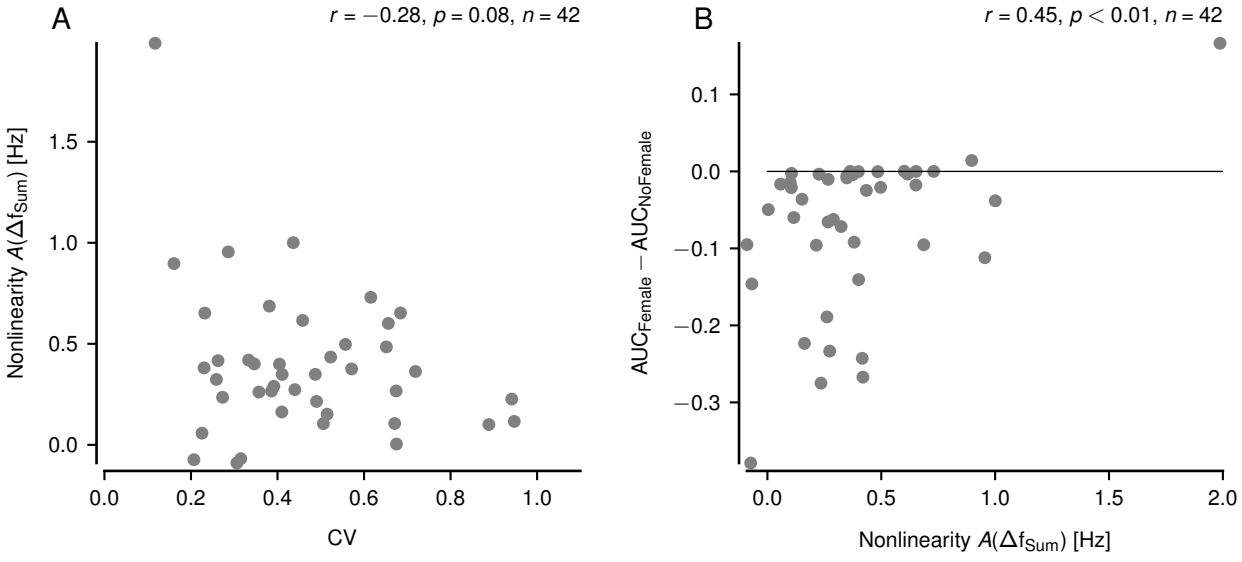

Figure 5.8: Population analysis of 42 P-unit LIF models (see table 2.1 for model parameters). For each cell in the population, the intruder-induced beat was equal to $0.3\,f_{\mathrm{Base}}$ and the female-induced beat was equal to $0.7\,f_{\mathrm{Base}}$, with $|\Delta f_{\mathrm{Female}}| + |\Delta f_{\mathrm{Intruder}}|$ being equal to f_{Base} for each cell. The nonlinearity was calculated at an intruder contrast of 3%.
A Nonlinearity plotted against the CV during baseline. Nonlinearity $A(\Delta f_{\mathrm{Sum}})$, measured as the amplitude of the sum frequency $|\Delta f_{\mathrm{Female}}| + |\Delta f_{\mathrm{Intruder}}|$ peak in the power spectrum of the P-unit firing rate (see methods section 2.10.4).
B Intruder improved by the female presence ($\mathrm{AUC}_{\mathrm{Female}} - \mathrm{AUC}_{\mathrm{NoFemale}}$, see methods section 2.10.3) plotted against the nonlinearity $A(\Delta f_{\mathrm{Sum}})$. Black line – the female does not alter the intruder detection. Values above black line – the female improves the intruder detection. Values below black line – the female decreases the intruder detection.

5.2 Discussion

In this chapter, the neuronal basis of the electrosensory cocktail party has been addressed. It was investigated how a receiver can detect and chase away a faint intruder at distances up to 180 cm, despite the presence of a strong and nearby female (Fig. 1.20). It was derived in a low-CV homogeneous P-unit model population, that the intruder detection can be improved by the presence of a female at specific intruder-female beat frequencies beyond intruder distances of 180 cm. This improved intruder detection was mediated by nonlinear effects appearing when the sum or the difference of the two beat frequencies was equal to the mean baseline firing rate f_{Base}. This chapter provided the potential behavioral implication of the nonlinear effects characterized in chapter 4.

5.2.1 Nonlinear effects mediate intruder detection

In the following, the influence of nonlinear effects on intruder detection will be discussed.

Improved faint signal detection in previous literature

In this chapter, it was demonstrated that the intruder detection improved by the presence of the female is mediated by nonlinear effects (Fig. 5.5, Fig. 5.7, Fig. 5.8). The here used ROC method was adapted based on previous work, where it has already been demonstrated that nonlinear effects at the sum and the difference of the input frequencies can lead to an improved faint signal detection despite the presence of a jamming signal (Schlungbaum and Lindner, 2023). There, the improved detection could be explained with the theory of weakly nonlinear interactions (Voronenko and Lindner, 2017). In both works (Schlungbaum and Lindner, 2023; Voronenko and Lindner, 2017) the driving force for the LIF models was the whole signal. In this chapter, it could be demonstrated with a LIF P-unit model, where the input was an amplitude-modulated EOD carrier, that the findings of the previous works were still valid.

Bursting enhances nonlinearity and might improve intruder detection

The nonlinear effects, improving the intruder detection, correspond to the nonlinear effects characterized in chapter 4. There nonlinear effects were found not only for low-CV cells but also in bursty high-CV cells, with bursting being identified as a factor influencing the nonlinearity at frequencies relevant for the electrosensory cocktail party (Fig. 4.8). If both frequencies were low, the nonlinearity was increased, but if one of the frequencies was higher the nonlinearity could be decreased or increased by bursting. Since those decrease frequencies were usually beyond the range relevant for the electrosensory cocktail party problem (black square in Fig. 5.7), bursting might overall contribute to an improved intruder detection by enhancing nonlinear effects. Although the P-unit model population used in this chapter, properly depicted the CV and the mean baseline firing rate f_{Base} of P-units (Grewe et al., 2017; Hladnik and Grewe, 2023) it did not contain bursty P-units. The influence of bursting on faint intruder detection should be tested in further studies.

Neuronal delays might deteriorate nonlinear effects

A potential restriction of the analysis in this chapter is that all stimulus repeats in a population started with the same phase. In previous works (Hladnik and Grewe, 2023) it was demonstrated in P-units that depending on the receptor position, the same signal arrives with different delays at the target neurons, thus deteriorating the stimulus encoding, with higher frequencies being affected stronger than lower frequencies. The high mean baseline frequencies f_{Base} of P-units

(up to 400 Hz) might be especially affected by such neuronal delays. How neuronal delays influence nonlinear effects and intruder detection should be tested in further studies.

Encoding of secondary envelopes during the electrosensory cocktail party

In a three-fish setting, the two generated beats are often slowly modulated at the difference between the two beat frequencies $||\Delta f_1| - |\Delta f_2||$, known as secondary or social envelope (Stamper et al., 2012). The encoding of social envelopes can be attributed to P-units with stronger nonlinearities, lower firing rates and higher CVs (Savard et al., 2011). Besides that, low-frequency secondary envelopes are extracted downstream of P-units in the ELL (Middleton et al., 2006) utilizing threshold nonlinear response curves of the involved neuron (Middleton et al., 2007). This encoding of secondary envelopes at downstream processing stages in the primary sensory afferent pathway might contribute to the solution of the electrosensory cocktail party problem (Henninger et al., 2018).

5.2.2 Readout from P-unit populations

In the following, the readout from P-units in *Apteronotus leptorhynchus* and its consequences for intruder detection in homogeneous and heterogeneous populations will be discussed.

Readout of sensory information in the ELL

There are about 8000 P-units on each side of the body of the fish (Carr et al., 1982). Each P-unit trifurcates and projects to pyramidal cells in three topographically organized maps in the cerebellar-like electrosensory lateral line lobe (ELL, Carr et al., 1982; Krahe and Maler, 2014; Maler, 2009). The centromedial segment (CMS) is the map with the highest number of pyramidal cells ($n \approx 2800$), the smallest receptive field size ($n \approx 20$ P-units) and the smallest receptive fields overlap of 5 % (Maler, 2009). The centrolateral segment (CLS) has fewer pyramidal cells ($n \approx 1400$), bigger receptive fields ($n \approx 100$ P-units), and a receptive fields overlap of approximately 22 %. The lateral segment (LS) is the segment with the least pyramidal cells ($n \approx 900$), with the largest receptive fields ($n \approx 1000$ P-units) and a receptive field overlap of approximately 50 % (Maler, 2009). A fourth segment in the ELL, the medial segment, receives input from ampullary cells (Heiligenberg and Dye, 1982; Krahe and Maler, 2014). All four segments have a similar laminar structure with a deep fiber layer (DFL) with primary electrosensory afferents, a granular cell layer (GCL) with interneurons, a pyramidal cell layer (PCL) and a molecular layer where pyramidal cells receive feedback from granule cells (Berman and Maler, 1998; Krahe and Maler, 2014).

Pyramidal cells can reliably extract features as up- and down-strokes of random amplitude modulations (Gabbiani et al., 1996; Oswald et al., 2004) and can be subdivided into two major classes: E-cells that are excited by an increase in EOD amplitude and I-cells that are excited by a decrease in EOD amplitude. E-cells receive direct input from P-units and I-cells receive disynaptic input from P-units via interneurons (Berman and Maler, 1998). E-cells in the CMS and I-cells from all segments low-pass filter the input signal (Krahe et al., 2008). There is a stimulus-dependent switch in E-cells in the CLS, with a low-pass filter for prey signals and a high-pass/band-pass filter for signals in a communication context (Krahe et al., 2008). In E-cells in the LS, the signal is high-pass filtered (Krahe et al., 2008).

The PCL can be subdivided into a superficial, an intermediate, and a deep layer. Cells in the superficial layer have large apical dendrites (Bastian and Courtright, 1991), low firing rates, high-CVs, are bursty (Bastian and Courtright, 1991), very nonlinear (Chacron, 2006) and have a center-surround organization of the receptive field (Bastian et al., 2002). Cells in the intermediate layer are intermediate considering their apical dendrites extent (Bastian and

Courtright, 1991), firing rates, CVs, bursting (Bastian and Courtright, 1991) and nonlinearity (Chacron, 2006) and have a center-surround organization of the receptive field (Bastian et al., 2002). Cells in the deep layer have small apical dendrites (Bastian and Courtright, 1991), high firing rates, low-CVs, are not bursty (Bastian and Courtright, 1991), mostly linear (Chacron, 2006) and have no center-surround organization of the receptive field (Bastian et al., 2002). A receptive field can be stimulated with a local stimulus, e.g. a prey signal, or with a global stimulus, mimicking the communication context. Superficial cells mostly encode local stimuli, and cells in the intermediate and deep layers encode both local and global stimuli (Bastian et al., 2002).

A single P-unit trifurcates to the three segments (CMS, CLS, LS), providing the same information to a column in all three layers, each containing a pair of E-cells and I-cells.

The intruder detection beyond 180 cm is possible with large homogeneous populations with the size of 100 or 1000 P-units

In this chapter, it was demonstrated in homogeneous P-unit model populations (same CV and f_{Base}) that intruder detection can be improved by the female presence beyond intruder distances of 180 cm (Fig. 5.6).

A distance of 180 cm is sufficient to explain intruder attacks observed in the field (Fig. 1.20), still the distance estimation in this chapter might be biased by several factors, described in the following paragraph. The input to the here used P-unit model is the field strength of the intruder, which has to be recalculated to a distance, to be meaningful in the context of the electrosensory cocktail party problem. In the case of an ideal dipole, the field potential decays with distance squared (see methods section 2.14.3, Henninger et al., 2020). Due to the properties of the terrain, e.g. the shallowness of the rivers, the field decay is usually not described by an ideal dipole but decays with a power smaller than two (Benda, 2020; Henninger et al., 2020; Fotowat et al., 2013). Besides that, the field decay is influenced by fish movement (Fotowat et al., 2013) or water conductivity (Henninger et al., 2020). In this chapter, the field-distance relationship was based on a dipole function where the free parameters were fitted to the data recorded in the field (Henninger et al., 2020). How the field-distance relationship and the population size required for a certain intruder detection are influenced by fish movement, changes in the river terrain, or water conductivity should be the subject of further studies.

In this chapter, it was demonstrated in homogeneous P-unit model populations that intruder detection can be improved by the female presence beyond intruder distances of 180 cm for populations with size $n = 100$ and $n = 1000$ (Fig. 5.6). The different population sizes, used in Fig. 5.6, mimic the receptive field sizes of different segments in the ELL with $n = 100$ corresponding to the receptive fields in the CLS and $n = 1000$ to receptive fields in the LS. The large receptive fields in the LS are optimal for the encoding of global communication signals. There, the intruder detection might be processed at intermediate and deep layers, which preferentially encode global stimuli, mediated by their weak center-surround receptive field organization (Bastian et al., 2002). It is known from previous literature, that a larger population size can be associated with a better stimulus encoding performance (Hladnik and Grewe, 2023).

The readout from P-units in pyramidal cells is heterogeneous

The findings in Fig. 5.6 are based on a low-CV P-unit model and might require a selective readout from a homogeneous population of low-CV cells to sustain. Since a receptive field is defined as a patch of adjacent receptors on the fish surface (Maler, 2009) and P-units have heterogeneous baseline properties (CV and f_{Base}) that do not depend on the location of the receptor on the fish body (Hladnik and Grewe, 2023) as a result each pyramidal cell in the

ELL will integrate over a heterogeneous and not homogeneous P-unit population. The center-surround receptive field organization of superficial and intermediate layer pyramidal cells in addition increases this heterogeneity of the integrated population. Heterogeneous populations with different baseline properties can be more advantageous for the encoding compared to homogeneous populations, as has been shown in P-units and models (Beiran et al., 2018; Hladnik and Grewe, 2023).

A heterogeneous readout might be not only physiologically plausible but also required to address the electrosensory cocktail party for all female-intruder combinations. In this chapter, the improved intruder detection was present only for specific beat frequencies (Fig. 5.7), corresponding to findings from previous literature (Schlungbaum and Lindner, 2023). If pyramidal cells would integrate only from P-units with the same mean baseline firing rate f_{Base} not all female-male encounters, relevant for the context of the electrosensory cocktail party, could be covered (black square, Fig. 5.7 C). Only a heterogeneous population with different f_{Base} (50–450 Hz, Grewe et al., 2017; Hladnik and Grewe, 2023) could lead to a vertical displacement of the improved intruder detection (red diagonals in Fig. 5.7 C). Weather integrating from such a heterogeneous population with different f_{Base} would cover this behaviorally relevant range in the electrosensory cocktail party should be addressed in further studies.

Although a heterogeneous population analysis was conducted in this chapter, with 42 model cells, the population size was not sufficient to systematically test different readout strategies from heterogeneous populations in the CLS ($n = 100$) or the LS ($n = 1000$). Although the CV and f_{Base} were represented properly in this population analysis, the population did not contain bursty cells. How the improved intruder detection could be read out from a large heterogeneous P-unit population with bursty cells and with different CVs and f_{Base} should be the subject of further studies.

5.2.3 Prerequisites for electrophysiological P-unit recordings for a ROC analysis

The improved intruder detection, demonstrated in this chapter, was based only on P-unit models and no electrophysiological P-unit data was presented. The utilized models were fitted to the baseline characteristics of recorded P-units and have been demonstrated to accurately predict the firing rate of P-units for a wide range of beat frequencies (Barayeu et al., 2023). In addition, the nonlinearities, necessary for improved intruder detection, were characterized in chapter 4 in models and in recorded P-units. Therefore, it is likely that an improved intruder detection would also be found once P-units are electrophysiologically recorded.

Several factors have to be considered for successful recordings for a detection analysis, such as the minimal recording duration for statistically significant ROC curves, measuring at the right beat frequencies, and in the right P-unit population (low-CV or bursty cells). How these factors can be implemented experimentally will be discussed in the following paragraphs.

Increasing recording duration leads to more data but to reduced data quality

A long recording duration in an experiment has the advantage that it allows for the acquisition of big data amounts. Still, it is problematic, since primary sensory afferents in weakly electric fish often slightly change their firing properties over time. The intuition is that due to small movements of the fish or the set-up, as the vibration in the building or room, the electrode and the cell might be slightly displaced in relation to each other, leading to firing rate changes. During P-unit recordings, the maximal positive voltage excursions of spikes, are usually captured accurately, while the minimal voltage values are limited by a noise floor. A P-unit recording can have spikes with larger and smaller voltage excursions. Displacement of

the electrode can lead to an increase of the noise floor with the smaller spikes gradually descending into the noise floor, reducing the recorded spike numbers and leading to a decreased mean baseline firing rate f_{Base}. For some analyses, e.g. the encoding of high beat frequencies in chapter 3, changes in f_{Base} are not crucial for the main findings. For the second-order susceptibility, which can depend on f_{Base} of the cell, changes in f_{Base} might be very important for the conclusion. The intruder detection, mediated by nonlinear effects, might also be sensitive to such recording quality changes. Before the experiment, the protocols should be designed to optimize the trade-off between the recording duration necessary for significant ROC curves and the minimal duration for the best recording quality.

Searching nonlinearities at the burst-corrected firing rate

Since the recording duration of electrophysiologically recorded P-units is limited, it is impossible to measure all possible female-intruder beat combinations (as in Fig. 5.7 C) in a single experiment with pure sine-wave stimulation. Thus the nonlinear beat frequencies of interest should be identified before such recording. In chapter 4 the nonlinear interactions of non-bursty low-CV P-units and bursty high-CV P-units were found to depend on the burst-corrected mean baseline firing rate $f_{BaseCorrected}$ (see methods section 2.9.1, Fig. 4.9 $\mathsf{A_{iv}}$). If $f_{BaseCorrected}$ is calculated as the mean of the burst-corrected spikes, the burst threshold has to be estimated. In previous literature burst spikes have been defined as spikes separated by less than 1.5 EOD periods (Chacron et al., 2004; Metzen et al., 2016). In this work, it was demonstrated that the bimodal ISI distribution is sometimes better separated by a threshold of 2.5, 3.5 or even more EOD periods. Alternatively $f_{BaseCorrected}$ can be identified as the strongest peak in the baseline power spectrum (Fig. 4.7 $\mathsf{A_i}$, right).

One of the two mentioned $f_{BaseCorrected}$ calculations should be applied online during an experiment. Then the according beat frequencies prone to nonlinearity can be estimated based on the second-order susceptibility structure in Fig. 4.5 B. Note that it is reasonable only to consider low-CV or bursty high-CV cells for the ROC recording since only these cells are expected to exhibit such strong nonlinear effects (see chapter 4).

The stimulus phase might be relevant for a population analysis

The ROC detection method (Schlungbaum and Lindner, 2023) requires a population with a size of at least $n > 1$. The intuition behind this is, that the firing rate calculated based on a single spike train has similar maxima and minima, which would result in no intruder detection for any intruder distances. The stimulus repeat number used for the ROC analysis mimics the receptive field size of pyramidal cells in the different ELL segments (CMS: $n = 20$, CLS: $n = 100$, LS: $n = 1000$, Maler, 2009). Since the nonlinear effects appearing in relation to f_{Base} can be rather fast oscillations (up to 450 Hz, Grewe et al., 2017; Hladnik and Grewe, 2023), slightly temporally displaced stimulus repeats might lead to a loss of these nonlinear effects. At first glance, stimulus alignment does not seem to be a problem during experiments, since the same stimulus can just be repeated several times in a P-unit recording. Still, the final signal, arriving at the electroreceptors of the fish, is the superposition of this stimulus with the EOD of the fish. The phases of the resulting beats and of the secondary envelope in the superimposed signal are influenced by the stimulus and the EOD phase, and both should be controlled in further P-unit recordings.

5.2.4 Electrosensory cocktail party problem for different species and cells

Although the electrosensory cocktail party was initially observed in the species *Apteronotus rostratus* (Henninger et al., 2018) such scenarios are conceivable for most weakly electric fish species and can be relevant for *Apteronotus leptorhynchus*, which can usually be found in groups of 2 (Stamper et al., 2010), and for *Eigenmannia virescens*, usually found in groups of 3–5 (Tan et al., 2005). As long as among the cells encoding the social context there are low-CV cells (as in *Eigenmannia virescens*) or bursting cells (as in *Apteronotus leptorhynchus*), the species might benefit from the improved intruder detection presented in this chapter. The findings of this chapter can be applied to problems beyond any communication context e.g. be relevant for prey detection in ampullary cells (Engelmann et al., 2010; Neiman and Russell, 2011), which also exhibit strong nonlinear effects (Fig. 4.3).

The here presented problem is reminiscent of the cocktail party problem (Cherry, 1953; Haykin and Chen, 2005; McDermott, 2009), a sound source separation problem described in humans, where a speech signal has to be separated from a noisy background. If this background signal contains several speakers the signal will be similar to a white noise signal (McDermott, 2009). In the previous chapter, it was demonstrated that nonlinear effects decrease with increasing noise amplitudes (Fig. 4.2, Fig. 4.6). These findings imply that the nonlinear effects and improved signal detection found in this chapter might decrease the noisier the environment during the cocktail party problem in human listeners. How exactly nonlinear effects influence the cocktail party in humans might be addressed in future studies.

5.2.5 Conclusion

In this chapter the neuronal basis of the electrosensory cocktail party (Henninger et al., 2018) was addressed. It was investigated how a receiver can detect and chase away a faint intruder despite the presence of a strong and nearby female at intruder distances up to 180 cm. It was demonstrated in a low-CV homogeneous P-unit model population, mimicking the receptive fields of the next-connected neurons, that the female presence can lead to an improved intruder detection, beyond intruder distances of 180 cm. This improvement was mediated by nonlinear effects, characterized in chapter 4. This chapter provided a potential behavioral benefit of those nonlinearities, stressing their relevance for weakly electric fish. The improved intruder detection was present only at specific intruder-female combinations and a heterogeneous readout in next-connected neurons would be required to cover the whole for the electrosensory cocktail party behaviorally relevant range. Whether the improved intruder detection would be sustained in heterogeneous P-unit populations, should be tested in further studies.

Chapter 6

Encoding of strong beat amplitudes

In the previous chapters, the focus was on fish encounters leading to intermediate beat amplitudes (as the female in the electrosensory cocktail party, Fig. 1.17 B) or faint beat amplitudes (as the intruder in the electrosensory cocktail party, Fig. 1.17 A). In the following the beat amplitude will be expressed as a contrast, where the EOD of the encountered fish is a percentage of the receiver fish's EOD. In previous works, the behaviorally relevant beat contrasts of *Apteronotus leptorhynchus* have been measured by recording the transdermal potential of freely swimming fish when they encountered another conspecific (Fotowat et al., 2013). During 70 % of all two-fish encounters the beat contrasts were below 20 %. These findings verified that the usually used 10–20 % contrasts in electrophysiological recordings are reasonable from a behavioral perspective (Fig. 1.17 B, Walz et al., 2014; Barayeu et al., 2023). Besides that, it was demonstrated that beat contrasts can reach 100 % in freely swimming fish (Fig. 1.17 D, Fotowat et al., 2013). The field strength of different individuals of the species *Apteronotus rostratus* can vary between 1.4–5.1 mV (Henninger et al., 2018), implying that if the receiver produces a weaker field than the encountered fish the contrast would exceed 100 %. In such a scenario the beat amplitude would not anymore be defined to the encountered fish EOD size, but to the receiver EOD size. How high contrasts are encoded in P-units is the subject of the following chapter.

The encoding of strong amplitude modulations has been addressed in P-units in several studies (Xu et al., 1996; Gussin et al., 2007; Benda et al., 2005; Nelson et al., 1997). The response of P-units to different EOD amplitudes (Fig. 6.1 A, see methods section 2.11.1) can be measured by increasing the amplitude of the EOD in steps (top) and observing changes in the spike response (middle) or the mean firing rate (bottom). P-units react with a strong initial response to the onset of the step (red, 7–55 ms). When the step is still on, P-units adapt to a steady-state response (green, 330–390 ms). After the step stimulus is switched off, P-units again react with a strong onset response in their firing rate (400–420 ms). The baseline firing rate of P-units is restored as a steady-state response after some time has passed (420–500 ms). P-units react with an increase in their firing rate to positive steps and with a decrease to negative steps. The response of P-units to different step stimuli is captured in the Frequency-Intensity (F-I) curves, which depict the mean firing rate onset-state response curve (red) and the mean steady-state response curve (green) for different step amplitudes (Fig. 6.1 B, Benda et al., 2005). This example P-unit saturates at contrasts of 30 % (Fig. 6.1 B) but the F-I curves of different P-units can saturate at contrasts between 10–30 % (Gussin et al., 2007; Benda et al., 2005). P-units increase their mean firing rate to stronger beat amplitudes, with a saturation after a certain beat amplitude has been reached (Nelson et al., 1997). Strong beat amplitudes, beyond the saturation of single P-units, are encoded with changes in the form of the firing rate, leading to clipping to a minimal and maximal firing rate value (Nelson et al., 1997).

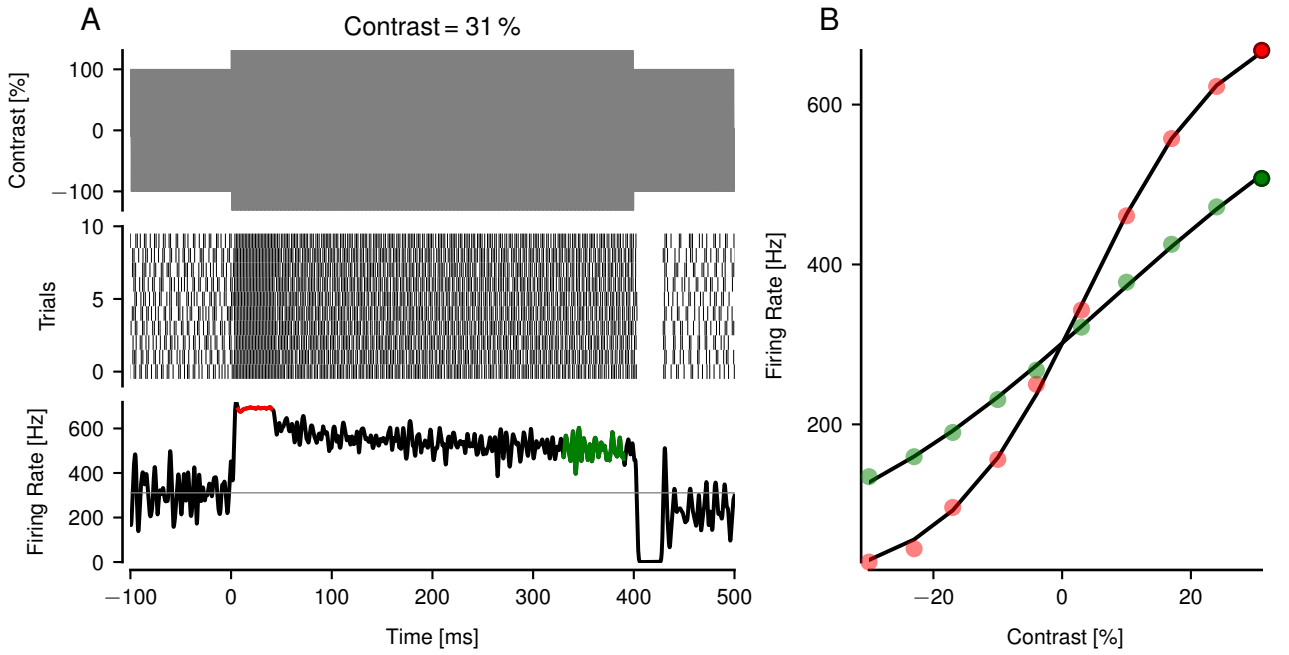

Figure 6.1: Frequency-Intensity (FI) curves in response to step stimuli in an electrophysiologically recorded P-unit.
A Top: Step increase of the EOD amplitude. Middle: Spikes trains in response to the step stimulus above. Bottom: Mean firing rate, based on the spikes above. Red – onset-state response. Green – steady-state response. Gray line – mean baseline firing rate, before the step stimulus onset.
B Onset-state response curve (red markers) and steady-state response curve (green markers). The outlined markers at 31 % correspond to the example in A.

How a wide dynamic range (as 0.001–100 % contrasts in weakly electric fish) can be encoded in a neuronal system is known as the dynamic range problem and found in most sensory modalities, as in the auditory system with a wide range of different sound pressure levels (Evans, 1981; Preyer and Gummer, 1996; Liberman, 1982) or in the visual system with many log units of luminance (Pugh Jr et al., 1999; Barlow et al., 1957). Nervous systems solve this problem by employing different mechanisms as the sound pressure compression of outer hair cells (Preyer and Gummer, 1996), heterogeneous populations in auditory nerve fibers (Liberman, 1982), sensitivity changes inside photoreceptors (Pugh Jr et al., 1999), changes in receptive field size on the retina (Barlow et al., 1957), or a match between the sensitivity of a cell and the natural statistics of the visual scene (Laughlin, 1981).

When the dynamic range problem of beat amplitudes is investigated in weakly electric fish, it has to be considered that the field around the fish consists of several components as the EOD of the receiver with frequency f_{EOD}, the EOD of the encountered fish with stimulus frequency f_{stim}, and the resulting beat with difference frequency $\Delta f = f_{stim} - f_{EOD}$. P-units can simultaneously represent all these frequencies in their firing rate (Sinz et al., 2020, Fig. 3.1). P-units probabilistically phase-lock to the EOD of the receiver, firing at a similar phase, but not at every EOD cycle, resulting in a multimodal ISI histogram with maxima at integer multiples of the EOD period (Fig. 1.15 B, left). P-units are tuned to the fish's own EOD frequency, as has been shown by silencing the EOD of the fish and probing the P-unit response to varying artificial EOD frequencies (Hopkins, 1976, Fig. A.3 A). The corresponding band-pass filter is assumed to be caused by electric resonance in the electroreceptor cells (Viancour, 1979). The representation of f_{EOD} in the firing rate of P-units is usually not subject in current weakly electric fish studies since the EOD amplitude is assumed to be long-term stable. Still, when

the field size of the encountered fish increases the relative EOD size of the receiver in the compound stimulus decreases. If both fish are very close, the EOD of the encountered fish can be even stronger than the EOD of the receiver. How different beat amplitudes influence the f_{EOD} representation in the firing rate of P-units will be investigated in this chapter.

The dynamic range problem in P-units becomes even more complicated if the three-fish setting as in chapter 5 is considered. In a three-fish scenario, the receiver with EOD frequency f_{EOD} on one hand encounters a fish with EOD frequency f_1, leading to a beat with beat frequency Δf_1 and a contrast c_1 and on the other hand encounters a fish with EOD frequency f_2, leading to a beat with frequency Δf_2 and a contrast c_2. How can both beats be represented in the firing rate of P-units for a wide range of beat contrasts? In the auditory system, the encoding of two tones with varying amplitudes has been investigated in the framework of two-tone suppression, the suppression of one tone in the neuronal system in the presence of another tone (Sachs and Kiang, 1968; Ruggero et al., 1992; Arthur et al., 1971; Jülicher et al., 2001). Similar effects have been demonstrated in psycho-acoustical masking experiments where a beat masker reduced the detectability of another beat (Millman et al., 2002; Dau et al., 1997; Ewert and Dau, 2000), leading to two-beat suppression. Such two-beat suppression has so far not been addressed in electrosensory afferents.

In this chapter, the influence of a wide dynamic range of beat contrasts on the representation of the two beat frequencies and the EOD frequency f_{EOD} will be investigated in LIF P-unit models and electrophysiologically recorded P-units.

6.1 Results

6.1.1 Two-beat suppression in a LIF P-unit model

In a three-fish scenario, the receiver with EOD frequency f_{EOD} encounters one fish with frequency f_1 (beat frequency Δf_1 and contrast c_1, Fig. 6.2 $\mathsf{A_i}$, top) and a second fish with EOD frequency f_2 (beat frequency Δf_2 and contrast c_2, Fig. 6.2 $\mathsf{A_{ii}}$, top). Two-beat suppression will be investigated in the P-unit LIF model by comparing the P-unit response between the one-beat conditions, where two fish are present ($f_{EOD}\&f_1$ in Fig. 6.2 $\mathsf{A_i}$, and $f_{EOD}\&f_2$ in Fig. 6.2 $\mathsf{A_{ii}}$), and the two-beat condition, where three fish are present ($f_{EOD}\&f_1\&f_2$, Fig. 6.2 $\mathsf{A_{iii}}$). In the one-beat conditions, the P-unit firing rate does not saturate, neither for the faint and slow Δf_1 beat (Fig. 6.2 $\mathsf{A_i}$, third row) nor for the stronger and faster Δf_2 beat (Fig. 6.2 $\mathsf{A_{ii}}$, third row). Even if both beats are present simultaneously, the firing rate is still not saturated, with no limitation to a maximal or minimal firing rate value (Fig. 6.2 $\mathsf{A_{iii}}$, third row). In this not-saturated scenario, no changes are observable in the Δf_1 peak size in the power spectrum of the P-unit firing rate, between the one-beat condition and the two-beat condition (compare brown and red markers in Fig. 6.2 A). The Δf_2 peak size is only slightly decreased in the power spectra between the one-beat and the two-beat condition (compare blue and cyan markers in Fig. 6.2 A).

The situation changes when the c_1 contrast increases and the P-unit firing rate starts to saturate, as can be seen by the limitation of the firing rate to a minimal value of 0 Hz (Fig. 6.2 $\mathsf{B_i}, \mathsf{B_{iii}}$, third row, Nelson et al., 1997). The Δf_1 peak amplitude, in the power spectrum of the firing rate, remains unaltered between its saturated one-beat and two-beat condition (compare brown and red markers in Fig. 6.2 $\mathsf{B_i}, \mathsf{B_{iii}}$), while the Δf_2 peak decreases in size from its not saturated one-beat condition to the saturated two-beat condition (compare blue and cyan markers in Fig. 6.2 $\mathsf{B_{ii}}, \mathsf{B_{iii}}$).

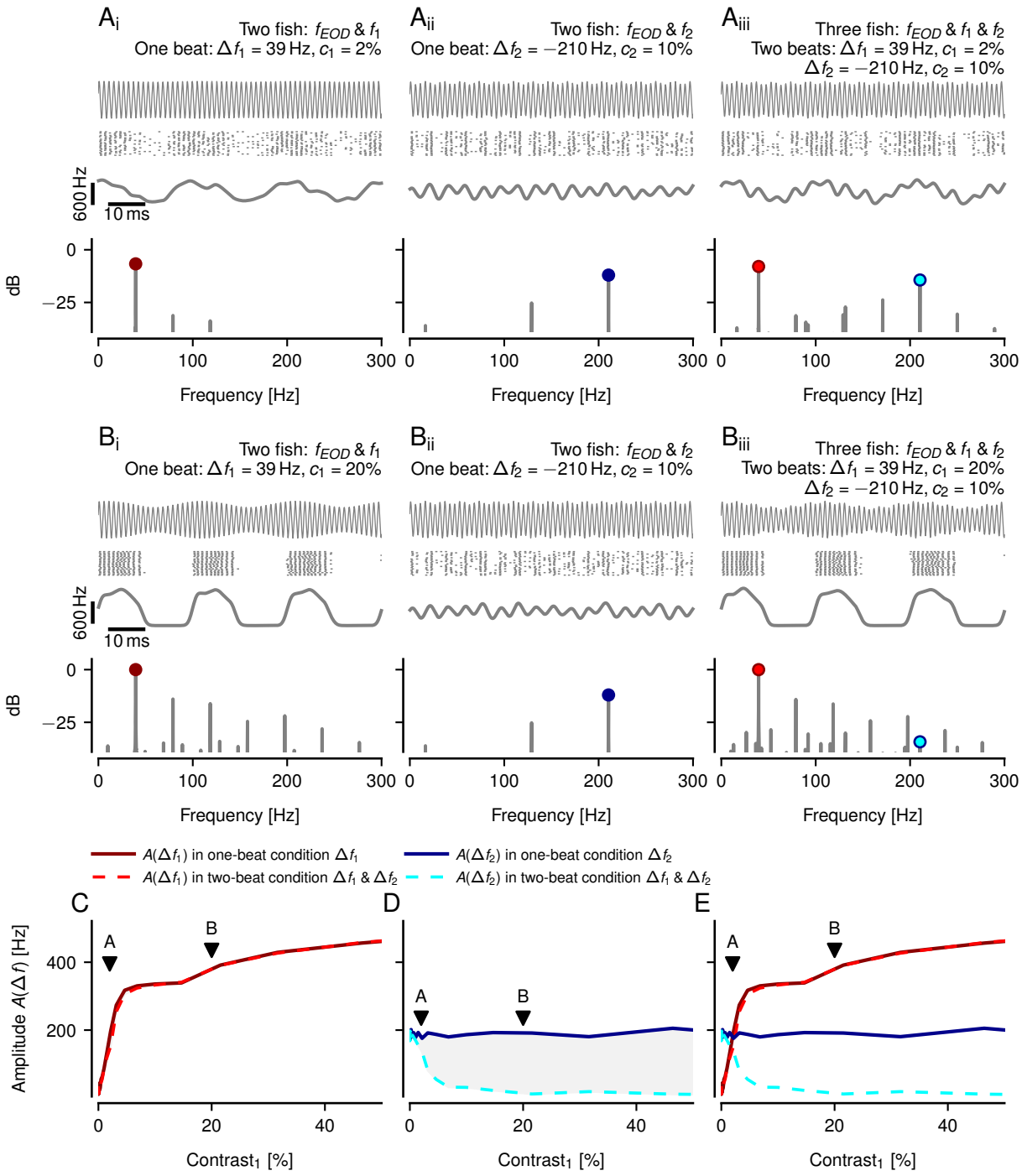

Figure 6.2: Response of a LIF P-unit model (2011-10-25-ad, see table 2.1 for model parameters) to different beat contrasts c_1. In this example only $A(\Delta f_2)$, the amplitude of Δf_2 in the power spectrum of the P-unit firing rate (see methods section 2.11.2), changes between the one-beat and two-beat condition (**E**).

A–B Top: EOD of the receiver plus the EODs of the other fish. Second row: Spike trains. Third row: Firing rate of the spike trains. Bottom: Power spectrum of the firing rate. Δf_1 is a low beat frequency, Δf_2 a high beat frequency and c_2 is an intermediate contrast.

A Low c_1 contrast.

A$_{\text{i}}$ One-beat condition: The receiver and a fish with EOD frequency f_1 are present.

A$_{\text{ii}}$ One-beat condition: The receiver and a fish with EOD frequency f_2 are present.

A$_{\text{iii}}$ Two-beat condition: The receiver and the fish with EOD frequencies f_1 and f_2 are present.

B Intermediate c_1 contrast.

C $A(\Delta f_1)$, amplitude of Δf_1 in the power spectrum of the firing rate, is plotted for varying c_1.

D $A(\Delta f_2)$, amplitude of Δf_2 in the power spectrum of the firing rate, is plotted for varying c_1.

E $A(\Delta f_1)$ and $A(\Delta f_2)$ are plotted for varying beat contrasts c_1.

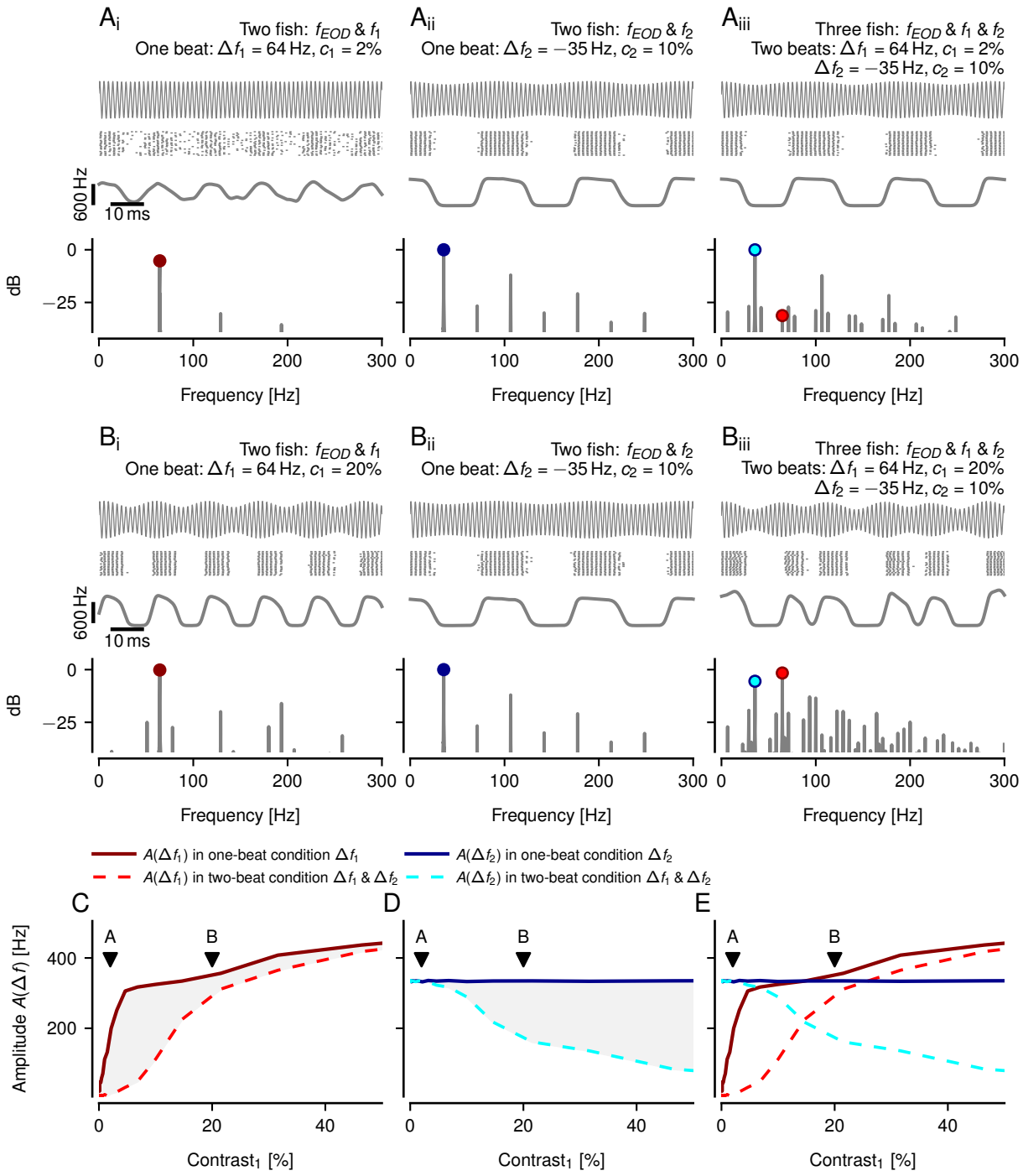

Figure 6.3: Response of a LIF P-unit model (2011-10-25-ad, see table 2.1 for model parameters) to different beat contrasts c_1. In this example $A(\Delta f_1)$ and $A(\Delta f_2)$ (see methods section 2.11.2) change between the corresponding one-beat and two-beat conditions (E).
A–B Top: EOD of the receiver plus the EODs of the other fish. Second row: Spike trains. Third row: Firing rate of the spike trains. Bottom: Power spectrum of the firing rate. Δf_1 and Δf_2 are low beat frequencies and c_2 is an intermediate contrast.
A Low c_1 contrast.
A$_{\text{i}}$ One-beat condition: The receiver and a fish with EOD frequency f_1 are present.
A$_{\text{ii}}$ One-beat condition: The receiver and a fish with EOD frequency f_2 are present.
A$_{\text{iii}}$ Two-beat condition: The receiver and the fish with EOD frequencies f_1 and f_2 are present.
B Intermediate c_1 contrast.
C $A(\Delta f_1)$, amplitude of Δf_1 in the power spectrum of the firing rate, is plotted for varying c_1.
D $A(\Delta f_2)$, amplitude of Δf_2 in the power spectrum of the firing rate, is plotted for varying c_1.
E $A(\Delta f_1)$ and $A(\Delta f_2)$ are plotted for varying beat contrasts c_1.

In the following the beat strength in the P-unit response will be represented as the amplitude at the beat frequency in the power spectrum of the time-resolved firing rate and abbreviated as $A(\Delta f)$ (see methods section 2.11.2). The changes between the not saturated (Fig. 6.2 A) and saturated regime (Fig. 6.2 B) can be systematically investigated when plotting $A(\Delta f_1)$ and $A(\Delta f_2)$ for different c_1 contrasts for the one-beat and two-beat conditions (Fig. 6.2 C, D, E). In this example, the amplitude $A(\Delta f_1)$ increases for higher beat contrasts equally in the one-beat and two-beat condition (compare brown and red lines in Fig. 6.2 C). The beat contrast does not influence $A(\Delta f_2)$ in the corresponding one-beat condition (straight blue line, Fig. 6.2 D), since no Δf_1 beat is present in the superimposed signal. Still, a higher c_1 contrast leads to a decrease of $A(\Delta f_2)$ in the two-beat condition (cyan line, Fig. 6.2 D).

So far, only $A(\Delta f_2)$ but not $A(\Delta f_1)$ changed between the one-beat and two-beat conditions (area enclosed by blue and cyan lines, Fig. 6.2 E). If the same P-unit model is now probed with other beat frequencies ($\Delta f_1 = 64.5\,\text{Hz}$, $\Delta f_2 = -35.5\,\text{Hz}$), both beat peak amplitudes in the power spectrum of the firing rate, $A(\Delta f_1)$ and $A(\Delta f_2)$, change between the corresponding one-beat and two-beat conditions (Fig. 6.3 E).

6.1.2 High difference between the beat frequencies: only one beat representation will be decreased in the two-beat condition

What is the reason that the amplitude $A(\Delta f_1)$ in the power spectrum of the P-unit firing rate for some beat frequencies does not vary between the one-beat and two-beat condition (compare brown and red lines in Fig. 6.4 $\mathsf{A_i}$), while for other frequencies there is a difference (Fig. 6.4 $\mathsf{B_i}$)? This can be explained if $A(\Delta f)$ is plotted not for different c_1 contrasts but for varying beat frequencies Δf_1 (Fig. 6.4 $\mathsf{A_{ii-iii}}$). The amplitude of the varied beat $A(\Delta f_1)$ in its one-beat condition (only varied beat with frequency Δf_1 present in the stimulus) corresponds to the tuning curve for different beat frequencies known from previous literature (compare brown line in Fig. 6.4 $\mathsf{A_{ii}}$ and Fig. 1.19 C, Walz et al., 2014). Contrary, $A(\Delta f_2)$ in its one-beat condition (only the not varied beat with frequency Δf_2 is present in the stimulus) does not depend on Δf_1 (blue line). When both beats have the same contrast of 10%, the $A(\Delta f_1)$ one-beat tuning curve includes a representation of $A(\Delta f_2)$ (similar values of both curves at $-260\,\text{Hz}$ in Fig. 6.4 $\mathsf{A_{ii}}$, top).

There is almost no change between $A(\Delta f_1)$ in its one-beat tuning curve and the two-beat tuning curve (compare brown and red lines), but a decrease of $A(\Delta f_2)$ between its one-beat condition and the two-beat condition (compare blue and cyan lines, Fig. 6.4 $\mathsf{A_{ii}}$, bottom). In this example, the $A(\Delta f_1)$ one-beat tuning curve is for most beat frequencies above the $A(\Delta f_2)$ one-beat tuning curve (Fig. 6.4 $\mathsf{A_{ii}}$, solid lines). The offset between these is highest for low Δf_1 beat frequencies, and these are the ones where $A(\Delta f_2)$ is decreasing the most in the two-beat condition (cyan line, Fig. 6.4 $\mathsf{A_{ii}}$, bottom).

Increasing the c_1 contrast elevates the $A(\Delta f_1)$ tuning curves (brown and red lines, Fig. 6.4 $\mathsf{A_{iii}}$). Now the contrast c_1 is not equal to the contrast c_2, thus the one-beat tuning curves do not intersect anymore (solid lines). Instead, they are separated by an offset, associated with a stronger decline of $A(\Delta f_2)$ in the two-beat condition (cyan line, Fig. 6.4 $\mathsf{A_{iii}}$, bottom).

6.1.3 Similar beat frequencies: both beat representation will be decreased in the two-beat condition

In the following, the one-beat condition tuning curves will be considered for the example where both, $A(\Delta f_1)$ and $A(\Delta f_2)$, change between the corresponding one-beat and two-beat conditions (Fig. 6.4 $\mathsf{B_i}$). In this example, the two beats have similar frequencies in the same contrast one-beat $A(\Delta f_1)$ tuning curve and have almost the same $A(\Delta f_1)$ and $A(\Delta f_2)$ values (intersection

between brown, blue and gray line, Fig. 6.4 B_{ii}). At low Δf_1 beat frequencies $A(\Delta f_1)$ and $A(\Delta f_2)$ are reduced to a similar extent in the two-beat condition (dashed lines, Fig. 6.4 B_{ii}, bottom). At high Δf_1 beat frequencies, where $A(\Delta f_2)$ is above $A(\Delta f_1)$ in the one-beat conditions (solid lines, Fig. 6.4 B_{ii}), $A(\Delta f_1)$ is reduced in the two-beat condition (red dashed line, Fig. 6.4 B_{ii}, bottom).

If the c_1 contrast is increased, the $A(\Delta f_1)$ one-beat tuning curve is elevated, surpassing the fairly high $A(\Delta f_2)$ values (compare solid lines, Fig. 6.4 B_{iii}, top). At low Δf_1 beat frequencies, where the $A(\Delta f_1)$ one-beat tuning curve surpasses the $A(\Delta f_2)$ one-beat tuning curve, there is no $A(\Delta f_1)$ loss but a $A(\Delta f_2)$ decrease in the two-beat condition (cyan line, Fig. 6.4 B_{iii}).

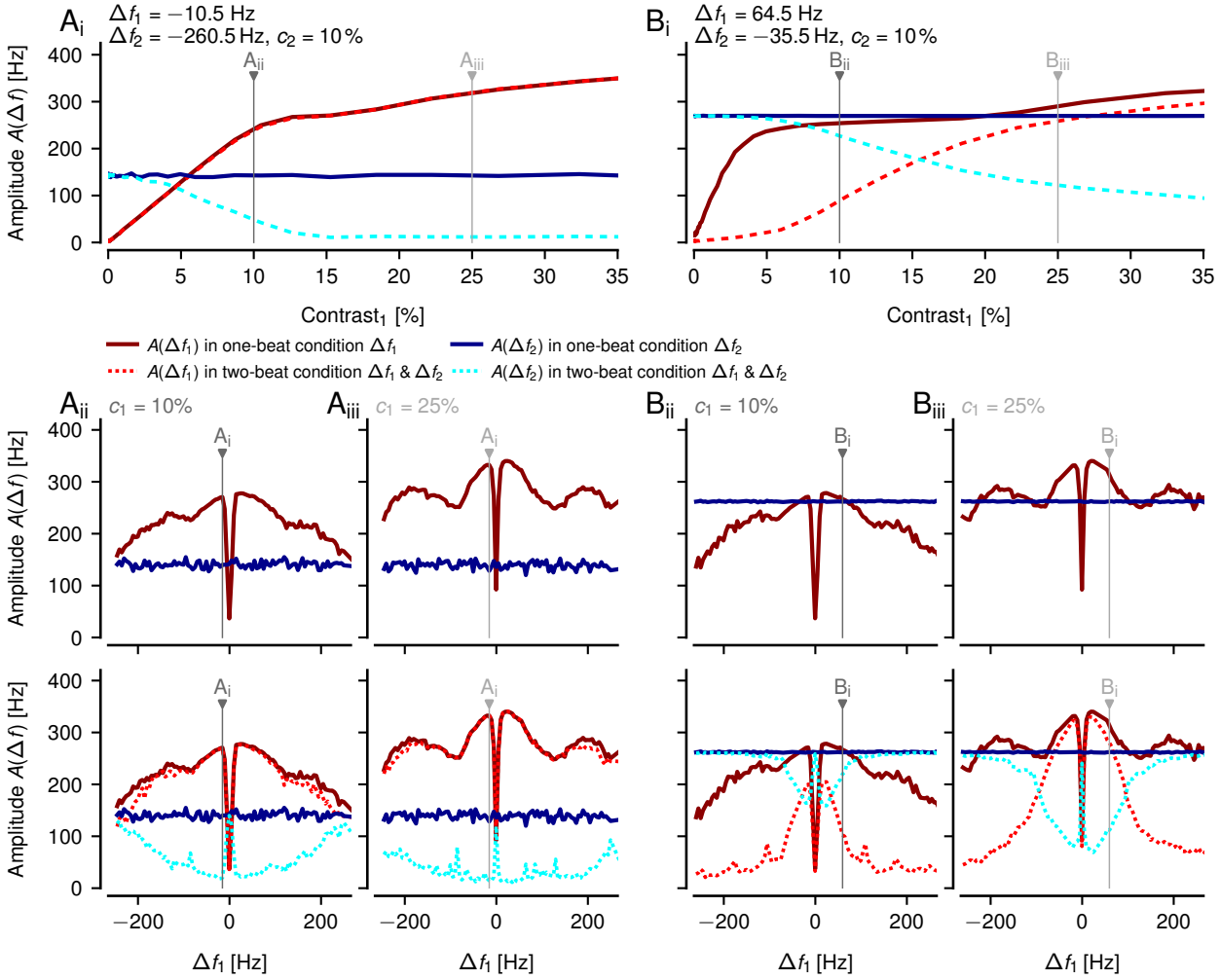

Figure 6.4: Both, $A(\Delta f_1)$ and $A(\Delta f_2)$, change between the one-beat and two-beat conditions if the beat frequencies are similar. The vertical lines connect the same contrasts and beat frequencies in A_i and A_{ii-iii}. See table 2.1 for model parameters of 2011-10-25-ad.

A $A(\Delta f_2)$ but not $A(\Delta f_1)$ changes between the corresponding one-beat and two-beat condition in A_i.

A_i $A(\Delta f_1)$ and $A(\Delta f_2)$ for different c_1 contrasts.

A_{ii-iii} $A(\Delta f_1)$ and $A(\Delta f_2)$ tuning curves for different Δf_1 beat frequencies in the one-beat conditions (solid lines in top and bottom) and in the two-beat condition (dashed lines, bottom).

A_{ii} All curves are based on beat contrasts of 10 % (c_1 and c_2). The blue $A(\Delta f_2)$ one-beat tuning curve is an extension of its intersection with the brown $A(\Delta f_1)$ one-beat tuning curve.

A_{iii} Intermediate contrast c_2 of 10 % and a higher contrast c_1 of 25%.

B $A(\Delta f_1)$ and $A(\Delta f_2)$ change between the corresponding one-beat and two-beat conditions in panel B_i.

6.1.4 Two-beat suppression in recorded P-units

So far, it was demonstrated with LIF P-unit models that the beat with the weaker beat amplitude $A(\Delta f)$ in the one-beat condition will be decreased in the two-beat condition (Fig. 6.4). These findings can be confirmed with electrophysiologically recorded P-units, where all beat frequency tuning curves were measured with a contrast of 10 % (Fig. 6.5).

When Δf_2 is a high beat frequency (Fig. 6.5 A), $A(\Delta f_2)$ is smaller than most $A(\Delta f_1)$ values in the one-beat condition (compare solid lines) and only $A(\Delta f_2)$ is decreased in the two-beat condition (cyan line). For an intermediate Δf_2 beat frequency, the $A(\Delta f_2)$ values increase (blue line, Fig. 6.5 B) and now both, $A(\Delta f_1)$ and $A(\Delta f_2)$, are slightly reduced in the two-beat condition (dashed lines). If the Δf_2 frequency is low, the $A(\Delta f_2)$ tuning curves are high (cyan and blue lines) and only $A(\Delta f_1)$ is reduced in the two-beat condition (red dashed line, Fig. 6.5 C).

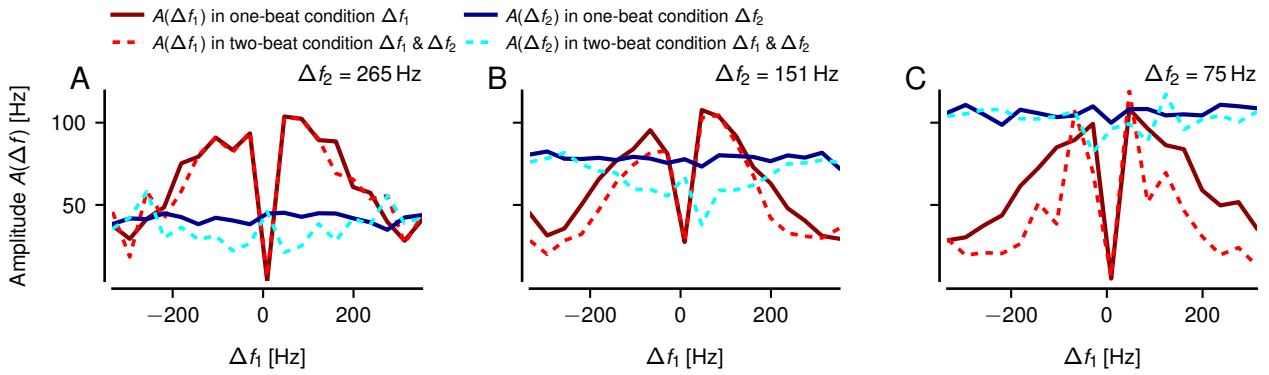

Figure 6.5: Electrophysiologically recorded P-unit in a three-fish setting. Tuning curves for different Δf_1 beat frequencies. Both beats have a contrast of 10 %.
A Δf_2 is a high beat frequency, with a low $A(\Delta f_2)$ value in the one-beat condition (blue). Only $A(\Delta f_2)$ is reduced in the two-beat condition (cyan).
B Δf_2 is an intermediate beat frequency. Both $A(\Delta f_1)$ and $A(\Delta f_2)$ decrease during the two-beat condition.
C Δf_2 is a low beat frequency. $A(\Delta f_2)$ has a high value in the one-beat condition (blue) and only $A(\Delta f_1)$ is decreased in the two-beat condition (red).

6.1.5 High contrasts can reduce the EOD representation in the P-unit firing rate

$A(\Delta f_1)$ changes not smoothly but in segments with different slopes for different contrasts (brown line, Fig. 6.6 D). In the chosen example $A(\Delta f_1)$ first increases rapidly at intermediate beat contrasts of 0–10 % and then slower at higher contrasts.

To understand this change in the beat amplitude $A(\Delta f_1)$ other frequencies, such as the EOD frequency of the receiver f_{EOD} (black marker) and the EOD frequency of the encountered fish f_1 (gray marker), will be considered in the power spectrum of the P-unit firing rate (Fig. 6.6). In this example, the peak size of f_{EOD} decreases with higher beat contrast (black markers, Fig. 6.6 A–C, bottom). The peak size of f_1 first increases for an intermediate contrast and then again decreases for a higher contrast (gray markers, Fig. 6.6 B, C, bottom). In this example the harmonics of Δf_1 around f_{EOD} are increased for a high beat contrast (light brown markers). The Δf_1 fundamental (brown marker) increases and becomes even stronger than the peaks of f_{EOD} and f_1(Fig. 6.6 C).

When plotting the amplitude of these peaks for different beat contrasts, the increase in $A(\Delta f_1)$ is accompanied by a decrease in $A(f_{EOD})$ and an initial increase followed by a decrease

in $A(f_1)$ (Fig. 6.6 D). This increase in $A(\Delta f_1)$ accompanied by a decrease in $A(f_{EOD})$, can also be observed in electrophysiologically recorded P-units (as in Fig. 6.7). Note that the shown P-units are examples and do not represent a heterogeneous P-unit population. Other P-units do not exhibit changes in the f_{EOD} amplitude in the P-unit firing rate for increasing beat contrasts (not shown).

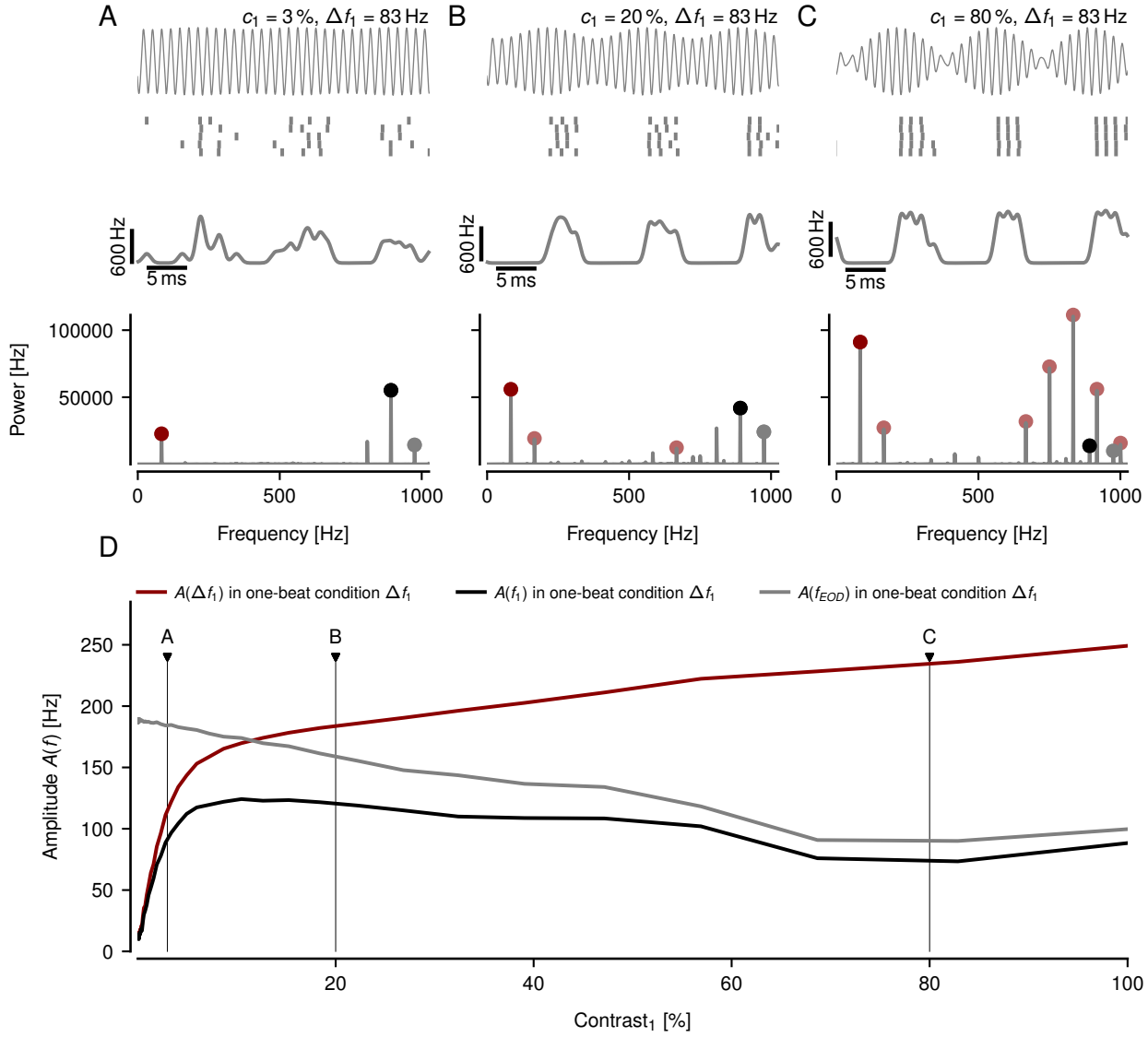

Figure 6.6: $A(\Delta f_1)$, $A(f_1)$ and $A(f_{EOD})$ for different beat contrasts in the P-unit LIF model. See table 2.1 for model parameters of cell 2012-05-10-ad. See methods section 2.11.2 for amplitude calculation.

A–C Top: EOD of the receiver superimposed with the EOD of the encountered fish, leading to a beat with frequency Δf_1. Second row: Spike trains. Third row: Firing rate of these spike trains. Bottom: Power spectrum of the firing rate. Brown marker – Δf_1. Light brown markers – harmonics of Δf_1. Gray marker – f_1. Black marker – f_{EOD}.

A Low c_1 contrast.

B Intermediate c_1 contrast.

C High c_1 contrast.

D $A(\Delta f_1)$, $A(f_1)$, and $A(f_{EOD})$ for different beat contrasts.

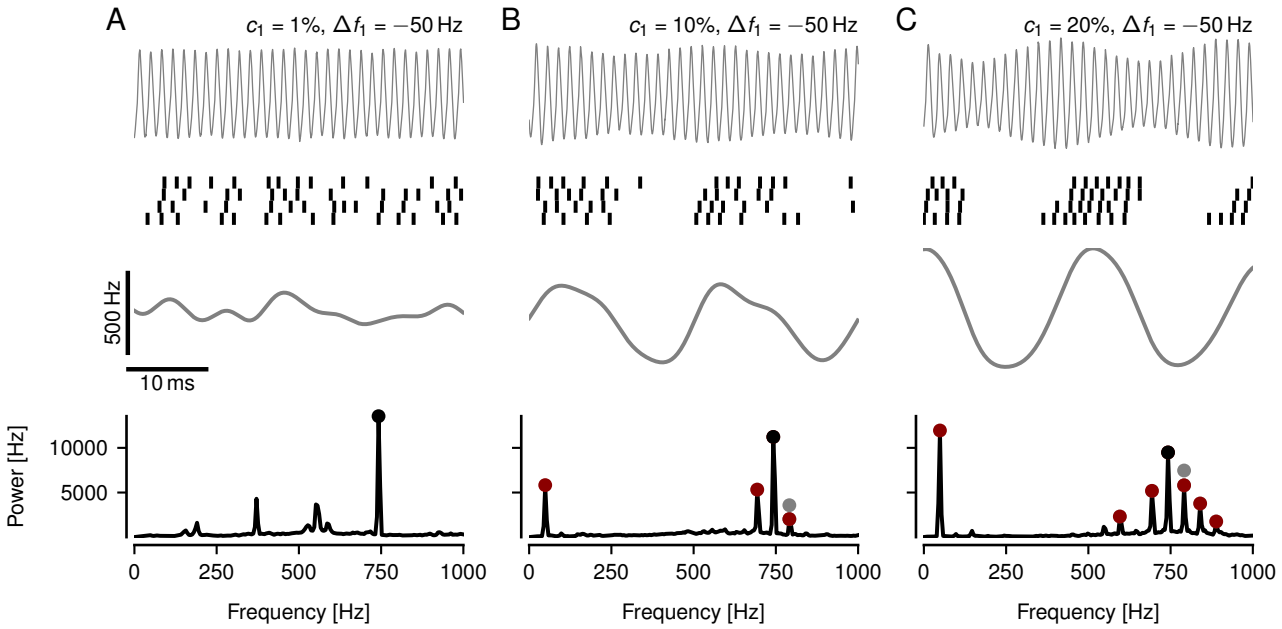

Figure 6.7: The increase of the beat contrast is accompanied by an increase of Δf_1 and its harmonics and a reduction of f_{EOD} in the power spectrum of the firing rate of an electrophysiologically recorded P-unit.
A–C First row: EOD of the receiver superimposed with the EOD of the encountered fish, leading to a beat with frequency Δf_1. Second row: Spike trains. Third row: Firing rate. Bottom: Power spectrum of the firing rate. Brown markers – $|\Delta f_1|$ and its harmonics. Gray marker – f_1. Black marker – f_{EOD}.
A Low c_1 contrast.
B Intermediate c_1 contrast.
C High c_1 contrast.

6.2 Discussion

In this chapter, the encoding of a wide range of beat contrasts (0.001–100 %) was addressed in P-units. Two-beat suppression could be observed at intermediate beat contrasts (10–30 %) in a three-fish setting, with one beat in the P-unit firing rate being suppressed by the presence of the other beat. It was demonstrated that the beat that was represented weaker in P-units in the one-beat condition will be suppressed in the two-beat condition. The encoding of high beat contrasts (up to 100 %) was investigated in the two-fish setting, associating the encoding of a wide dynamic range of beat contrasts with a reduction of the receiver EOD representation in the P-unit firing rate.

6.2.1 Two-beat suppression in P-units

In this chapter, two-beat suppression was found to be present in P-units at intermediate beat contrasts (around 20 %). In two-beat suppression, the representation of one beat in the firing rate of P-units is decreased by the presence of another beat in the stimulus. Two-beat suppression occurs when P-units start to saturate and both beat frequencies cannot be represented in the two-beat condition anymore, as they were in their less saturated one-beat conditions (Fig. 6.2). This reduction of one beat in the presence of another beat is reminiscent of two-tone suppression, discussed in the auditory system (Ruggero et al., 1992; Arthur et al., 1971; Sachs and Kiang, 1968; Schmiedt, 1982; Delgutte, 1990). Two-tone suppression is defined as the re-

duced response to one tone in the presence of another tone and has been observed in auditory nerve fibers (Sachs and Kiang, 1968) and the basilar membrane (Ruggero et al., 1992, 1997). Two-beat suppression has mainly been addressed in psycho-acoustical masking experiments, where a beat masker was demonstrated to reduce the detectability of another beat (Millman et al., 2002; Dau et al., 1997; Ewert and Dau, 2000). In this work two-beat suppression was for the first time demonstrated in the electrosensory system, thus highlighting it as a universal feature to occur during saturation of neurons.

In the following, the behavioral implications of the two-beat suppression for weakly electric fish of the species *Apteronotus leptorhynchus* will be discussed.

The perception of the fish with the same sex as the receiver will be favored

In the two-beat suppression examples in this chapter one beat had the same intermediate contrast c_2, indicating the presence of a stationary and distant fish. The other beat, where the contrast c_1 was varied, mimicked an approaching fish. In the first two-beat suppression example (Fig. 6.2), the distant fish induced a high beat frequency, whereas the approaching fish induced a low beat frequency. Low beat frequencies have higher values on the P-unit tuning curve (Fig. 1.19 C, Walz et al., 2014) and represent same-sex encounters (Henninger et al., 2018) and high beat frequencies have lower values on the P-unit tuning curve and represent opposite-sex encounters.

If the receiver in the example in Fig. 6.2 would be a male, the distant fish (with the high difference frequency) would be a female and the approaching fish (with the low beat frequency) would be a male. Then the representation of the distant female but not of the approaching male would be decreased in the P-unit firing rate in the two-beat setting. This accurate male representation in the neuronal system of the male receiver might be behaviorally reasonable since male-to-male interactions often include attacks and aggressive behavior (Hupé and Lewis, 2008; Henninger et al., 2018). Male-to-female interactions include courtship behavior (Henninger et al., 2018) and since the other male could be a threat to the successful courting process it might be reasonable to first chase away the potential competitor.

If instead, the receiver would be a female a high beat frequency would indicate the presence of a distant male and a low beat frequency would indicate that the approaching fish is a female. For the female receiver, the perception of the distant male would be deteriorated in favor of the approaching female. These findings imply that the perception of the same-sex fish will be favored over the perception of the opposite-sex fish in *Apteronotus leptorhynchus*.

The perception of closer and bigger fish is favored

In the other example in this chapter (Fig. 6.3), both fish, encountered by the receiver, induced similar beat frequencies, implying that both had the same sex. In this scenario, the representation of both encountered fish was decreased equally, when both fish were at the same distance. Still, it was demonstrated that if one fish would approach the receiver, the more distant fish representation would be decreased in favor of the approaching fish. In addition, if one of the encountered fish would have a stronger EOD than the other fish the representation of the fish with the weaker EOD would be suppressed. Larger fish are known to produce stronger EODs (Knudsen, 1975) that are associated with dominance in males (Raab et al., 2019; Dunlap and Oliveri, 2002). Thus it would be reasonable to favor the perception of the more dominant fish in the neuronal system, as it was demonstrated in this chapter.

These findings highlight that even though one beat had always the same amplitude in the stimulus, its representation in the neuronal system was not absolute, but varied depending on the other beat. These findings imply that the encountered conspecifics are not absolutely

depicted in the neuronal system, but that their representation is influenced by different behaviorally relevant factors (e.g. sex, distance or EOD field strength). Whether these findings, based on models and electrophysiologically recorded P-units, have implications for the behavior of these fish should be tested in further studies.

6.2.2 Has the reduction of the EOD in the response of P-units an attention-orienting function?

In this chapter, it was demonstrated that the EOD can be either fully present or disappear completely in the firing rate of model P-units (Fig. 6.6). *Apteronotus leptorhynchus* does not receive information about the activity of its electric organ by corollary discharge, as do other species of weakly electric fish (Fukutomi and Carlson, 2020; Salazar and Silva, 2022). Information about the EOD is encoded in different populations of primary sensory afferents, in P-units and T-units, that are both tuned to the EOD (Scheich et al., 1973; Hopkins, 1976). T-units encode the phase of the EOD (Scheich et al., 1973; Hopkins, 1976), and the phase of the beat (Heiligenberg and Partridge, 1981). Since the EOD frequency of these fish is assumed to be long-term stable, a constant EOD frequency representation might be not necessary. Still, the decreased EOD representation in P-units might reduce the information about the fish itself.

Such strong EOD representation changes might be perceived as qualitative, leading to a categorical perception of the state when the fish is alone or the state where a conspecific is close to the receiver. A switch between such states might have an important attention-orienting function for the fish, stressing that the other fish is closer than a critical distance, where an attack would be not preventable. In such a scenario perception of the other fish might be more important than self-perception.

Approaching or looming signals are perceived as threatening in the visual system (Ball and Tronick, 1971; Schiff et al., 1962). Approaching auditory signals have been identified as warning cues, leading to an increased autonomic orienting reflex and activation of the amygdala (Bach et al., 2008). In addition, such signals can lead to the activation of other modalities e.g. increasing the excitability of the visual system (Romei et al., 2009). Looming signals are salient stimuli, inducing bottom-up attention and orientation of behavior (Knudsen, 2007).

6.2.3 Nonlinear effects in P-units at high beat contrasts

In this chapter, it was demonstrated that the beat can be sustained in the firing rate of a single P-unit for a wide dynamic range of beat contrasts (up to 100 %). The increase of the beat frequency was associated with a decrease in the receiver EOD frequency in the P-unit response (Fig. 6.6, Fig. 6.7). This trade-off between the EOD and beat frequency might contribute to the encoding of a wide range of beat contrasts.

In previous studies, P-units have been found to saturate in their firing rate at contrasts between 10–30 % (Fig. 6.1, Gussin et al., 2007). The encoding of high beat contrasts is behaviorally relevant, since beat contrasts of up to 100 % can be found during the encounter of freely swimming fish (Fotowat et al., 2013). In previous literature it was demonstrated that once saturation is reached in P-units, higher contrasts are encoded by a limitation of the mean firing rate to a maximal and minimal saturation value (as in Fig. 6.3 B, third row, Nelson et al., 1997). Previous works elaborated on how P-units can simultaneously represent several frequencies in their firing rate for intermediate beat frequencies (Sinz et al., 2020). In this work it was for the first time demonstrated how different frequencies, such as the EOD of the receiver, the EOD of the encountered fish and the beat, are simultaneously represented in P-units at high beat contrasts.

Note, that the shown model and electrophysiological data are examples observed in some P-units but are not representative of a heterogeneous P-unit population (Grewe et al., 2017; Hladnik and Grewe, 2023). In the shown examples, the EOD representation reduction was always accompanied by increasing beat harmonics in the P-unit response for high beat contrasts (Fig. 6.6, Fig. 6.7). Other P-units might not change their EOD representation with varying beat contrast. The bursting of P-units, which has been found to enhance nonlinearity in chapter 4, might be an important factor influencing the encoding of P-units during strong beat amplitudes. Further studies should systematically quantify the nonlinearity appearing for strong beat amplitudes in a heterogeneous P-unit population.

6.2.4 Dynamic range encoding of beat contrasts associated with two encoding regimes

In this work, it was demonstrated that the beat representation in P-units had an initial rapid increase at intermediate beat contrasts, followed by a further increase with a flatter slope for higher beat contrasts (Fig. 6.6 D). Similar encoding can be observed in auditory nerve fibers, where at intermediate amplitudes, a tone is encoded with an increase of its neuronal representation with one slope and with a flatter slope for even stronger stimuli (Sachs and Abbas, 1974; Yin et al., 2019). In both scenarios, different slopes in response strength in a single cell can contribute to the solution of the dynamic range problem (Yin et al., 2019). Different slopes of amplitude encoding have also been observed in sound pressure compression of outer hair cells in the auditory system (Preyer and Gummer, 1996). Other mechanisms to address the dynamic range problem are sensitivity changes inside photoreceptors (Pugh Jr et al., 1999), changes in receptive field size on the retina (Barlow et al., 1957) or heterogeneous populations in auditory nerve fibers (Liberman, 1982). How the dynamic range problem is addressed in a heterogeneous P-unit population could be further elaborated in future studies.

6.2.5 Encoding of strong beat amplitudes in the auditory system

In this chapter, it was demonstrated in P-units that the increased beat representation during high-beat contrasts can be accompanied by a reduced EOD frequency representation in P-units. Are these findings also expected in auditory nerve fibers, that share several features with P-units (Joris and Yin, 1992; Joris et al., 2004; Khanna and Teich, 1989)?

In auditory nerve fibers, higher beat contrasts are encoded with an increasing synchronization of the firing rate to the beat frequency with saturation at contrasts around 80 % (Joris and Yin, 1992; Joris et al., 2004). As in P-units both, the AM and the carrier, are represented in the firing rate of auditory nerve fibers (Khanna and Teich, 1989). How the carrier representation is influenced in auditory nerve fibers at high beat contrasts, might be the subject of further studies.

In this chapter, it was demonstrated that the increased beat and decreased EOD representation for high beat contrasts can be accompanied by a bell-shaped increase of beat harmonics close to the EOD frequency (Fig. 6.6). P-units are tuned to frequencies close to the EOD frequency, as has been demonstrated by silencing the EOD and probing P-units with sine wave stimuli with different frequencies (Hopkins, 1976). The corresponding band-pass filter is assumed to be caused by electric resonance in the electroreceptor cells (Viancour, 1979). This tuning might be the reason behind the beat harmonics increase around the EOD frequency. Auditory fibers are also tuned to a range of pure tones (Yin et al., 2019; Palmer and Russell, 1986) caused by a harmonic oscillator (Hudspeth and Lewis, 1988). Strong pure tone amplitudes can lead to harmonics in the response of auditory nerve fibers, known as “peak splitting” (Cai and Geisler, 1996; Heil and Peterson, 2017). With this, an increase in beat harmonics

might also be conceivable for strong amplitude-modulated stimuli in auditory nerve fibers and could be addressed in further studies.

6.2.6 Conclusion

In this chapter, the question of how P-units can encode a wide dynamic range of beat contrasts (0.001–100 %), beyond the firing rate saturation of single P-units, was addressed in the three-fish setting. Two-beat suppression, with one of the beats being reduced by the presence of the other beat, has been demonstrated in the firing rate of P-units at intermediate contrasts (10–30 %). This two-beat suppression shares several features with two-tone suppression (Jülicher et al., 2001; Ruggero et al., 1992; Sachs and Kiang, 1968) and masking experiments with two beats in the auditory system (Millman et al., 2002; Dau et al., 1997; Ewert and Dau, 2000). If both encountered fish had the same sex, both beats were degraded equally in the P-units response. If the two encountered conspecific were from the opposite sex, the same-sex fish representation was favored in the P-units of the receiver. The increase of the beat frequency response with two different slopes in P-units was associated with a decrease in the representation of the receiver EOD. These two identified beat encoding regimes might contribute to a wider dynamic range encoding of beat contrasts in a single cell. The reduction of the EOD representation for strong beats might be a qualitative change providing a cue to differentiate between the state where the fish is alone or another fish is approaching. The close presence of a conspecific might be behaviorally relevant and require attention orienting towards the encountered fish, which might be a threat and issue an attack. Similar changes in the carrier representation for high beat contrasts might also be expected in auditory nerve fibers.

Chapter 7

Conclusion

In this work, the nonlinearities of primary electrosensory afferents, the P-units of weakly electric fish of the species *Apteronotus leptorhynchus* and *Eigenmannia virescens*, were addressed for a wide range of stimulus regimes, with varying beat frequencies and amplitudes.

In chapter 3 it was demonstrated that a smooth nonlinearity at the synapse, between the electroreceptors and the afferent P-unit, enables beat perception at high beat frequencies. High beat frequencies might be the basis for interspecies communication, thus providing a new stimulus encoding regime. P-units share several features with mammalian auditory nerve fibers and beat perception of high beat frequencies, also known as mistuned octaves, has already been addressed by Ohm (1839). These findings made on electroreceptors suggest a physiological mechanism, in addition to nonlinearities at the basilar membrane, that is intrinsic to the receptor cells.

In chapter 4 nonlinearities were characterized as the second-order susceptibility of P-units, in a setting where at least three fish were present. The nonlinear responses of P-units were especially strong in regular firing or bursty P-units, with bursting being identified as a factor enhancing nonlinear interactions. In chapter 5 those nonlinearities were identified to improve the detection of a faint signal in the presence of a strong signal during a three-fish setting, the so-called electrosensory cocktail party. The electrosensory cocktail party problem shares several features with the cocktail party problem in humans, a sound source separation problem where a behaviorally relevant stimulus has to be separated from a noisy environment (Cherry, 1953; Haykin and Chen, 2005). As in electroreceptor afferents, nonlinear effects in mammalian auditory nerve fibers might contribute to the encoding of the cocktail party problem in the human auditory system.

In chapter 6 the encoding of strong beat amplitudes, beyond the saturation of single P-units, was addressed. Two-beat suppression and the change in the EOD representation in the P-unit firing rate were nonlinearities identified to contribute to the encoding of a wide dynamic range of beat amplitudes in the same P-unit. Changes in representation of the own EOD might influence the self-perception of the fish and facilitate attention orienting towards behaviorally relevant strong beat amplitudes. These findings contribute to the numerous mechanisms addressing the dynamic range problem known in most sensory modalities as audition (Evans, 1981; Preyer and Gummer, 1996; Liberman, 1982) or vision (Pugh Jr et al., 1999; Barlow et al., 1957; Laughlin, 1981).

All these chapters have in common that new stimulus regimes, such as the high beat frequencies or the wide dynamic range between faint and strong beat amplitudes, were addressed. Although those are clearly behaviorally relevant for these fish (Henninger et al., 2018), they were mostly neglected in previous investigations (Walz et al., 2014; Benda et al., 2006; Grewe et al., 2017; Bastian, 1981; Nelson et al., 1997). In this work, it was demonstrated that nonlinearities inevitably contribute to the encoding of these stimulus regimes in electroreceptor

afferents. Although these findings are made in the electrosensory system, similar problems can be identified in the auditory system as the perception of mistuned octaves (Ohm, 1839), the detection of faint signals in the cocktail party problem (Cherry, 1953), the dynamic range encoding of different amplitudes (Evans, 1981; Preyer and Gummer, 1996; Liberman, 1982), two-tone suppression (Jülicher et al., 2001; Ruggero et al., 1992; Sachs and Kiang, 1968) and masking experiments with two beats, similar to two-beat suppression (Millman et al., 2002; Dau et al., 1997; Ewert and Dau, 2000). Electroreceptor afferents differ from mammalian auditory nerve fibers since no cochlea is preceding them. This simplicity of the model organism weakly electric fish allowed to retrieve fundamental mathematical principles of beat processing, that might also apply to primary sensory afferents in the auditory system.

Bibliography

Abel, C. and Kössl, M. (2009). Sensitive response to low-frequency cochlear distortion products in the auditory midbrain. *Journal of Neurophysiology*, 101(3):1560–1574.

Adelson, E. H. and Bergen, J. R. (1985). Spatiotemporal energy models for the perception of motion. *Journal of the Optical Society of America*, 2(2):284–299.

Albert, J. (2001). Species diversity and phylogenetic systematics of American knifefishes (Gymnotiformes, Teleostei). 190.

Amoore, J. (1986). Effects of chemical exposure on olfaction in humans. *Toxicology of the Nasal Passages*, pages 155–190.

Arthur, R., Pfeiffer, R., and Suga, N. (1971). Properties of "two-tone inhibition" in primary auditory neurones. *The Journal of Physiology*, 212(3):593–609.

Avoli, M. and Olivier, A. (1989). Electrophysiological properties and synaptic responses in the deep layers of the human epileptogenic neocortex in vitro. *Journal of Neurophysiology*, 61(3):589–606.

Bach, D. R., Schächinger, H., Neuhoff, J. G., Esposito, F., Salle, F. D., Lehmann, C., Herdener, M., Scheffler, K., and Seifritz, E. (2008). Rising sound intensity: an intrinsic warning cue activating the amygdala. *Cerebral Cortex*, 18(1):145–150.

Ball, W. and Tronick, E. (1971). Infant responses to impending collision: optical and real. *Science*, 171(3973):818–820.

Barayeu, A., Schäfer, R., Grewe, J., and Benda, J. (2023). Beat encoding at mistuned octaves within single electrosensory neurons. *iScience*, 26(7):106840.

Barlow, H., Fitzhugh, R., and Kuffler, S. (1957). Change of organization in the receptive fields of the cat's retina during dark adaptation. *The Journal of Physiology*, 137(3):338.

Bastian, J. (1981). Electrolocation I. How electroreceptors of *Apteronotus albifrons* code for moving objects and other electrical stimuli. *Journal of Comparative Physiology*, 144:465–479.

Bastian, J., Chacron, M. J., and Maler, L. (2002). Receptive field organization determines pyramidal cell stimulus-encoding capability and spatial stimulus selectivity. *Journal of Neuroscience*, 22(11):4577–4590.

Bastian, J. and Courtright, J. (1991). Morphological correlates of pyramidal cell adaptation rate in the electrosensory lateral line lobe of weakly electric fish. *Journal of Comparative Physiology A*, 168:393–407.

Beiran, M., Kruscha, A., Benda, J., and Lindner, B. (2018). Coding of time-dependent stimuli in homogeneous and heterogeneous neural populations. *Journal of Computational Neuroscience*, 44:189–202.

Benda, J. (2020). The physics of electrosensory worlds. In Fritsch, B. and Bleckmann, H., editors, *The senses: a comprehensive reference*, volume 7, pages 228–254. Elsevier, Academic Press.

Benda, J., Longtin, A., and Maler, L. (2005). Spike-frequency adaptation separates transient communication signals from background oscillations. *Journal of Neuroscience*, 25(9):2312–2321.

Benda, J., Longtin, A., and Maler, L. (2006). A synchronization-desynchronization code for natural communication signals. *Neuron*, 52:347–358.

Berman, N. J. and Maler, L. (1998). Inhibition evoked from primary afferents in the electrosensory lateral line lobe of the weakly electric fish *(Apteronotus leptorhynchus)*. *Journal of Neurophysiology*, 80(6):3173–3196.

Birmingham, J., Szuts, Z., Abbott, L., and Marder, E. (1999). Encoding of muscle movement on two time scales by a sensory neuron that switches between spiking and bursting modes. *Journal of Neurophysiology*, 82(5):2786–2797.

Briand, L. and Salles, C. (2016). Taste perception and integration. In *Flavor*, pages 101–119. Elsevier.

Brincat, S. L. and Connor, C. E. (2004). Underlying principles of visual shape selectivity in posterior inferotemporal cortex. *Nature Neuroscience*, 7(8):880–886.

Brownell, W. E. (1990). Outer hair cell electromotility and otoacoustic emissions. *Ear Hearing*, 11(2):82.

Bushdid, C., Magnasco, M. O., Vosshall, L. B., and Keller, A. (2014). Humans can discriminate more than 1 trillion olfactory stimuli. *Science*, 343(6177):1370–1372.

Cai, Y. and Geisler, C. D. (1996). Temporal patterns of the responses of auditory-nerve fibers to low-frequency tones. *Hearing Research*, 96(1-2):83–93.

Caldwell, J. and Daw, N. (1978). New properties of rabbit retinal ganglion cells. *The Journal of Physiology*, 276(1):257–276.

Carr, C. E., Maler, L., and Sas, E. (1982). Peripheral organization and central projections of the electrosensory nerves in gymnotiform fish. *Journal of Comparative Neurology*, 211:139–153.

Carriot, J., Jamali, M., Cullen, K. E., and Chacron, M. J. (2017). Envelope statistics of self-motion signals experienced by human subjects during everyday activities: Implications for vestibular processing. *PLoS One*, 12(6):e0178664.

Chacron, M. J. (2006). Nonlinear information processing in a model sensory system. *Journal of Neurophysiology*, 95(5):2933–2946.

Chacron, M. J., Longtin, A., and Maler, L. (2001). Negative interspike interval correlations increase the neuronal capacity for encoding time-dependent stimuli. *Journal of Neuroscience*, 21(14):5328–5343.

Chacron, M. J., Longtin, A., and Maler, L. (2004). To burst or not to burst? *Journal of Computational Neuroscience*, 17:127–136.

Chacron, M. J., Longtin, A., St-Hilaire, M., and Maler, L. (2000). Suprathreshold stochastic firing dynamics with memory in P-type electroreceptors. *Physical Review Letters*, 85(7):1576.

Chacron, M. J., Maler, L., and Bastian, J. (2005). Electroreceptor neuron dynamics shape information transmission. *Nature Neuroscience*, 8(5):673–678.

Chakravarthy, K., Kent, A. R., Raza, A., Xing, F., and Kinfe, T. M. (2018). Burst spinal cord stimulation: review of preclinical studies and comments on clinical outcomes. *Neuromodulation: Technology at the Neural Interface*, 21(5):431–439.

Cherry, E. C. (1953). Some experiments on the recognition of speech, with one and with two ears. *The Journal of the Acoustical Society of America*, 25(5):975–979.

Chialvo, D. R., Longtin, A., and Müller-Gerking, J. (1997). Stochastic resonance in models of neuronal ensembles. *Physical Review E*, 55(2):1798.

Clevert, D., Unterthiner, T., and Hochreiter, S. (2015). Fast and accurate deep network learning by exponential linear units (ELUs). *arXiv preprint arXiv:1511.07289*.

Csicsvari, J., Hirase, H., Czurko, A., and Buzsáki, G. (1998). Reliability and state dependence of pyramidal cell–interneuron synapses in the hippocampus: an ensemble approach in the behaving rat. *Neuron*, 21(1):179–189.

Cunningham, D. G., Baker, D. H., and Peirce, J. W. (2017). Measuring nonlinear signal combination using EEG. *Journal of Vision*, 17(5):10–10.

Cunningham, M. O., Whittington, M. A., Bibbig, A., Roopun, A., LeBeau, F. E., Vogt, A., Monyer, H., Buhl, E. H., and Traub, R. D. (2004). A role for fast rhythmic bursting neurons in cortical gamma oscillations in vitro. *Proceedings of the National Academy of Sciences*, 101(18):7152–7157.

Dau, T., Kollmeier, B., and Kohlrausch, A. (1997). Modeling auditory processing of amplitude modulation. I. Detection and masking with narrow-band carriers. *The Journal of the Acoustical Society of America*, 102(5):2892–2905.

De Ridder, D., Vanneste, S., Plazier, M., van der Loo, E., and Menovsky, T. (2010a). Burst spinal cord stimulation: toward paresthesia-free pain suppression. *Neurosurgery*, 66(5):986–990.

De Ridder, D., Vanneste, S., van der Loo, E., Plazier, M., Menovsky, T., and Van de Heyning, P. (2010b). Burst stimulation of the auditory cortex: a new form of neurostimulation for noise-like tinnitus suppression. *Journal of Neurosurgery*, 112(6):1289–1294.

Delgutte, B. (1990). Two-tone rate suppression in auditory-nerve fibers: Dependence on suppressor frequency and level. *Hearing Research*, 49(1-3):225–246.

Destexhe, A., Babloyantz, A., and Sejnowski, T. J. (1993). Ionic mechanisms for intrinsic slow oscillations in thalamic relay neurons. *Biophysical Journal*, 65(4):1538–1552.

Dunlap, K. D. and Oliveri, L. M. (2002). Retreat site selection and social organization in captive electric fish, *Apteronotus leptorhynchus*. *Journal of Comparative Physiology A*, 188:469–477.

Dux, P. E., Ivanoff, J., Asplund, C. L., and Marois, R. (2006). Isolation of a central bottleneck of information processing with time-resolved fMRI. *Neuron*, 52(6):1109–1120.

Edwards, M., Bigham, A., Tan, J., Li, S., Gozdzik, A., Ross, K., Jin, L., and Parra, E. J. (2010). Association of the *OCA2* polymorphism His615Arg with melanin content in east Asian populations: further evidence of convergent evolution of skin pigmentation. *PLoS Genetics*, 6(3):e1000867.

Egerland, C. H. (2021). Estimation and approximation of the nonlinear response of stochastic neuron models with adaptation. *Unpublished master thesis*, Humboldt-Universität zu Berlin.

Eggermont, J. J. and Smith, G. M. (1996). Burst-firing sharpens frequency-tuning in primary auditory cortex. *Neuroreport*, 7(3):753–757.

Engelmann, J., Gertz, S., Goulet, J., Schuh, A., and von der Emde, G. (2010). Coding of stimuli by ampullary afferents in *Gnathonemus petersii*. *Journal of Neurophysiology*, 104(4):1955–1968.

Engler, G. and Zupanc, G. K. (2001). Differential production of chirping behavior evoked by electrical stimulation of the weakly electric fish, *Apteronotus leptorhynchus*. *Journal of Comparative Physiology A*, 187(9):747–756.

Evans, E. (1972). The frequency response and other properties of single fibres in the guinea-pig cochlear nerve. *The Journal of Physiology*, 226(1):263–287.

Evans, E. (1981). The dynamic range problem: place and time coding at the level of cochlear nerve and nucleus. In *Neuronal Mechanisms of Hearing*, pages 69–85. Springer.

Ewert, S. D. and Dau, T. (2000). Characterizing frequency selectivity for envelope fluctuations. *The Journal of the Acoustical Society of America*, 108(3):1181–1196.

Ferwerda, J. A., Pattanaik, S. N., Shirley, P., and Greenberg, D. P. (1996). A model of visual adaptation for realistic image synthesis. In *Proceedings of the 23rd annual conference on computer graphics and interactive techniques*, pages 249–258.

Ford, H. A., Parkin, D. T., and Ewing, A. W. (1973). Divergence and evolution in Darwin's finches. *Biological Journal of the Linnean Society*, 5(3):289–295.

Foster, K., Gaska, J. P., Nagler, M., and Pollen, D. (1985). Spatial and temporal frequency selectivity of neurones in visual cortical areas V1 and V2 of the macaque monkey. *The Journal of Physiology*, 365(1):331–363.

Fotowat, H., Harrison, R., and Krahe, R. (2013). Statistics of the electrosensory input in the freely swimming weakly electric fish *Apteronotus leptorhynchus*. *Journal of Neuroscience*, 33(34):13758–13772.

Fourcaud-Trocmé, N., Hansel, D., van Vreeswijk, C., and Brunel, N. (2003). How spike generation mechanisms determine the neuronal response to fluctuating inputs. *Journal of Neuroscience*, 23(37):11628–11640.

Fukutomi, M. and Carlson, B. A. (2020). A history of corollary discharge: contributions of mormyrid weakly electric fish. *Frontiers in Integrative Neuroscience*, 14:42.

Furutsu, K. (1963). On the statistical theory of electromagnetic waves in a fluctuating medium. *Journal of Research of the National Bureau of Standards*, 67:303–323.

Gabbiani, F., Metzner, W., Wessel, R., and Koch, C. (1996). From stimulus encoding to feature extraction in weakly electric fish. *Nature*, 384(6609):564–567.

Glorot, X., Bordes, A., and Bengio, Y. (2011). Deep sparse rectifier neural networks. In *Proceedings of the fourteenth international conference on artificial intelligence and statistics*, pages 315–323.

Grahn, J. A. (2012). Neural mechanisms of rhythm perception: current findings and future perspectives. *Topics in Cognitive Science*, 4(4):585–606.

Grewe, J., Kruscha, A., Lindner, B., and Benda, J. (2017). Synchronous spikes are necessary but not sufficient for a synchrony code in populations of spiking neurons. *Proceedings of the National Academy of Sciences*, 114(10):E1977–E1985.

Gross, C. G. (2002). Genealogy of the "grandmother cell". *The Neuroscientist*, 8(5):512–518.

Gussin, D., Benda, J., and Maler, L. (2007). Limits of linear rate coding of dynamic stimuli by electroreceptor afferents. *Journal of Neurophysiology*, 97(4):2917–2929.

Hawken, M., Shapley, R. M., and Grosof, D. (1996). Temporal-frequency selectivity in monkey visual cortex. *Visual neuroscience*, 13(3):477–492.

Haykin, S. and Chen, Z. (2005). The cocktail party problem. *Neural Computation*, 17(9):1875–1902.

Heil, P. and Peterson, A. J. (2017). Spike timing in auditory-nerve fibers during spontaneous activity and phase locking. *Synapse*, 71(1):5–36.

Heiligenberg, W. and Altes, R. A. (1978). Phase sensitivity in electrorecption. *Science*, 199:1001–1003.

Heiligenberg, W. and Dye, J. (1982). Labelling of electroreceptive afferents in a gymnotoid fish by intracellular injection of HRP: the mystery of multiple maps. *Journal of Comparative Physiology*, 148:287–296.

Heiligenberg, W. and Partridge, B. L. (1981). How electroreceptors encode JAR-eliciting stimulus regimes: reading trajectories in a phase-amplitude plane. *Journal of Comparative Physiology*, 142:295–308.

Helmholtz, H. L. (1875). *On the sensations of tone as a physiological basis for the theory of music*. Cambridge University Press.

Henninger, J., Kirschbaum, F., Grewe, J., Krahe, R., and Benda, J. (2017). Court and spark in the wild: communication at the limits of sensation. *bioRxiv:114249*.

Henninger, J., Krahe, R., Kirschbaum, F., Grewe, J., and Benda, J. (2018). Statistics of natural communication signals observed in the wild identify important yet neglected stimulus regimes in weakly electric fish. *Journal of Neuroscience*, 38:5456–5465.

Henninger, J., Krahe, R., Sinz, F., and Benda, J. (2020). Tracking activity patterns of a multispecies community of gymnotiform weakly electric fish in their neotropical habitat without tagging. *Journal of Experimental Biology*, 223:jeb206342.

Hladnik, T. C. and Grewe, J. (2023). Receptive field sizes and neuronal encoding bandwidth are constrained by axonal conduction delays. *PLoS Computational Biology*, 8(19).

Hopkins, C. D. (1974). Electric communication in the reproductive behavior of *Sternopygus macrurus* (Gymnotoidei). *Zeitschrift für Tierpsychologie*, 35:518–535.

Hopkins, C. D. (1976). Stimulus filtering and electroreception: tuberous electroreceptors in three species of gymnotoid fish. *Journal of Comparative Physiology*, 111:171–207.

Howard, J. and Hudspeth, A. J. (1988). Compliance of the hair bundle associated with gating of mechanoelectrical transduction channels in the bullfrog's saccular hair cell. *Neuron*, 1:189–199.

Hubel, D. H. and Wiesel, T. N. (1959). Receptive fields of single neurones in the cat's striate cortex. *The Journal of Physiology*, 148(3):574.

Hubel, D. H. and Wiesel, T. N. (1962). Receptive fields, binocular interaction and functional architecture in the cat's visual cortex. *The Journal of Physiology*, 160(1):106.

Hubel, D. H. and Wiesel, T. N. (1965). Receptive fields and functional architecture in two nonstriate visual areas (18 and 19) of the cat. *Journal of Neurophysiology*, 28(2):229–289.

Hudspeth, A. and Lewis, R. (1988). Kinetic analysis of voltage-and ion-dependent conductances in saccular hair cells of the bull-frog, Rana catesbeiana. *The Journal of Physiology*, 400(1):237–274.

Hupé, G. and Lewis, J. (2008). Electrocommunication signals in free swimming brown ghost knifefish, *Apteronotus leptorhynchus*. *Journal of Experimental Biology*, 211:1657–67.

Izhikevich, E. M. (2000). Neural excitability, spiking and bursting. *International Journal of Bifurcation and Chaos*, 10(06):1171–1266.

Joris, P., Schreiner, C., and Rees, A. (2004). Neural processing of amplitude-modulated sounds. *Physiological Reviews*, 84(2):541–577.

Joris, P. X. and Yin, T. C. (1992). Responses to amplitude-modulated tones in the auditory nerve of the cat. *The Journal of the Acoustical Society of America*, 91(1):215–232.

Juergens, E., Guettler, A., and Eckhorn, R. (1999). Visual stimulation elicits locked and induced gamma oscillations in monkey intracortical-and EEG-potentials, but not in human EEG. *Experimental Brain Research*, 129:247–259.

Jülicher, F., Andor, D., and Duke, T. (2001). Physical basis of two-tone interference in hearing. *Proceedings of the National Academy of Sciences*, 98(16):9080–9085.

Kalmijn, A. J. (1974). The detection of electric fields from inanimate and animate sources other than electric organs. In Fessard, A., editor, *Electroreceptors and other specialized receptors in lower vertrebrates*, pages 148–194. Springer, Heidelberg.

Kandel, E. R., Schwartz, J. H., Jessell, T. M., Siegelbaum, S., Hudspeth, A. J., Mack, S., et al. (2000). *Principles of neural science*, volume 4. McGraw-hill New York.

Karri, J., Joshi, M., Polson, G., Tang, T., Maxwell, L., Orhurhu, V., Deer, T., and Abd-Elsayed, A. (2020). Spinal cord stimulation for chronic pain syndromes: a review of considerations in practice management. *Pain Physician*, 23(6):599.

Kemp, D. T. (1978). Stimulated acoustic emissions from within the human auditory system. *The Journal of the Acoustical Society of America*, 64(5):1386–1391.

Khanbabaie, R., Nesse, W. H., Longtin, A., and Maler, L. (2010). Kinetics of fast short-term depression are matched to spike train statistics to reduce noise. *Journal of Neurophysiology*, 103(6):3337–3348.

Khanna, S. and Teich, M. (1989). Spectral characteristics of the responses of primary auditory-nerve fibers to amplitude-modulated signals. *Hearing Research*, 39(1-2):143–157.

Kiskinis, E., Kralj, J. M., Zou, P., Weinstein, E. N., Zhang, H., Tsioras, K., Wiskow, O., Ortega, J. A., Eggan, K., and Cohen, A. E. (2018). All-optical electrophysiology for high-throughput functional characterization of a human iPSC-derived motor neuron model of ALS. *Stem Cell Reports*, 10(6):1991–2004.

Knight, B. W. (1972). Dynamics of encoding in a population of neurons. *The Journal of General Physiology*, 59:734–766.

Knudsen, E. (1974). Behavioral thresholds to electric signals in high frequency electric fish. *Journal of Comparative Physiology*, 91(4):333–353.

Knudsen, E. (1975). Spatial aspects of the electric fields generated by weakly electric fish. *Journal of Comparative Physiology*, 99(2):103–118.

Knudsen, E. I. (2007). Fundamental components of attention. *Annual Review of Neuroscience*, 30:57–78.

Koelsch, S. and Siebel, W. A. (2005). Towards a neural basis of music perception. *Trends in Cognitive Sciences*, 9(12):578–584.

König, R. (1876). LI. On the simultaneous sounding of two notes. *The London, Edinburgh, and Dublin Philosophical Magazine and Journal of Science*, 1(6):417–446.

Köppl, C. (1997). Phase locking to high frequencies in the auditory nerve and cochlear nucleus magnocellularis of the barn owl, Tyto alba. *Journal of Neuroscience*, 17(9):3312–3321.

Kozmik, Z., Ruzickova, J., Jonasova, K., Matsumoto, Y., Vopalensky, P., Kozmikova, I., Strnad, H., Kawamura, S., Piatigorsky, J., Paces, V., et al. (2008). Assembly of the cnidarian camera-type eye from vertebrate-like components. *Proceedings of the National Academy of Sciences*, 105(26):8989–8993.

Krahe, R., Bastian, J., and Chacron, M. J. (2008). Temporal processing across multiple topographic maps in the electrosensory system. *Journal of Neurophysiology*, 100(2):852–867.

Krahe, R. and Gabbiani, F. (2004). Burst firing in sensory systems. *Nature Reviews Neuroscience*, 5(1):13–23.

Krahe, R. and Maler, L. (2014). Neural maps in the electrosensory system of weakly elcectric fish. *Current Opinion in Neurobiology*, 24:13–21.

Kramer, B., Kirschbaum, F., and Markl, H. (1981). Species specificity of electric organ discharges in a sympatric group of gymnotoid fish from Manaus (Amazonas). In Szabó, T. and Czéh, G., editors, *Sensory physiology of aquatic lower vertebrates*, pages 195–219. Pergamon.

Kujawa, S., Fallon, M., and Bobbin, R. (1995). Time-varying alterations in the f2- f1 DPOAE response to continuous primary stimulation I: Response characterization and contribution of the olivocochlear efferents. *Hearing Research*, 85(1-2):142–154.

Kunkel, T. and Reinhard, E. (2010). A reassessment of the simultaneous dynamic range of the human visual system. In *Proceedings of the 7th symposium on applied perception in graphics and visualization*, pages 17–24.

Lamore, P., Muijser, H., and Keemink, C. (1986). Envelope detection of amplitude-modulated high-frequency sinusoidal signals by skin mechanoreceptors. *The Journal of the Acoustical Society of America*, 79(4):1082–1085.

Laughlin, S. B. (1981). A simple coding procedure enhances a neuron's information capacity. *Zeitschrift für Naturforschung*, 36C:910–912.

Lavoué, S., Miya, M., Arnegard, M. E., Sullivan, J. P., Hopkins, C. D., and Nishida, M. (2012). Comparable ages for the independent origins of electrogenesis in African and South American weakly electric fishes. *PLoS One*, 7(5):e36287.

Leek, M. R. (2001). Adaptive procedures in psychophysical research. *Perception & Psychophysics*, 63(8):1279–1292.

Lewicki, M. S. (2002). Efficient coding of natural sounds. *Nature Neuroscience*, 5(4):356–363.

Liberman, M. (1982). Single-neuron labeling in the cat auditory nerve. *Science*, 216(4551):1239–1241.

Lisman, J. E. (1997). Bursts as a unit of neural information: making unreliable synapses reliable. *Trends in Neurosciences*, 20(1):38–43.

Longtin, A. and Hinzer, K. (1996). Encoding with bursting, subthreshold oscillations, and noise in mammalian cold receptors. *Neural Computation*, 8(2):215–255.

Longtin, A., Middleton, J. W., Cieniak, J., and Maler, L. (2008). Neural dynamics of envelope coding. *Mathematical Biosciences*, 214(1-2):87–99.

Maler, L. (2009). Receptive field organization across multiple electrosensory maps. I. columnar organization and estimation of receptive field size. *Journal of Comparative Neurology*, 516:376–393.

Margolskee, R. F. (2002). Molecular mechanisms of bitter and sweet taste transduction. *Journal of Biological Chemistry*, 277(1):1–4.

Marsat, G. and Pollack, G. S. (2010). The structure and size of sensory bursts encode stimulus information but only size affects behavior. *Journal of Comparative Physiology A*, 196:315–320.

Marsat, G. and Pollack, G. S. (2012). Bursting neurons and ultrasound avoidance in crickets. *Frontiers in Neuroscience*, 6:95.

McDermott, J. H. (2009). The cocktail party problem. *Current Biology*, 19(22):R1024–R1027.

Merkel, F. and Wiltschko, W. (1965). Magnetismus und Richtungsfinden zugunruhiger Rotkehlchen (Erithacus rubecula). *Vogelwarte*, 23(1):71–77.

Metzen, M. G., Krahe, R., and Chacron, M. J. (2016). Burst firing in the electrosensory system of gymnotiform weakly electric fish: mechanisms and functional roles. *Frontiers in Computational Neuroscience*, 10:81.

Middleton, J. W., Harvey-Girard, E., Maler, L., and Longtin, A. (2007). Envelope gating and noise shaping in populations of noisy neurons. *Physical Review E*, 75:021918.

Middleton, J. W., Longtin, A., Benda, J., and Maler, L. (2006). The cellular basis for parallel neural transmission of a high-frequency stimulus and its low-frequency envelope. *Proceedings of the National Academy of Sciences*, 103:14596–14601.

Millman, R. E., Lorenzi, C., Apoux, F., Füllgrabe, C., Green, G. G., and Bacon, S. P. (2002). Effect of duration on amplitude-modulation masking. *The Journal of the Acoustical Society of America*, 111(6):2551–2554.

Moser, T. and Starr, A. (2016). Auditory neuropathy — neural and synaptic mechanisms. *Nature Reviews Neurology*, 12:189–149.

Myers, L., Lowery, M., O'malley, M., Vaughan, C., Heneghan, C., Gibson, A. S. C., Harley, Y., and Sreenivasan, R. (2003). Rectification and non-linear pre-processing of EMG signals for cortico-muscular analysis. *Journal of Neuroscience Methods*, 124(2):157–165.

Neiman, A. B. and Russell, D. F. (2011). Sensory coding in oscillatory electroreceptors of paddlefish. *Chaos: An Interdisciplinary Journal of Nonlinear Science*, 21(4).

Nelson, M. E. and MacIver, M. A. (1999). Prey capture in the weakly electric fish *Apteronotus albifrons*: sensory acquisition strategies and electrosensory consequences. *Journal of Experimental Biology*, 202(10):1195–1203.

Nelson, M. E., Xu, Z., and Payne, J. R. (1997). Characterization and modeling of P-type electrosensory afferent responses to amplitude modulations in a wave-type electric fish. *Journal of Comparative Physiology A*, 181(5):532–544.

Novikov, E. A. (1965). Functionals and the random-force method in turbulence theory. *Journal of Experimental Theoretical Physics*, 20(5):1290–1294.

Nowak, L. G., Azouz, R., Sanchez-Vives, M. V., Gray, C. M., and McCormick, D. A. (2003). Electrophysiological classes of cat primary visual cortical neurons in vivo as revealed by quantitative analyses. *Journal of Neurophysiology*, 89(3):1541–1566.

Ohm, G. S. (1839). Bemerkungen über Combinationstöne und Stösse. *Annalen der Physik*, 123(7):463–466.

Oswald, A. M., Chacron, M. J., Doiron, B., Bastian, J., and Maler, L. (2004). Parallel processing of sensory input by bursts and isolated spikes. *Journal of Neuroscience*, 24(18):4351–4362.

Ott, A. (2020). Modeling the heterogeneity of electrosensory afferents in electric fish. *Unpublished master thesis*, Eberhard Karls Universität Tübingen.

Özçete, O. D. and Moser, T. (2020). A sensory cell diversifies its output by varying Ca^{2+} influx-release coupling among active zones. *The EMBO Journal*, 40:e106010.

Palmer, A. and Russell, I. (1986). Phase-locking in the cochlear nerve of the guinea-pig and its relation to the receptor potential of inner hair-cells. *Hearing Research*, 24(1):1–15.

Peterson, A. J. and Heil, P. (2019). Phase locking of auditory-nerve fibers reveals stereotyped distortions and an exponential transfer function with a level-dependent slope. *Journal of Neuroscience*, 39(21):4077–4099.

Plomp, R. (1967). Beats of mistuned consonances. *The Journal of the Acoustical Society of America*, 42(2):462–474.

Preyer, S. and Gummer, A. W. (1996). Nonlinearity of mechanoelectrical transduction of outer hair cells as the source of nonlinear basilar-membrane motion and loudness recruitment. *Audiology and Neurotology*, 1(1):3–11.

Pugh Jr, E., Nikonov, S., and Lamb, T. (1999). Molecular mechanisms of vertebrate photoreceptor light adaptation. *Current Opinion in Neurobiology*, 9(4):410–418.

Quiroga, R. Q., Reddy, L., Kreiman, G., Koch, C., and Fried, I. (2005). Invariant visual representation by single neurons in the human brain. *Nature*, 435(7045):1102–1107.

Raab, T., Linhart, L., Wurm, A., and Benda, J. (2019). Dominance in habitat preference and diurnal explorative behavior of the weakly electric fish *Apteronotus leptorhynchus*. *Frontiers in Integrative Neuroscience*, 13:21.

Rhode, W. S. and Greenberg, S. (1994). Encoding of amplitude modulation in the cochlear nucleus of the cat. *Journal of Neurophysiology*, 71(5):1797–1825.

Rieke, F., Warland, D., Van Steveninck, R. d. R., and Bialek, W. (1999). *Spikes: exploring the neural code*. MIT press.

Roddey, J. C., Girish, B., and Miller, J. P. (2000). Assessing the performance of neural encoding models in the presence of noise. *Journal of Computational Neuroscience*, 8:95–112.

Roeber, A. (1834). Untersuchungen des Hrn. Scheibler in Crefeld über die sogenannten Schläge, Schwebungen oder Stösse. *Annalen der Physik*, 108(31-33):492–520.

Romani, G. L., Williamson, S. J., and Kaufman, L. (1982). Tonotopic organization of the human auditory cortex. *Science*, 216(4552):1339–1340.

Romei, V., Murray, M. M., Cappe, C., and Thut, G. (2009). Preperceptual and stimulus-selective enhancement of low-level human visual cortex excitability by sounds. *Current Biology*, 19(21):1799–1805.

Roux, I., Safieddine, S., Nouvian, R., Grati, M., Simmler, M.-C., Bahloul, A., Perfettini, I., Le Gall, M., Rostaing, P., Hamard, G., et al. (2006). Otoferlin, defective in a human deafness form, is essential for exocytosis at the auditory ribbon synapse. *Cell*, 127(2):277–289.

Ruggero, M. A., Rich, N. C., Recio, A., Narayan, S. S., and Robles, L. (1997). Basilar-membrane responses to tones at the base of the chinchilla cochlea. *The Journal of the Acoustical Society of America*, 101(4):2151–2163.

Ruggero, M. A., Robles, L., and Rich, N. C. (1992). Two-tone suppression in the basilar membrane of the cochlea: Mechanical basis of auditory-nerve rate suppression. *Journal of Neurophysiology*, 68(4):1087–1099.

Sachs, M. B. and Abbas, P. J. (1974). Rate versus level functions for auditory-nerve fibers in cats: tone-burst stimuli. *The Journal of the Acoustical Society of America*, 56(6):1835–1847.

Sachs, M. B. and Kiang, N. Y. (1968). Two-tone inhibition in auditory-nerve fibers. *The Journal of the Acoustical Society of America*, 43(5):1120–1128.

Salazar, V. and Silva, A. (2022). Neural processing: Cracking the code to extract relevant social information. *Current Biology*, 32(1):R32–R34.

Salazar, V. L., Krahe, R., and Lewis, J. E. (2013). The energetics of electric organ discharge generation in gymnotiform weakly electric fish. *Journal of Experimental Biology*, 216(13):2459–2468.

Savard, M., Krahe, R., and Chacron, M. (2011). Neural heterogeneities influence envelope and temporal coding at the sensory periphery. *Neuroscience*, 172:270–284.

Scheich, H., Bullock, T. H., and Hamstra Jr, R. (1973). Coding properties of two classes of afferent nerve fibers: high-frequency electroreceptors in the electric fish, *Eigenmannia*. *Journal of Neurophysiology*, 36(1):39–60.

Schiff, W., Caviness, J. A., and Gibson, J. J. (1962). Persistent fear responses in rhesus monkeys to the optical stimulus of "looming". *Science*, 136(3520):982–983.

Schlungbaum, M. and Lindner, B. (2023). Detecting a periodic signal by a population of spiking neurons in the weakly nonlinear response regime. *The European Physical Journal E*, 46(11):108.

Schmiedt, R. A. (1982). Boundaries of two-tone rate suppression of cochlear-nerve activity. *Hearing Research*, 7(3):335–351.

Schneider, A. D., Cullen, K. E., and Chacron, M. J. (2011). In vivo conditions induce faithful encoding of stimuli by reducing nonlinear synchronization in vestibular sensory neurons. *PLoS Computational Biology*, 7(7):e1002120.

Sinz, F. H., Sachgau, C., Henninger, J., Benda, J., and Grewe, J. (2020). Simultaneous spike-time locking to multiple frequencies. *Journal of Neurophysiology*, 123(6):2355–2372.

Smith, G. T. (2013). Evolution and hormonal regulation of sex differences in the electrocommunication behavior of ghost knifefishes (Apteronotidae). *Journal of Experimental Biology*, 216:2421–2433.

Stamper, S. A., Carrera-G, E., Tan, E. W., Fugère, V., Krahe, R., and Fortune, E. S. (2010). Species differences in group size and electrosensory interference in weakly electric fishes: Implications for electrosensory processing. *Behavioural Brain Research*, 207(2):368 – 376.

Stamper, S. A., Madhav, M. S., Cowan, N. J., and Fortune, E. S. (2012). Beyond the Jamming Avoidance Response: weakly electric fish respond to the envelope of social electrosensory signals. *Journal of Experimental Biology*, 215:4196–4207.

Steinbach, A. B. (1970). Diurnal movements and discharge characteristics of electric gymnotid fishes in the Rio Negro, Brazil. *The Biological Bulletin*, 138:200–210.

Stoewer, A., Kellner, C. J., Benda, J., Wachtler, T., and Grewe, J. (2014). File format and library for neuroscience data and metadata. *Frontiers of Neuroinformatics*, 8(27):10–3389.

Sumner, C. J. and Palmer, A. R. (2012). Auditory nerve fibre responses in the ferret. *European Journal of Neuroscience*, 36(4):2428–2439.

Szabo, T. (1965). Sense organs of the lateral line system in some electric fish of the Gymnotidae, Mormyridae and Gymnarchidae. *Journal of Morphology*, 117(2):229–249.

Tan, E. W., Nizar, J. M., Carrera-G, E., and Fortune, E. S. (2005). Electrosensory interference in naturally occurring aggregates of a species of weakly electric fish, *Eigenmannia virescens*. *Behavioural Brain Research*, 164:83–92.

Treutwein, B. and Strasburger, H. (1999). Fitting the psychometric function. *Perception & Psychophysics*, 61(1):87–106.

Viancour, T. A. (1979). Electroreceptors of a weakly electric fish. *Journal of Comparative Physiology*, 133(4):327–338.

Vilà, C., Maldonado, J. E., and Wayne, R. K. (1999). Phylogenetic relationships, evolution, and genetic diversity of the domestic dog. *Journal of Heredity*, 90(1):71–77.

Voronenko, S. O. and Lindner, B. (2017). Weakly nonlinear response of noisy neurons. *New Journal of Physics*, 19(3):033038.

Wachtel, A. W. and Szamier, R. B. (1966). Special cutaneous receptor organs of fish: the tuberous organs of *Eigenmannia*. *Journal of Morphology*, 119:51–80.

Wallach, A., Melanson, A., Longtin, A., and Maler, L. (2022). Mixed selectivity coding of sensory and motor social signals in the thalamus of a weakly electric fish. *Current Biology*, 32:51–63.

Walz, H., Grewe, J., and Benda, J. (2014). Static frequency tuning accounts for changes in neural synchrony evoked by transient communication signals. *Journal of Neurophysiology*, 112:752–765.

Walz, H., Hupé, G. J., Benda, J., and Lewis, J. E. (2013). The neuroethology of electrocommunication: How signal background influences sensory encoding and behaviour in *Apteronotus leptorhynchus*. *Journal of Physiology-Paris*, 107:13–25.

Watanabe, A. and Takeda, K. (1963). The change of discharge frequency by A.C. stimulus in a weak electric fish. *Journal of Experimental Biology*, 40:57–66.

Wöhr, M. and Schwarting, R. K. (2007). Ultrasonic communication in rats: can playback of 50-kHz calls induce approach behavior? *PloS one*, 2(12):e1365.

Womack, M. D. and Khodakhah, K. (2004). Dendritic control of spontaneous bursting in cerebellar Purkinje cells. *Journal of Neuroscience*, 24(14):3511–3521.

Wypych, M., Wang, C., Nagy, A., Benedek, G., Dreher, B., and Waleszczyk, W. J. (2012). Standardized F1–A consistent measure of strength of modulation of visual responses to sine-wave drifting gratings. *Vision Research*, 72:14–33.

Xu, Z., Payne, J. R., and Nelson, M. E. (1996). Logarithmic time course of sensory adaptation in electrosensory afferent nerve fibers in a weakly electric fish. *Journal of Neurophysiology*, 76(3):2020–2032.

Yin, T. C., Smith, P. H., and Joris, P. X. (2019). Neural mechanisms of binaural processing in the auditory brainstem. *Comprehensive Physiology*, 9(4):1503–1575.

Young, E. D. and Sachs, M. B. (1979). Representation of steady-state vowels in the temporal aspects of the discharge patterns of populations of auditory-nerve fibers. *The Journal of the Acoustical Society of America*, 66(5):1381–1403.

Yu, N., Hupé, G., Garfinkle, C., Lewis, J. E., and Longtin, A. (2005). Coding conspecific identity and motion in the electric sense. *PLoS Computational Biology*, 8:e1002564.

Zakon, H. H., Oestreich, J., Tallarovic, S., and Triefenbach, F. (2002). EOD modulations of brown ghost electric fish: JARs, chirps, rises, and dips. *Journal of Physiology-Paris*, 96(5–6):451–458.

Zeldenrust, F., Wadman, W. J., and Englitz, B. (2018). Neural coding with bursts—current state and future perspectives. *Frontiers in Computational Neuroscience*, 12:48.

Appendix A

Appendix

A.1 Mathematical derivations

These mathematical derivations have already been published in Barayeu et al. (2023).

A.1.1 Analytic signal

The analytic signal that corresponds to the original signal is constructed using the Hilbert transform. With this method any signal can be expressed as a product

$$x(t) = A(t)\cos(\varphi(t)) \tag{A.1}$$

where $\varphi(t)$ is the phase of the analytic signal and the amplitude modulation $A(t)$ is the absolute value of the analytic signal. The carrier $\cos(\varphi(t))$ amplitude is modulated by $A(t)$. The Hilbert transform itself is a linear operation, but taking the absolute value is a nonlinear operation.

For the superimposed cosines in Eq. (3.1), we get the amplitude modulation

$$A(t) = |x(t)| = \sqrt{1 + \alpha^2 + 2\alpha\cos((\omega_2 - \omega_1)t)} \tag{A.2}$$

and for the phase

$$\varphi(t) = \frac{\omega_1 + \omega_2}{2}\,t + \arctan\left(\frac{1-\alpha}{1+\alpha}\cdot\tan\left(\frac{\omega_1 - \omega_2}{2}\,t\right)\right) \tag{A.3}$$

(Stamper et al., 2012), that is an exact identity. The Hilbert transform is a mathematical trick to transform any signal into such a product of a cosine carrier and an amplitude modulation.

For $\alpha = 1$ both cosine waves have the same amplitude and this reduces to the well-known identity

$$x(t) = 2\cos\left(\frac{\omega_2 - \omega_1}{2}t\right)\cos\left(\frac{\omega_1 + \omega_2}{2}t\right) \tag{A.4}$$

Thereby the carrier signal of frequency $(\omega_1 + \omega_2)/2$ is multiplied with an amplitude modulation with frequency $(\omega_1 - \omega_2)/2$ and the latter frequency is half the frequency of the beating amplitude modulation.

For small amplitudes $\alpha \to 0$ the expansion of the amplitude modulation to first-order results in

$$A(t) \approx 1 + \alpha\cos(\Delta\omega t) \tag{A.5}$$

Thereby, this amplitude modulation has a constant zero-frequency component in the Fourier spectrum and one at the difference frequency $\Delta\omega = \omega_2 - \omega_1$. More and more harmonics of this peak appear for larger amplitudes.

This is exactly what is expected for low difference frequencies, i.e. for stimulus frequencies ω_2 close to ω_1. However, for higher difference frequencies, the analytic signal amplitude Eq. (A.5) suggests that the beat frequency keeps increasing with increasing difference frequency, no matter how large the difference frequency is (Fig. A.1 A). This amplitude does not explain the aliasing structure we observe in the signals and the response of P-units. This does not imply that the analytic signal is incorrect. Rather the amplitude term Eq. (A.5) does not capture the obvious aliasing structure of the beats, that is hidden in the phase term Eq. (A.3).

At first glance, for small amplitudes, the carrier phase simplifies to $\varphi(t) = \omega_1 t$. But, this is valid only for $\alpha = 0$, since only then $\frac{1-\alpha}{1+\alpha} = 1$ is in Eq. (A.3). The resulting small-amplitude approximation

$$x(t) \approx (1 + \alpha \cos(\Delta\omega t)) \cos(\omega_1 t) \tag{A.6}$$

is in reality not a good approximation. The Fourier spectrum now has two side-peaks at $\omega_1 \pm \Delta\omega$ instead of one at $\omega_1 + \Delta\omega = \omega_2$ flanking the carrier at ω_1. Eq. (A.6) is no longer a beat resulting from the superposition of two cosine waves, but instead, it is a sinusoidal amplitude modulation (SAM). The approximation fails because the $\frac{1-\alpha}{1+\alpha}$-term in Eq. (A.3) quickly deviates from one with a slope of -2 as the amplitude increases.

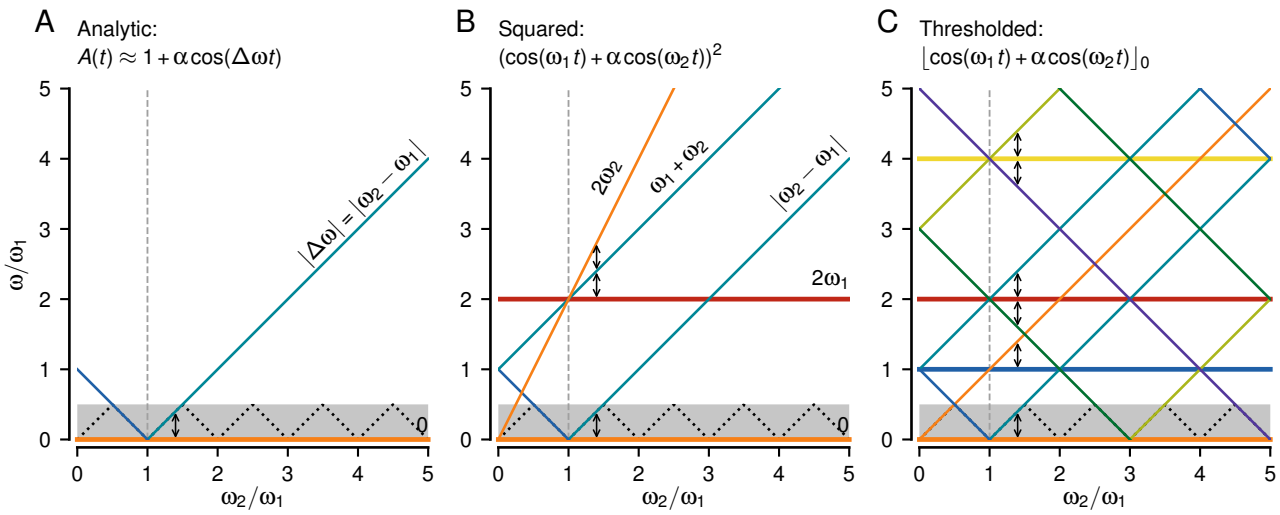

Figure A.1: Spectral peaks in analytic, squared, and thresholded signals of superimposed cosine waves, Eq. (3.1). Related to Fig. 3.5. Plotted are the positions of peaks in the spectrum as a function of the stimulus frequency ω_2 relative to the carrier frequency ω_1. For a given stimulus frequency, the corresponding spectrum is a vertical slice through the graph. Vertical arrows highlight the difference frequency $\Delta\omega = \omega_2 - \omega_1$. Frequencies below $\omega_1/2$ are marked by the gray background at the bottom. The black dotted line in this frequency band indicates the folded frequencies at $\omega_f = |\omega_2 - \omega_1 \lfloor \omega_2/\omega_1 \rceil|$.
A The amplitude modulation Eq. (A.5) computed as the magnitude of the analytic signal utilizing a Hilbert transform has peaks only at 0 and at the absolute difference frequency $|\Delta\omega|$.
B Squaring also generates the difference frequency and an offset at zero frequency. In addition, three more peaks appear at $2\omega_1$, $2\omega_2$, and $\omega_1 + \omega_2$, Eq. (A.7).
C Thresholding the signal results in many more peaks. Convolution of the spectrum of the pulsetrain, Eqs. (A.8) and (A.9), with the one of the carrier results in horizontal lines at even multiples of ω_1, Eq. (A.11), and at ω_1, Eq. (A.12). Of interest, however, are the peaks that depend on ω_2. They appear around odd multiples of ω_1, Eq. (A.13), and around 0, Eq. (A.14).

A.1.2 Squaring

An alternative method to retrieve the amplitude modulation is to square the signal and subsequently low-pass filter it. Squaring the beat Eq. (3.1), using the binomial theorem and the trigonometric power reduction formula results in

$$\begin{aligned} x^2(t) =& \tfrac{1}{2}(1+\alpha^2) + \tfrac{1}{2}\cos(2\omega_1 t) + \tfrac{1}{2}\alpha^2\cos(2\omega_2 t) \\ &+ \alpha\cos((\omega_2-\omega_1)t) + \alpha\cos((\omega_1+\omega_2)t) \end{aligned} \tag{A.7}$$

While the original signal Eq. (3.1) has two peaks in the power spectrum at ω_1 and ω_2 and no peak at the beat frequency, the power spectrum of the squared signal Eq. (A.7) now has five peaks, one for each term (Fig. A.1 B). Shifting or generating new peaks in the spectrum are hallmarks of nonlinear operations. The squaring operation on the one hand doubles the two original frequencies and also creates a new high-frequency peak at the sum of the two frequencies. A new peak representing the non-zero mean of the squared signal occurs at zero. Another peak, that represents the amplitude modulation, appears at the difference frequency $\omega_2 - \omega_1$. This peak can be isolated by subsequent low-pass filtering and this way the amplitude modulation can be retrieved. As for the analytic signal, none of the five terms can explain the aliasing structure of the beat at high difference frequencies.

A.1.3 Thresholding

The Fourier spectrum of the pulse train, Eq. (3.4), has peaks at odd multiples of ω_1 with amplitudes

$$\begin{aligned} c_k =& \frac{\omega_1}{2\pi}\int_{-\frac{\pi}{2\omega_1}}^{+\frac{\pi}{2\omega_1}} e^{-i\omega_1 k t}\, dt = \frac{1}{\pi k}\sin\left(\tfrac{\pi}{2}k\right) \\ =& \frac{1}{\pi k}(-1)^{\frac{k-1}{2}}\ , \quad k \text{ odd} \end{aligned} \tag{A.8}$$

and a peak at zero frequency with amplitude

$$c_0 = \frac{\omega_1}{2\pi}\left[t\right]_{-\frac{\pi}{2\omega_1}}^{+\frac{\pi}{2\omega_1}} = \frac{1}{2} \tag{A.9}$$

Thresholding a cosine with the same frequency ω_1 can be approximated by multiplying the cosine with the pulse train in Eq. (3.4):

$$\lfloor\cos(\omega_1 t)\rfloor_0 = \cos(\omega_1 t)\cdot p(\omega_1 t) \tag{A.10}$$

The corresponding Fourier spectrum is the convolution of the spectrum of the pulse train with the spectrum of the cosine with peaks of amplitude 1/2 at $\pm\omega_1$. The cosine peaks are shifted to the positions of pulse train peaks and multiplied with their amplitudes. Two neighboring peaks of the pulse train at odd multiples of ω_1 contribute to a peak at even multiples of ω_1 with amplitude

$$\tilde{a}_k = \frac{1}{2}c_{k+1} + \frac{1}{2}c_{k-1} = \frac{1}{\pi}(-1)^{\frac{k}{2}}\frac{1}{1-k^2}\ , \quad k \text{ even} \tag{A.11}$$

The zero-frequency peak of the pulse train gives rise to peaks at $\pm\omega_1$ with amplitude

$$\tilde{a}_{\pm 1} = \frac{1}{2}c_0 = \frac{1}{4} \tag{A.12}$$

The spectrum of the thresholded superimposed cosine waves (Fig. A.1 C) is composed of the spectrum of the pulse train convolved with the spectrum of the stimulus cosine with peaks of

amplitude $\alpha/2$ at frequencies $\pm\omega_2$ and with the spectrum of the carrier cosine, Eqs. (A.11) and (A.12). For the stimulus cosine, each peak of the pulse train at odd multiples of ω_1 is replaced by a pair of peaks at frequencies $k\omega_1 \pm \omega_2$ with amplitudes

$$a_k = \frac{\alpha}{2} c_k = \frac{\alpha}{2} \frac{1}{\pi k} (-1)^{\frac{k-1}{2}} \quad , \quad k \text{ odd} \tag{A.13}$$

These amplitudes are negative, so they introduce a phase shift by π, for every second odd k ($k = 3, 7, 11, \ldots$).

The zero-frequency peak of the pulse train, Eq. (A.9), leads to two peaks at $\pm\omega_2$ with amplitude

$$a_0 = \frac{\alpha}{2} c_0 = \frac{\alpha}{4} \tag{A.14}$$

The relative amplitudes $\bar{a}_k = a_k/a_0$ introduced by thresholding up to $k = 5$ multiples of ω_1 of the envelope frequencies are $\bar{a}_0 = 100\,\%$, $\bar{a}_1 = \frac{2}{\pi} \approx 64\,\%$, $\bar{a}_2 = 0$, $\bar{a}_3 \approx -\frac{2}{3\pi} = -21\,\%$, $\bar{a}_4 = 0$, and $\bar{a}_5 \approx \frac{2}{5\pi} = 13\,\%$.

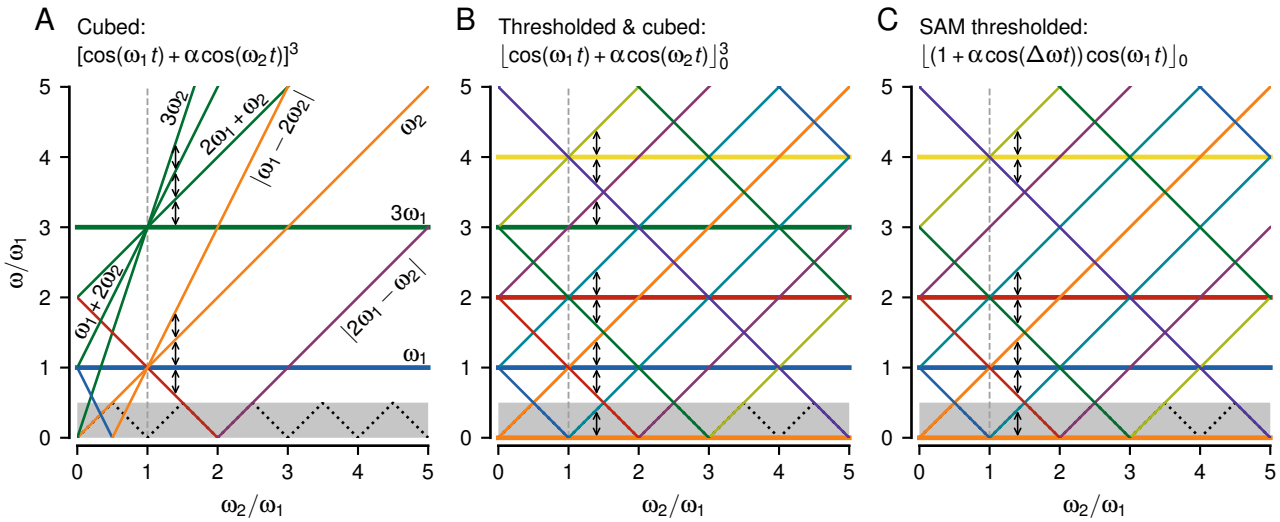

Figure A.2: Spectral peaks in cubed and cubed-thresholded superimposed cosine waves as well as for thresholded SAMs. Related to Fig. 3.6. Same style as Fig. A.1.
A Spectral peaks, Eq. (A.15), resulting from taking the signal to the power of three.
B Major peaks resulting from thresholding and cubing the signal. Peaks not depending on ω_2 (horizontal lines) appear at even multiples of ω_1, Eq. (A.17), at ω_1, Eq. (A.18), and $3\omega_1$, Eq. (A.19). The dominant stimulus-dependent peaks (diagonal lines) appear around odd multiples of ω_1, Eq. (A.20), and the zeroth multiple, Eq. (A.21), as for the threshold operation without exponent. In addition, however, we get a stimulus-dependent peak around twice the carrier frequency, Eq. (A.22).
C All spectral peaks of a thresholded SAM stimulus, Eq. (A.23). Below half the carrier frequency (gray band) it results in the very same peaks as thresholded and cubed superimposed cosines.

A.1.4 Threshold cubed

Taking the signal in Eq. (3.1), to the power of three results in

$$\begin{aligned} x^3(t) &= (\cos(\omega_1 t) + \alpha\cos(\omega_2 t))^3 && \text{(A.15)}\\ &= \tfrac{3}{4}(1+2\alpha^2)\cos(\omega_1 t) + \underline{\tfrac{3}{4}(2\alpha+\alpha^3)\cos(\omega_2 t)}\\ &\quad + \tfrac{1}{4}\cos(3\omega_1 t) + \tfrac{1}{4}\alpha\cos(3\omega_2 t)\\ &\quad + \underline{\tfrac{3}{4}\alpha\cos((2\omega_1+\omega_2)t)} + \underline{\tfrac{3}{4}\alpha\cos((2\omega_1-\omega_2)t)}\\ &\quad + \tfrac{3}{4}\alpha^2\cos((\omega_1+2\omega_2)t) + \tfrac{3}{4}\alpha^2\cos((\omega_1-2\omega_2)t) && \text{(A.16)} \end{aligned}$$

(Fig. A.2 A). The dominant peaks that depend on ω_2 are at ω_2 and $|2\omega_1 \pm \omega_2|$ (underlined).

Convolving the spectrum of the cubed signal, Eq. (A.16), with the spectrum of the pulse train, Eqs. (A.8) and (A.9), approximating the threshold operation, Eq. (3.2), boils down to replacing all the peaks in the pulse train spectrum with the ones of the cubed signal spectrum shifted to the respective positions (Fig. 3.6 A–C). In the following calculations we ignore all terms of higher order in α.

The two purely ω_1-dependent terms with peaks at $\pm\omega_1$ and $\pm 3\omega_1$ result in peaks at even multiples of ω_1 with amplitudes

$$\begin{aligned} \tilde{b}_k &= \tfrac{1}{2}\tfrac{3}{4}(c_{k+1}+c_{k-1}) + \tfrac{1}{2}\tfrac{1}{4}(c_{k+3}+c_{k-3})\\ &= \frac{3}{4\pi}(-1)^{\frac{k}{2}}\left(\frac{1}{1-k^2} - \frac{1}{9-k^2}\right), \quad k \text{ even} \end{aligned} \qquad \text{(A.17)}$$

and also in peaks directly at $\pm\omega_1$ and $\pm 3\omega_1$ with amplitudes

$$\tilde{b}_{\pm 1} = \tfrac{1}{2}\tfrac{3}{4}c_0 = \frac{3}{16} \qquad \text{(A.18)}$$

$$\tilde{b}_{\pm 3} = \tfrac{1}{2}\tfrac{1}{4}c_0 = \frac{1}{16} \qquad \text{(A.19)}$$

(horizontal lines in Fig. A.2 B). The latter peak at the third harmonics of ω_1 is a new peak that is not generated by the threshold without exponent.

Convolving the dominant ω_2 dependent terms in Eq. (A.15) with the peaks at odd multiples of ω_1 of the pulse train, Eq. (A.8), lead to peaks at $k\omega_1 \pm \omega_2$ for odd k with amplitudes

$$\begin{aligned} b_k &= \tfrac{1}{2}\tfrac{3}{4}2\alpha c_k + \tfrac{1}{2}\tfrac{3}{4}\alpha(c_{k+2}+c_{k-2})\\ &= \frac{3}{\pi}\alpha(-1)^{\frac{k+1}{2}}\frac{1}{k(k^2-4)}, \quad k \text{ odd} \end{aligned} \qquad \text{(A.20)}$$

These are the same frequency peaks as for the threshold without exponent but with different amplitudes.

From the convolution with the zero-frequency term of the pulse train, Eq. (A.9), additional peaks at $\pm\omega_2$ and $\pm(2\omega_1 \pm \omega_2)$ appear with amplitudes

$$b_0 = \tfrac{1}{2}\tfrac{3}{4}2\alpha c_0 = \frac{3}{8}\alpha \qquad \text{(A.21)}$$

$$b_{\pm 2} = \tfrac{1}{2}\tfrac{3}{4}\alpha c_0 = \frac{3}{16}\alpha \qquad \text{(A.22)}$$

The latter peak is the one the power of three adds to the folding frequencies around the second ω_1 multiple (Fig. A.2 B).

The relative amplitudes $\bar{b}_k = b_k/b_0$ of the envelope frequencies introduced by a threshold with an exponent of three are all positive and read $\bar{b}_0 = 100\,\%$, $\bar{b}_1 = \frac{8}{3\pi} \approx 85\,\%$, $\bar{b}_2 = \frac{1}{2} = 50\,\%$, $\bar{b}_3 \approx \frac{8}{15\pi} = 17\,\%$, $\bar{b}_4 = 0$, and $\bar{b}_5 \approx \frac{8}{105\pi} = 2.4\,\%$.

A.1.5 Thresholding a SAM

A sinusoidal amplitude modulation (SAM) of frequency $\Delta\omega$ and amplitude α is multiplied with a carrier signal with frequency ω_1:

$$x(t) = (1 + \alpha \cos(\Delta\omega t)) \cos(\omega_1 t) \tag{A.23}$$

According to the convolution theorem, the spectrum of this signal is a convolution of the spectrum of the amplitude modulation with a peak of amplitude 1 at 0 and two peaks at $\pm\Delta\omega$ with amplitudes $\frac{\alpha}{2}$ and the spectrum of the carrier with peaks at $\pm\omega_1$ and amplitude $\frac{1}{2}$. The resulting SAM signal spectrum has peaks at $\pm\omega_1$ with amplitude $\frac{1}{2}$, at $\pm(\omega_1 + \Delta\omega) = \pm\omega_2$ with amplitude $\frac{\alpha}{4}$, and at $\pm(\omega_1 - \Delta\omega) = \pm(2\omega_1 - \omega_2)$ also with amplitude $\frac{\alpha}{4}$. These latter are additional peaks that are not present in the superimposed cosine signal, Eq. (3.1).

For the SAM the threshold operation, Eq. (3.2), can be replaced by a multiplication with a pulse train, Eqs. (3.3) and (3.4). Since the amplitude modulation does not change the zero crossings of the signal, this is possible for all stimulus amplitudes $\alpha < 1$. Using the results from above, the convolution of the peaks at $\pm\omega_1$ with the pulse spectrum results in peaks at even multiples of ω_1 and at ω_1 with amplitudes Eqs. (A.11) and (A.12), respectively. The convolution of the peaks at $\pm\omega_2$ results in peaks at $k\omega_1 \pm \omega_2$ for odd k and $k = 0$ with half of the amplitudes given in Eqs. (A.13) and (A.14), respectively. The new peaks of the SAM at $\pm(\omega_1 - \Delta\omega)$ are shifted to the peaks of the pulse train and appear at $k\omega_1 \pm (\omega_1 - \Delta\omega) = (k \pm 2)\omega_1 \mp \omega_2$ for odd k with half the amplitudes of Eq. (A.13) and for $k = 0$ at $\pm(2\omega_1 - \omega_2)$ with half the amplitude of Eq. (A.14). The latter peaks fill in the envelope frequencies close to two multiples of ω_1.

A.1.6 Harmonics of the carrier

In reality, the carrier EOD is not a cosine but a complex periodic wave and thus already has harmonics at multiples of the carrier frequency. Are these not enough to explain the aliasing structure of the signal envelopes without any nonlinearities?

Even if the carrier has harmonics, still at least a threshold would be required. The reason is that the only frequency component depending on the stimulus frequency without any nonlinearity still would be the stimulus itself. With a threshold, Eq. (3.2), that is approximated by multiplication with a pulse train, Eq. (3.4), the harmonics of the carrier EOD still would add peaks to the resulting spectrum only at multiples of the carrier frequency. Then the stimulus frequency still would be just convolved with the spectrum of the pulse train. As in the case of the pure sine-wave carrier, the stimulus frequency would then appear only as envelope frequencies around odd multiples of the carrier frequency and around zero frequency, Eqs. (A.13) and (A.14), but not at even carrier multiples.

The carrier EOD harmonics modify the waveform. Thus it is not a sine wave anymore staying positive for exactly half of the time and negative for the other half. Instead, the harmonics can distort the waveform in a way that one would need a pulse train with a duty cycle different than 50 % to emulate a threshold. Some *A. leptorhynchus* have a waveform that is wider than a sine wave at its zero crossings (Fig. 3.9 A) and a matching pulse train would need a higher duty cycle (Fig. 3.9 B). To account for this effect we parameterize the pulse train by its duty cycle δ:

$$p(\omega_1 t; \delta) = \begin{cases} 1 & ; \quad -\delta\frac{\pi}{\omega_1} < t \bmod \frac{2\pi}{\omega_1} < \delta\frac{\pi}{\omega_1} \\ 0 & ; \quad \text{else} \end{cases} \tag{A.24}$$

Changing the duty cycle leads to modifications of the pulse train spectrum:

$$c_k(\delta) = \frac{1}{\pi k} \sin(\pi k \delta) \ , \quad k \neq 0 \tag{A.25}$$

$$c_0(\delta) = \delta \ , \quad k = 0 \tag{A.26}$$

(Fig. 3.9 B). In particular, a peak at the second carrier multiple appears with amplitude $c_2(\delta) = \frac{1}{2\pi}\sin(2\pi\delta)$. This peak is then convolved with the stimulus and can fill in envelope frequencies around the second multiple (Fig. 3.9 C). The amplitude of the second multiple of the pulse train equals zero for $\delta = \frac{1}{2}$ and grows linearly in δ according to $c_2(\delta) \approx \frac{1}{2} - \delta$ as the duty cycle deviates from $\frac{1}{2}$. According to $c_2/c_1 = \cos(\pi\delta)$, if the duty cycle approaches zero or one the amplitude of the second multiple can get as large as the one of the fundamental. But now the envelope frequencies at the third multiple are missing because increasing the duty cycle reduces the third multiple of the pulse train.

In summary, the carrier harmonics themselves cannot contribute to the extraction of envelope frequencies. However, the changed carrier waveform duty cycle modifies the spectrum of the corresponding pulse train, approximating the threshold operation. Depending on this duty cycle of the carrier some harmonics are suppressed and others enhanced.

A.1.7 Harmonics of the stimulus

Alternatively, one could keep the carrier as a sine wave and use a realistic EOD for the stimulus. The signal spectrum components relevant for explaining envelope frequencies resulting from the convolution of the spectrum of a pulse train with a 50 % duty cycle, Eqs. (A.8) and (A.9), matching the sinusoidal carrier, with all the harmonics of the stimulus. However, for extracting the aliasing structure of the envelopes, only the stimulus fundamental is relevant. The higher harmonics introduce frequencies depending on stimulus frequency multiples and thus cannot explain the envelope frequencies that grow directly proportionally with the stimulus frequency.

A.1.8 Tuning of P-units to EOD frequency

When silencing the fish's EOD and measuring the minimum amplitude of an artificial replacement EOD that makes a P-unit fire action potentials one can retrieve in V-shaped threshold curves that are centered at the fish's EOD frequency (Fig. A.3 A, Hopkins (1976)). The reason for the corresponding band-pass filter is probably the electric resonance in the electroreceptor cells (Viancour, 1979). This behavior could be modeled by a damped harmonic oscillator that filters the input signal before it is thresholded at the receptor synapse (Sinz et al., 2020).

To model this resonance filter in the P-unit models the stimulus $x(t)$ is replaced Eqs. (2.13) – (2.12), by the output $y(t)$ of a harmonic oscillator

$$\frac{d^2y(t)}{dt^2} + 2\zeta w_0 \frac{dy(t)}{dt} + \zeta w_0^2 y(t) = x(t) \tag{A.27}$$

multiplied with a normalization factor β. Thereby the external force to the oscillator is the stimulus $x(t)$, ζ is the damping ratio of the harmonic oscillator, and

$$w_0 = \frac{w_R}{\sqrt{1-2\zeta^2}} \tag{A.28}$$

is the eigenfrequency. Thereby $w_R = 2\pi f_R$ is the resonance frequency that was set to the measured f_{EOD} of each fish. The normalization factor

$$\beta = 70 w_R \sqrt{(2w_0\zeta)^2 + (w_R^2 - w_0^2)^2/w_R^2} \tag{A.29}$$

makes sure that the fish's EOD passes through the damped oscillator with a gain of one. The harmonic oscillator was solved by using the differential equation solver from SciPy.

Here ζ was varied from almost no damping (0.7) to a very strong damping (0.1). A too-strong damping factor of high frequencies can be compensated by increasing the exponent at the

threshold. Thereby several damping factor and threshold exponent combinations yield similar results of P-units' responses.

An exponent of $p = 5$ and a mild damping coefficient of $\zeta = 0.45$ sufficient to reproduce the tuning of P-unit responses to f_{EOD} as reported by Hopkins (1976) (Fig. A.3 B). This model still can reproduce the responses to beats up to three multiples of the f_{EOD} (Fig. A.3 C, D). This suggests that the EOD filter does not impede the response of P-units to high difference frequencies.

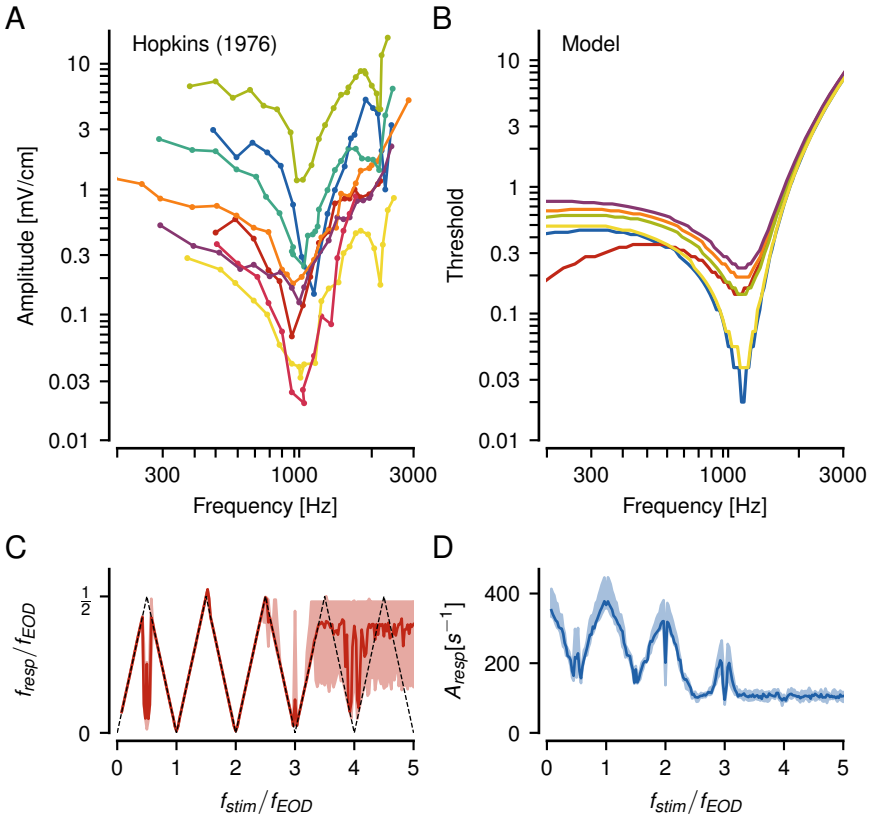

Figure A.3: . Effects of the EOD frequency filter of P-units.
A Sensitivity of P-unit afferents to EOD frequency as reported by Hopkins (1976). The measured stimulus amplitudes were the minimum amplitude required to elicit a just noticeable difference in firing rates of the P-units.
B Corresponding sensitivities of the here used LIF models supplemented by a harmonic oscillator Eq. (A.27). The amplitudes elicited an increase in firing rate of 10 % compared to the baseline rate without stimulus.
C & D The frequency f_{resp} and corresponding response amplitudes of these P-unit models to beats still reproduce the observed P-unit tuning to beats in Fig. 3.3 despite the EOD filter.

Appendix B

Statement of Contributions

B.1 Chapter 3: Nonlinearity at high beat frequencies

- Electrophysiological experiments: 80% Ramona Schäfer, 20% Alexandra Barayeu
- Behavioral experiments: Alexandra Barayeu
- Data analysis: Alexandra Barayeu
- Modeling and simulations: Alexandra Barayeu
- First draft of the manuscript: Alexandra Barayeu
- Editing and finalizing of the manuscript: Alexandra Barayeu, Jan Benda, Jan Grewe
- Mathematics (see section A.1): Jan Benda
- In regular meetings Jan Benda and Jan Grewe provided valuable input to the process of data analysis, modeling and writing. Experiments were supervised by Jan Grewe.

B.2 Chapter 4: Second-order susceptibility in a three-fish setting

- Electrophysiological experiments: Reused data previously recorded in the lab of Jan Benda.
- Data analysis: Alexandra Barayeu
- Modeling and simulations: Alexandra Barayeu
- Writing of the thesis chapter: Alexandra Barayeu
- In regular meetings Benjamin Lindner, Maria Schlungbaum, Jan Benda and Jan Grewe provided valuable input to the process of data analysis, modeling and writing.

B.3 Chapter 5: Nonlinearities can improve faint signal detection

- Modeling, simulations and analysis: Alexandra Barayeu

- Writing of the thesis chapter: Alexandra Barayeu
- In regular meetings Benjamin Lindner, Maria Schlungbaum, Jan Benda and Jan Grewe provided valuable input to the process of modeling and writing.

B.4 Chapter 6: Encoding of strong beat amplitudes

- Electrophysiological experiments: Alexandra Barayeu
- Data analysis: Alexandra Barayeu
- Modeling and simulations: Alexandra Barayeu
- Writing of the thesis chapter: Alexandra Barayeu
- Jan Benda and Jan Grewe provided valuable input to the process of data analysis, modeling and writing.